

1004 413

AE

AFFDL-TR-72-83

Volume I

**PREDICTION OF SIX-DEGREE-OF-FREEDOM  
STORE SEPARATION TRAJECTORIES  
AT SPEEDS UP TO THE CRITICAL SPEED**

**Volume I - Theoretical Methods and Comparisons  
With Experiment**

*NIELSEN ENGINEERING & RESEARCH, INC.*

*TR-37*

TECHNICAL REPORT AFFDL-TR-72-83, VOLUME I

OCTOBER 1974

Approved for public release; distribution unlimited.

AE

AIR FORCE FLIGHT DYNAMICS LABORATORY  
AIR FORCE SYSTEMS COMMAND  
WRIGHT-PATTERSON AIR FORCE BASE, OHIO 45433

## NOTICE

When Government drawings, specifications, or other data are used for any purpose other than in connection with a definitely related Government procurement operation, the United States Government thereby incurs no responsibility nor any obligation whatsoever; and the fact that the Government may have formulated, furnished, or in any way supplied the said drawings, specifications, or other data, is not to be regarded by implication or otherwise as in any manner licensing the holder or any other person or corporation, or conveying any rights or permission to manufacture, use, or sell any patented invention that may in any way be related thereto.

Copies of this report should not be returned unless return is required by security considerations, contractual obligations, or notice on a specific document.

PREDICTION OF SIX-DEGREE-OF-FREEDOM  
STORE SEPARATION TRAJECTORIES AT  
SPEEDS UP TO THE  
CRITICAL SPEED

Volume I - Theoretical Methods and Comparisons  
With Experiment

Frederick K. Goodwin  
Marnix F. E. Dillenius  
Jack N. Nielsen

Approved for public release; distribution unlimited

FOREWORD

This report, "Prediction of Six-Degree-of-Freedom Store Separation Trajectories at Speeds up to the Critical Speed," describes a combined theoretical-experimental program directed toward developing a computer program for predicting the trajectory of an external store dropped from an aircraft of the fighter-bomber type at speeds up to the critical speed. This volume, Volume I - "Theoretical Methods and Comparisons with Experiment," describes the theoretical approach and presents extensive comparisons with experimental data. The second volume, Volume II - "Users Manual for the Computer Programs," presents detailed instructions on the use of the computer programs.

The work was carried out by Nielsen Engineering & Research, Inc., 850 Maude Avenue, Mountain View, California 94040, under Contract No. F33615-71-C-1116. The contract was initiated under Project 8219, Task 821902, of the Air Force Flight Dynamics Laboratory. The Air Force Project Engineer on the contract was Mr. Jerry E. Jenkins, AFFDL/FGC. The report number assigned by Nielsen Engineering & Research, Inc. is NEAR TR 37.

The authors wish to thank Mr. Jenkins for his assistance during the course of the investigation. Also, they would like to thank Mr. Willard E. Summers and Mr. Robert H. Roberts of the 4T Projects Branch, Propulsion Wind-Tunnel Facility, Arnold Engineering Development Center, for the timely performance of the experimental test program.

The work documented in this report was started on December 11, 1970, and was effectively concluded with the submission of this report. The report was released by the authors in March, 1972.

This technical report has been reviewed and is approved for publication.

FOR THE COMMANDER

  
\_\_\_\_\_  
JERRY E. JENKINS  
Project Engineer  
Flight Control Division

  
\_\_\_\_\_  
E. H. FLINN, Chief  
Control Criteria Branch  
Flight Control Division

## ABSTRACT

The primary objective of this report is to present a prediction method for determining the forces, moments, and six-degree-of-freedom trajectories associated with stores released from single, TER, or MER configurations on fighter-bomber aircraft up to the critical speed. A secondary objective is to present important experimental results and comparison with theory from an extensive wind-tunnel test program designed to provide data to test the theory through systematic measurements of flow fields, store load distributions, store forces and moments, and captive-store trajectories. Extensive comparisons are made for flow-field angles, store loading distributions, store forces and moments, and store six-degree-of-freedom trajectories. Store normal-force distributions and side-force distributions are presented for single stores as influenced by airplane angle of attack, vertical location under the aircraft, and presence of the pylon. Similar results are presented for interference effects in TER configurations. Interference between the two clusters in a MER configuration is shown. Empennage effects are presented and compared with theory for a range of roll angles and angles of attack. Comparisons are presented between captive-store trajectories, and those predicted by the six-degree-of-freedom program. Cases are shown for a single store without empennage and with empennage. A case of a store released from a TER configuration is also compared with the captive store trajectory. Generally, the method does a good job of predicting detailed store loading and six-degree-of-freedom trajectories. It should serve as a useful preliminary design tool.

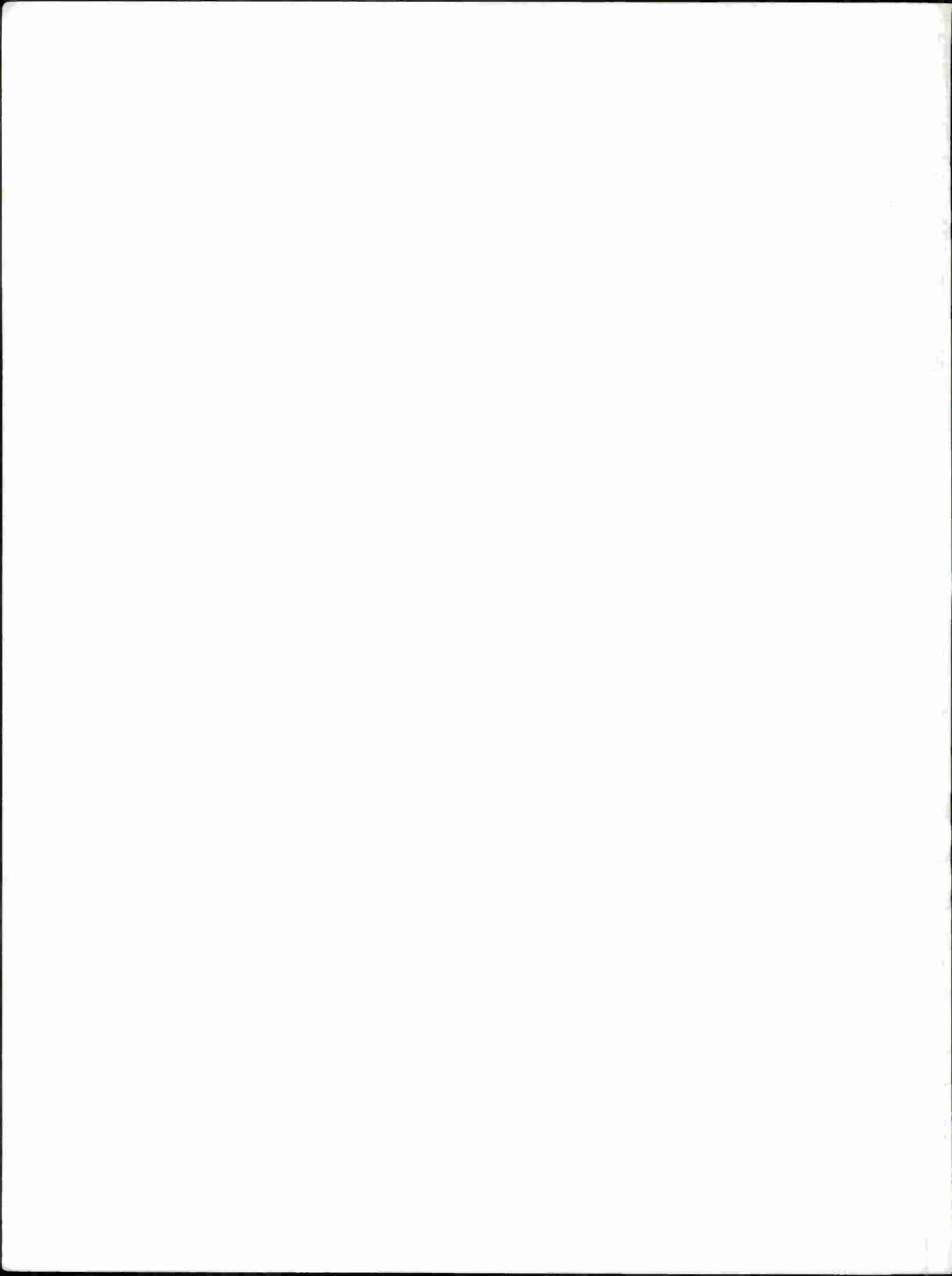


## TABLE OF CONTENTS

<u>Section</u>	<u>Page No.</u>
1. INTRODUCTION	1
2. GENERAL METHOD OF APPROACH	2
3. COMPRESSIBILITY CORRECTION	5
4. MATHEMATICAL MODELS FOR DETERMINING FLOW FIELD	6
4.1 Fuselage and Store Flow Model	6
4.2 Wing-Pylon Flow Model	8
4.2.1 Configuration characteristics	8
4.2.2 Vortex-lattice model	9
4.2.3 Thickness model	15
4.3 TER or MER Rack Flow Model	20
5. FORCE AND MOMENT CALCULATION	20
5.1 Calculation of the Velocity Field Including Damping	21
5.2 Body Forces and Moments	26
5.2.1 Buoyancy forces and moments	27
5.2.2 Slender-body forces and moments	28
5.2.3 Viscous crossflow forces and moments	29
5.3 Empennage Forces and Moments	30
6. CALCULATION OF STORE TRAJECTORIES	33
6.1 Equations of Motion	33
6.2 Description of Computer Program	38
7. COMPARISONS WITH EXPERIMENTAL DATA	41
7.1 Flow Field and Loading Predictions For Single Stores	42
7.1.1 Effect of pylon on flow field and attached store load distribution	43
7.1.2 Effect of store position and angle of attack on store forces	43
7.2 Flow Field and Loading Predictions for TER Configurations	44
7.2.1 Flow-field predictions	44
7.2.2 Loading predictions	45

<u>Section</u>	<u>Page No.</u>
7.3 MER Interference Effects	46
7.4 Empennage Contributions to Forces and Moments	48
7.5 Effect of Store Boattail on Loadings and Forces	49
7.5.1 Effect of store boattail on store loading in uniform flow	49
7.5.2 Effect of boattail on store loading in presence of wing-body combination	51
7.5.3 Effect of boattail on empennage forces and moments	52
7.6 Trajectory Studies	53
7.6.1 Statically unstable single store dropped beneath wing	54
7.6.2 Statically stable single store dropped beneath wing	54
7.6.3 Statically unstable store dropped from TER group beneath wing	55
8. CONCLUDING REMARKS	55
FIGURES 1 THROUGH 37	58
APPENDIX I - CALCULATION OF FORCES AND MOMENTS DUE TO THE EMPENNAGE OF AN EXTERNAL STORE IN A NONUNIFORM AIRFLOW	116
APPENDIX II - EQUATIONS OF MOTION OF A RIGID BODY WITH MASS AND INERTIA ASYMMETRIES	131
APPENDIX III - A REFINED THEORY FOR THE CALCULATION OF NORMAL- AND SIDE-FORCE DISTRIBUTIONS ON BODIES OF REVOLUTION IN NONUNIFORM FLOW	146
REFERENCES	161

## LIST OF ILLUSTRATIONS

<u>Figure</u>	<u>Page No.</u>
1.- Coordinate system for an axisymmetric body.	58
2.- Coordinate systems for wing-pylon and horseshoe vortices.	59
3.- Vortex-lattice model of a wing-pylon.	60
4.- Flow tangency boundary condition for wing and pylon.	61
5.- Coordinate system for wing thickness source strips.	62
6.- Coordinate system for pylon thickness source strips.	63
7.- Details of TER rack.	64
8.- Coordinate systems fixed in ejected store and used in force and moment calculation.	65
9.- Coordinate systems used in trajectory calculation.	66
10.- Coordinate systems used in empennage force and moment calculation.	67
11.- Wing-fuselage combination.	68
12.- Aircraft components used with wing-fuselage combination. (a) Pylon used with single store and MER and TER racks.	69
12.- Continued. (b) MER rack.	70
12.- Continued. (c) Large store with cylindrical afterbody and rectangular cruciform fins.	71
12.- Continued. (d) Large store with boattail afterbody and rectangular cruciform fins.	72
12.- Concluded. (e) Small boattail MER store with cruciform empennage.	73
13.- Large store with cylindrical afterbody under wing-fuselage configuration.	74
14.- Effect of pylon on flow field of wing-body combination at centerline location of attached store.	75
15.- Effect of pylon on load distributions of attached store. (a) Normal-force distribution.	76
15.- Concluded. (b) Side-force distribution.	77
16.- Effect of vertical location on normal-force and side-force coefficients of store.	78

LIST OF ILLUSTRATIONS (cont.)

<u>Figure</u>	<u>Page No.</u>
17.- Effect of angle of attack on normal-force and side-force coefficients of store.	79
18.- Large stores with cylindrical afterbody in a TER arrangement under the wing.	80
19.- Effect of vertical position on downwash and sidewash under TER configuration (parent aircraft - WBPTS <sub>2</sub> S <sub>3</sub> ).	81
20.- Effect of angle of attack on downwash and sidewash under TER configuration (parent aircraft - WBPTS <sub>2</sub> S <sub>3</sub> ).	82
21.- Effect of vertical position on loading distributions on store S <sub>1</sub> of TER configuration (parent aircraft WBPTS <sub>2</sub> S <sub>3</sub> ).	83
21.- Concluded. (b) Side-force distribution.	84
22.- Effect of angle of attack on loading distributions on S <sub>1</sub> in TER configuration (parent aircraft - WBPTS <sub>2</sub> S <sub>3</sub> ). (a) Normal-force distribution.	85
22.- Concluded. (b) Side-force distribution.	86
23.- Effect of TER on loading of store S <sub>1</sub> (parent aircraft - WBPT and WBP). (a) Normal-force distribution.	87
23.- Concluded. (b) Side-force distribution.	88
24.- Effect of vertical position on loading distribution of shoulder store S <sub>2</sub> of TER configuration (parent aircraft WBPTS <sub>3</sub> ).	89
24.- Concluded. (b) Side-force distribution.	90
25.- Effect of angle of attack on loading distribution of shoulder store S <sub>2</sub> of TER configuration (parent aircraft - WBPTS <sub>3</sub> ). (a) Normal-force distribution.	91
25.- Concluded. (b) Side-force distribution.	92
26.- Small boattail stores in a MER arrangement under the fuselage.	93
27.- Effects of S <sub>5</sub> , S <sub>6</sub> on S <sub>1</sub> and S <sub>1</sub> , S <sub>2</sub> , S <sub>3</sub> on S <sub>4</sub> in MER configuration; no empennages. (a) Normal-force coefficient. (b) Pitching-moment coefficient.	94
28.- Effects of S <sub>5</sub> , S <sub>6</sub> on S <sub>1</sub> and S <sub>1</sub> , S <sub>2</sub> , S <sub>3</sub> on S <sub>4</sub> in MER configuration; with empennages. (a) Normal-force coefficient. (b) Pitching-moment coefficient.	95

LIST OF ILLUSTRATIONS (cont.)

<u>Figure</u>	<u>Page No.</u>
29.- Effect of roll angle on empennage contributions to store $S_C$ forces and moments in the attached position (parent aircraft WBP). (a) Normal-force and side-force coefficients.	96
29.- Continued. (b) Pitching-moment and yawing-moment coefficients.	97
29.- Concluded. (c) Rolling-moment coefficients.	98
30.- Effects of store boattail on store loading in uniform flow. (a) $\alpha = 4^\circ$ .	99
30.- Continued. (b) $\alpha = 8^\circ$ .	100
30.- Continued. (c) $\alpha = 12^\circ$ .	101
30.- Concluded. (d) $\alpha = 16^\circ$ .	102
31.- Effects of boattail on location of separation on store afterbody; uniform flow. (a) Separation location. (b) Non-dimensional separation location.	103
32.- Effects of boattail on normal-force distribution of store in presence of wing-body combination. (a) $\alpha = 4^\circ$ .	104
32.- Concluded. (b) $\alpha = 16^\circ$ .	105
33.- Effects of boattail on side-force distribution of store in presence of wing-body combination. (a) $\alpha = 4^\circ$ .	106
33.- Concluded. (b) $\alpha = 16^\circ$ .	107
34.- Effects of boattail on the forces and moments due to the empennage (parent aircraft WBP). (a) Normal-force coefficient.	108
34.- Continued. (b) Side-force coefficient.	109
34.- Continued. (c) Pitching-moment coefficient.	110
34.- Continued. (d) Yawing-moment coefficient.	111
34.- Concluded. (e) Rolling-moment coefficient.	112
35.- Comparison between calculated trajectory and captive-store trajectory of store $S_C$ released at one-third semispan location; $M_\infty = 0.4$ .	113

LIST OF ILLUSTRATIONS (cont.)

<u>Figure</u>	<u>Page</u> <u>No.</u>
36.- Comparison between calculated trajectories and captive-store trajectories of store $S_c$ with empennage released at one-third semispan location; $M_\infty = 0.4$ .	114
37.- Comparison between calculated trajectory and captive-store trajectory of finless store $S_1$ released from TER group at one-third semispan location; $M_\infty = 0.4$ .	115

LIST OF SYMBOLS

$a$	local body radius
$a_{\max}$	maximum body radius
$[A]$	direction cosine matrix given by equation (28)
$[A]'$	transpose of direction cosine matrix of equation (28)
$c_{d_c}$	section drag coefficient of a circular cylinder normal to airstream
$C_A$	axial-force coefficient, axial force/ $q_{\infty} S_R$
$C_l$	rolling-moment coefficient, rolling moment/ $q_{\infty} S_R l_R$
$C_m$	pitching-moment coefficient, pitching moment/ $q_{\infty} S_R l_R$
$C_n$	yawing-moment coefficient, yawing moment/ $q_{\infty} S_R l_R$
$C_N$	normal-force coefficient, normal force/ $q_{\infty} S_R$
$C_Y$	side-force coefficient, side force/ $q_{\infty} S_R$
$\Delta C_l, \Delta C_m, \dots, \Delta C_Y$	changes in forces and moments due to adding aircraft or store component
$d$	maximum diameter of store
$\vec{e}$	unit vector
$F_u, F_v, F_w$	backwash, sidewash, and downwash influence coefficients given by equations (10), (11), and (12); positive in the $x, y,$ and $z$ directions of figure 2
$F_x, F_y, F_z$	sums of all forces acting on ejected store; positive in the $x, y, z$ directions shown in figure 8
$g$	gravitational acceleration
$g_x, g_y, g_z$	gravitational acceleration components in $x, y, z$ directions of figure 8

$I_{xx}, I_{yy}, I_{zz}$	moments of inertia about $x, y, z$ axes of figure 8; taken about store moment center
$I_{yz}, I_{xz}, I_{xy}$	products of inertia about $x, y, z$ axes of figure 8; taken about store moment center
$l_R$	reference length; store length in incompressible space in section 4.1, store maximum diameter, $d$ , elsewhere
$l_s$	store length
$m$	mass of ejected store
$M_x, M_y, M_z$	sums of all moments acting on ejected store; positive in the $p, q, r$ directions of figure 9
$M_\infty$	aircraft free-stream Mach number
$p, q, r$	rotational velocities about $x, y, z$ axes of figure 8; positive as shown in figure 9
$\dot{p}, \dot{q}, \dot{r}$	rotational accelerations; time derivatives of $p, q, r$
$q_{\infty s}$	ejected store free-stream dynamic pressure; $1/2 \rho_\infty V_\infty^2$
$Q_k$	strength of $k^{\text{th}}$ point source
$Q_k^*$	$Q_k / 4\pi l_R^2 V_\infty$
$r$	radial distance in $y-z$ plane of figure 1
$r^*$	$r / l_R$
$s$	vortex semispan in section 4.2.2; wing semispan elsewhere
$s_h$	semispan of horizontal tail fins (fig. 10)
$s_v$	semispan of vertical tail fins (fig. 10)
$S_R$	reference area taken equal to body frontal area, $\pi a_{\text{max}}^2$
$t$	time

$u, v, w$	compressible space perturbation velocities in $x, y, z$ directions of figure 10 except in section 4 where they are incompressible velocities
$u', v', w'$	incompressible space perturbation velocities
$\Delta u, \Delta v, \Delta w$	incompressible space perturbation velocity due to one source strip
$u_i, v_i, w_i$	incompressible space externally induced perturbation velocities in section 4.2.2
$u_s, v_s, w_s$	sum of all perturbation velocities; positive in $x_s, y_s, z_s$ directions of figure 8
$u_\xi, u_\eta, u_\zeta$	sum of all perturbation velocities in $\xi, \eta, \zeta$ directions of figure 9
$U_s, V_s, W_s$	total velocities as seen by store, positive in $x_s, y_s, z_s$ directions of figure 8
$U_s^*, V_s^*, W_s^*$	$U_s/V_{\infty_s}, V_s/V_{\infty_s}, W_s/V_{\infty_s}$
$U_{\infty_{s,x}}, V_{\infty_{s,y}}, W_{\infty_{s,z}}$	free-stream velocity components as seen by store; positive in $x, y, z$ directions shown in figure 8
$U_{\infty_{s,x_s}}, V_{\infty_{s,y_s}}, W_{\infty_{s,z_s}}$	free-stream velocity components as seen by store; positive in $x_s, y_s, z_s$ directions shown in figure 8
$v_r$	radial velocity in $y-z$ plane of figure 1
$v_r^*$	$v_r/V_{\infty}$
$V_c^*$	$\sqrt{(V_s^*)^2 + (W_s^*)^2}$
$V_{\infty}$	aircraft free-stream velocity
$V_{\infty_s}$	ejected store free-stream velocity
$x, y, z$	section 3, coordinate system in compressible space; section 4.1, coordinate system in incompressible space with origin at body nose (fig. 1); section 4.2.2, coordinate system in incompressible space with origin at the midspan of a horseshoe vortex (fig. 2); elsewhere, coordinate system in compressible space fixed in store with origin at store moment center (fig. 8)
$x', y', z'$	coordinate system in incompressible space

$\bar{x}, \bar{y}, \bar{z}$	location of center of mass of ejected store relative to store moment center
$x^*$	$x/l_R$
$x_f, y_f, z_f$	coordinate system in compressible space fixed in store empennage (fig. 10)
$\Delta x_i$	chord of the $i^{\text{th}}$ source strip
$x_k$	$x$ -location of $k^{\text{th}}$ point source
$x_k^*$	$x_k/l_R$
$x_s, y_s, z_s$	coordinate system in compressible space fixed in ejected store with origin at store nose (fig. 8)
$x_{s,m}$	$x_s$ -location of store moment center
$x_{s,o}$	$x_s$ -location of separation
$\dot{x}_o, \dot{y}_o, \dot{z}_o$	components of store translational velocity, relative to inertial coordinate system, in $x, y, z$ coordinate system
$X, Y, Z$	coordinate system in incompressible space fixed in wing with origin at leading edge of wing-root chord (figs. 2, 5, and 6)
$X_1, Y_1, Z_1$	$X, Y, Z$ coordinates of a point on a source strip
$\Delta z$	vertical location of store measured from carriage position on pylon or rack
$\alpha$	angle of attack
$\alpha_f$	fuselage angle of attack
$\alpha_\ell$	local angle of attack due to wing twist and camber
$\beta$	$\sqrt{1 - M_\infty^2}$
$\gamma_f$	flight path angle of fuselage
$\Gamma_n$	strength of a horseshoe vortex
$\theta$	local slope of wing thickness envelope, positive as shown in figure 5

$\theta_p$	local slope of pylon thickness envelope, positive as shown in figure 6
$\lambda_i$	local wing sweep angle measured positive as shown in figure 5
$\lambda_{Pi}$	local pylon sweep angle measured positive as shown in figure 6
$\xi, \eta, \zeta$	inertial coordinate system fixed in fuselage nose, positive forward along longitudinal axis, positive laterally to the right, and positive vertically downward respectively
$\Delta\xi, \Delta\eta, \Delta\zeta$	location of store center of moments in inertial coordinate system relative to the carriage position on pylon or rack
$\dot{\xi}, \dot{\eta}, \dot{\zeta}$	velocity components of store center of moments in inertial system
$\ddot{\xi}, \ddot{\eta}, \ddot{\zeta}$	acceleration components of store center of moments in inertial system
$\rho_\infty$	free-stream mass density
$\phi_i$	dihedral angle of a wing segment, positive as shown in figure 2
$\Delta\phi$	potential due to one source strip
$\phi_f$	orientation of store tail fins with respect to $x_s, y_s, z_s$ coordinate system (fig. 10)
$\phi_{Pt}$	pylon thickness envelope slope measured positive as shown in figure 6
$\phi_t$	wing thickness envelope slope measure positive as shown in figure 5
$\psi$	sweep angle of a horseshoe vortex bound leg measured in wing or pylon chordal plane, positive swept back on left wing panel or pylon
$\psi_i$	sweep angle of a source strip (figs. 5 and 6)
$\psi_p$	sweep angle of a horseshoe vortex bound leg measured in wing or pylon planform plane positive swept back on left wing panel or pylon
$\Psi, \theta, \phi$	store yaw, pitch and roll angles specifying angular orientation of store $x, y, z$ coordinate system relative to $\xi, \eta, \zeta$ inertial system, see figure 9

$\Delta\Psi, \Delta\theta, \Delta\phi$

changes in store yaw, pitch, and roll angles from carriage position values

$\dot{\Psi}, \dot{\theta}, \dot{\phi}$

time rates of change of  $\Psi, \theta,$  and  $\phi$

PREDICTION OF SIX-DEGREE-OF-FREEDOM STORE SEPARATION  
TRAJECTORIES AT SPEEDS UP TO THE CRITICAL SPEED

Volume I - Theoretical Methods and Comparisons  
With Experiment

1. INTRODUCTION

This report is the final technical report describing a combined theoretical-experimental program which has been carried out with the objective of developing a method for predicting the six-degree-of-freedom trajectories of external stores separated from aircraft of the fighter-bomber type at speeds up to the critical speed. The work documented in this report represents an extension and improvement of the work reported in reference 1. In that work the method was limited to three degrees of freedom. The pylon was not accounted for, nor was the TER or MER rack. The pylon and rack are accounted for in the present work. In addition a new vortex-lattice model has been adopted which allows for mutual interference between wing and pylon, as well as wing dihedral, two things which were not included in the vortex-lattice model of reference 1. A new wing- pylon thickness model has been adopted. The six-degree-of-freedom equations of motion used in the trajectory calculations allow for mass and inertia asymmetries of the store.

The experimental program carried out in conjunction with the present theoretical program was directed toward supplementing the data obtained during the experimental program conducted simultaneously with the theoretical work of reference 1. These earlier data are tabulated in reference 2 and the data obtained in the present program are tabulated in reference 3. Some of the data are summarized in graphical form in four AEDC reports, references 4 through 7. The overall experimental program was designed such that interference effects could be isolated through a component by component build-up of the parent aircraft. At each stage of the build-up flow field survey, pressure distribution, and force and moment data were taken. A representative set of trajectories was also obtained for comparison with theory.

The next sections of this report will discuss the general method of approach to the interference problem, the mathematical models for the aircraft components, the calculation of the flow field, the calculation of the forces and moments, and finally the calculation of the trajectory. Methods which have not changed from the work of reference 1 will be

summarized and new methods will be described in detail. Among the latter are the new wing-pylon model, the empennage force and moment calculation, and the equations of motion with mass and inertia asymmetries.

Finally, extensive comparisons are made with selected results from the wind-tunnel program for flow-field angles, store loading distributions, store forces and moments, and store six-degree-of-freedom trajectories. Store normal-force distributions and side-force distributions are presented for single stores as influenced by airplane angle of attack, vertical location under the aircraft, and presence of the pylon. Similar results are presented for interference effects in TER configurations for both the bottom store and the shoulder stores. In addition, the effect of the TER rack is shown. Interference between the two clusters in a MER configuration is shown. Empennage effects are presented and compared with theory for a range of roll angles and angles of attack. A special assessment is made of the effects of store boattail on store loading distributions, forces and moments, and boundary-layer separation characteristics. Also, the effects of store boattail on empennage forces and moments are investigated. Comparisons are presented between captive-store trajectories, and those predicted by the six-degree-of-freedom program. Cases are shown for a single store without an empennage and with an empennage. A case of a store released from a TER configuration is also compared with the captive-store trajectory. Using the computer program, the effect of damping is shown for a finned store.

## 2. GENERAL METHOD OF APPROACH

The determination of the forces and moments acting on an external store due to the complete aircraft is a complicated problem in aerodynamic interference. The approach used herein is to make a first approximation to the gross interference effect termed the primary interference, and then to consider the small residual interference as an additional interference. The primary interference can be viewed as the first term in an iterative procedure. Consider the entire airframe except the store in question which produces a nonuniform flow field at the position to be occupied by the store. If we now place the store in this nonuniform flow field and determine its reaction, we have accounted for primary interference. If now we consider the effect of the store on the airframe, additional velocities are induced normal to wing, fuselage, and pylon

which must be cancelled by additional source and vortex distributions. This interference is termed additional interference and depends on the store location.

In the present method, the pylon is considered part of the airframe so that the primary interference contains most of the interference even for the attached store. The success of this method is in proportion to the degree to which the primary interference encompasses all the significant effects so that the additional interference can be neglected. Methods for calculating additional interference have been developed in reference 1, where it is shown that the effect of the additional interference on the store is small. However, the effect of the additional interference on the airframe may not be small.

An important advantage realized by making the additional interference effect on the store negligible is that the necessity of having to solve the complete mutual interference problem for the store and airframe is eliminated. The matrix necessary to solve the complete mutual interference problem requires store control points at about 20 axial stations and at a number of azimuthal stations in addition to the control points on the airframe. Elimination of those additional control points probably reduces the time to calculate the interference field to about 1/4 of what it would be for a complete mutual interference calculation. Another even more significant fact is that the airframe singularity distributions yielding the primary interference field do not change with store position so that it is not necessary to re-solve the interference problem at each point in the store trajectory. As a consequence, it is possible to calculate a store trajectory on existing computing machines in a reasonable time.

In the method described in this report the following aircraft components are accounted for:

- (1) Fuselage volume
- (2) Fuselage angle of attack
- (3) Wing thickness
- (4) Wing angle of attack, camber, and twist
- (5) Pylon thickness
- (6) Pylon loading due to induced sidewash field

- (7) Rack volume
- (8) Store volume

Fuselage volume is taken into account by approximating the shape by an axisymmetric body and representing this body by a series of three-dimensional point sources placed on the body axis. The volumes of the rack and all of the stores present are accounted for in the same manner. Fuselage angle of attack is taken into account as a simple Beskin upwash. Wing and pylon thickness are accounted for by representing their thickness distributions by a distribution of three-dimensional source panels. The wing angle of attack, camber, and twist and the pylon loading are represented by a vortex lattice.

Certain interference effects between aircraft components are accounted for in the wing-pylon vortex-lattice calculation. These are

- (1) Fuselage in uniform flow on wing and pylon
- (2) Stores in uniform flow on wing and pylon
- (3) Rack in uniform flow on wing and pylon
- (4) Wing thickness on pylon
- (5) Pylon thickness on wing

The interference velocities induced normal to the wing and pylon are treated as an induced camber and are included in the boundary condition used in determining the strengths of the vortices. This represents a first iteration on the complete mutual interference problem.

A second iteration would be to allow the wing and pylon to induce velocities in the regions of the fuselage, rack, and stores thus causing them to be in a nonuniform flow field. Since the source distributions used to model these bodies are for a uniform flow, higher order singularities would have to be used to account for this nonuniform flow. The influence of these higher-order singularities would die off more rapidly with distance and thus it is considered a second-order effect and is not included.

With the source and vorticity distributions which represent the various aircraft components determined, the trajectory can be calculated. This requires that the forces and moments acting on the ejected store, including damping, be calculated at each point in the trajectory. This is done by calculating the three-dimensional velocity field in which the store is operating as seen by the store. To do this the store is removed

from the flow field and the perturbation velocity field due to the aircraft components is calculated at a number of points in the region the store had occupied. The store is then placed back in this velocity field. The free-stream velocity the store sees is added to the perturbation field as are the store angular velocities. The velocity field is calculated over the store length in this manner. The axial distribution of store body forces and moments is calculated from this field and then integrated over the store length. A similar procedure is used to determine the empennage forces and moments with the velocity field calculated at a number of points over each tail fin. The method presently treats planar and cruciform empennages.

### 3. COMPRESSIBILITY CORRECTION

The compressibility correction used in the present work is the same as that used in the work of reference 1 (see section 3 of that report). The compressible space  $(x, y, z)$  and the incompressible space  $(x', y', z')$  are related by the following transformation

$$x' = \frac{x}{\sqrt{1 - M_\infty^2}} = \frac{x}{\beta}, \quad y' = y, \quad z' = z \quad (1)$$

and the velocities are related by

$$u = \frac{u'}{\beta^2}, \quad v = \frac{v'}{\beta}, \quad w = \frac{w'}{\beta} \quad (2)$$

Also in reference 1 it is shown that the incompressible angle of attack,  $\alpha'$ , is given by

$$\alpha' = \beta\alpha \quad (3)$$

The procedure used to calculate the perturbation velocity field used in determining the forces and moments acting on a store in the presence of a parent aircraft will now be briefly described. The first step is to determine the source and vorticity distributions which model the various components of the parent aircraft. To do this the entire configuration (fuselage, wing, pylon, rack and store(s)) is transformed to an equivalent one for incompressible flow. A common coordinate system whose origin is at the fuselage nose is adopted and all components are located in this

system. For a given Mach number the transformation given by equation (1) is applied to determine the equivalent incompressible configuration. This transformation results in an increase in the lengths of the fuselage, rack, and store(s), a stretching of the wing and pylon chords and an increase in their sweep angles. In addition, if the wing, rack, or store(s) is at incidence with respect to the fuselage longitudinal axis, the incidence angle is reduced by the factor  $\beta$ . The fuselage angle of attack is also reduced by this factor. Source distributions are then obtained to represent the volume distributions of the equivalent fuselage, rack, and stores. The vortex-lattice and source-strip distributions are laid out on the equivalent wing-pylon combination which is stretched in the chordwise direction. Using the common fuselage coordinate system, the perturbation velocities induced by the equivalent configuration at points of interest in the incompressible space are calculated by considering each component separately and then adding up all their effects. These incompressible perturbation velocities are then transformed back to compressible space using equation (2).

In calculating the store forces and moments, these velocities are calculated in the region the store longitudinal axis and tail fins would occupy if the store were in the flow field. This perturbation velocity field is then resolved into the store coordinate system.

#### 4. MATHEMATICAL MODELS FOR DETERMINING FLOW FIELD

The methods to be presented for determining the forces and moments acting on a store require a detailed knowledge of the flow field in the region of the store in its absence. In order to calculate this flow field all of the components of the parent aircraft must be modeled mathematically. It is the purpose of this section of the report to describe these models. First, the flow model for the fuselage and stores is described. Next the wing-pylon model is presented and finally, an approximate model for a rack is discussed. All of these models are for the equivalent incompressible configuration.

##### 4.1 Fuselage and Store Flow Model

The flow model used to represent the volume distributions of the equivalent incompressible fuselage and stores is the same as that presented in section 4.1 of reference 1. The shapes are approximated by

axisymmetric bodies and the resulting volume distributions represented by a distribution of three-dimensional point sources along the body longitudinal axis. The source strengths are determined in the manner described in reference 1.

With the source strengths determined, the perturbation velocity field due to the body can be calculated. Consider figure 1 which shows a right-hand  $x, y, z$  coordinate system fixed in the body nose with positive directions as shown. Also shown are the axial and radial perturbation velocities at a field point,  $u$  and  $v_r$  respectively, with positive directions as shown. From reference 1 the expressions for these velocities produced by  $N$  sources are

$$u^*(x^*, r^*) = \sum_{k=1}^N \frac{Q_k^*(x^* - x_k^*)}{[(x^* - x_k^*)^2 + r^{*2}]^{3/2}} \quad (4)$$

$$v_r^*(x^*, r^*) = \sum_{k=1}^N \frac{Q_k^* r^*}{[(x^* - x_k^*)^2 + r^{*2}]^{3/2}} \quad (5)$$

where

$$x^* = \frac{x}{l_R}, \quad r^* = \frac{r}{l_R} = \frac{\sqrt{y^2 + z^2}}{l_R}$$

$$u^* = \frac{u}{V_\infty}, \quad v_r^* = \frac{v_r}{V_\infty}$$

$$Q_k^* = \frac{Q_k}{4\pi l_R^2 V_\infty}$$

and where  $l_R$  is a reference length which for convenience will be taken as the length of the incompressible body. The quantities  $Q_k^*$  and  $x_k^*$  are the source strength and location, respectively, of the  $k^{\text{th}}$  point source, and the point  $(x^*, r^*)$  designates the field point in cylindrical coordinates. In resolving  $v_r$  into components in the  $y$  and  $z$  direction,  $v$  and  $w$  respectively, proper account must be taken of the quadrant.

## 4.2 Wing-Pylon Flow Model

In order to represent the wing-pylon combination by a potential flow model, two types of singularities are used simultaneously. A three-dimensional vortex lattice is laid out on the surfaces of both wing and pylon to account for aerodynamic loadings, and a distribution of a special type of sources accounts for thickness effects. The source strengths are proportional to the thickness envelope slopes of the wing and the pylon. The flow tangency boundary condition, including all wing-pylon interference, is applied at a finite number of points on the wing-pylon combination resulting in a set of simultaneous equations from which the vortex strengths are determined. A Prandtl-Glauert similarity rule (see section 3) is used to account for compressibility.

### 4.2.1 Configuration characteristics

The configuration of interest is a wing with one pylon under each wing panel. The right wing panel with pylon is the image of the left wing panel and pylon. The various wing-pylon parameters included in the computer program are listed below.

#### Wing Panels:

**Thickness distribution:** Specified at large number of chordwise locations and at the same number of spanwise locations as used in the vortex lattice which represents the wing as a lifting surface.

**Mean-camber surface:** May have both twist and camber.

**Leading-edge shape:** Up to thirty straight line segments of differing sweep.

**Trailing-edge shape:** Same as for leading edge.

**Taper:** Controlled by shape of leading- and trailing-edges.

**Tips:** Straight.

**Dihedral:** Variable across wing panel.

#### Pylon:

**Thickness distribution:** Same method of description as for wing panel.

**Mean-camber surface:** Planar.

**Leading-edge shape:** Straight line which may be swept.

**Trailing-edge shape:** Same as for leading-edge except sweep angle may be different.

Taper: Uniform.

Tip: Parallel to pylon root chord (pylon-wing junction).

Orientation: Vertical and streamwise.

#### 4.2.2 Vortex-lattice model

The three-dimensional horseshoe vortex-lattice approach that is used to represent the wing-pylon lifting surfaces follows the methods developed in references 8 and 9. In what follows, the theory and layout of the vortex lattice will be described first. The flow tangency boundary conditions specified for the wing and pylon will show how mutual interference due to aerodynamic loading as well as thickness effects are accounted for. The theory and layout of the sources superimposed on the vortex lattice to account for thickness will be discussed in section 4.2.3.

The wing vortex-lattice method used in the previous store trajectory work, reference 1, has been extensively modified to treat a wing-pylon combination as an integral unit. The new lattice program also allows for breaks in wing sweep and dihedral. Wing twist is assumed small and is accounted for only in the flow tangency boundary condition. As such, the twist is not included in the geometry of the wing-pylon combination so that the wing tip is not twisted relative to the wing root chord. The wing and horseshoe vortex coordinate systems for a wing with breaks in leading and trailing edge sweep and dihedral are illustrated in figure 2. Figure 3 shows the vortex-lattice arrangement for a swept wing with constant dihedral and pylons. The wing panels and pylons are divided into trapezoidal area elements. A horseshoe vortex is placed in each area element such that the spanwise bound leg lies along the element quarter chord and its trailing legs along the sides of the element. The trailing legs are assumed to lie in the plane of the area element. The area elements in each chordwise row have equal chords and spans. In the spanwise direction, the area element widths need not be equal to allow for closer spacing where large spanwise loading gradients exist. For a wing with breaks in sweep, the area elements are arranged spanwise so that the breaks in leading- and/or trailing-edge sweep lie on the line formed by one of the sides of a chordwise row of elements. A similar procedure is followed when there are breaks in dihedral. The wing-pylon

junction is also made to lie along a common boundary between two adjacent rows of elements. Consequently, the trailing legs of the upper vortices on the pylon lie at the junction, as shown in figure 3. The length of the wing-pylon junction, the pylon root chord, need not be equal to the wing local chord.

On the wing, the flow tangency boundary condition should be expressed at the camber surface but instead it is applied at a finite set of control points given by the midpoint of the 3/4-chord line of each area element located in the wing chordal plane. This is the planar approximation. The chordal plane of wing segment  $i$  is the plane containing the leading and trailing edges of the wing segment and making dihedral angle  $\phi_i$  with the  $Z = 0$  plane. On the camberless pylon, the flow tangency condition is applied likewise at control points situated in its chordal plane determined by halving the thickness envelope.

The boundary condition states that there is no flow through the wing and pylon surfaces at each control point. The condition is illustrated in figure 4 for the wing. The velocities normal to the wing consist of a component of the free stream, perturbation velocities  $u$ ,  $v$ , and  $w$  induced by the wing-pylon horseshoe vortex system, and perturbation velocities  $u_i$ ,  $v_i$ , and  $w_i$  induced by the distribution of sources, accounting for thickness superimposed on the vortex-lattice. Velocities  $u_i$ ,  $v_i$ , and  $w_i$  may also include other externally induced perturbation velocities such as those due to the fuselage and stores. With  $M$  control points on the left wing panel and  $MP$  on the left pylon, the boundary condition on the left wing panel is given by

$$\begin{aligned} & \sum_{n=1}^M \frac{\Gamma_n}{4\pi V_\infty} \left( F_{w_{v,n}} \cos \phi_v - F_{v_{v,n}} \sin \phi_v \right) \\ & + \sum_{n=M+1}^{M+MP} \frac{\Gamma_n}{4\pi V_\infty} \left( F_{w_{v,n}} \cos \phi_v - F_{v_{v,n}} \sin \phi_v \right) \\ & = (\alpha + \alpha_{l_v}) \cos \phi_v + \frac{v_{i,v}}{V_\infty} \sin \phi_v \\ & - \left( \frac{u_{i,v}}{V_\infty} \alpha_{l_v} + \frac{w_{i,v}}{V_\infty} \right) \cos \phi_v; \quad v=1,2,\dots,M \end{aligned} \quad (6)$$

The wing angle of attack is  $\alpha$  and  $\alpha_\ell$  is the local angle of attack due to wing camber and twist. Both angles are assumed small. With the camberless pylon at zero incidence, the pylon boundary condition is written for MP control points as:

$$-\sum_{n=1}^M \frac{\Gamma_n}{4\pi V_\infty} F_{v_{v,n}} - \sum_{n=M+1}^{M+MP} \frac{\Gamma_n}{4\pi V_\infty} F_{v_{v,n}} = \frac{v_{i,v}}{V_\infty}; \quad v=M+1, M+2, \dots, M+MP \quad (7)$$

The right-hand side of equation (6) represents the free-stream component and the externally induced perturbation velocities normal to the wing chordal plane. The right-hand side of equation (7) consists only of an external perturbation velocity normal to the pylon chordal plane since there is no pylon incidence. The first summation on the left-hand side of the equations represents the perturbation velocities induced by vorticity on the left and right wing panels. The second summation represents the velocities induced by vorticity on the left and right pylons. The functions inside the summations will be discussed next.

The functions  $F_u$ ,  $F_v$ , and  $F_w$  are influence functions relating the perturbation velocity components, induced at some point by a horseshoe vortex, to its circulation and the coordinates of the point relative to the vortex. The relationship is obtained from the Biot-Savart law, see reference 10. For example, the wash velocities at a point, induced by a horseshoe vortex on the wing, are

$$\begin{aligned} u(x,y,z) &= \frac{\Gamma}{4\pi} F_u(x,y,z,s,\psi,\phi) \\ v(x,y,z) &= \frac{\Gamma}{4\pi} F_v(x,y,z,s,\psi,\phi) \\ w(x,y,z) &= \frac{\Gamma}{4\pi} F_w(x,y,z,s,\psi,\phi) \end{aligned} \quad (8)$$

The influence functions depend only upon the coordinates  $(x,y,z)$  relative to the horseshoe vortex of the point at which the velocity is to be computed, and the vortex span,  $s$ , bound leg sweep angle  $\psi$ , and wing segment dihedral angle,  $\phi$ .

Consider first a vortex on the left wing panel. The coordinate system is shown in figure 2. Since the horseshoe vortex lies in the

chordal plane (the plane of the wing panel), the bound-leg sweep angle  $\psi$  used is the angle in the chordal plane, whereas the sweep angle is generally specified in the planform plane,  $\psi_p$ . The two are related by the dihedral angle as

$$\tan \psi = \tan \psi_p \cos \phi \quad (9)$$

The induced velocity is computed by integrating over the lengths of the two trailing legs and the bound leg. For a horseshoe vortex on the left wing panel, the resulting influence functions are as follows. The backwash influence coefficient, positive forward, is

$$F_u(x, y, z, s, \psi, \phi) = \frac{(z \cos \phi - y \sin \phi) \cos \psi}{\left[ x \cos \psi - (y \cos \phi + z \sin \phi) \sin \psi \right]^2 + (z \cos \phi - y \sin \phi)^2} \cdot \left\{ \frac{(x + s \tan \psi) \sin \psi + (y + s \cos \phi) \cos \psi \cos \phi + (z + s \sin \phi) \cos \psi \sin \phi}{\left[ (x + s \tan \psi)^2 + (y + s \cos \phi)^2 + (z + s \sin \phi)^2 \right]^{1/2}} - \frac{(x - s \tan \psi) \sin \psi + (y - s \cos \phi) \cos \psi \cos \phi + (z - s \sin \phi) \cos \psi \sin \phi}{\left[ (x - s \tan \psi)^2 + (y - s \cos \phi)^2 + (z - s \sin \phi)^2 \right]^{1/2}} \right\} \quad (10)$$

The sidewash influence coefficient, positive to the right, is

$$F_v(x, y, z, s, \psi, \phi)$$

$$\begin{aligned}
&= \frac{-z \sin \psi + x \cos \psi \sin \phi}{[x \cos \psi - (y \cos \phi + z \sin \phi) \sin \psi]^2 + (z \cos \phi - y \sin \phi)^2} \\
&\cdot \left\{ \frac{(x + s \tan \psi) \sin \psi + (y + s \cos \phi) \cos \psi \cos \phi + (z + s \sin \phi) \cos \psi \sin \phi}{[(x + s \tan \psi)^2 + (y + s \cos \phi)^2 + (z + s \sin \phi)^2]^{1/2}} \right. \\
&- \left. \frac{(x - s \tan \psi) \sin \psi + (y - s \cos \phi) \cos \psi \cos \phi + (z - s \sin \phi) \cos \psi \sin \phi}{[(x - s \tan \psi)^2 + (y - s \cos \phi)^2 + (z - s \sin \phi)^2]^{1/2}} \right\} \\
&+ \frac{(z - s \sin \phi)}{(y - s \cos \phi)^2 + (z - s \sin \phi)^2} \\
&\cdot \left\{ 1 - \frac{(x - s \tan \psi)}{[(x - s \tan \psi)^2 + (y - s \cos \phi)^2 + (z - s \sin \phi)^2]^{1/2}} \right\} \\
&- \frac{(z + s \sin \phi)}{(y + s \cos \phi)^2 + (z + s \sin \phi)^2} \\
&\cdot \left\{ 1 - \frac{(x + s \tan \psi)}{[(x + s \tan \psi)^2 + (y + s \cos \phi)^2 + (z + s \sin \phi)^2]^{1/2}} \right\} \quad (11)
\end{aligned}$$

The downwash influence coefficient, positive downward, is

$$F_w(x, y, z, s, \psi, \phi)$$

$$\begin{aligned}
&= \frac{-x \cos \psi \cos \phi + y \sin \psi}{[x \cos \psi - (y \cos \phi + z \sin \phi) \sin \psi]^2 + (z \cos \phi - y \sin \phi)^2} \\
&\cdot \left\{ \frac{(x + s \tan \psi) \sin \psi + (y + s \cos \phi) \cos \psi \cos \phi + (z + s \sin \phi) \cos \psi \sin \phi}{[(x + s \tan \psi)^2 + (y + s \cos \phi)^2 + (z + s \sin \phi)^2]^{1/2}} \right. \\
&- \left. \frac{(x - s \tan \psi) \sin \psi + (y - s \cos \phi) \cos \psi \cos \phi + (z - s \sin \phi) \cos \psi \sin \phi}{[(x - s \tan \psi)^2 + (y - s \cos \phi)^2 + (z - s \sin \phi)^2]^{1/2}} \right\} \\
&- \frac{(y - s \cos \phi)}{(y - s \cos \phi)^2 + (z - s \sin \phi)^2}
\end{aligned}$$

(Continued on next page)

$$\begin{aligned}
& \cdot \left\{ 1 - \frac{(x - s \tan \psi)}{[(x - s \tan \psi)^2 + (y - s \cos \phi)^2 + (z - s \sin \phi)^2]^{1/2}} \right\} \\
& + \frac{(y + s \cos \phi)}{(y + s \cos \phi)^2 + (z + s \sin \phi)^2} \\
& \cdot \left\{ 1 - \frac{(x + s \tan \psi)}{[(x + s \tan \psi)^2 + (y + s \cos \phi)^2 + (z + s \sin \phi)^2]^{1/2}} \right\} \quad (12)
\end{aligned}$$

For the case of unyawed vortices,  $\psi = 0^\circ$ , the influence coefficients given above degenerate to the equations given by Blackwell, reference 11.

Once the influence coefficient for the vortex on the left-wing panel is obtained, the coefficient for the vortex at the image position on the right-wing panel can be obtained by changing appropriate signs in equations (10) through (12) and by taking into account the change in the  $y$  coordinate. Thus, for both wing panels,

$$F_u = F_u(x, y_\ell, z, s, \psi, \phi) + F_u(x, y_r, z, s, -\psi, -\phi) \quad (13)$$

where the first term is the left panel vortex contribution and the second term the right panel contribution. The same transformations hold for  $F_v$  and  $F_w$ .

In similar fashion, the contributions of the vortices on the pylons can be obtained from the left wing panel expressions. Thus, for the pylons

$$F_u = F_u(x, y_\ell, z, s, \psi, \phi = -\pi/2) + F_u(x, y_r, z, s, -\psi, \phi = \pi/2) \quad (14)$$

where the first term is the contribution of the left pylon, which has a "dihedral angle" of  $-\pi/2$ , and the second term represents the right pylon contribution. The same transformations again hold for  $F_v$  and  $F_w$ .

Equations (6) and (7) represent a set of  $M+MP$  simultaneous equations in which the unknowns are the  $M+MP$  values of circulation strength  $\Gamma$ . Therefore, the values can be obtained through a matrix solution for a given angle of attack and a specified set of externally induced perturbation velocities  $\frac{u_i}{V_\infty}$ ,  $\frac{v_i}{V_\infty}$ ,  $\frac{w_i}{V_\infty}$  caused by wing and pylon thickness effects or from additional external sources such as fuselage, rack and stores.

### 4.2.3 Thickness model

The three-dimensional source method used to account for wing and pylon thickness is known as the spanwise source strip method and is quite similar to that used by Fernandes in reference 12. The wing will be dealt with first. The coordinate system and angle convention used in connection with the theory and layout of these source strips is shown in figure 5 for the left wing panel with specified thickness envelope. It is noted that this coordinate system is the same as the one used for the vortex-lattice method, figure 2. The incompressible velocity potential due to a surface with chord  $|X_b - X_a|$  and span  $|Y_b - Y_a|$  shown in figure 5 on the wing may be obtained from reference 13 or 14 with a simple coordinate transformation. The result is

$$\frac{\Delta\phi}{V_\infty} = \frac{1}{2\pi} \int_{X_b}^{X_a} \int_{Y_b}^{Y_a} \frac{\tan \phi_t dX_1 dY_1}{\sqrt{(X_1 - X)^2 + (Y - Y_1)^2 + (Z_1 - Z)^2}} \quad (15)$$

for a surface located at  $Z_1 = \text{constant}$  and with local incidence angle  $\phi_t$  measured from the positive  $X$  direction, see figure 5. The integrations are performed over the span and chord of the surface and coordinates  $X, Y, Z$  locate the field point at which the velocity potential is determined. To simplify the integrations, spanwise strips are arranged on the wing such that inclination angle  $\phi_t$  is approximately constant. These strips are swept with the wing and have much smaller chord than span dimension. Then the  $X_1$  coordinates of points in the narrow strip are approximated by

$$X_1 = X_c + Y_1 \tan \lambda_i \quad (16)$$

where  $\lambda_i$  is the sweep angle measured from a direction parallel to the positive  $Y$ -axis, see figure 5, and  $X_c$  is the value of  $X_1$  when  $Y_1$  is zero.

The integral then simplifies to

$$\frac{\Delta\phi}{V_\infty} = \frac{\tan \phi_t \Delta X_i}{2\pi} \int_{Y_b}^{Y_a} \frac{dY_1}{\sqrt{(X_c + Y_1 \tan \lambda_i - X)^2 + (Y - Y_1)^2 + (Z_1 - Z)^2}} \quad (17)$$

where  $\Delta X_i = X_a - X_b$ . Note that  $X_a$  and  $X_b$  as shown in figure 5 are negative. The integration can be performed and noting that  $\lambda_i = 180^\circ + \psi_i$  and  $\tan \phi_t = -\tan \theta \approx -\theta$ , the velocity potential due to one strip with span  $|Y_b - Y_a|$  at  $Z_1$  equals

$$\begin{aligned} \frac{\Delta \phi}{V_\infty} = & \frac{\theta \Delta X_i}{2\pi} \cos \psi_i \left\{ \ln \left[ \sqrt{(X_c + Y_a \tan \psi_i - X)^2 + (Y - Y_a)^2 + (Z_1 - Z)^2} \right. \right. \\ & \left. \left. - \frac{Y_a}{\cos \psi_i} + (X - X_c) \sin \psi_i + Y \cos \psi_i \right] \right. \\ & \left. - \ln \left[ \sqrt{(X_c + Y_b \tan \psi_i - X)^2 + (Y - Y_b)^2 + (Z_1 - Z)^2} - \frac{Y_b}{\cos \psi_i} \right. \right. \\ & \left. \left. + (X - X_c) \sin \psi_i + Y \cos \psi_i \right] \right\} \end{aligned} \quad (18)$$

where on the left wing panel  $Y_a$  and  $Y_b$  are negative. Differentiating with respect to  $X, Y, Z$  to obtain the perturbation velocities due to one strip results in the following expressions:

$$\begin{aligned} \frac{\Delta u}{V_\infty} = \frac{\partial}{\partial X} \left( \frac{\Delta \phi}{V_\infty} \right) &= \frac{\theta \Delta X_i}{2\pi} \cos \psi_i \\ & \bullet \left\{ \frac{-(X_c - X + Y_a \tan \psi_i) + B \sin \psi_i}{AB} - \frac{-(X_c - X + Y_b \tan \psi_i) + D \sin \psi_i}{CD} \right\} \\ \frac{\Delta v}{V_\infty} = \frac{\partial}{\partial Y} \left( \frac{\Delta \phi}{V_\infty} \right) &= \frac{\theta \Delta X_i}{2\pi} \cos \psi_i \left\{ \frac{Y - Y_a + B \cos \psi_i}{AB} - \frac{Y - Y_b + D \cos \psi_i}{CD} \right\} \\ \frac{\Delta w}{V_\infty} = \frac{\partial}{\partial Z} \left( \frac{\Delta \phi}{V_\infty} \right) &= \frac{\theta \Delta X_i}{2\pi} \cos \psi_i \left\{ \frac{-(Z_1 - Z)}{AB} - \frac{-(Z_1 - Z)}{CD} \right\} \end{aligned} \quad (19)$$

where

$$\left. \begin{aligned}
A &= \sqrt{(X_c - X + Y_a \tan \psi_i)^2 + (Y - Y_a)^2 + (Z_1 - Z)^2} \\
&\quad - \frac{Y_a}{\cos \psi_i} + (X - X_c) \sin \psi_i + Y \cos \psi_i \\
B &= \sqrt{(X_c - X + Y_a \tan \psi_i)^2 + (Y - Y_a)^2 + (Z_1 - Z)^2} \\
C &= \sqrt{(X_c - X + Y_b \tan \psi_i)^2 + (Y - Y_b)^2 + (Z_1 - Z)^2} \\
&\quad - \frac{Y_b}{\cos \psi_i} + (X - X_c) \sin \psi_i + Y \cos \psi_i \\
D &= \sqrt{(X_c - X + Y_b \tan \psi_i)^2 + (Y - Y_b)^2 + (Z_1 - Z)^2}
\end{aligned} \right\} \quad (20)$$

Similar expressions can be derived for the corresponding source strip on the right wing panel. The resulting expressions are identical to equations (19) and (20) except that  $Y_a$  and  $Y_b$  are interchanged, since  $Y_a$  is still the inboard side of the strip, and  $\tan \psi_i$  is replaced by  $-\tan \psi_i$  and  $\cos \psi_i$  is replaced by  $-\cos \psi_i$ . On the right wing panel  $Y_a$  and  $Y_b$  are positive. At a field point  $(X, Y, Z)$  the perturbation velocity components  $\frac{u}{V_\infty}$ ,  $\frac{v}{V_\infty}$ ,  $\frac{w}{V_\infty}$  induced by wing thickness are then given by equations (19) and (20) summed over all wing source strips on both the left wing panel and right wing panel.

The coordinate system and angle convention used with the pylon thickness model is shown in figure 6. This coordinate system is also the same as the vortex-lattice coordinate system. Analogous to the wing thickness model, the incompressible potential due to a surface at  $Y_p = \text{constant}$  and with chord  $|X_b - X_a|$  and span  $|Z_b - Z_a|$  may also be obtained from reference 13 or 14 with a simple coordinate transformation. With the local incidence angle  $\phi_{pt}$  measured from the positive X-direction, the result is

$$\frac{\Delta\phi}{V_\infty} = -\frac{1}{2\pi} \int_{X_b}^{X_a} \int_{Z_b}^{Z_a} \frac{\tan \phi_{pt} dZ_1 dX_1}{\sqrt{(X_1 - X)^2 + (Y_1 - Y)^2 + (Z_1 - Z)^2}} \quad (21)$$

The integrations are performed over the span and chord of the surface and coordinates  $X, Y, Z$  locate the field point at which the velocity potential is determined. As was done on the wing, spanwise strips are arranged on the pylon such that angle  $\phi_{pt}$  is approximately constant. The strips are swept with the pylon and have much smaller chord than span dimension. In terms of the coordinate system indicated in figure 6, the wing coordinate system, the  $X$ -coordinates of the narrow strip are given by

$$X_1 = X_{p_c} + Z_1 \tan \lambda_{p_i} \quad (22)$$

where sweep angle  $\lambda_{p_i}$  is measured from the positive (downward)  $Z$ -axis, positive for forward sweep. With the assumption of narrow strips and for a pylon located at  $Y_1 = Y_p$ , equation (21) simplifies to

$$\frac{\Delta\phi}{V_\infty} = - \frac{\tan \phi_{pt} \Delta X_i}{2\pi} \int_{Z_b}^{Z_a} \frac{dZ_1}{\sqrt{(X_{p_c} + Z_1 \tan \lambda_{p_i} - X)^2 + (Y_p - Y)^2 + (Z_1 - Z)^2}} \quad (23)$$

where  $\Delta X_i = X_a - X_b$ . Since  $\tan \phi_{pt} = \tan (180^\circ - \theta_p) \approx -\theta_p$  and  $\lambda_{p_i} = -\psi_i$ , see figure 6, the velocity potential due to one strip on the pylon is then given by

$$\begin{aligned} \frac{\Delta\phi}{V_\infty} = & \frac{\theta \Delta X_i}{2} \cos \psi_i \left\{ \ln \left[ \sqrt{(X_{p_c} - X - Z_a \tan \psi_i)^2 + (Y_p - Y)^2 + (Z_a - Z)^2} \right. \right. \\ & \left. \left. + \frac{Z_a}{\cos \psi_i} - (X_{p_c} - X) \sin \psi_i - Z \cos \psi_i \right] \right. \\ & \left. - \ln \left[ \sqrt{(X_{p_c} - X - Z_b \tan \psi_i)^2 + (Y_p - Y)^2 + (Z_b - Z)^2} \right. \right. \\ & \left. \left. + \frac{Z_b}{\cos \psi_i} - (X_{p_c} - X) \sin \psi_i - Z \cos \psi_i \right] \right\} \quad (24) \end{aligned}$$

Differentiating with respect to X,Y,Z yields the perturbation velocities induced by one spanwise source strip on the pylon. The results are

$$\begin{aligned}
 \frac{\Delta u}{V_\infty} &= \frac{\theta \Delta X_i}{2\pi} \cos \psi_i \\
 &\cdot \left\{ \frac{-X_{p_c} + X + Z_a \tan \psi_i + F \sin \psi_i}{EF} - \frac{-X_{p_c} + X + Z_b \tan \psi_i + H \sin \psi_i}{GH} \right\} \\
 \frac{\Delta v}{V_\infty} &= \frac{\theta \Delta X_i}{2\pi} \cos \psi_i \left\{ \frac{-Y_p + Y}{EF} - \frac{-Y_p + Y}{GH} \right\} \\
 \frac{\Delta w}{V_\infty} &= \frac{\theta \Delta X_i}{2} \cos \psi_i \left\{ \frac{-Z_a + Z - F \cos \psi_i}{EF} - \frac{-Z_b + Z - H \cos \psi_i}{GH} \right\}
 \end{aligned} \tag{25}$$

where

$$\begin{aligned}
 E &= \sqrt{(X_{p_c} - X - Z_a \tan \psi_i)^2 + (Y_p - Y)^2 + (Z_a - Z)^2} + \frac{Z_a}{\cos \psi_i} \\
 &\quad - (X_{p_c} - X) \sin \psi_i - Z \cos \psi_i \\
 F &= \sqrt{(X_{p_c} - X - Z_a \tan \psi_i)^2 + (Y_p - Y)^2 + (Z_a - Z)^2} \\
 G &= \sqrt{(X_{p_c} - X - Z_b \tan \psi_i)^2 + (Y_p - Y)^2 + (Z_b - Z)^2} + \frac{Z_b}{\cos \psi_i} \\
 &\quad - (X_{p_c} - X) \sin \psi_i - Z \cos \psi_i \\
 H &= \sqrt{(X_{p_c} - X - Z_b \tan \psi_i)^2 + (Y_p - Y)^2 + (Z_b - Z)^2}
 \end{aligned} \tag{26}$$

At a field point (X,Y,Z) the perturbation velocity components induced by pylon thickness are then given by equations (25) summed over all pylon source strips on both left and right pylons. The specification of the  $Y_p$  coordinate determines which pylon is accounted for.

In connection with the flow tangency boundary conditions, equations (6) and (7), perturbation velocities induced by the thickness envelopes of the wing and pylons are computed at the control points associated with the vortex lattice area elements on the wing-pylon combination. In general, these velocities are obtained by adding the result of summing equations (19) over all wing source strips to the result of summing equations (25) over all pylon source strips. The final sums are then added to the set of externally induced perturbation velocities  $u_i/V_\infty$ ,  $v_i/V_\infty$ ,  $w_i/V_\infty$  that appear in the flow tangency boundary conditions. In this way, all interference effects induced by the wing on the pylon and vice versa are accounted for and will be reflected in the resulting circulation strength distribution on the wing-pylon combination.

#### 4.3 TER or MER Rack Flow Model

The remaining aircraft component to be modeled is the rack used for multiple carriage of stores such as a triple ejector rack, TER, or a multiple ejector rack, MER. A wind-tunnel model of a TER rack is shown in figure 7. This can be approximated by an axisymmetric body to which are attached three short pylons. The model used in the present work for modeling racks of this type is one which accounts only for the volume distribution associated with the axisymmetric body portion of the rack. This is represented by a distribution of three-dimensional point sources along the longitudinal axis. The source strengths and perturbation velocities are determined in the same manner as described in section 4.1 for the fuselage and stores.

The short pylons have been neglected in the present work. Their effect could be included, however, it has not been done. The importance of neglecting these short pylons will be discussed in section 7.2.

#### 5. FORCE AND MOMENT CALCULATION

The calculation of the trajectory of a store dropped from an aircraft requires a knowledge of the forces and moments acting on the store at each point in the trajectory. In order to calculate these forces and

moments, the nonuniform velocity field in which the store is immersed, as seen by the store, must be determined at each point in time. This field includes the free-stream velocity, the perturbation velocities induced by the parent aircraft, and the angular velocities due to the store's pitch, yaw, and roll motions. The distribution along the body axis is required in order to calculate the forces and moments acting on the body and, if an empennage is present, the distribution over the tail fin surfaces is required for the empennage force and moment calculation.

This section will first describe the calculation of the velocity field utilizing the flow models of section 4. Following this the methods employed to calculate the body and empennage forces and moments from this nonuniform flow field will be presented.

#### 5.1 Calculation of the Velocity Field Including Damping

The  $x_s, y_s, z_s$  coordinate system to be used in the force and moment calculations is shown in figure 8. It is fixed in the store with the origin at the store nose with the velocities  $U_s, V_s,$  and  $W_s$  positive in the directions shown. These are the total velocities as seen by a point on the store and each is composed of a free-stream component, a perturbation component due to the parent aircraft, and a damping component due to the store's rotational motion.

Before writing the expressions for these velocities let us examine figure 9 which shows the coordinate systems used in the trajectory calculation. The equations of motion will be presented in section 6. Two coordinate systems are shown in figure 9. The  $\xi, \eta, \zeta$  system is an inertial system fixed in the aircraft which is in rectilinear flight at uniform velocity. The positive  $\xi$  axis is forward along the fuselage longitudinal axis, the  $\eta$  axis is positive laterally to the right, and the  $\zeta$  axis is positive downward perpendicular to the fuselage longitudinal axis. The origin of this system is fixed in the fuselage nose.

The  $x, y, z$  coordinate system is fixed in the store with the origin at the store moment center. Referring back to figure 8, the  $x$ -axis lies along the store longitudinal axis but is positive forward. The  $y$ -axis is parallel to the  $y_s$  axis and positive in the same direction and the  $z$  axis is parallel to the  $z_s$  axis but positive downward. The  $x, y, z$  system shown in figure 8 is a right-hand system and the store angular velocity components about the three axes are  $p, q,$  and  $r$  respectively.

In figure 9 the origins of the two coordinate systems have been drawn to coincide in order to show the angles used to determine the orientation of the store with respect to the inertial  $(\xi, \eta, \zeta)$  axes. The system of angles chosen consists of three rotations in the yaw,  $\Psi$ ; pitch,  $\theta$ ; and roll,  $\phi$ ; sequence (ref. 15). The two coordinate systems are then related by

$$\begin{bmatrix} \xi \\ \eta \\ \zeta \end{bmatrix} = [A] \begin{bmatrix} x \\ y \\ z \end{bmatrix} \quad (27)$$

where

$$[A] = \begin{bmatrix} \cos \theta \cos \Psi & \sin \phi \sin \theta \cos \Psi & \cos \phi \sin \theta \cos \Psi \\ & -\cos \phi \sin \Psi & +\sin \phi \sin \Psi \\ \cos \theta \sin \Psi & \sin \phi \sin \theta \sin \Psi & \cos \phi \sin \theta \sin \Psi \\ & +\cos \phi \cos \Psi & -\sin \phi \cos \Psi \\ -\sin \theta & \sin \phi \cos \theta & \cos \phi \cos \theta \end{bmatrix} \quad (28)$$

The three velocity components,  $U_s$ ,  $V_s$ , and  $W_s$ , are

$$\left. \begin{aligned} U_s &= U_{\infty, x_s} + u_s \\ V_s &= V_{\infty, y_s} + v_s + r(x_s - x_{s,m}) \\ W_s &= W_{\infty, z_s} + w_s + q(x_s - x_{s,m}) \end{aligned} \right\} \quad (29)$$

The first term on the right side of the equal sign in each of the above expressions is the component of the free-stream velocity vector. If the parent aircraft is moving at velocity,  $V_\infty$ , and flying at angle of attack,  $\alpha_f$ , then the velocity of the inertial coordinate system relative to a point in space is

$$\vec{V}_\infty = V_\infty \cos \alpha_f \vec{e}_\xi + V_\infty \sin \alpha_f \vec{e}_\zeta \quad (30)$$

The velocity of the store moment center relative to the moving inertial system is

$$\vec{V}_m = \dot{\xi} \vec{e}_\xi + \dot{\eta} \vec{e}_\eta + \dot{\zeta} \vec{e}_\zeta \quad (31)$$

so that the velocity of the store relative to a point in space is

$$\begin{aligned} \vec{V}_{\infty_s} &= \vec{V}_\infty + \vec{V}_m \\ &= (V_\infty \cos \alpha_f + \dot{\xi}) \vec{e}_\xi + \dot{\eta} \vec{e}_\eta \\ &\quad + (V_\infty \sin \alpha_f + \dot{\zeta}) \vec{e}_\zeta \end{aligned} \quad (32)$$

Since the velocity components needed in equation (29) are those as seen by a point fixed in the store and moving with the store, equation (32) becomes

$$\begin{aligned} \vec{V}_{\infty_s} &= - (V_\infty \cos \alpha_f + \dot{\xi}) \vec{e}_\xi - \dot{\eta} \vec{e}_\eta \\ &\quad - (V_\infty \sin \alpha_f + \dot{\zeta}) \vec{e}_\zeta \end{aligned} \quad (33)$$

The components in the  $x, y, z$  coordinate system of figure 8 are then

$$\begin{bmatrix} U_{\infty_{s,x}} \\ V_{\infty_{s,y}} \\ W_{\infty_{s,z}} \end{bmatrix} = [A]' \begin{bmatrix} - (V_\infty \cos \alpha_f + \dot{\xi}) \\ - \dot{\eta} \\ - (V_\infty \sin \alpha_f + \dot{\zeta}) \end{bmatrix} \quad (34)$$

where  $[A]'$  is the transpose, or inverse since  $[A]$  is orthogonal, of the matrix given in equation (28). These velocity components are related to those in the coordinate system of figure 8 by

$$\left. \begin{aligned}
 U_{\infty s, x_s} &= - U_{\infty s, x} \\
 V_{\infty s, y_s} &= V_{\infty s, y} \\
 W_{\infty s, z_s} &= - W_{\infty s, z}
 \end{aligned} \right\} \quad (35)$$

The second term in the three expressions of equation (29) is the perturbation velocity term. This is comprised of the perturbation velocities induced by the fuselage, wing, pylon, rack and other stores and is calculated by the methods presented in section 4. It is to be remembered that these methods apply to the equivalent incompressible configuration. At each point in the trajectory the points at which the velocities are required must be located in the incompressible space. The perturbation velocities induced by the fuselage, rack, and store volumes are calculated using equations (4) and (5), those induced by the wing- pylon vortex lattice are determined by equation (8) by summing over all vortices, and those induced by the wing and pylon thickness distribution are obtained from equations (19) and (25) by summing over all thickness strips. The velocities calculated using these equations are in the coordinate system of each aircraft component. Prior to transforming these back to the compressible space they must be summed up in the fuselage coordinate system since this is the coordinate system in which the compressibility correction was applied. This system is the  $(\xi, \eta, \zeta)$  system of figure 9.

Let  $u_{\xi}'$ ,  $v_{\eta}'$ , and  $w_{\zeta}'$  be the sums in the  $\xi, \eta$ , and  $\zeta$  directions respectively. Then from equation (2) the compressible perturbation velocities are

$$u_{\xi} = \frac{u_{\xi}'}{\beta^2}, \quad v_{\eta} = \frac{v_{\eta}'}{\beta}, \quad w_{\zeta} = \frac{w_{\zeta}'}{\beta} \quad (36)$$

The velocity components in the  $x$ ,  $y$ , and  $z$  directions of figure 8 are

$$\begin{bmatrix} u \\ v \\ w \end{bmatrix} = [A]' \begin{bmatrix} u_\xi \\ v_\eta \\ w_\zeta \end{bmatrix} \quad (37)$$

and, finally, the components in the coordinate system of figure 8 are

$$u_s = -u, \quad v_s = v, \quad w_s = -w \quad (38)$$

In calculating the velocity field for the case of a store released from under the fuselage the presence of the wing is ignored for the reasons discussed in section 5.1 of reference 1. The arguments presented there apply to the present case even though the configuration is more complicated. Fuselage angle of attack effects are included for this case and given by

$$w_\zeta' = V_\infty \sin \alpha_f' \left[ 1 - \left( \frac{a}{\zeta'} \right)^2 \right] \quad (39)$$

where  $w_\zeta'$  is the velocity normal to the fuselage axis in the incompressible space a distance  $\zeta'$  from the axis,  $a$  is the local fuselage radius, and  $\alpha_f'$  is the fuselage angle of attack in the incompressible space. This velocity field is added to the pylon-induced and volume-induced velocity fields. Equation (39) is obtained from the complex potential for a circular cylinder in uniform flow given on page 29 of reference 16. For stores under the wing this velocity is not included in the perturbation field for reasons which are also discussed in section 5.1 of reference 1.

The last terms on the right side of the expressions for  $V_s$  and  $W_s$  in equation (29) are the yaw and pitch damping terms. The positive directions of the rotational velocities are shown in figure 9. It can be seen that  $r$  is positive for nose-to-the-right motion and  $q$  is positive for nose-up motion. The means of accounting for roll damping will be discussed in the section describing the empennage force and moment calculation, section 5.3. The rotational velocities,  $p$ ,  $q$ , and  $r$ ,

are determined as a function of time during the integration of the equations of motion.

The velocities to be used in the force and moment calculations are made dimensionless by the store free-stream velocity. Thus, equation (29) becomes

$$\left. \begin{aligned} U_S^* &= \frac{U_S}{V_{\infty S}} = V_{\infty S, X_S}^* + u_S^* \\ V_S^* &= \frac{V_S}{V_{\infty S}} = V_{\infty S, Y_S}^* + v_S^* + \frac{r(x_S - x_{S,m})}{V_{\infty S}} \\ W_S^* &= \frac{W_S}{V_{\infty S}} = W_{\infty S, Z_S}^* + w_S^* + \frac{q(x_S - x_{S,m})}{V_{\infty S}} \end{aligned} \right\} \quad (40)$$

where from equation (32) or (33)

$$V_{\infty S} = \left[ (V_{\infty} \cos \alpha_f + \dot{\xi})^2 + \dot{\eta}^2 + (V_{\infty} \sin \alpha_f + \dot{\zeta})^2 \right]^{1/2} \quad (41)$$

At any point in time during the trajectory the forces and moments are determined by removing the store from the flow field, determining the velocities at a series of points which the store longitudinal axis and tail fins occupied, and then immersing the store in this flow field.

## 5.2 Body Forces and Moments

The store body force and moment calculations have not changed significantly since reference 1. Slender-body theory is the basis for calculating the body normal-force and side-force distributions which yield forces and moments. A simplified method of calculating the buoyant force has been introduced which eliminates the necessity of calculating the lateral and vertical pressure gradients and speeds the computation. As in reference 1, when large values of the combined angle resulting from upwash and sidewash occur, such that the body boundary layer separates, the slender-body theory calculation is not continued. Simple viscous crossflow theory is used downstream of the separation location.

### 5.2.1 Buoyancy forces and moments

In the work of reference 1 the buoyancy normal-force distribution was determined from the vertical pressure gradient acting on the body. This required the calculation of the velocity field not only along the body longitudinal axis but also along the upper and lower surfaces of the body. In the present work the buoyancy side-force distribution is also required which would necessitate calculating the velocities along the two sides of the store as well. Since calculating the velocity field at five points at each axial station would be very time consuming, a simplified method for calculating the buoyancy forces and moments has been adopted which yields comparable accuracy.

This simplified method was discussed in reference 1. There it is shown that if it is assumed that the flow in planes perpendicular to the axis of the store obeys Laplace's equation and that the upwash and sidewash velocities vary along the store length, and the potential is constructed on this basis, then integration of the body pressures obtained from the unsteady Bernoulli equation yield both the buoyancy forces and the slender-body forces. The final expression for the buoyancy normal-force coefficient is given by equation (63) of reference 1. The derivation is carried out in Appendix I of that reference with the final expression which contains both the buoyancy and slender-body terms given by equation (I-14).

The expressions which have been used in the present work to calculate the buoyancy normal-force and side-force coefficients, derived in this manner, are

$$(C_N)_{BY} = \frac{2\pi}{S_R} \int_0^{\ell_s} a^2 \frac{dW_s^*}{dx_s} dx_s \quad (42)$$

and

$$(C_Y)_{BY} = \frac{2\pi}{S_R} \int_0^{\ell_s} a^2 \frac{dV_s^*}{dx_s} dx_s \quad (43)$$

The expressions for the pitching-moment and yawing-moment coefficients, with the moment taken about  $x_{s,m}$  (see fig. 8), are

$$(C_m)_{BY} = \frac{2\pi}{S_R l_R} \int_0^{l_S} (x_{s,m} - x_s) a^2 \frac{dW_s^*}{dx_s} dx_s \quad (44)$$

and

$$(C_n)_{BY} = \frac{2\pi}{S_R l_R} \int_0^{l_S} (x_{s,m} - x_s) a^2 \frac{dV_s^*}{dx_s} dx_s \quad (45)$$

### 5.2.2 Slender-body forces and moments

The slender-body forces and moments are determined in the same manner as described in section 6.2.1 of reference 1. The derivation will not be repeated here. The expressions for the forces and moments, from that reference are

$$(C_N)_{SB} = \frac{2\pi}{S_R} \int_0^{x_{s,0}} \frac{d}{dx_s} (a^2 W_s^*) dx_s \quad (46)$$

$$(C_Y)_{SB} = \frac{2\pi}{S_R} \int_0^{x_{s,0}} \frac{d}{dx_s} (a^2 V_s^*) dx_s \quad (47)$$

$$(C_m)_{SB} = \frac{2\pi}{S_R l_R} \int_0^{x_{s,0}} (x_{s,m} - x_s) \frac{d}{dx_s} (a^2 W_s^*) dx_s \quad (48)$$

$$(C_n)_{SB} = \frac{2\pi}{S_R l_R} \int_0^{x_{s,0}} (x_{s,m} - x_s) \frac{d}{dx_s} (a^2 V_s^*) dx_s \quad (49)$$

The upper limit on the above integrals is the assumed separation location, that is, the point at which viscous forces become important.

No definite rules for the selection of a value of  $x_{s,0}$  can be given. For stores with cylindrical afterbodies  $x_{s,0}$  should probably be taken as  $l_S$ , the store base. For stores with boattailed afterbodies  $x_{s,0}$  should probably be less than  $l_S$ . A further discussion is given in sections 6.2 and 8.2 of reference 1. In that discussion the work of

Hopkins (ref. 17) is mentioned. In this work he correlated, for bodies of revolution in uniform flow, the maximum extent of applicability of potential flow as a function of the location of the maximum negative rate of change of body cross-sectional area. From that reference

$$\frac{x_{s,0}}{l_s} = 0.378 + 0.527 \frac{x_{s,1}}{l_s} \quad (50)$$

where  $x_{s,0}/l_s$  is the location on the body where potential flow is no longer applicable and viscous forces are important and  $x_{s,1}/l_s$  is the location on the body of the maximum negative rate of change of cross-sectional area. Whether or not this correlation applies to nonuniform flow is not known but it can be used in estimating the value of  $x_{s,0}$ .

### 5.2.3 Viscous crossflow forces and moments

From the assumed separation location to the base of the store a viscous crossflow calculation is used in place of the slender body calculation. The expressions for normal force and pitching moment are derived in section 6.2.2 of reference 1. The expressions for side force and yawing moment are derived in a similar manner. The expressions for the two forces and two moments are

$$(C_N)_{CF} = \frac{2c_{dc}}{S_R} \int_{x_{s,0}}^{l_s} aV_c^* W_s^* dx_s \quad (51)$$

$$(C_Y)_{CF} = \frac{2c_{dc}}{S_R} \int_{x_{s,0}}^{l_s} aV_c^* V_s^* dx_s \quad (52)$$

$$(C_m)_{CF} = \frac{2c_{dc}}{S_R l_R} \int_{x_{s,0}}^{l_s} (x_{s,m} - x_s) aV_c^* W_s^* dx_s \quad (53)$$

$$(C_n)_{CF} = \frac{2c_{dc}}{S_R l_R} \int_{x_{s,0}}^{l_s} (x_{s,m} - x_s) aV_c^* V_s^* dx_s \quad (54)$$

where

$$V_c^* = \sqrt{(V_s^*)^2 + (W_s^*)^2} \quad (55)$$

and  $c_{d_c}$  is the section-drag coefficient of a cylinder normal to the free stream. That is

$$c_{d_c} = \frac{\text{drag per unit length}}{q_{\infty_s} (2a)}$$

### 5.3 Empennage Forces and Moments

A method of calculating the forces and moments associated with planar or cruciform empennages will now be presented. It has been noted from experimental data that the variation in flow velocity normal to the empennage panels varies very little in the chordwise direction, for fins with small chords, as compared to the spanwise direction. Accordingly, the effective shape of the empennage panels is essentially that of pure twist with zero camber. For such panels, it is possible to calculate the empennage forces using reverse-flow theorems. The net force generated by a panel, including that carried over onto the store body, can be obtained in terms of an integral, across the span of the panel, of the product of the twist angle times an influence function which corresponds to span loading of an associated empennage in uniform reverse flow. Influence functions have been derived for calculating empennage normal force, side force, pitching moment, yawing moment, and rolling moment for planar and cruciform empennages. For cruciform empennages panel-panel interference has been accounted for. Complete mathematical details of the method are contained in Appendix I.

A crossflow plane in the empennage region is shown in figure 10 for a cruciform empennage. The tail fins are numbered  $F_1$ ,  $F_2$ ,  $F_3$ , and  $F_4$  such that, for a planar empennage, fins  $F_3$  and  $F_4$  are not present. This crossflow plane is the plane in which the empennage forces are assumed to act and will be taken as that which contains the quarter chord of the mean aerodynamic chord of the exposed panels. In the present work all of the fins will be assumed to have the same planform.

The  $x_f$ ,  $y_f$ ,  $z_f$  coordinate system is fixed in the tail fins such that the  $x_f$ ,  $y_f$  plane contains the horizontal fins and, in the case of a cruciform empennage, the  $x_f$ ,  $z_f$  plane contains the vertical fins.

This coordinate system is rolled an angle  $\phi_f$  from the  $x_s, y_s, z_s$  store body coordinate system of figure 8. Both coordinate systems move with the store during the trajectory. In the trajectory calculation the  $x_s, z_s$  plane is assumed to be parallel to the  $\xi, \zeta$  plane in the inertial system (see fig. 9) at time  $t = 0$  seconds. Thus, the specification of the angle  $\phi_f$  allows a trajectory to be started with the fins in other than the vertical and horizontal positions.

Also shown in figure 10 are the velocities required for the empennage force and moment calculation. The arrows indicate the positive directions. The velocities on each fin are required at  $n$  equally spaced points between the body radius and the tip of the panel. The coordinates of the points are  $(i = 1, \dots, n)$

$$\left. \begin{aligned}
 F_1: y_{f,i} &= a + \frac{(i-1)}{(n-1)} (s_h - a); z_{f,i} = 0 \\
 F_2: Y_{f,i} &= -a - \frac{(i-1)}{(n-1)} (s_h - a); z_{f,i} = 0 \\
 F_3: z_{f,i} &= -a - \frac{(i-1)}{(n-1)} (s_v - a); Y_{f,i} = 0 \\
 F_4: z_{f,i} &= a + \frac{(i-1)}{(n-1)} (s_v - a); Y_{f,i} = 0
 \end{aligned} \right\} \quad (56)$$

The  $x_f$  location of all points is the same, that is, the axial location of the quarter chord of the mean aerodynamic chord,  $l_f$  in figure 8. In calculating the velocities normal to the fins the coordinates of the points given by equation (56) are first transformed to the store body coordinate system, the  $x_s, y_s, z_s$  system, and then the velocities in this system are calculated as described in section 5.1. These velocities are given by equation (29) and include the store translational motion as well as the yaw and pitch rotations. The velocities normal to the fins are then obtained by summing up the components of  $W_s$  and  $V_s$  normal to the fins.

$$\left. \begin{aligned}
 W_1 &= W_S \cos \phi_f + V_S \sin \phi_f \\
 W_2 &= W_S \cos \phi_f + V_S \sin \phi_f \\
 V_1 &= -W_S \sin \phi_f + V_S \cos \phi_f \\
 V_2 &= -W_S \sin \phi_f + V_S \cos \phi_f
 \end{aligned} \right\} \quad (57)$$

The equations presented in Appendix I determine the forces and moments produced by the empennage in the  $x_f, y_f, z_f$  coordinate system of figure 10. The force given by equation (I-13) is positive in the  $z_f$  direction and the force given by equation (I-18) is positive in the  $y_f$  direction. The moment given by equation (I-21) is positive nose up about the  $y_f$  axis and that of equation (I-22) is positive nose to the right about the  $z_f$  axis. Since the  $x_f$  and  $x_s$  axes coincide the rolling moment expressions, equations (I-30) and (I-52), apply to both coordinate systems and the positive sense is right wing down.

In the store body coordinate system, which is the system the forces and moments must be in for the trajectory calculation, the normal-force and side-force coefficients are, from equations (I-13) and (I-18),

$$\begin{aligned}
 (C_N)_E &= \cos \phi_f \left[ (C_Z)_{BH} - (C_Z)_B \right]_f \\
 &\quad - \sin \phi_f \left[ (C_Y)_{BV} - (C_Y)_B \right]_f
 \end{aligned} \quad (58)$$

$$\begin{aligned}
 (C_Y)_E &= \sin \phi_f \left[ (C_Z)_{BH} - (C_Z)_B \right]_f \\
 &\quad + \cos \phi_f \left[ (C_Y)_{BV} - (C_Y)_B \right]_f
 \end{aligned} \quad (59)$$

Similarly, from equations (I-21) and (I-22), the pitching-moment and yawing-moment coefficients are

$$\begin{aligned}
 (C_m)_E &= \cos \phi_f \left[ (C_m)_{BH} - (C_m)_B \right]_f \\
 &\quad - \sin \phi_f \left[ (C_n)_{BV} - (C_n)_B \right]_f
 \end{aligned} \quad (60)$$

$$\begin{aligned}
(C_n)_E &= \sin \phi_f \left[ (C_m)_{BH} - (C_m)_B \right]_f \\
&+ \cos \phi_f \left[ (C_n)_{BV} - (C_n)_B \right]_f
\end{aligned}
\tag{61}$$

The rolling-moment coefficient for a planar empennage is given by equation (I-30)

$$(C_l)_E = (C_l)_H \tag{62}$$

and that for a cruciform empennage by equation (I-52)

$$(C_l)_E = (C_l)_{HV} \tag{63}$$

## 6. CALCULATION OF STORE TRAJECTORIES

In the preceding sections of this report, methods have been presented for modeling the various aircraft components, for calculating the non-uniform flow field due to the aircraft, and for calculating the forces and moments acting on a store immersed in this flow field at any location relative to the aircraft. Utilizing these tools a computer program has been written which integrates the equations of motion of the store to determine its location and orientation relative to the parent aircraft as a function of time. In the work of reference 1, this motion was restricted to three degrees of freedom. In the present work the equations of motion allow six degrees of freedom.

In this section of the report the equations of motion will first be discussed and then the computer program will be described.

### 6.1 Equations of Motion

The complete derivation of the equations of motion of a rigid body with mass and inertia asymmetries is presented in Appendix II. Generally the body, a store in the present application, will have axes of geometrical symmetry about which the store forces and moments are determined. By mass asymmetry it is meant that the store center of mass does not have to lie at the origin of this coordinate system. By inertia asymmetry it is meant that the principal axes of inertia of the store do not coincide

with the geometric axes of symmetry so that the tensor of inertia possesses off-diagonal terms, the products of inertia.

In the derivation of Appendix II the two coordinate systems discussed earlier in conjunction with the velocity field calculation, section 5.1, are used. They are shown in figure 9. The  $x, y, z$  coordinate system is fixed in the store and rotates with the store. The  $x$ -axis lies along the store longitudinal axis and is positive forward, the  $y$ -axis is positive to the right, and the  $z$ -axis is positive downward. These axes coincide with the geometric axes of symmetry with the origin at the point about which the moments and products of inertia and the aerodynamic moments are calculated. The equations of motion are derived in this coordinate system since, by allowing the coordinate system to rotate with the store, the time derivatives of the moments and products of inertia do not appear in the rotational equations of motion. The equations of motion in this coordinate system are given by equations (II-15) and (II-40) of Appendix II.

Since the store coordinate system in which these equations of motion are written does not allow the store position and orientation to be determined relative to the parent aircraft, a coordinate system is introduced which is fixed in the fuselage nose, the  $\xi, \eta, \zeta$  system of figure 9. In the present work it is assumed that the parent aircraft is flying at constant velocity, constant angle of attack, and constant flight path angle relative to the horizontal so that this system is a non-rotating system. As such, it can be regarded as an inertial system and the store motion relative to this moving system calculated.

The  $\xi, \eta, \zeta$  system is fixed in the fuselage nose with  $\xi$  forward along the fuselage longitudinal axis,  $\eta$  laterally to the right, and  $\zeta$  vertically downward. In order to determine the orientation of the store with respect to these axes, a system of angles must be introduced. These angles are also shown in figure 9 and consist of three rotations in the yaw,  $\Psi$ ; pitch,  $\theta$ ; roll,  $\phi$ ; sequence. In order to determine the time histories of these angles differential equations expressing them as a function of the store rotational velocities,  $p, q,$  and  $r,$  are required. These are given by equation (II-1) of Appendix II. The rotational velocities,  $p, q,$  and  $r,$  are shown in figure 9. The velocity about the  $x$ -axis is  $p$  and is positive right-wing down. Those about the  $y$ - and  $z$ -axes are  $q$  and  $r$  respectively and are positive nose up and nose to the right.

The final differential equations which are to be integrated to determine the store position and orientation relative to the inertial system fixed in the fuselage are equations (II-1), (II-16) through (II-18), and (II-41) through (II-43). The latter six equations are obtained from equations (II-15) and (II-40) by using the direction cosines relating the two coordinate systems, equation (II-2). In the equations,  $\ddot{\xi}$ ,  $\ddot{\eta}$ , and  $\ddot{\zeta}$  are the accelerations of the store moment center, the point about which the moments and products of inertia are taken, in the inertial coordinate system. The velocities in this system are  $\dot{\xi}$ ,  $\dot{\eta}$ , and  $\dot{\zeta}$  and the quantities  $\dot{x}_o$ ,  $\dot{y}_o$ , and  $\dot{z}_o$  are these velocities resolved into the store body coordinate system. That is

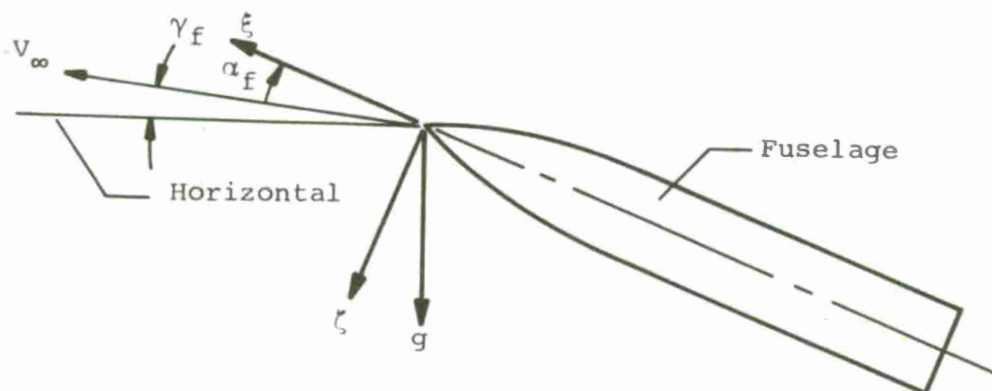
$$\begin{bmatrix} \dot{x}_o \\ \dot{y}_o \\ \dot{z}_o \end{bmatrix} = [A]' \begin{bmatrix} \dot{\xi} \\ \dot{\eta} \\ \dot{\zeta} \end{bmatrix} \quad (64)$$

where  $[A]'$  is the transpose of the matrix given by equation (II-2). The location of the store center of mass relative to the store moment center in store body coordinates is  $\bar{x}$ ,  $\bar{y}$ ,  $\bar{z}$ . The three rotational velocities in the store body coordinate system are  $p$ ,  $q$ , and  $r$  and the corresponding accelerations are  $\dot{p}$ ,  $\dot{q}$ , and  $\dot{r}$ . The quantities  $I_{xx}$ ,  $I_{yy}$ , and  $I_{zz}$  are the moments of inertia and  $I_{yz}$ ,  $I_{xz}$ , and  $I_{xy}$  are the products of inertia. They are defined by equation (II-36).

The remaining parameters in the equations of motion are the store mass,  $m$ , and the forces,  $F_x$ ,  $F_y$ , and  $F_z$ , and moments,  $M_x$ ,  $M_y$ , and  $M_z$ , acting on the store which are positive in the positive  $x$ ,  $y$ ,  $z$ ,  $p$ ,  $q$ , and  $r$  directions respectively. The three forces are

$$\left. \begin{aligned} F_x &= mg_x - q_{\infty} S_R C_A \\ F_y &= mg_y + q_{\infty} S_R C_Y \\ F_z &= mg_z - q_{\infty} S_R C_N \end{aligned} \right\} \quad (65)$$

In these equations  $g_x$ ,  $g_y$ , and  $g_z$  are the component of the gravitational acceleration vector  $\vec{g}$  in the store body coordinate system. Consider the following sketch



which shows the fuselage flying at velocity  $V_\infty$ , angle of attack  $\alpha_f$ , and flight path angle  $\gamma_f$ . The gravitational force acts normal to the local horizontal so that in the inertial coordinate system

$$\vec{g} = -g \sin (\alpha_f + \gamma_f) \vec{e}_\xi + g \cos (\alpha_f + \gamma_f) \vec{e}_\zeta \quad (66)$$

Then

$$\begin{bmatrix} g_x \\ g_y \\ g_z \end{bmatrix} = [A] \begin{bmatrix} -g \sin (\alpha_f + \gamma_f) \\ 0 \\ g \cos (\alpha_f + \gamma_f) \end{bmatrix} \quad (67)$$

The second terms in equation (65) are the aerodynamic forces acting on the store. The axial-force coefficient,  $C_A$ , is specified and is positive in the negative  $x$  direction. The sideforce and normal force coefficients,  $C_Y$  and  $C_N$ , are calculated by the methods described in section 5 and are positive in the positive  $y$  and negative  $z$  directions respectively. These coefficients are the sums of all of the components calculated in section 5. For example

$$C_N = (C_N)_{BY} + (C_N)_{SB} + (C_N)_{CF} + (C_N)_E \quad (68)$$

The parameters  $q_{\infty_s}$  and  $S_R$  are the dynamic pressure and reference area used in nondimensionalizing the forces. In the present work they are taken as the store free-stream dynamic pressure and the store maximum cross-sectional area

$$q_{\infty_s} = \frac{1}{2} \rho_{\infty} V_{\infty_s}^2 \quad (69)$$

$$S_R = \pi a_{\max}^2 \quad (70)$$

The density  $\rho_{\infty}$  is assumed constant at the value for the aircraft flight altitude at time  $t = 0$  and the store free-stream velocity is given by equation (41).

The three moments about the store moment center are

$$\left. \begin{aligned} M_x &= q_{\infty_s} S_R l_R C_l + m(g_z \bar{y} - g_y \bar{z}) \\ M_y &= q_{\infty_s} S_R l_R C_m + m(g_x \bar{z} - g_z \bar{x}) \\ M_z &= q_{\infty_s} S_R l_R C_n + m(g_y \bar{x} - g_x \bar{y}) \end{aligned} \right\} \quad (71)$$

The first term on the right-hand side of each of the above expressions is the aerodynamic moment. The moment coefficients,  $C_l$ ,  $C_m$ , and  $C_n$ , are calculated by the methods of section 5. The reference length,  $l_R$ , is taken as the maximum store diameter

$$l_R = 2a_{\max} \quad (72)$$

The second terms are moments produced by the gravitational force when the location of the store center of mass does not coincide with the center of moments.

In order to integrate the equations of motion given by equations (II-16) through (II-18) and (II-41) through (II-43) and the equations determining the angular orientation, equation (II-1), initial conditions of the variables must be specified. These are the position of the store center of moments  $(\xi, \eta, \zeta)$ , the translational velocity of this point  $(\dot{\xi}, \dot{\eta}, \dot{\zeta})$ , the angular velocities about the three store axes

$p, q, r$ ), and the initial orientation angles ( $\Psi, \theta, \phi$ ). With these specified the equations can be integrated with the aerodynamic forces and moments being recalculated at each point in the trajectory.

## 6.2 Description of Computer Program

The computer program which has been written to calculate the trajectory of a store ejected from an aircraft consists of two programs, an axisymmetric source distribution program and a trajectory program. The calculation of the source distributions to represent the various axisymmetric bodies has been kept separate for two reasons. First, a number of runs may have to be made with the program to obtain a source distribution which adequately reproduces the shape of the body. The second reason is that once the source distribution is obtained for a specific Mach number it need not be recalculated since for a given body shape the distribution is only a function of Mach number.

For a given aircraft-stores combination and Mach number source distributions must be obtained for the fuselage, each different store shape, and the ejection rack if one is present. The various shapes are specified by a series of segmented polynomials and the program calculates and prints the source locations and strengths. The locations are determined by the program from two input parameters, the location of the source nearest the nose and the distance between sources which is specified as a fraction of the local body radius.

The trajectory program consists of three main sections. The first section reads in the input data and calculates quantities from these data, the second section solves for the vorticity distribution which represents the wing-pylon loading, and the third section calculates the trajectory.

The input data section of the program reads in the following information:

- (1) Aircraft flight conditions
- (2) Indices specifying what aircraft components are present
- (3) Fuselage data
- (4) Wing data
- (5) Pylon data
- (6) Rack data
- (7) Store data

The aircraft flight conditions are the angle of attack, flight path angle, Mach number, free-stream air density, and flight velocity.

Item (2) consists of four indices. The first three specify whether or not the fuselage, pylon, and rack are present and the fourth specifies the number of stores. The program in its present form will handle a maximum of ten stores.

The fuselage input data consist of the length, maximum radius, and source distribution.

The wing input data locate the wing relative to the fuselage, including its incidence, and supply information required to lay out the vorticity and thickness distributions. The data also include the twist and camber distribution and the slope distribution of the thickness envelope.

The pylon input data locate the pylon, from which the store is to be ejected, laterally relative to the fuselage longitudinal axis and longitudinally relative to the leading edge of the local wing chord. As for the wing, data required to lay out the vorticity and thickness distributions are input together with the slope distribution of the thickness envelope. The pylon is assumed to have zero twist and camber.

The rack is assumed to be immediately below the pylon. The input data for the rack locate its nose relative to the local wing chord and specify its incidence relative to the wing root chord. In addition the rack length and maximum radius are input.

For each store present on the aircraft, data are input which assign it a store number and specify a shape number, the length, and the maximum radius. Each store is located by specifying its lateral position relative to the wing root chord and the longitudinal and vertical position of the store nose relative to the wing chord immediately above the store. The incidence of the store relative to the wing root chord is also specified. A source distribution is input for each different store shape.

The second main part of the program calculates the wing-ylon vorticity distribution. This is done using equations (6) and (7) of section 4.2.2. The coefficient matrix is first calculated and then the right-hand side is determined. The strengths of the vortices are then calculated by solving the set of simultaneous equations.

The third and last main part of the trajectory program is the trajectory calculation. This section of the program consists of the following steps:

- (1) Input additional information to describe ejected store.
- (2) Input empennage data if store has one.
- (3) Initialize for trajectory calculation.
- (4) Calculate aerodynamic forces and moments.
- (5) Calculate accelerations and rates of change of orientation angles.
- (6) Integrate equation of motion.

The additional data describing the store to be ejected include indices specifying which store is to be ejected, the number of segments the body is to be broken into for the force calculation, the separation location, and whether the store has an empennage. Also, the store mass and inertia characteristics are read in along with the location of the point about which the aerodynamic moments are to be calculated. This is the point about which the moments and products of inertia were taken. The location of the store center of mass relative to this point is also specified as are the store axial force coefficient and the value of the crossflow drag coefficient to be used in the viscous crossflow force and moment calculation.

Three other indices are input which pertain to options included in the computer program. Provision has been made to include or exclude the damping terms in the velocity field calculation. Also, for stores with empennages, rolling moment may or may not be included in the acceleration determination. The third option pertains to the calculation of free-flight trajectories as opposed to captive-store trajectories as obtained in the wind tunnel. In wind-tunnel captive-store testing it is customary to change the store pitch and yaw angles to account for translational motion only while measuring the aerodynamic forces and moments. This changes its position in the nonuniform flow field. Provision has been made in the computer program to simulate this.

For a store with an empennage, additional quantities must be specified. These data are an index indicating whether the empennage is planar or cruciform, the tail-fin semispan, the average body radius in the tail-fin region, the initial roll orientation of the fins, and the

lift-curve slope of the fins alone. In addition the axial position at which the forces are assumed to act must be specified.

In the trajectory initialization certain store ejection conditions are specified. These are an initial velocity in the vertical plane perpendicular to the store longitudinal axis and an initial pitching velocity. The store lateral velocity and yawing and rolling velocities are initially zero.

The integration of the equations of motion is done by a standard numerical integration technique with the aerodynamic forces and moments calculated at each point required by the integration scheme. The calculation of the nonuniform velocity field and the resulting forces and moments was described in section 5.

## 7. COMPARISONS WITH EXPERIMENTAL DATA

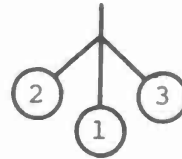
This section of the report will present comparisons with experimental data in order to assess the accuracy of the theoretical methods used to predict the nonuniform flow field, store body loading distribution and forces and moments, empennage forces, and store trajectories. In addition MER interference effects are examined as is the effect of store boattail on the loadings and forces. Many more comparisons have been made with experimental data than are presented here. The degree of agreement to be shown, however, is typical of that obtained for other conditions.

All of the data comparison to be shown use wind-tunnel data from references 2 and 3. The wind-tunnel model used in these investigations is an idealized fighter-bomber aircraft. The wing-fuselage combination is shown in figure 11 and the pylon, MER rack, and stores used in conjunction with the wing-fuselage are shown in figure 12. The TER rack used was shown in figure 7. The large store with cylindrical afterbody shown in figure 12(c) was tested singly with and without empennage and in the TER configuration without empennage. The large store with boattail afterbody shown in figure 12(d) was also tested singly with empennage to evaluate boattail effects. Pressure instrumented versions of both large stores without empennages were used for obtaining loading distributions. The forces and moments for the boattailed store without empennage were obtained by integrating the loading distributions. In figure 12(e)

is shown the small boattail store which was tested in the MER configuration under the fuselage with and without the empennage. A table of ordinates for the body of this store is given in Table I of reference 1.

In the discussion which follows, the various aircraft components are designated as

W	wing
B	fuselage
P	pylon
$S_c$	large store with cylindrical afterbody tested without other stores
$S_b$	large store with boattail afterbody
$S_1, S_2, S_3$	large store with cylindrical afterbody when tested in TER configuration. The cyclic order is shown below viewed from the rear



$S_1, S_2, S_3, S_4, S_5, S_6$	small boattail stores tested in MER configuration. $S_1, S_2,$ and $S_3$ are the front three with the same cyclic order as the TER configuration and $S_4, S_5, S_6$ are the rear three in the corresponding cyclic order
T	TER rack
M	MER rack

Whether the empennages are present is taken from the context. In addition, the parent aircraft and the store are at the same angle of attack in all cases to be shown.

### 7.1 Flow Field and Loading Predictions for Single Stores

The comparisons to be presented in this section are all for the configuration shown in figure 13. The large store with cylindrical afterbody, but without the cruciform fins shown in figure 12(c), is mounted at the one-third semispan location  $y/s = -0.333$ . The pylon is not shown in figure 13 but the store is shown in the position it would be in if it were attached to the pylon.

### 7.1.1 Effect of pylon on flow field and attached store load distribution

The upwash angle  $W_s/V_{\infty_s}$  and the sidewash angle  $V_s/V_{\infty_s}$  are shown in figure 14 for  $6^\circ$  angle of attack and Mach number 0.25 at the position the centerline of the attached store would occupy if it were present at the one-third semispan position of the left wing panel. Data with and without the pylon present are compared with theory. The sidewash is outboard everywhere and there is a small measured effect of the pylon on the sidewash which is less than the predicted effect. There is a large upwash along the store centerline, and its modification due to the pylon is well predicted by the theory.

The normal-force distributions along the store due to the upwash fields just described are shown in figure 15(a). It is seen that the load distribution with the pylon present is very irregular, and it is predicted quite well. A number of stations along the store axis are necessary to describe such a load distribution if it is to be integrated to obtain the force and moment. A minimum number of about 20 stations is required. It is noted from the previous figure that the upwash is positive everywhere and has an average value corresponding to about  $3.5^\circ$ . Behind the shoulder of the store all the loading is due to flow curvature (rate of change of upwash with axial distance) since the store after-body is cylindrical. It is seen that the net lift is nearly zero, and the influence of flow curvature is very important in determining the force and moment on the store in the present attached position. The effect of the pylon is pronounced.

The data shown in figure 15(b) exhibit a small influence of the pylon on the side-force distribution for the same conditions shown in figures 14 and 15(a). The small magnitude of the pylon effect is somewhat under predicted.

### 7.1.2 Effect of store position and angle of attack on store forces

As the store drops below its attached position for the configuration of figure 13, the influence of the pylon on the loading distributions diminishes rapidly but the gross forces do not change greatly. Consider figure 16 which shows the variation of store normal force and side force with vertical location at a fixed angle of attack of  $6^\circ$ . The distance  $\Delta z$  is zero for the attached position. There is not much change in normal force or side force acting on the store for several diameters beneath the pylon, and the theory predicts this trend well.

In figure 17, the variations with angle of attack of the store normal-force coefficient and side-force coefficient are shown. The store is one diameter below the attached position  $\Delta z/d = 1.0$ . The variations with angle of attack are surprisingly small and are predicted well by the theory.

## 7.2 Flow-Field and Loading Predictions for TER Configurations

In this section, the comparisons to be presented are for the TER configuration shown in figure 18. The large stores with cylindrical afterbody and no fins are used in the TER grouping. As shown in figure 18, the stores are in the carriage position when the pylon of figure 12(a) and the TER of figure 7 are present. They are not shown in figure 18 for clarity. As in the single store case, the stores are at the one-third semispan location. For all comparisons to be shown the Mach number is 0.25.

### 7.2.1 Flow-field predictions

The flow field has been measured for a number of positions beneath a TER configuration with the bottom store missing. The TER rack is longer than the pylon and has been approximated by an equivalent body or revolution in the prediction method. The values of  $V_s/V_\infty$  and  $W_s/W_\infty$  are shown in figure 19 along the position the axis of store  $S_1$  would occupy for the attached store location,  $\Delta z/d = 0$ , and for one diameter below the attached location  $\Delta z/d = 1.0$ . In the figure title, WBPTS<sub>2</sub>S<sub>3</sub> indicates the parent aircraft configuration generating the flow field. There is considerable difference in the upwash between these vertical locations which is well predicted by the theory. In the theory the effect of the shoulder stores  $S_2$  and  $S_3$  has been predicted using three-dimensional source terms. Higher harmonics such as dipoles fall off more rapidly with distance from the store than source terms which dominate the flow far away. It is clear that neglecting these high harmonics yields fairly accurate results for both  $V_s/V_\infty$  and  $W_s/W_\infty$  in the present instance.

The variations with angle of attack of the sidewash and upwash angles are shown in figure 20 for a position of the store one diameter beneath its attached position. Both the sidewash and upwash angles are predicted well for  $\alpha = 0^\circ$  and  $\alpha = 6^\circ$ . The calculative method thus predicts well the effects of vertical location and angle of attack of the aircraft on the flow field acting on the store.

### 7.2.2 Loading predictions

The normal-force distribution on store  $S_1$  of the TER configuration for the attached store and for a location one diameter below its attached position are shown in figure 21(a). The loading on the attached store is somewhat underpredicted in the region of the pylon. However, at one diameter beneath the pylon the prediction is very good. Similar results for the side-force distribution are shown in figure 21(b) with the same general results for comparison between theory and experiment. The loading theory utilizes predicted flow field quantities and does not include the special rack effect discussed subsequently.

The effect of angle of attack on the normal-force distribution of  $S_1$  of the TER configuration is shown in figure 22(a) for a distance of the store one diameter beneath its attached position. Experiment and theory are in good agreement for the angles of attack of  $0^\circ$  and  $6^\circ$  shown in the figure. Analogous results are shown in figure 22(b) for the side-force distribution with good comparison between experiment and theory.

The effect of the rack on the loading distribution on store  $S_1$  in the attached position is shown in figure 23. The rack, shown in figure 7, can be modeled approximately by a body of revolution with a pylon beneath it. The theory shown in figure 23 for the rack effect is based solely on the source distribution corresponding to its equivalent body of revolution. As such it causes the change in theoretical load distribution given in figures 23(a), but it has no effect on the side-force distribution shown in figure 23(b). Actually, the effect of the rack on the normal-force distribution exhibited by figure 23(a) is qualitatively similar to the effect of the pylon on the normal-force distribution on a single store as shown in figure 15(a). Accordingly, the discrepancy between theory and experiment shown in figure 23(a) can probably be ascribed to neglect of the rack pylon in the model. This effect is of importance only for attached loads, and is negligible for the store one diameter below its attached position. It can be included in the present computer program, but has not been at this time. The rack pylon can also have an effect on side-force distribution as shown in figure 23(b). The theoretical curves for the two cases are identical since the source distribution representing the rack produces no side load.

The loading distributions on store  $S_2$  of the TER configuration after  $S_1$  has been released are shown in figure 24 for the attached position and one diameter beneath the attached position. For the attached position there are effects on normal force and side force, which are probably associated with the secondary pylon, not accounted for by the theory. At a distance of one diameter beneath its attached position, the experiment and theory are in good agreement for both normal force and side force.

For a position of  $S_2$  one diameter below its attached position the loading distributions are shown for  $\alpha = 0^\circ$  and  $\alpha = 6^\circ$  in figure 25. The normal force distribution is predicted quite well for both angles of attack in figure 25(a) and the side-force distribution predictions shown in figure 24(b) exhibit similar agreement.

### 7.3 MER Interference Effects

The interference effects previously described for a TER configuration also exist in a MER configuration, but in addition there is interference between the front three stores and the rear three stores. A MER configuration has been tested under the fuselage as shown in figure 26. The stores used on the MER rack of figure 12(b) are those shown in figure 12(e). Tests have been conducted for stores with and without cruciform empennages. For all comparisons to be shown the Mach number is 0.40.

In figure 27, the squares indicate the influence of the front three stores,  $S_1, S_2$ , and  $S_3$ , on the normal force and pitching moment of store  $S_4$ , the bottom rear store. The circles indicate the influence of the rear two shoulder stores,  $S_5$  and  $S_6$ , on the normal force and pitching moment of store  $S_1$ . The inclusion of store  $S_4$  in the latter group was not feasible because  $S_1$  was sting mounted.

The normal-force coefficient increments shown in figure 27(a) are small in accordance with predictions of theory. The theory is based on determining the interference flow field of the stores by three-dimensional source distributions. The pitching-moment coefficient increments for  $S_1$  and  $S_4$  have opposite signs. This effect is explained by the theory. Stores  $S_1, S_2$ , and  $S_3$  produce a downwash over the length of  $S_4$  which decreases with distance behind the nose of  $S_4$ . Accordingly, a down load is induced on the nose of  $S_4$  which produces a negative moment. Stores  $S_5$  and  $S_6$  produce a downwash on store  $S_1$  which is greatest at the rear

and least at the nose. Accordingly, the down load at the rear dominates, and a positive pitching moment results. If all of the stores were symmetrical about their mid-points, the theoretical normal-force increments on  $S_1$  and  $S_4$  would be equal, and the moment coefficient increments would be equal in magnitude and opposite in sign (considering  $S_4$  to be included in the rear grouping).

These data also show that no serious interference effect associated with body doublets or trailing vortices occurs up to angles of attack of  $10^\circ$ . A change with angle of attack of the increments would be associated with changes in store doublet strengths and changes in trailing-vortex characteristics. Since the effects of doublets fall off more rapidly with distance than those of sources, the source effects will dominate the interference. More precise results can be obtained by including the doublet and trailing-vortex effects.

Experimental results analogous to those of figure 27 are shown in figure 28 for the stores with cruciform empennages. It is of importance to discuss the interference effects of  $S_1$  separately from those of  $S_4$  since the empennage trailing-vortex systems of  $S_1$ ,  $S_2$ , and  $S_3$  come close to  $S_4$  while those of  $S_5$  and  $S_6$  have negligible influence on  $S_1$ . The difference in the force and moment acting on  $S_1$  (with empennage) with and without  $S_5$  and  $S_6$  present is due to loadings induced separately on its body and its empennage. If the downwash induced along  $S_1$  by  $S_5$  and  $S_6$  is not influenced significantly by their empennages, then the  $S_1$  body loading contributions due to  $S_5$  and  $S_6$  will be the same with or without empennages on all stores. The rest of the contribution will be due solely to the addition of the  $S_1$  empennage into the induced downwash field. Accordingly, if the contribution in figure 27 for  $S_1$  is subtracted from the corresponding body contribution in figure 28, the result should be the empennage contribution of  $S_1$  due to the addition of  $S_5$  and  $S_6$ . When increments  $\Delta C_N$  and  $\Delta C_m$  are calculated in this fashion, it is found that the incremental center of pressure given by  $\Delta C_m / \Delta C_N$  lie on the empennage of  $S_1$ , thus supporting the above explanation of the interference effects of  $S_5$  and  $S_6$  on  $S_1$ .

In the assessment of the effects of  $S_1$ ,  $S_2$ , and  $S_3$  on  $S_4$ , it is noted that the wakes of  $S_1$ ,  $S_2$ , and  $S_3$  all pass downstream along the entire length of  $S_4$  so that the downwash distribution along  $S_4$  is

definitely influenced by the empennages of  $S_1$ ,  $S_2$ , and  $S_3$ . Accordingly, the center of pressure of the interference effects determined in the preceding manner will not necessarily lie on the empennage. In fact, it is found to lie approximately 1.5 diameters behind the center of moments of  $S_4$ , the store mid-point.

#### 7.4 Empennage Contributions to Forces and Moments

Comparison between experiment and theory for forces and moments due to the presence of the empennage are now considered. It is clear that the method of determining flow fields acting on the store is equally applicable to the store empennage forces in a nonuniform flow field. A method of determining empennage contributions to  $C_N$ ,  $C_Y$ ,  $C_m$ ,  $C_n$ , and  $C_l$  based on reversed flow theorems has been described in section 5.3. This method has been used with experimental flow-field data to estimate the above quantities for comparison with measurements.

In figure 29, the forces and moments for store  $S_c$  mounted at or near the attached position, shown in figure 13, are shown as a function of roll angle and compared with theory for angles of attack of  $8^\circ$  and  $16^\circ$ . A roll angle of  $0^\circ$  places the fins vertical and horizontal. The incremental coefficients are the difference between the coefficients with the empennage on and with the empennage off.

The variations of normal-force and side-force coefficient increments with roll angle are shown in figure 29(a). The theory is in fair agreement with the data at both angles of attack. A measure of the accuracy of the theory can be made by comparing the data at  $\phi = 0^\circ$  and  $\phi = 90^\circ$ . In the side-force coefficient increments, the difference between theory and experiment generally does not exceed the difference between the  $\phi = 0^\circ$  and  $\phi = 90^\circ$  experimental values of these increments. Any difference can be due to measurement inaccuracy or to slight fin misalignment. We can conclude that the agreement is within the accuracy of the data.

With regard to the comparisons for pitching moment shown in figure 29(b) the data agrees with the theory quite well when accounts are taken of the suppressed origin of the vertical scale and the difference in the data at  $\phi = 0^\circ$  and  $\phi = 90^\circ$ . With regard to yawing moment, the difference between theory and experiment at  $\alpha = 8^\circ$  cannot be entirely accounted for by data inaccuracy. At  $\alpha = 16^\circ$  the agreement between experiment and theory is within the accuracy of the data.

Comparison between theory and experiment are shown for rolling-moment coefficient in figure 29(c). In this case, all the rolling moment is due to the empennage. For  $\alpha = 8^\circ$  the comparison between experiment and theory is fairly good. The difference, which at some points amounts to an increment in rolling-moment coefficient of 0.02, corresponds to about 0.35 degrees of roll control for a single opposing pair of panels. The agreement at  $\alpha = 16^\circ$  is not as good with the discrepancies being about twice those for the  $\alpha = 8^\circ$  case. The nature of rolling moment for a cruciform empennage is of interest in assessing the comparisons between experiment and theory. In general, the rolling moment due to one opposing pair of panels is large and opposes that due to the other pair of opposing panels with a small net rolling moment. Since the net rolling-moment coefficients shown in figure 29(c) are small, the degree of agreement between experiment and theory is considered fair.

#### 7.5 Effect of Store Boattail on Loadings and Forces

In the comparisons shown so far for the single store, the store afterbody has been cylindrical and this store is designated  $S_c$ . In order to study the effects of boattail on the store loadings and forces, a special pressure distribution store with boattail,  $S_b$ , as described in figure 12(d), but without empennage was constructed and fitted with sufficient pressure orifices to obtain accurate loading distributions. The nose of this store is identical to the nose of  $S_c$ . Before studying the effects of boattailing in a nonuniform flow, it is worthwhile studying the effects in uniform flow.

##### 7.5.1 Effect of store boattail on store loading in uniform flow

In figure 30 the normal-force loading distributions for uniform flow for stores  $S_b$  and  $S_c$  are compared for several angles of attack to show the experimental effect of the store boattail on the loading. Figure 30(a) through 30(d) both show identical experimental loadings on the identical noses, a fact indicating little or no upstream influence of the separated flow regions downstream of the nose. However, the boat-tailed afterbody carries more negative load than the cylindrical afterbody as might be expected.

Several theories are shown on the figure for comparison with the data. Slender-body theory, section 5.2.2, does a fair job of calculating the load distribution at  $\alpha = 4^\circ$ . In order to obtain a more precise

theoretical prediction for attached flow for assessing separation effects, a fully three-dimensional source and doublet calculation, D. S., was made by the method of Appendix III. The question of the Kutta condition for a body of revolution was ignored, and the blunt base of the body was continued smoothly to a point. It is presumed that this solution will give an accurate estimate of the load distribution for the body except possibly close to the base. The boundary conditions of thickness and angle of attack were satisfied at the body surface, and the full Bernoulli equation was used in determining the loadings.

It can be seen that the data are in excellent agreement with the doublet theory up to the body separation region. Assuming that the separation region for the present purposes can be taken as that region where the experimental loading departs from the theoretical one, one finds a smooth forward movement of the separation region with increase in angle of attack as shown in figure 31(a). In this figure the separation regions are shown as estimated from figure 30. A mean line has been faired through the regions. The mean value of  $\bar{x}_s$  from this curve has been used in determining the curve in figure 31(b), which shows the distance of the separation point behind the shoulder of the store in multiples of the maximum diameter. Separation lies within about 1 to 2 maximum diameters behind the store shoulder for the boattail body for most of the useful angle-of-attack range

The source-doublet theory is also given in figure 30 for the store with the cylindrical afterbody. The separation parameters have been determined from these data and are shown on figure 31 for comparison with those for the boattail store. It is noted that boattail moves the separation region forward as would be expected.

With regard to the additional loading behind the separation point due to cross-flow drag, analysis of the data does not correspond to a uniform cross-flow drag coefficient. It has been found that an estimate of body loading can be made by assuming the loading to be uniform downstream of separation, at its separation value. A slight effect of the base is evident very close to the base.

### 7.5.2 Effect of boattail on store loading in presence of wing-body combination

Normal-force and side-force loadings were measured on the store in the carriage position in the presence of the wing-body combination, see figure 13, without the pylon present. The normal-force loading distributions with and without boattail are shown in figure 32 for  $\alpha = 4^\circ$  and  $\alpha = 16^\circ$ . The theory shown for  $\alpha = 4^\circ$  is the slender-body theory which predicts quite well the loading distribution with and without boattail. The theory is based on theoretical flow angles at  $\alpha = 4^\circ$  so that the agreement between experiment and theory includes the errors in the flow-field prediction method and the loading calculation method.

At  $\alpha = 16^\circ$  the data as shown in figure 32(b) exhibit a small effect of boattail. On the nose the results for both stores would be identical except for possible upstream influence of the afterbody or possible experimental error. The experiments were made many months apart. It is noted that slender-body theory over-predicts the magnitude of the loading distribution at this large angle of attack.

The differences between the data and slender-body theory are due in part to an overprediction of the angle-of-attack distribution along the store and in part to an overprediction in the loading distribution calculation. To eliminate both these sources of error in the theory a source-doublet calculation, Appendix III, was made similar to that for uniform flow previously described in connection with figure 30 using the experimental downwash distribution as input. The improved theory indicates generally improved agreement with experiment especially when the buoyancy correction is included in the theory. This was made using the method of section 5.2.1. These comparisons are of interest because they tend to show that separation seen for uniform flow is of reduced extent for the store at the same angle of attack under the wing-body combination. This result can be explained by the fact that the wing-body combination turns the flow more parallel to the store and reduces the average angle of attack in the attached position. For instance, with  $\alpha = 16^\circ$ , the local angle of attack at the nose is about  $13^\circ$  while that on the rear half of the store is about  $6^\circ$ . Whether there is any separation over the rear part of the store cannot be determined with certainty because the accuracy of the improved theory, Appendix III, for attached flow cannot be guaranteed in the region of the body base because of the unknown wake effects and the lack of a Kutta condition applicable to bodies of revolution.

Once the store leaves the attached position, it is not clear that the angle-of-attack distribution along the store will be small. Large angles of attack may occur once the straightening effect of the wing is reduced, and extensive separation similar to that in uniform flow may occur. In this case, a method of calculating the loading distribution similar to that suggested for uniform flow may be worthwhile. This point has not been pursued in the current investigation since an accurate method of determining the wing flow field at high angles of attack is unavailable. Data are available for a boattail store at distances up to a diameter below the carriage position but no further.

Results similar to those in figure 32 for normal force are shown in figure 33 for side force. At  $\alpha = 4^\circ$  the effects of boattail on side-force loading distribution are small and are well predicted by slender-body theory. At  $\alpha = 16^\circ$  slender-body theory overpredicts the magnitudes of the loading distribution. The use of the more precise doublet-source method yields better agreement with experiment although the correction for buoyancy tends not to improve the agreement. The sidewash angle varies from  $9.2^\circ$  at the nose to  $4.3^\circ$  at the base in a nearly linear fashion. This decreasing local sidewash angle in the streamwise direction probably tends to inhibit separation although the extent of separation, if any, cannot be determined precisely from the results of the figure.

### 7.5.3 Effect of boattail on empennage forces and moments

All forces and moments except drag have been measured on  $S_c$  and  $S_b$  with and without empennages. The changes in  $C_N$ ,  $C_Y$ ,  $C_m$ ,  $C_n$  and  $C_l$  due to adding the empennage are shown in figure 34 as a function of roll orientation. In these tests the pylon was present, and the store is slightly below the pylon,  $\Delta z/d = 0.1333$ . The experimental differences due to boattail can be seen by comparing solid and open symbols. The theory is based on measured flow quantities in the region to be occupied by the empennage together with reverse flow theorems.

For normal force and side force, the effect of boattail is to increase the magnitude of the coefficients by an amount in good accordance with theory. The discrepancy between experiment and theory is within the accuracy of the experimental data judged by comparing values for  $\phi = 0^\circ$  and  $\phi = 90^\circ$ , which should be equal. The increase in the magnitude of the normal force due to boattail is about 12 percent and about 30 percent for side force.

The results for pitching moment and yawing moment shown in figures 34(c) and 34(d) are in good accord with theory when account is taken of the suppressed origin and the inaccuracy of the data exhibited by comparison of the values at  $\phi = 0^\circ$  and  $\phi = 90^\circ$ .

The results for rolling moment shown in figure 34(e) exhibit the same behavior as those in figure 29(c).

## 7.6 Trajectory Studies

The methods of flow-field predictions and store force and moment determinations presented in sections 4 and 5 have been combined into one program with the six-degree-of-freedom equations of motion of section 6 to yield a trajectory prediction method. A number of sample trajectories have been run to provide predictions for comparison with captive-store trajectories.

In order to represent full-scale conditions, the wind-tunnel models shown in figures 7, 11, and 12 have been scaled up by a factor of twenty. The following input quantities have been used for all trajectories to be shown:

$$\text{Store Mass} = 15.53 \text{ slugs}$$

$$I_{xx} = 8 \text{ slug-ft}^2$$

$$I_{yy} = I_{zz} = 80 \text{ slug-ft}^2$$

$$I_{xy} = I_{yz} = I_{xz} = 0$$

$$\bar{x} = \bar{y} = \bar{z} = 0$$

$$\text{Altitude} = 5000 \text{ ft}$$

$$\dot{\zeta}_{t=0} = 10 \text{ ft/sec (initial vertical velocity of ejected store)}$$

$$\zeta_{t=0} = 0.625 \text{ ft (initially, ejected store is one radius below attached position)}$$

Initial store and aircraft angles of attack are equal.

### 7.6.1 Statically unstable single store dropped beneath wing

A comparison between the calculated trajectory and the captive-store trajectory for no damping is shown in figure 35 for the cylindrical afterbody store (fig. 12(c)) with no empennage. It is released at time  $t = 0$  one store radius beneath its attached position on the pylon at the one-third semispan position, figure 13, with  $\alpha = 4^\circ$  for both the aircraft and the store. In figure 35 the three left-hand curves show the position of the store center of gravity relative to its carriage position. The quantities  $\Delta\xi$ ,  $\Delta\eta$ , and  $\Delta\zeta$  are respectively positive forward, positive to the right (toward the fuselage), and positive down. The left-hand curves show a slight rearward movement of the store, no lateral movement, and a vertical movement equivalent to free fall. The two right-hand curves show a substantial yaw  $\Delta\Psi$  of the store nose outboard and a large pitch up  $\Delta\theta$  of the store which is somewhat overpredicted by the computer program.

The fact that the pitch up is overpredicted can be readily explained. The nose-up motion of the store places it at an angle of attack of about  $12^\circ$  at  $t = 0.4$  seconds. At this time the store is well below the wing so that the flow is nearly uniform. At this condition the captive store balance yields a pitching-moment coefficient of 0.9, the store alone in a uniform field yields 1.05, and the computer program yields 1.3. It appears that the captive-store measurements are too low and the computer program result is too high. Figure 30(c) shows the store loading at  $\alpha = 12^\circ$  in uniform flow. It is seen that slender-body theory overpredicts the loading on the store nose at this angle of attack and that the contribution of the afterbody to the pitching moment is small. Increased accuracy of prediction would then be obtained using the improved source-doublet method described in connection with figure 30.

The effect of damping for this statically unstable case is of little interest and was not studied. The calculated trajectory shown required approximately 5 to 6 minutes on a Univac 1108 computer.

### 7.6.2 Statically stable single store dropped beneath wing

A comparison similar to that of figure 35 is shown in figure 36 for the same store and initial conditions except that a cruciform empennage has been added to produce static stability. Results are shown for angles of attack of  $\alpha = 0^\circ$  and  $\alpha = 4^\circ$ . The store center of gravity coordinates

( $\Delta\xi$ ,  $\Delta\eta$ ,  $\Delta\zeta$ ) show the same general behavior as the previous case. The pitching and yawing motions from the computer program and the captive-store trajectory are in good agreement for both angles of attack. The pitching motion is nose down in this instance compared to a pitch-up in the previous case. It is noted that a few degrees of roll occur. The roll excursions are so small that they have no effect on the calculated trajectories.

In order to assess the importance of damping on the motion, the trajectory was also calculated including damping in all three angular motions. The damping effect is negligible except in the pitching oscillation which was reduced in maximum amplitude by about one degree as the result of pitch damping.

#### 7.6.3 Statically unstable store dropped from TER group beneath wing

Stores  $S_c$  without empennages were mounted in a TER group under the wing, figure 18, and the trajectory of the bottom store was calculated using the computer program and measured by the captive-store technique. The comparison between the two sets of results is shown in figure 37. As in the preceding case, the center-of-gravity location shows the same behavior with the same good agreement between theory and measurement. The store exhibits divergence in both pitch and yaw. The overprediction of the pitch up in this case is similar to that shown in figure 35 for the same reasons.

### 8. CONCLUDING REMARKS

This report presents the results of an investigation which has been conducted with the objectives of extending and improving the store separation prediction method of reference 1. In this earlier work the trajectory was limited to three degrees of freedom, the pylon and ejector rack were not modeled, wing dihedral was not included, a two-dimensional wing thickness model was utilized, and a simple method was used to calculate the empennage normal force which could not be used to determine rolling moment. All of these shortcomings have been eliminated in the present work.

The fuselage and store volumes are represented by distributions of three-dimensional point sources along the body longitudinal axes. The

same method is used to model the body of the ejector rack. The short pylons on the rack have not been included in the present method.

The wing model used in the work of reference 1 has been replaced by a wing-pylon model which includes complete mutual interference between the wing and pylon. The wing-pylon thickness distribution is represented by three-dimensional source strips and superimposed upon this is a vortex lattice which represents the loading distribution. The boundary condition imposed in determining the vortex strengths includes wing angle of attack and twist and camber, mutual interference between wing and pylon, and interference due to the fuselage, rack, and stores. The wing model allows for breaks in sweep and dihedral. The pylon can be swept but breaks in sweep are not allowed.

Calculations utilizing the flow models just described have been compared with experimental flow-field data obtained under various parent aircraft configurations. The agreement is quite good except for the case of a store in the carriage position on a TER rack where the short pylon which is part of the rack produces an effect not accounted for by the theory. This effect disappears rapidly as the store moves off of the rack. This pylon can be accounted for within the framework of the present theory but has not at this time.

Methods are presented for calculating all of the aerodynamic forces and moments except axial force. The methods for calculating the body forces and moments are the same as those used in reference 1 except that a simpler method based on slender-body theory is used for the buoyancy forces and moments. Angle of attack effects are accounted for by a combination of slender-body theory and viscous crossflow theory. The empennage forces and moments, including rolling moment, are calculated using reverse flow theorem. Good agreement between calculated and experimental forces and moments is obtained except at high angles of attack where slender body theory overpredicts the lift on the store nose. It is shown that by using a more precise method for calculating the forces the agreement is significantly improved. For a group of six stores mounted on a MER rack the theory predicts the interference of one cluster of three on the other cluster quite well.

Theory and experiment have been used to determine the effect of store boattail on the location of flow separation from the body.

The results indicate that the effect of boattail is to cause a forward movement of the separation location for the store in uniform flow. With a parent aircraft the effect is not as pronounced since the wing tends to align the flow with the body axis thus reducing the average angle of attack over the rear half of the store.

The flow field and force and moment prediction methods have been included with the six-degree-of-freedom equations of motion in a computer program which calculates the trajectory of a store dropped from an aircraft flying at constant velocity in rectilinear flight. The stores can be mounted singly on a pylon or in groups on a rack. The equations of motion allow for mass and inertia assymetries of the ejected store. Comparisons have been made between predicted trajectories and captive-store trajectories obtained in the wind tunnel. Very good agreement is obtained for stable stores. For unstable stores very good agreement is shown except for the store pitch angle. The theory overpredicts the pitch excursion from its initial value due to slender-body theory overpredicting the load on the store nose.

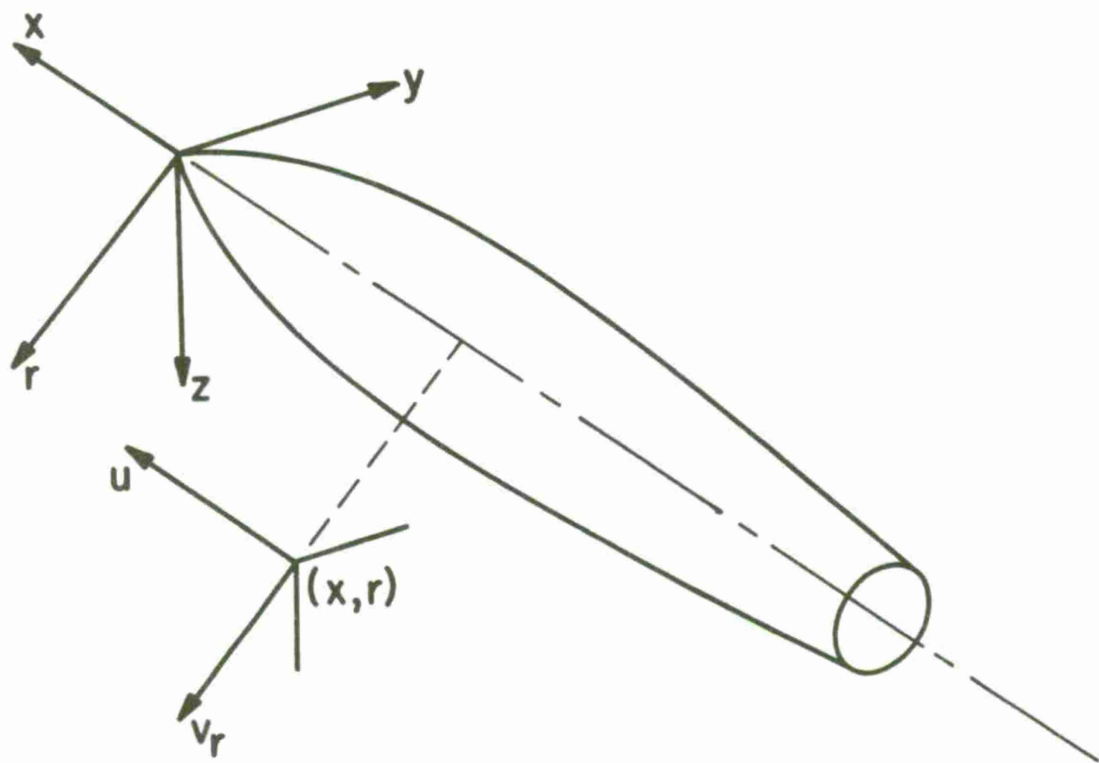


Figure 1.- Coordinate system for an axisymmetric body.

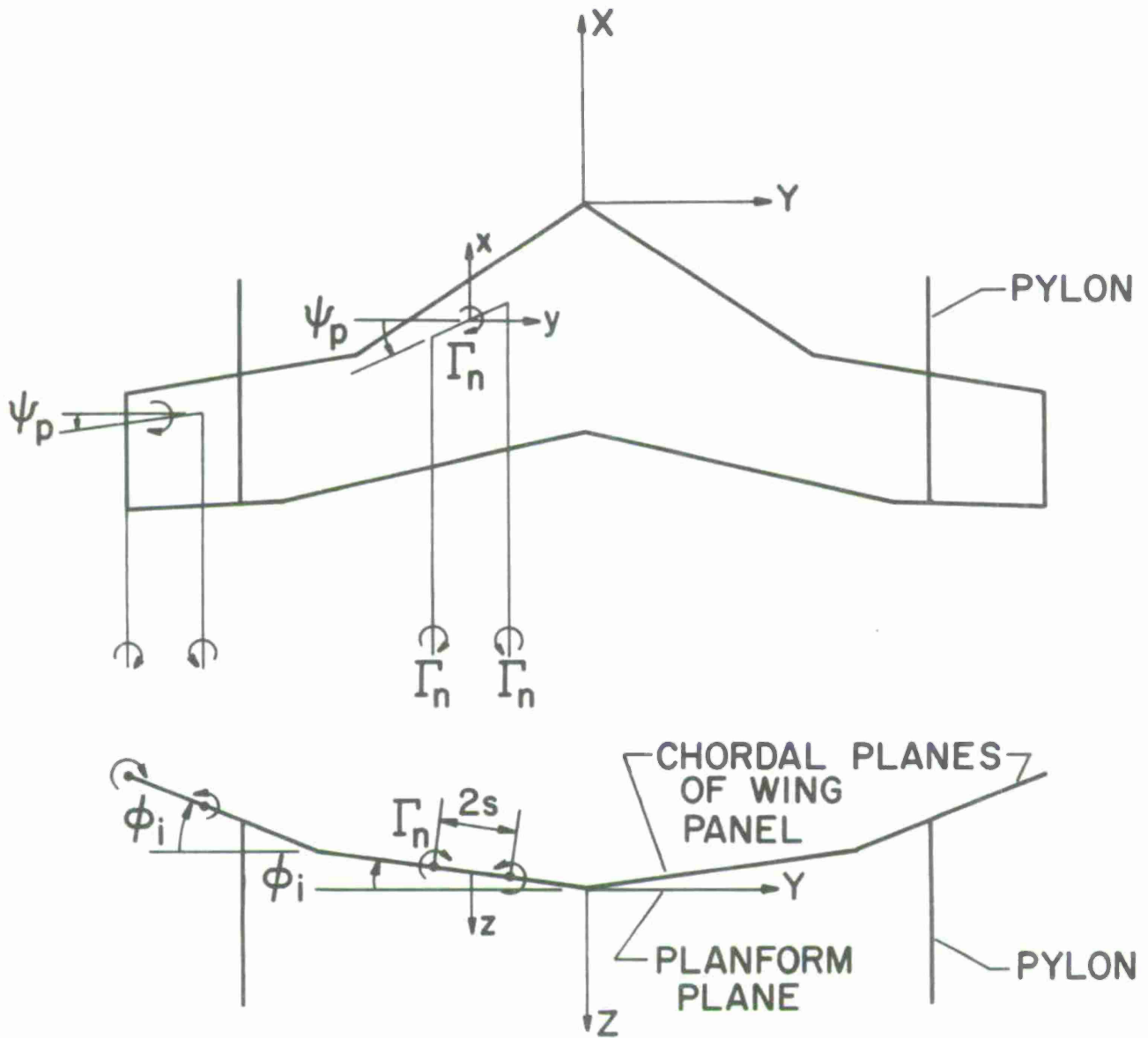


Figure 2.- Coordinate systems for wing-pylon and horseshoe vortices.

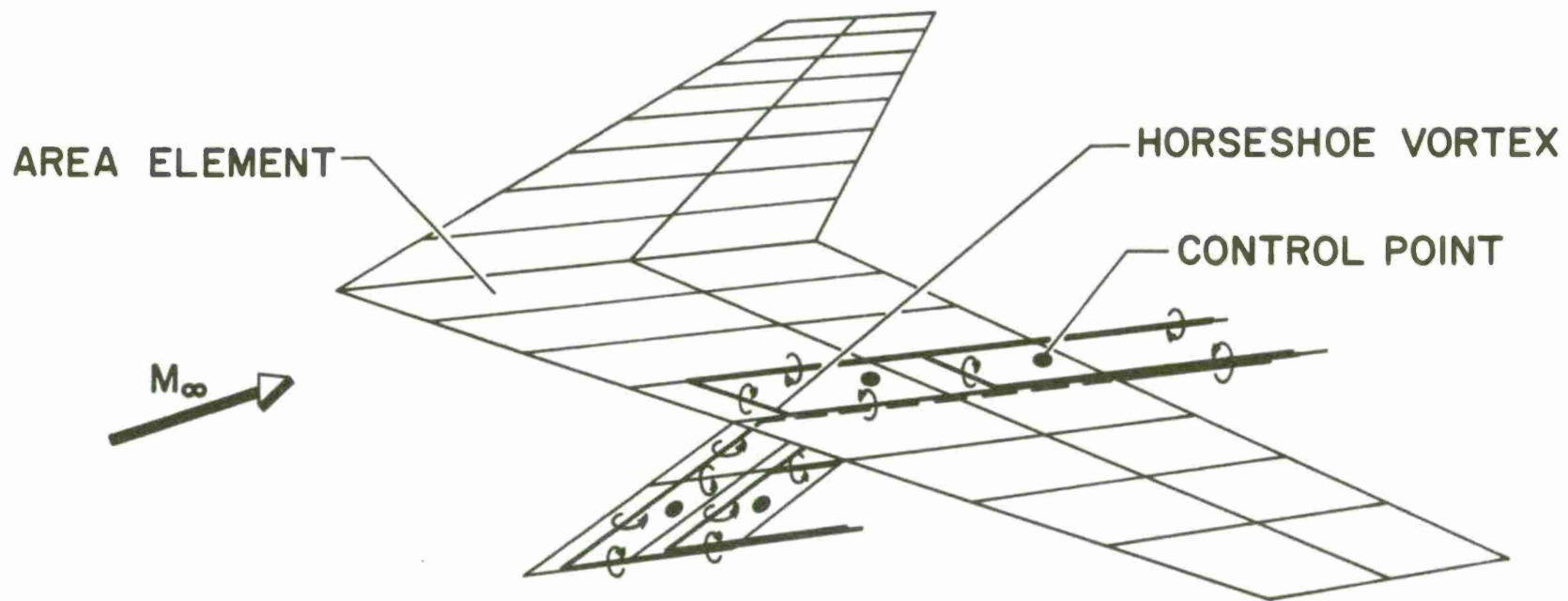


Figure 3.- Vortex-lattice model of a wing-pylon.

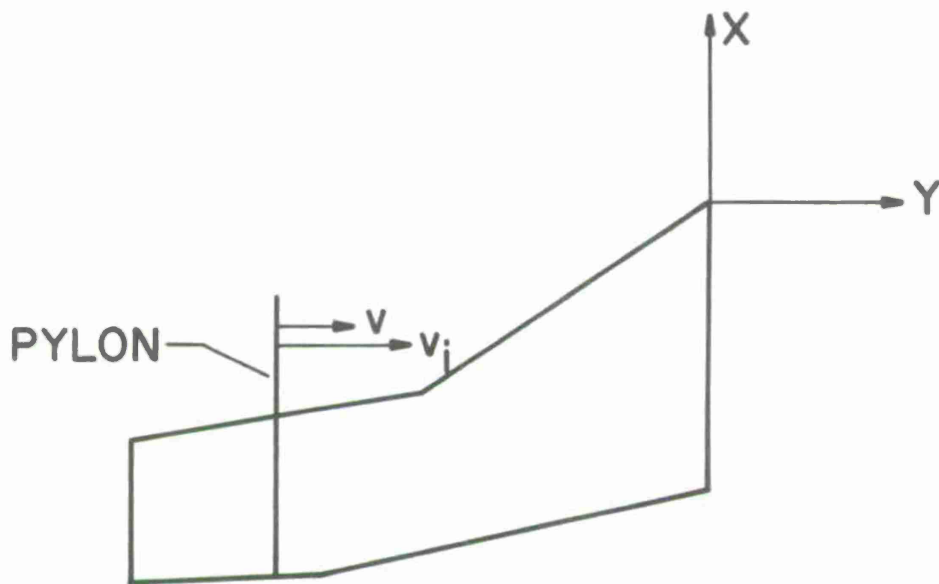
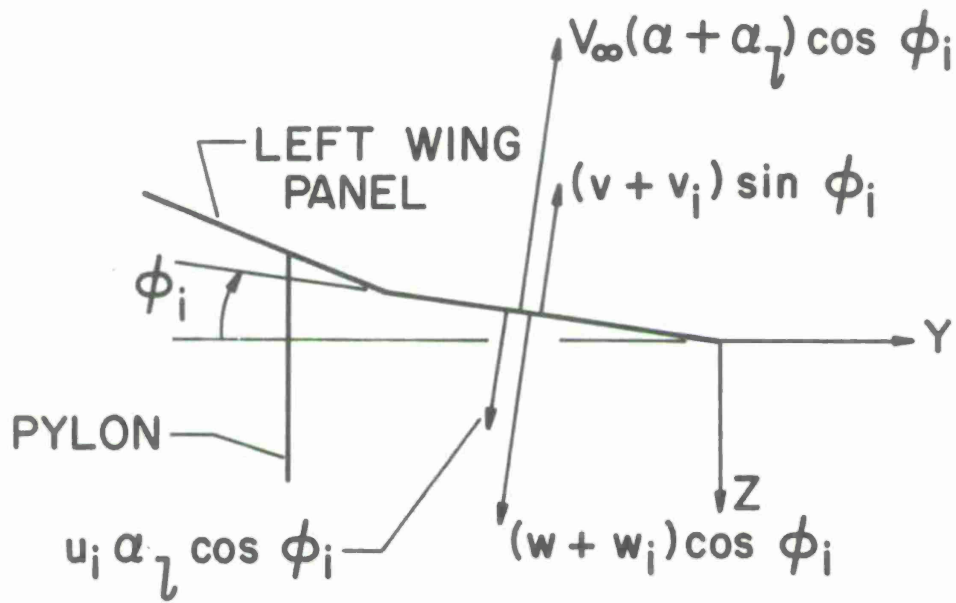


Figure 4 - Flow tangency boundary conditions for the wing and pylon.

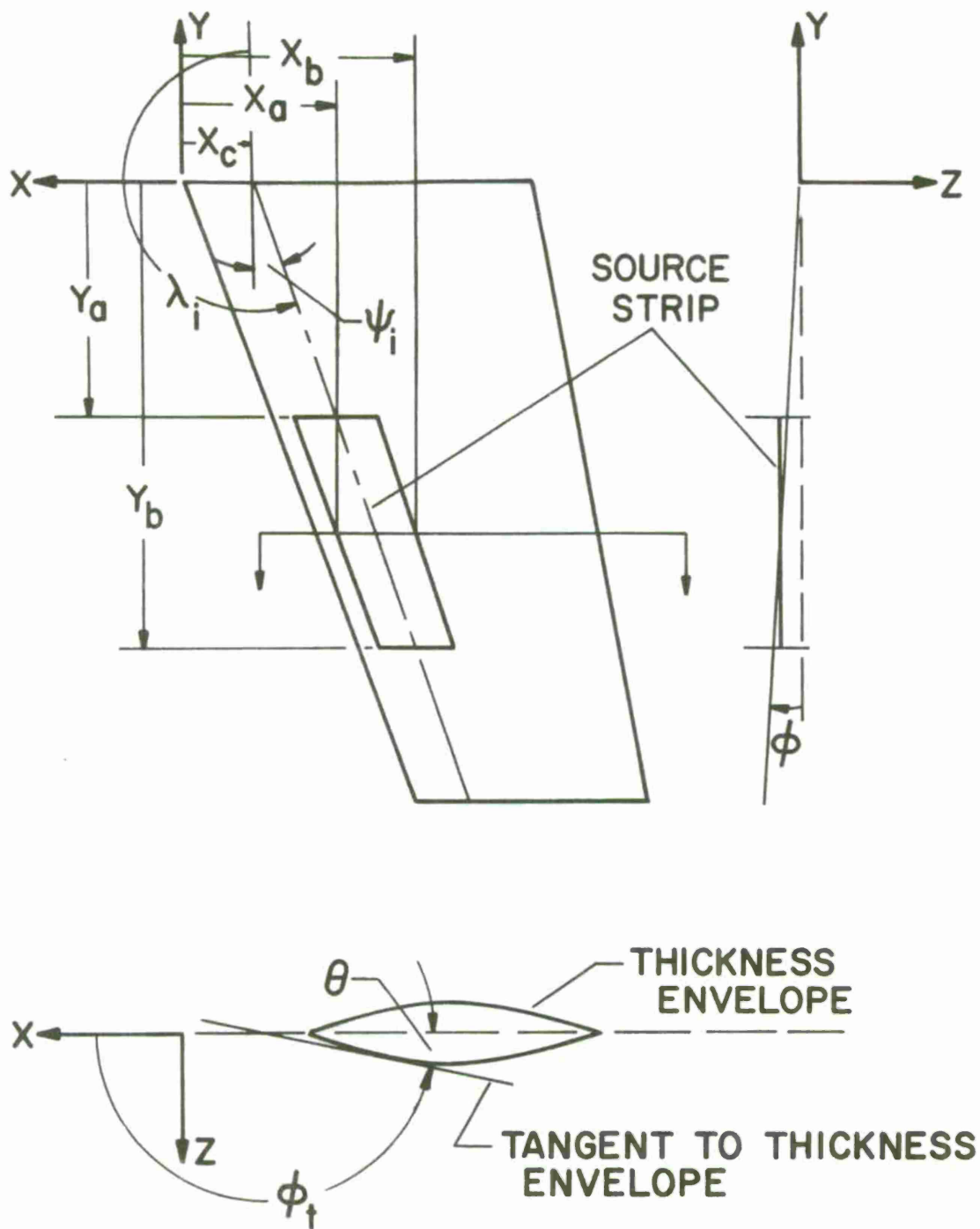


Figure 5.- Coordinate system for wing thickness source strips.

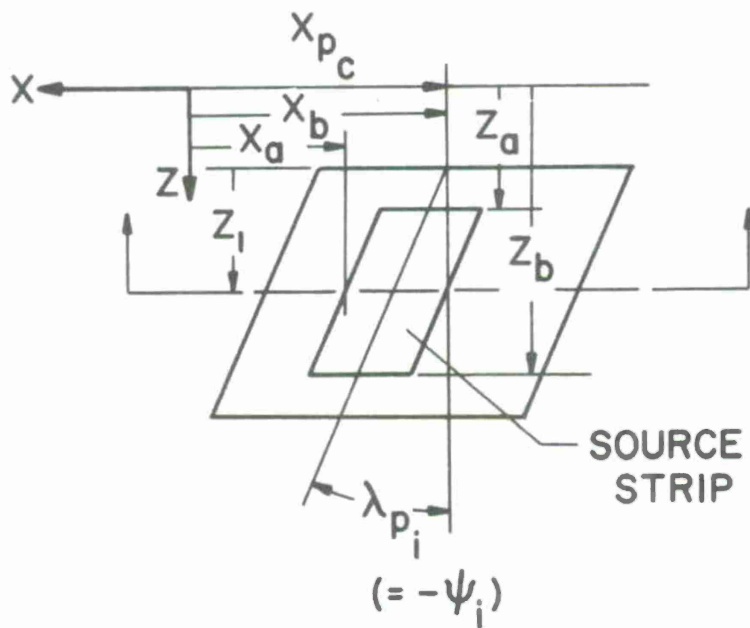
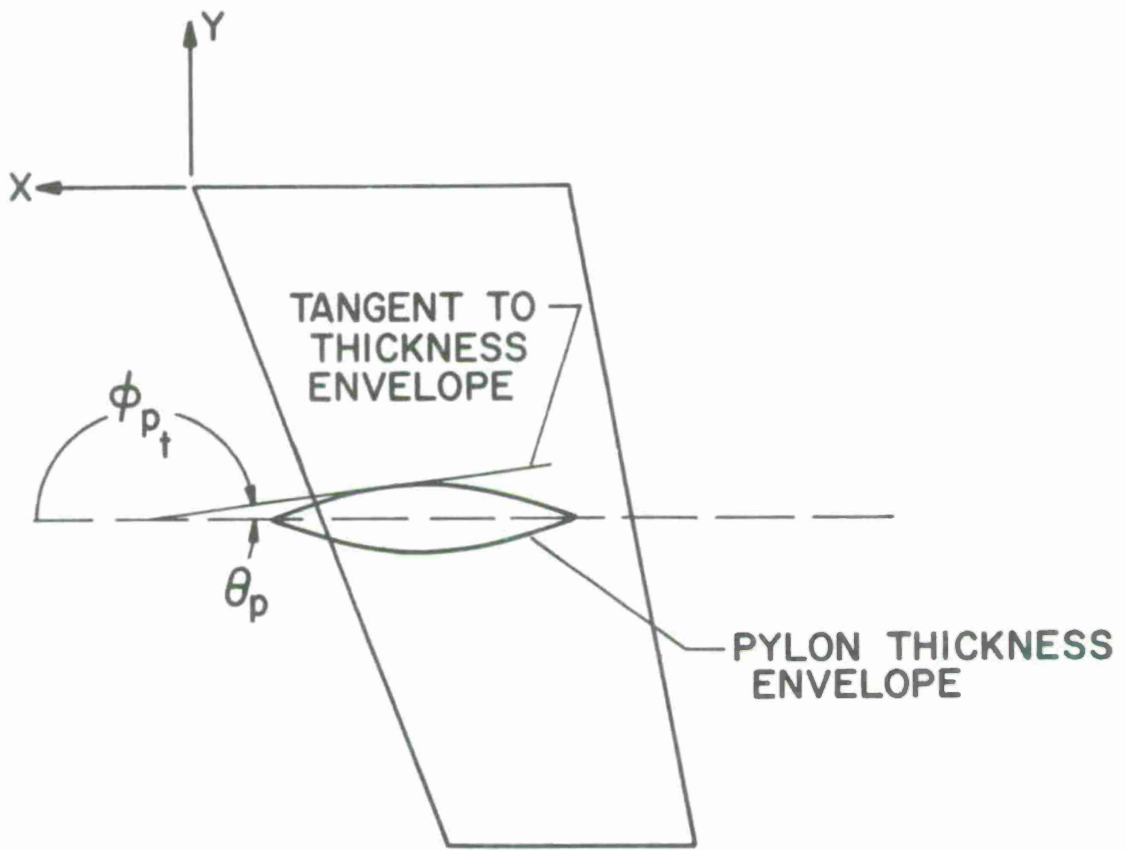


Figure 6.- Coordinate system for pylon thickness source strips.

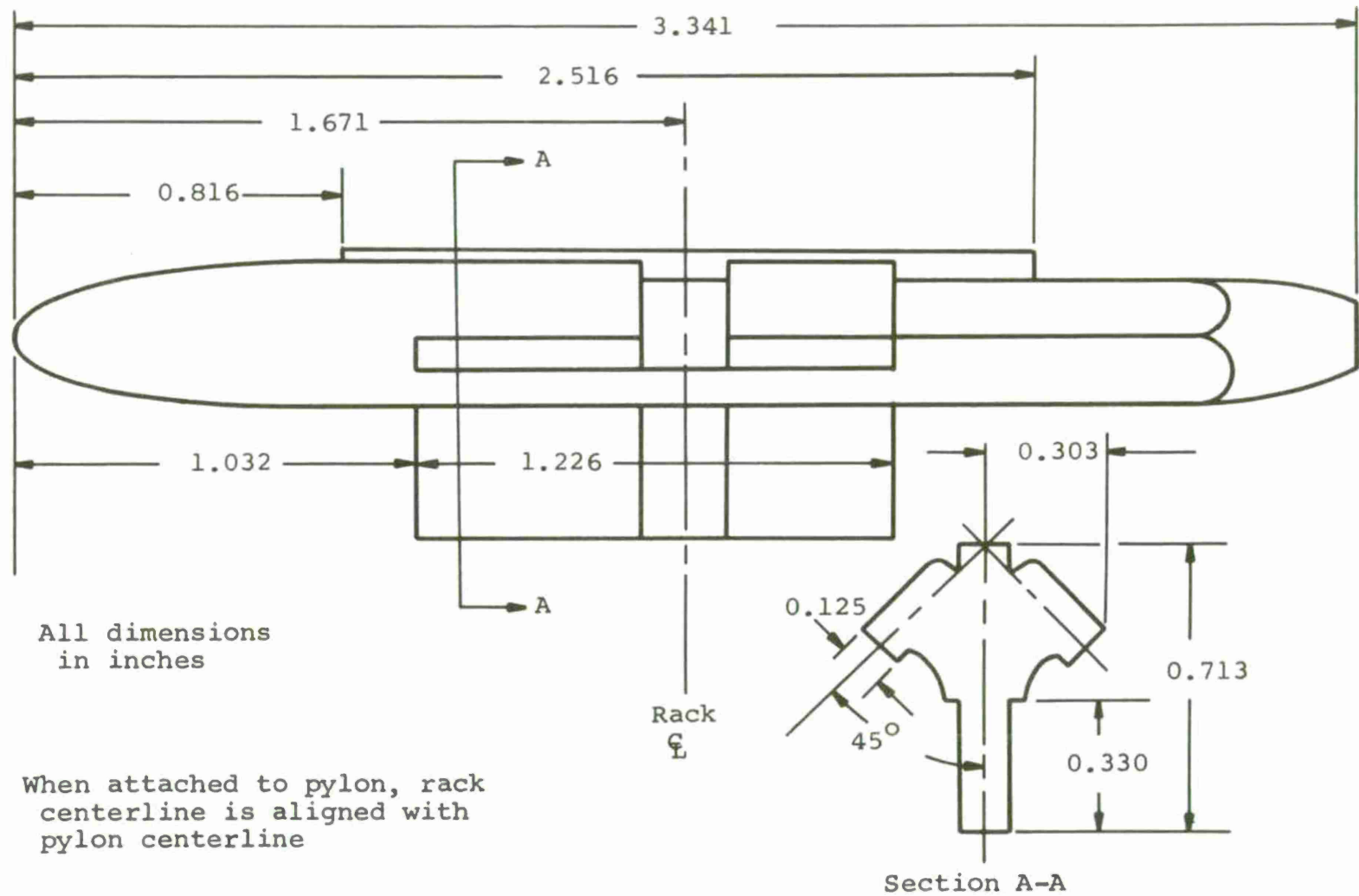


Figure 7.- Details of TER rack.

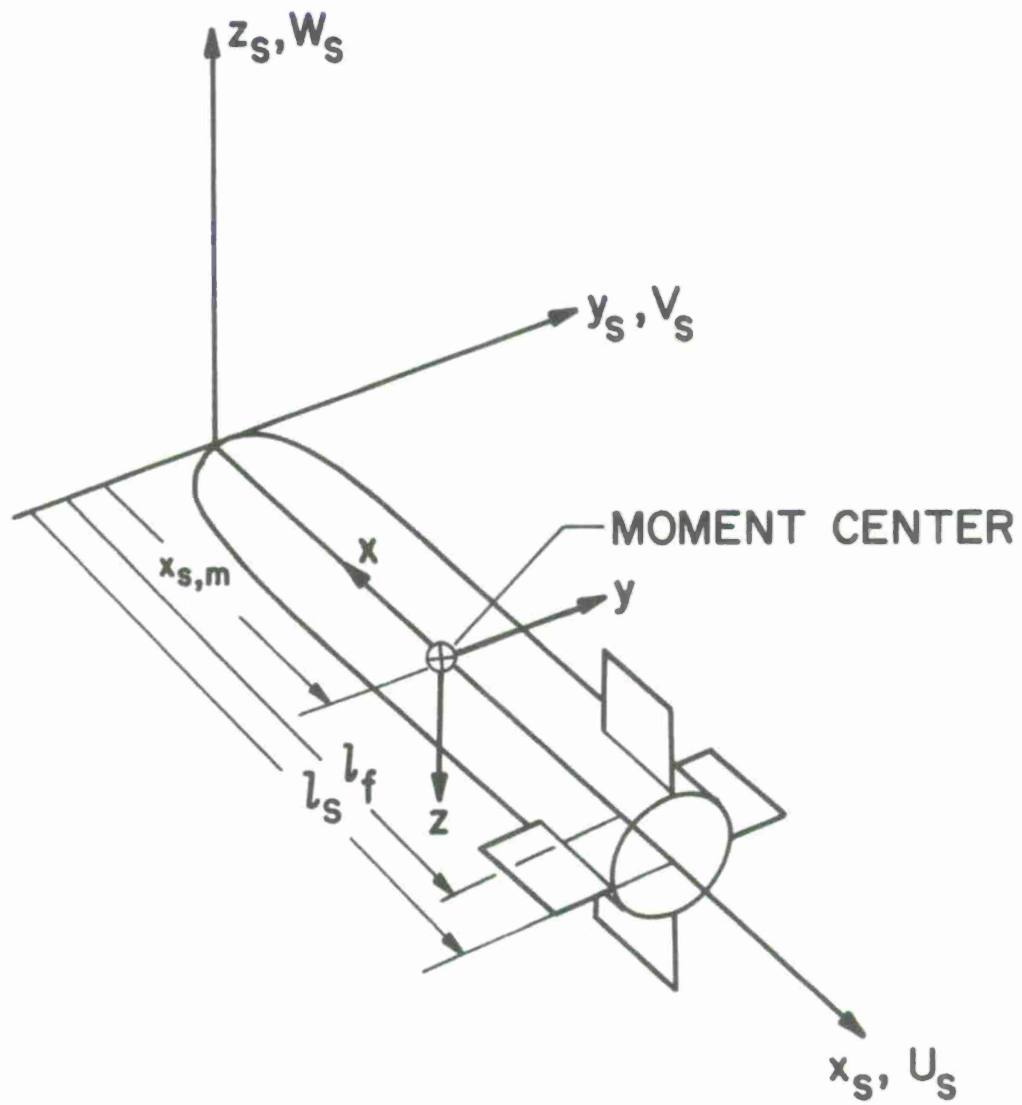


Figure 8.- Coordinate systems fixed in ejected store and used in force and moment calculation.

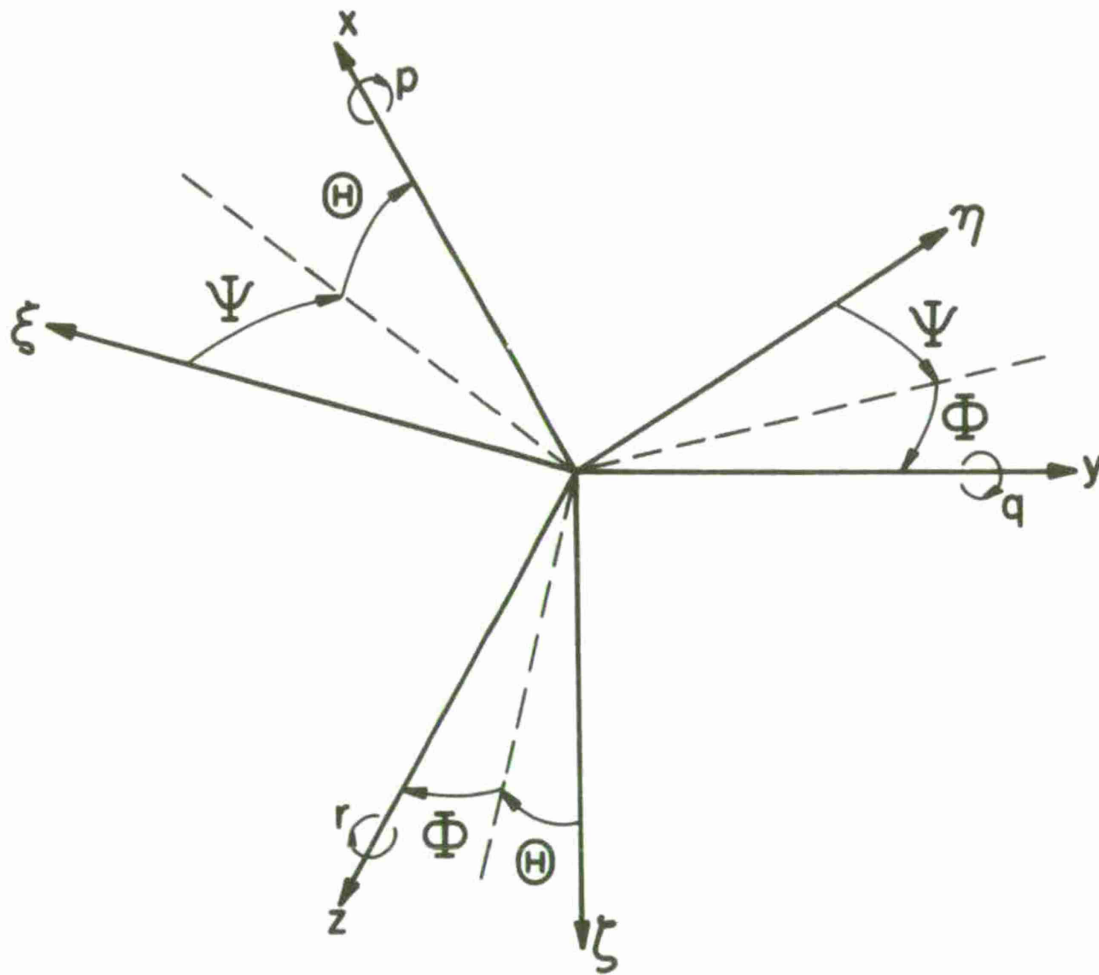


Figure 9.- Coordinate systems used in trajectory calculation.

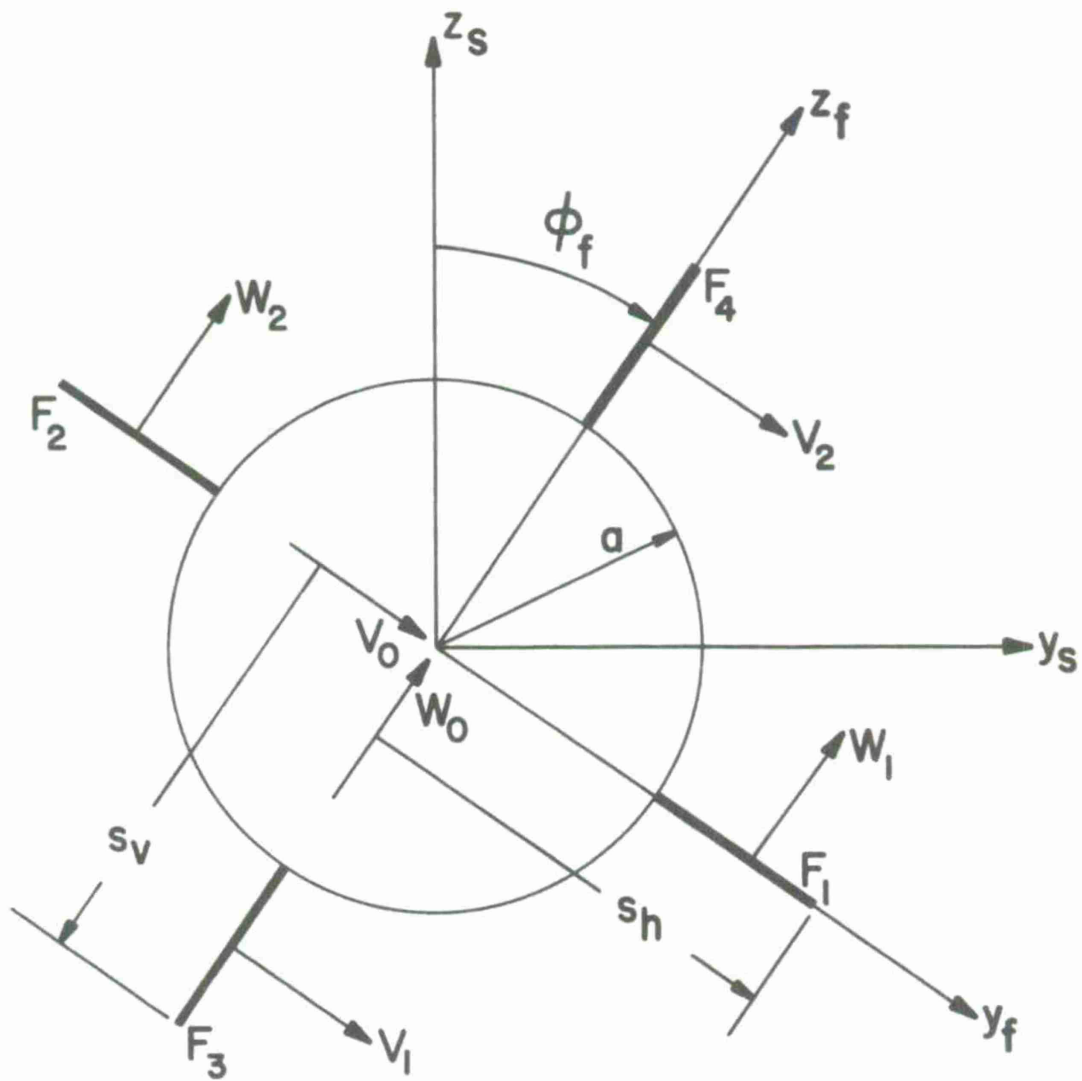


Figure 10.- Coordinate systems used in empennage force and moment calculation.

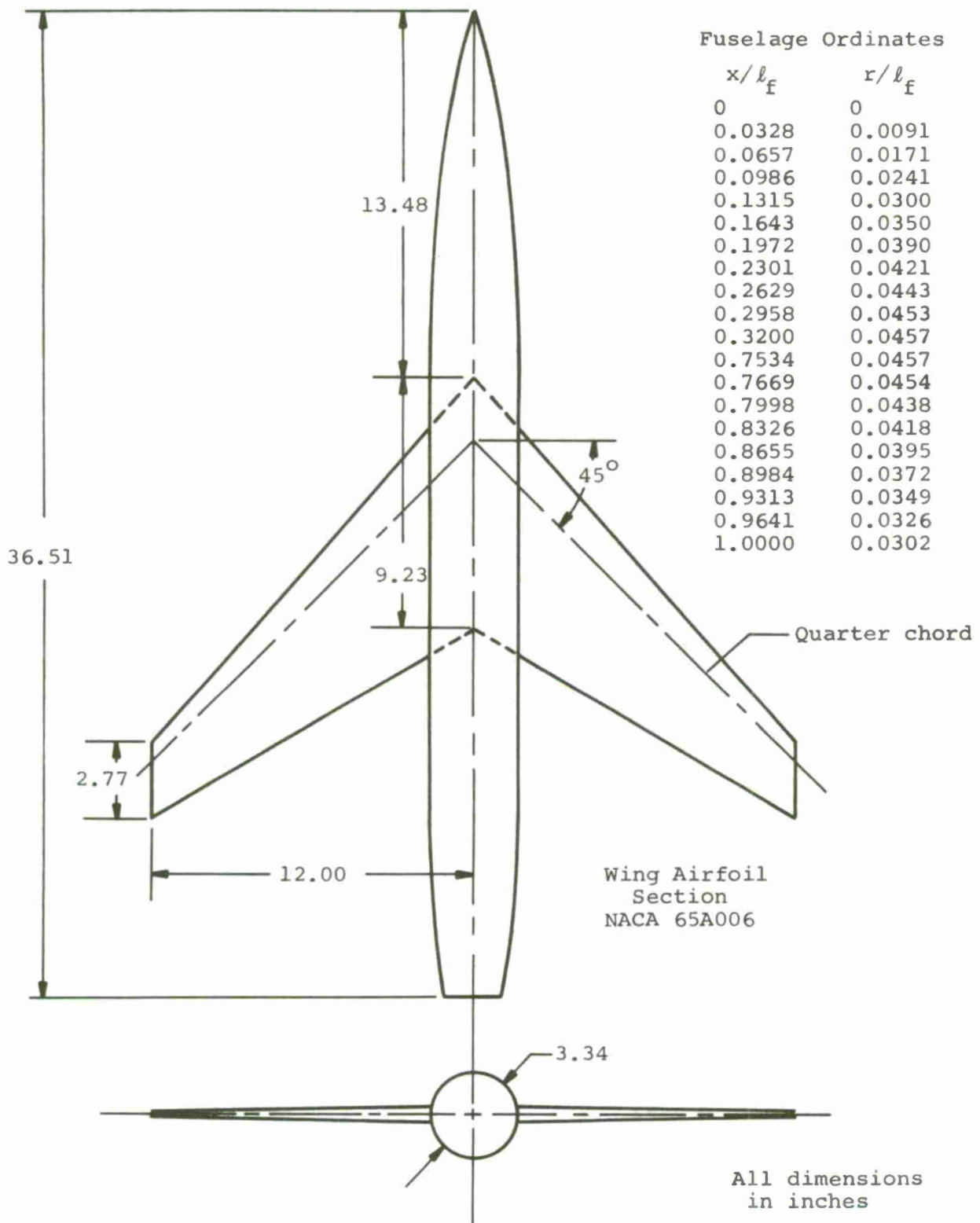
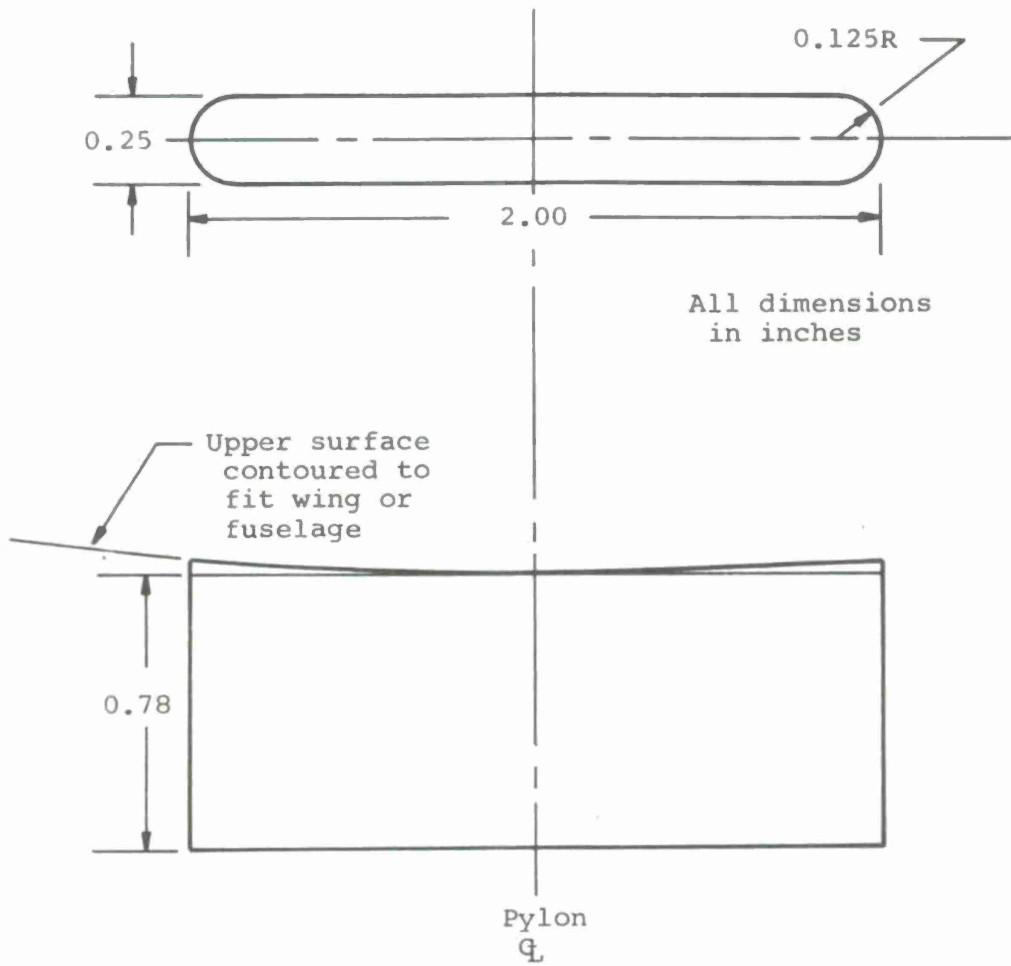


Figure 11.- Wing-fuselage combination.

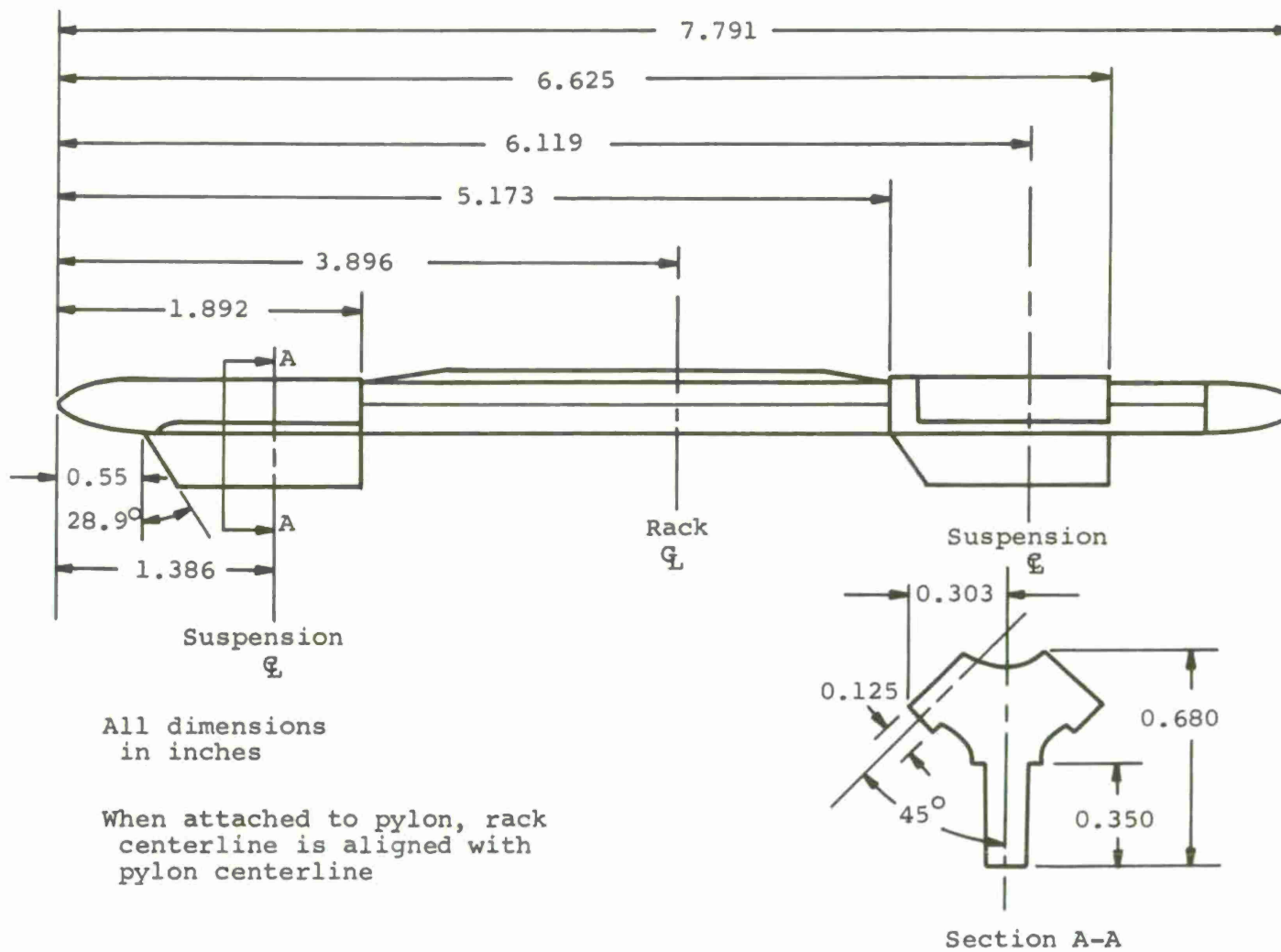


For wing pylons, pylon centerline located at 40% wing chord.

For fuselage pylon, pylon centerline located 19.43 inches aft of fuselage nose.

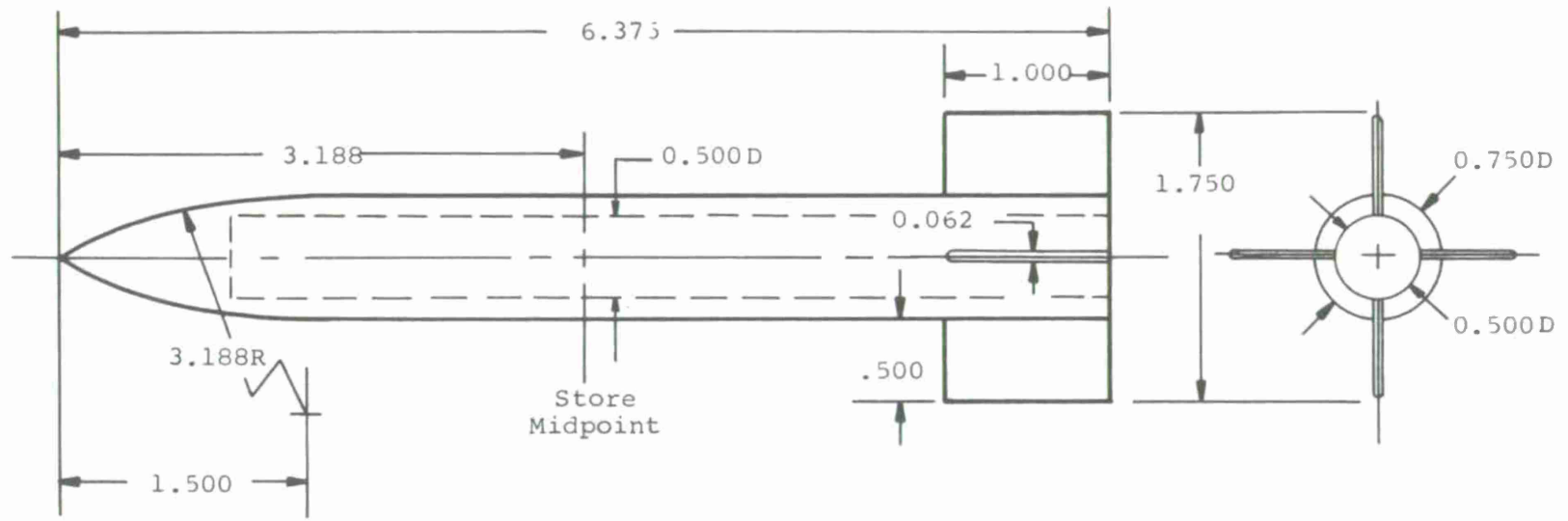
(a) Pylon used with single store and MER and TER racks.

Figure 12.- Aircraft components used with wing-fuselage combination.



(b) MER rack.

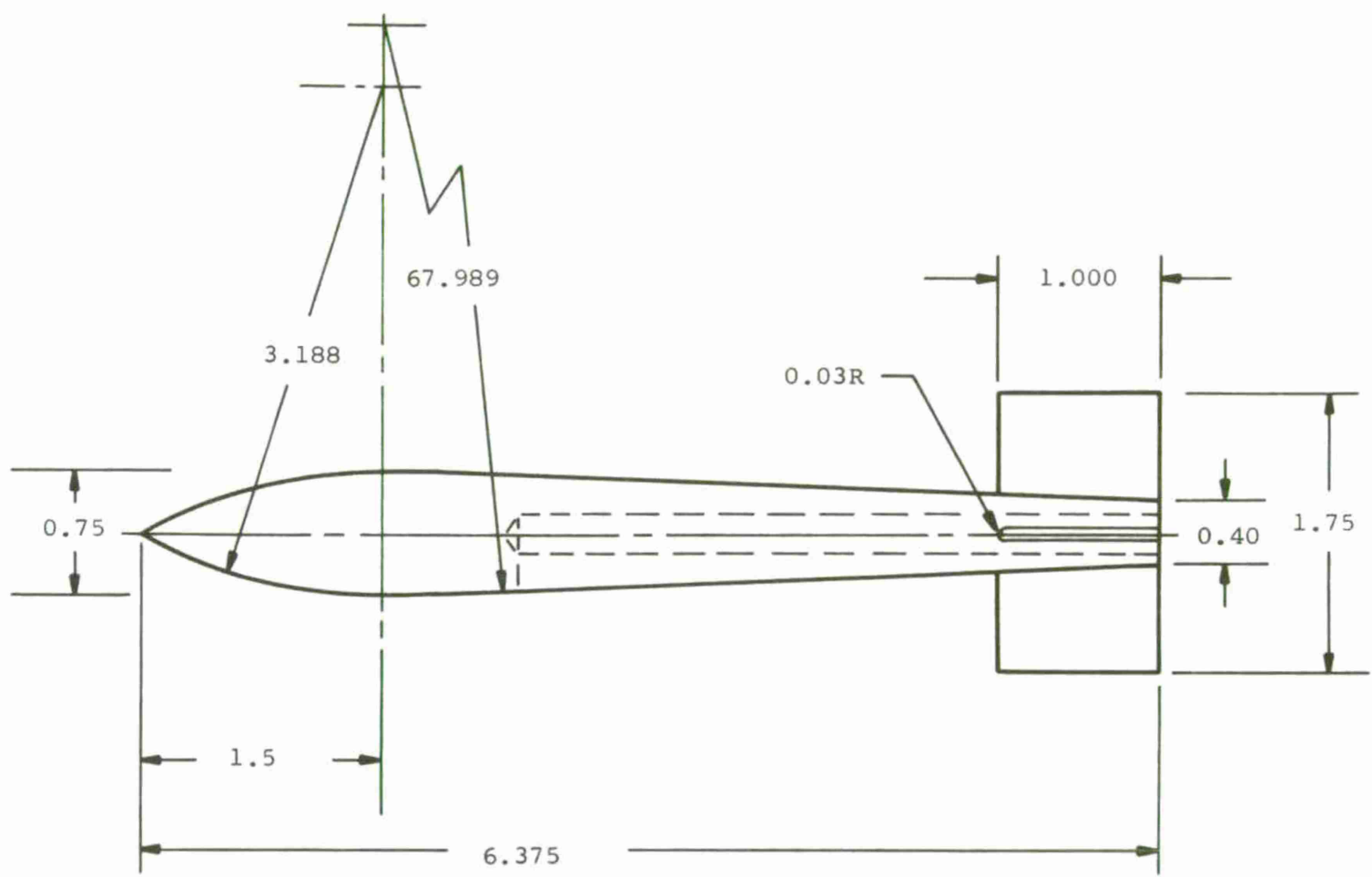
Figure 12.- Continued.



All dimensions in inches.

(c) Large store with cylindrical afterbody and rectangular cruciform fins.

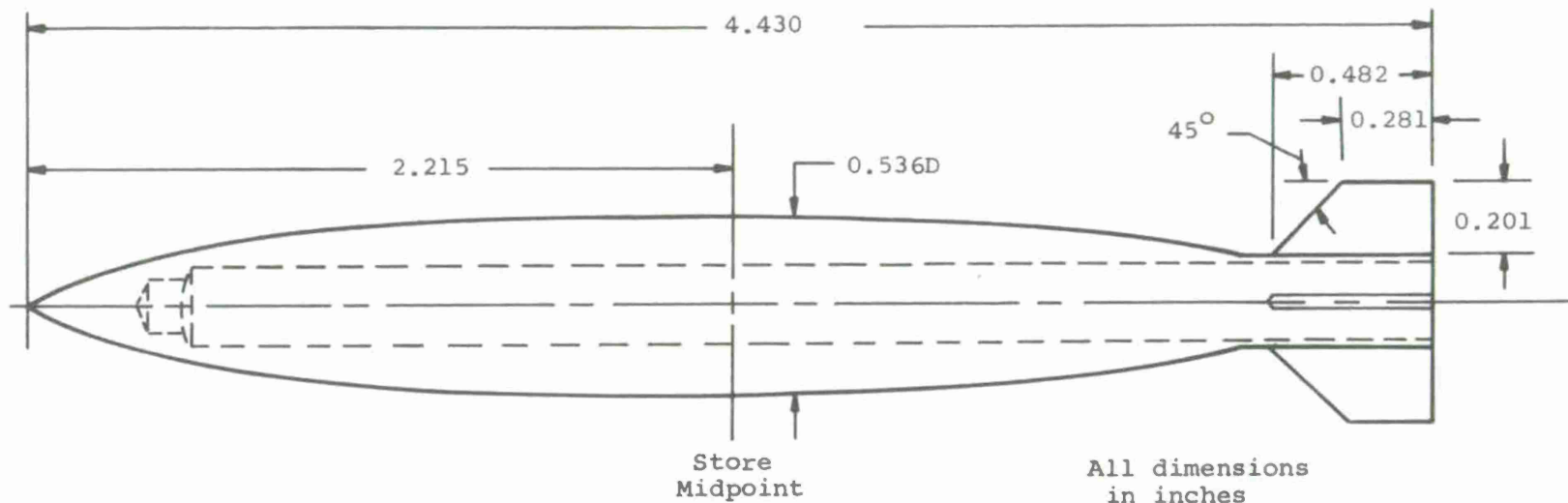
Figure 12.- Continued.



All dimensions in inches.

(d) Large store with boattail afterbody and rectangular cruciform fins.

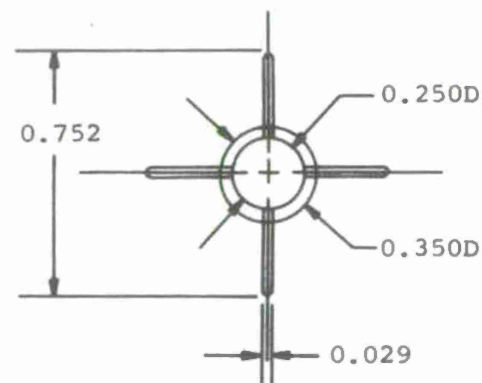
Figure 12.- Continued.



Store midpoint aligned with suspension centerline on MER rack when in carriage position.

Unfinned force and moment model same as finned model except for omission of fins.

Finned and unfinned dummy stores same as respective force and moment stores except for omission of center bore for balance mounting.



(e) Small boattail MER store with cruciform empennage.

Figure 12.- Concluded.

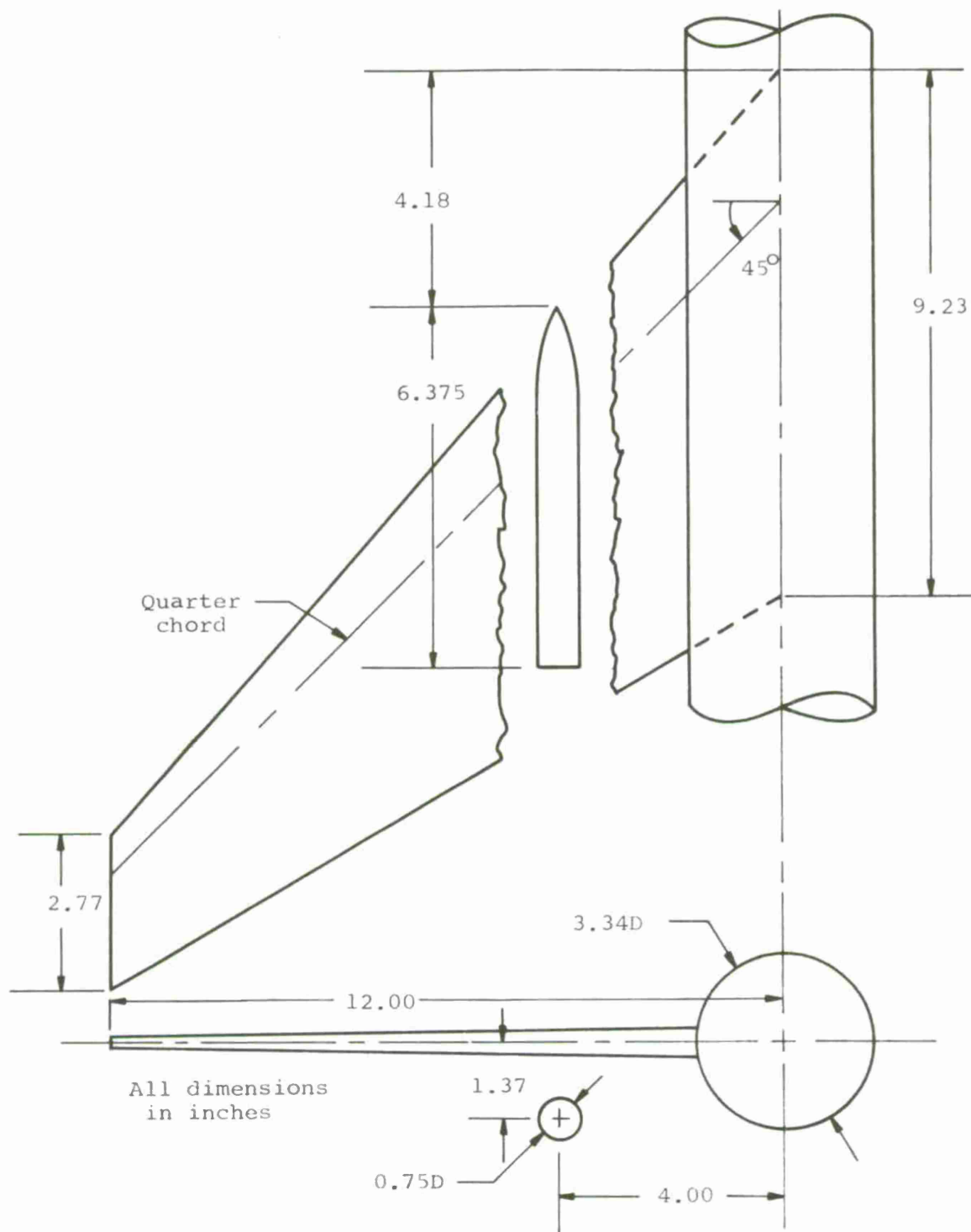


Figure 13.- Large store with cylindrical afterbody under wing-fuselage configuration.

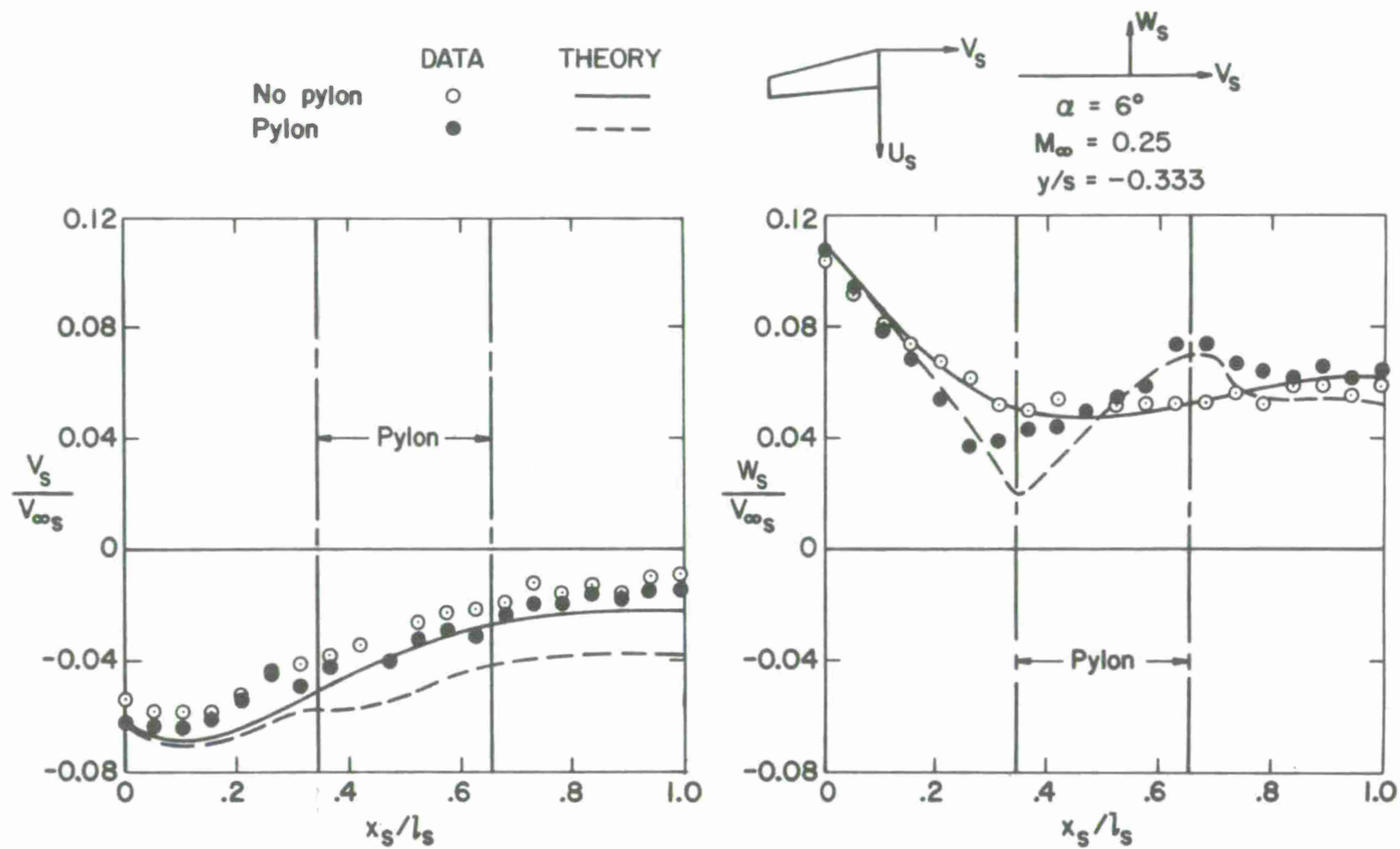
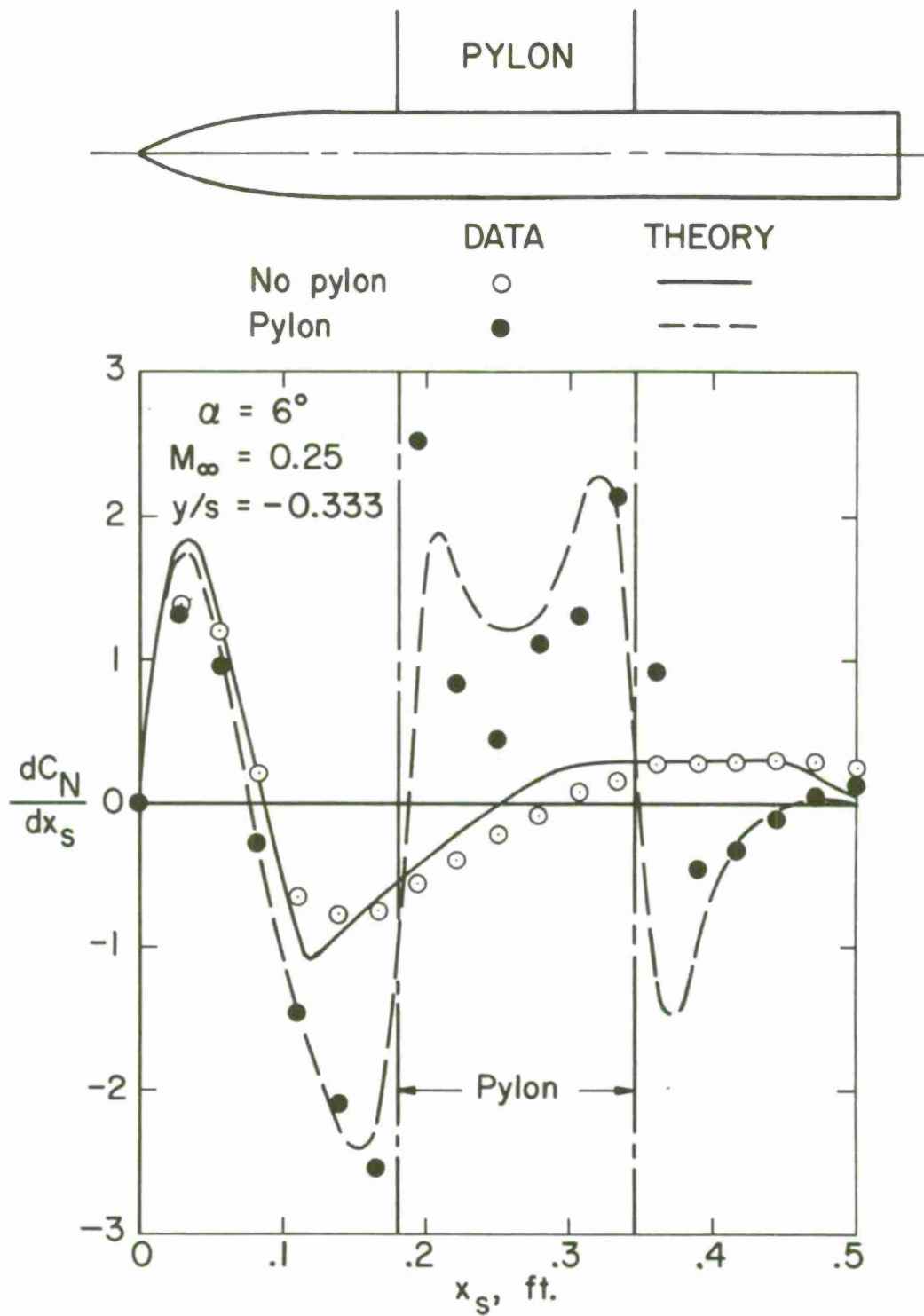
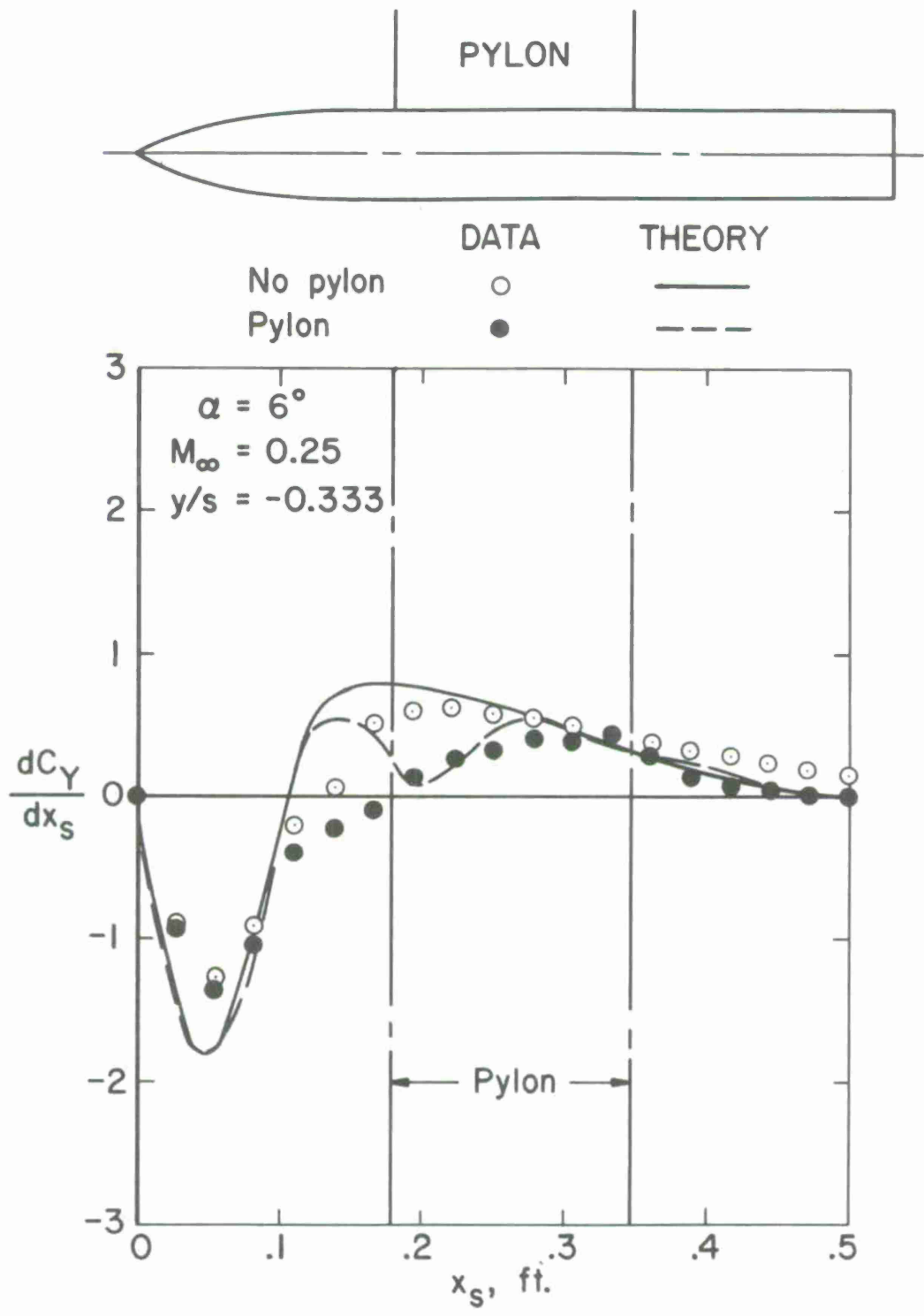


Figure 14.- Effect of pylon on flow field of wing-body combination at centerline location of attached store.



(a) Normal-force distribution.

Figure 15.- Effect of pylon on load distributions of attached store.



(b) Side-force distribution.

Figure 15.- Concluded.

$\alpha = 6^\circ$   
 $M_\infty = 0.25$   
 $y/s = -0.333$

DATA  $\circ$   
THEORY — — —

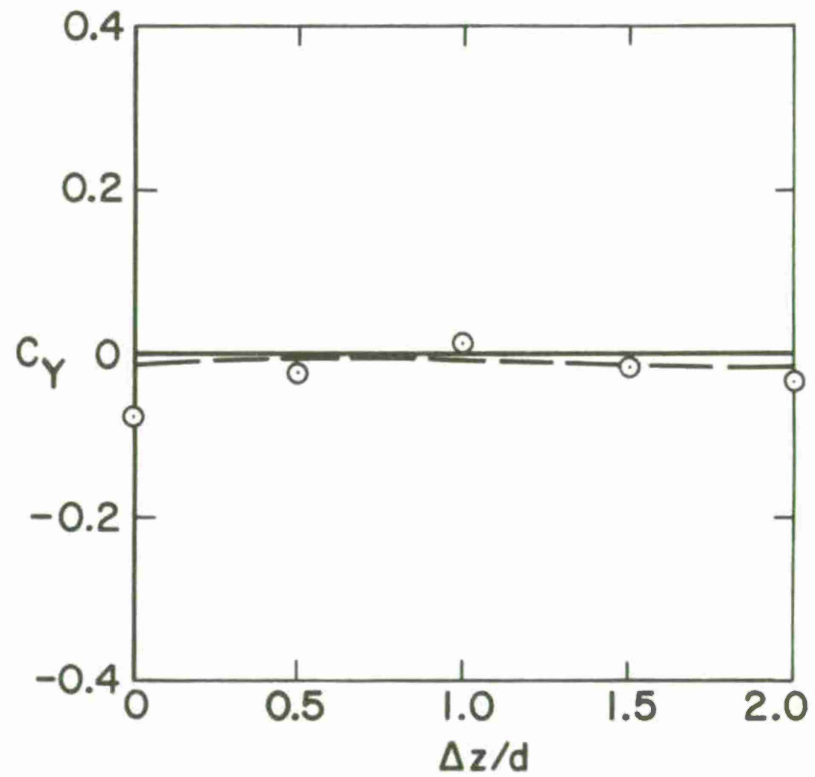
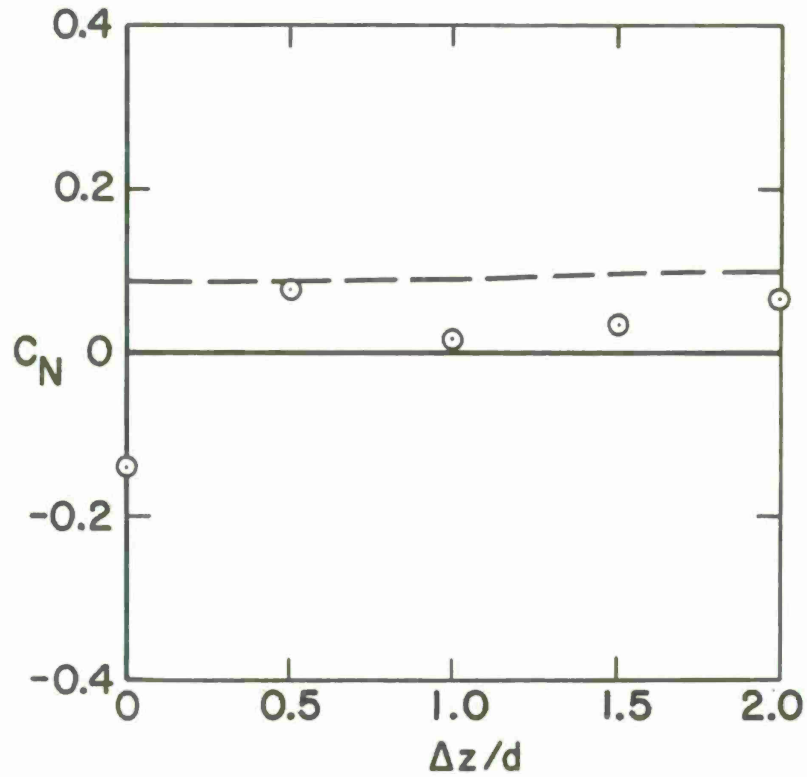


Figure 16.- Effect of vertical location on normal-force and side-force coefficients of store.

$\Delta z/d = 1.0$   
 $M_\infty = 0.25$   
 $y/s = -0.333$

DATA  $\circ$   
 THEORY - - -

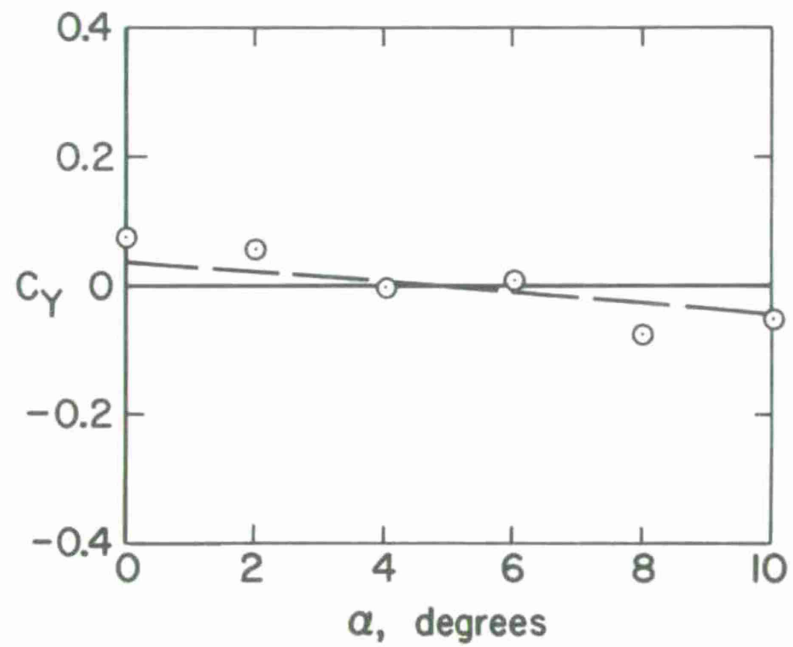
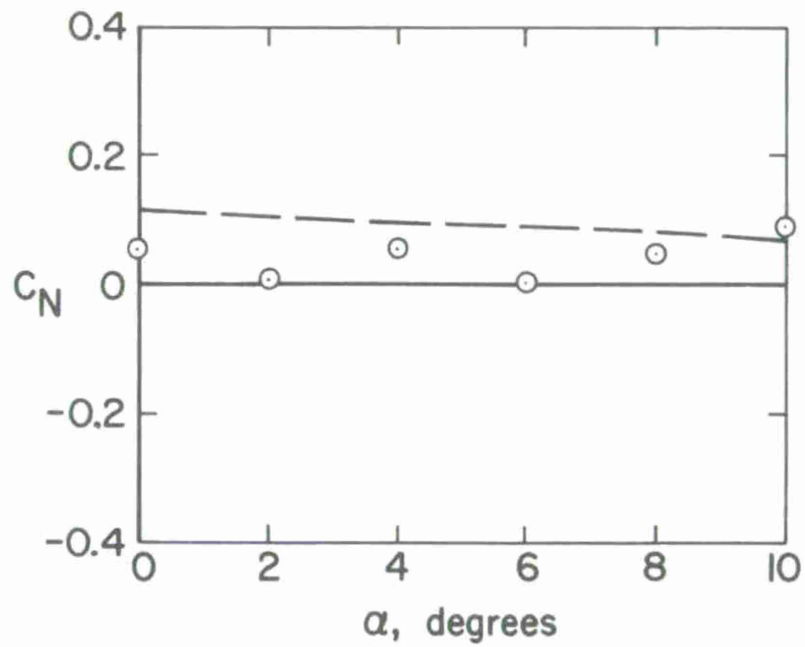


Figure 17.- Effect of angle of attack on normal-force and side-force coefficients of store.

TER Store  
Numbering System  
Viewed from Rear

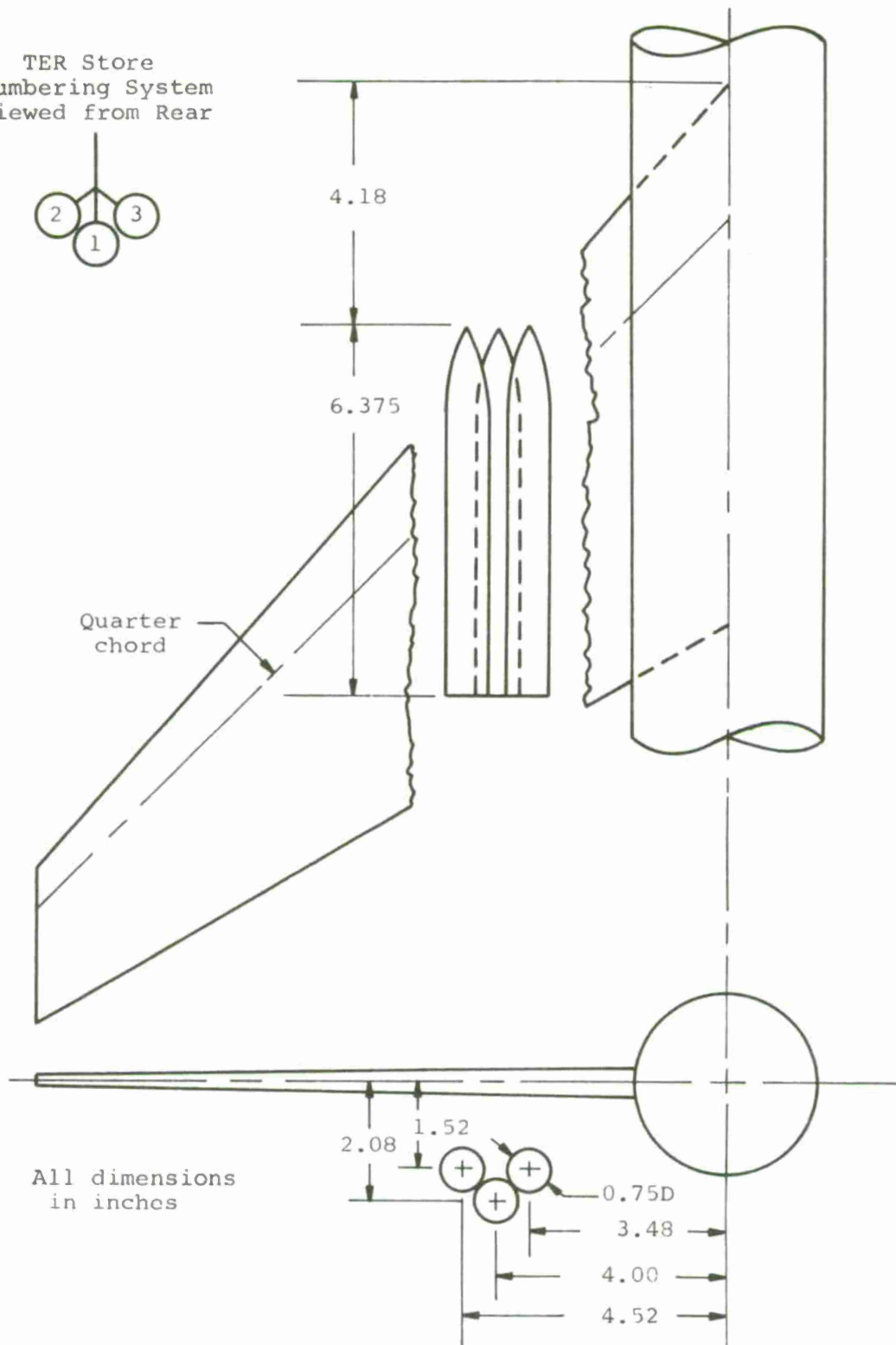
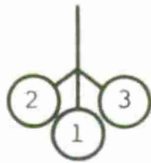


Figure 18.- Large stores with cylindrical afterbody in a TER arrangement under the wing.

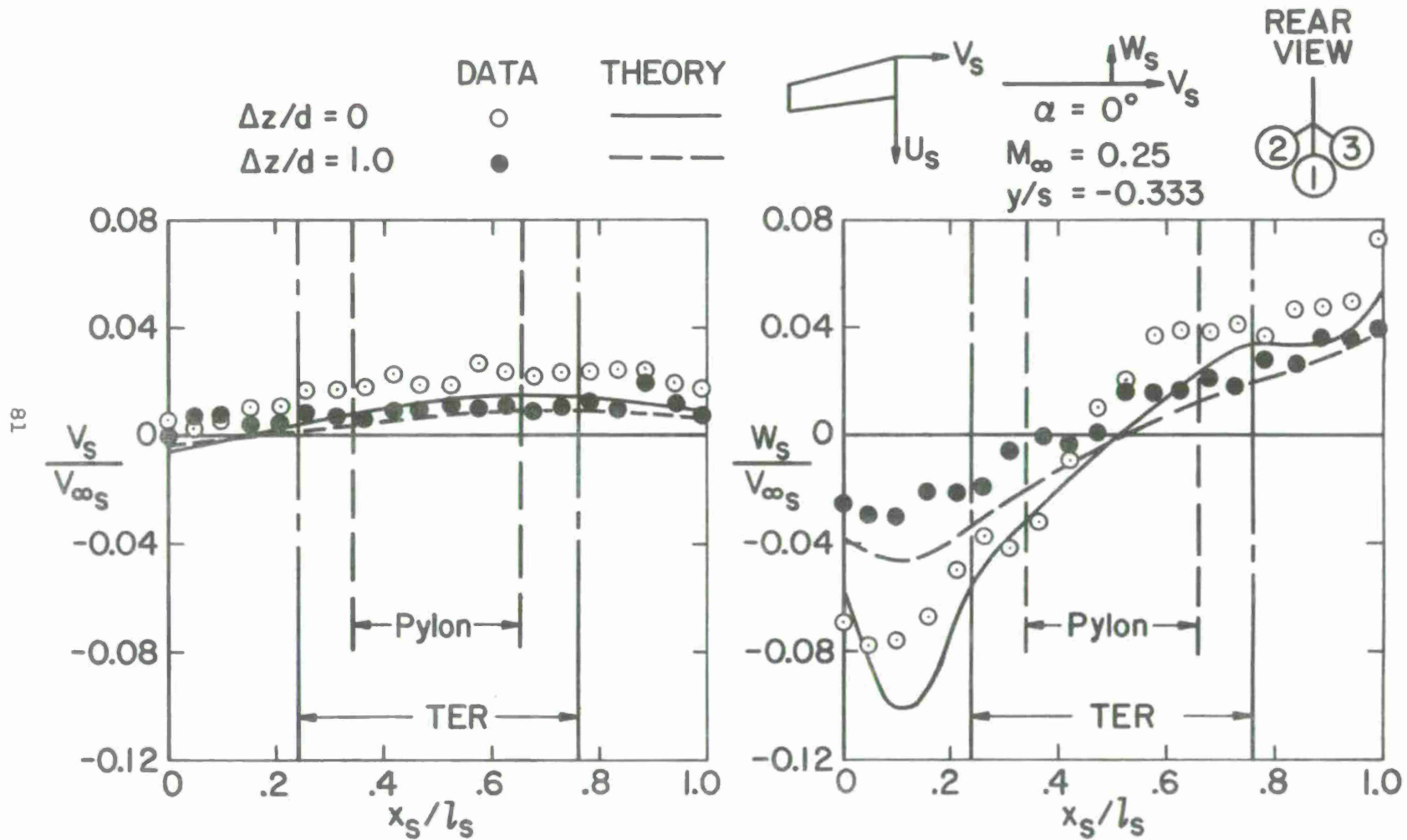


Figure 19.- Effect of vertical position on downwash and sidewash under TER configuration (parent aircraft - WBPTS<sub>2</sub>S<sub>3</sub>).

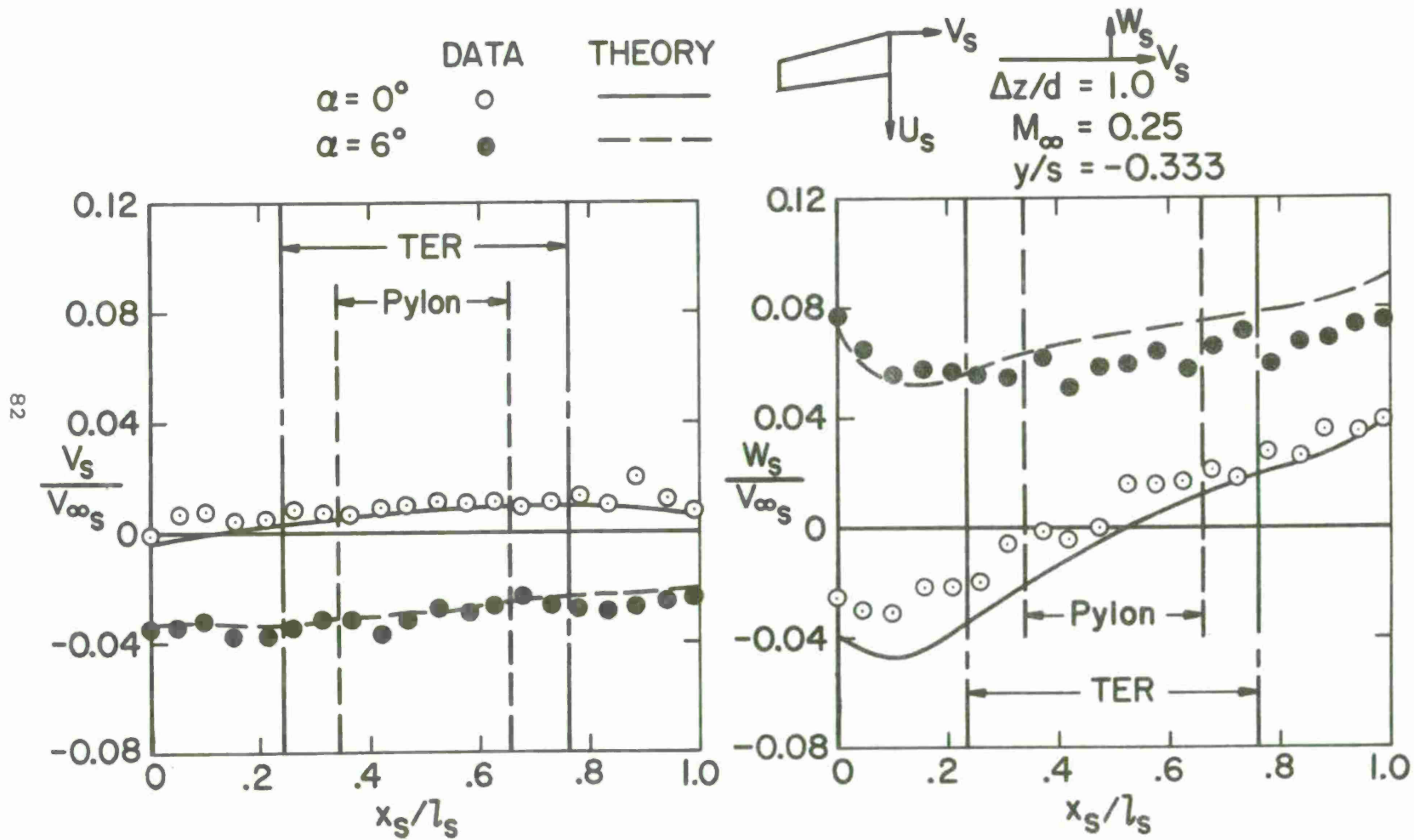
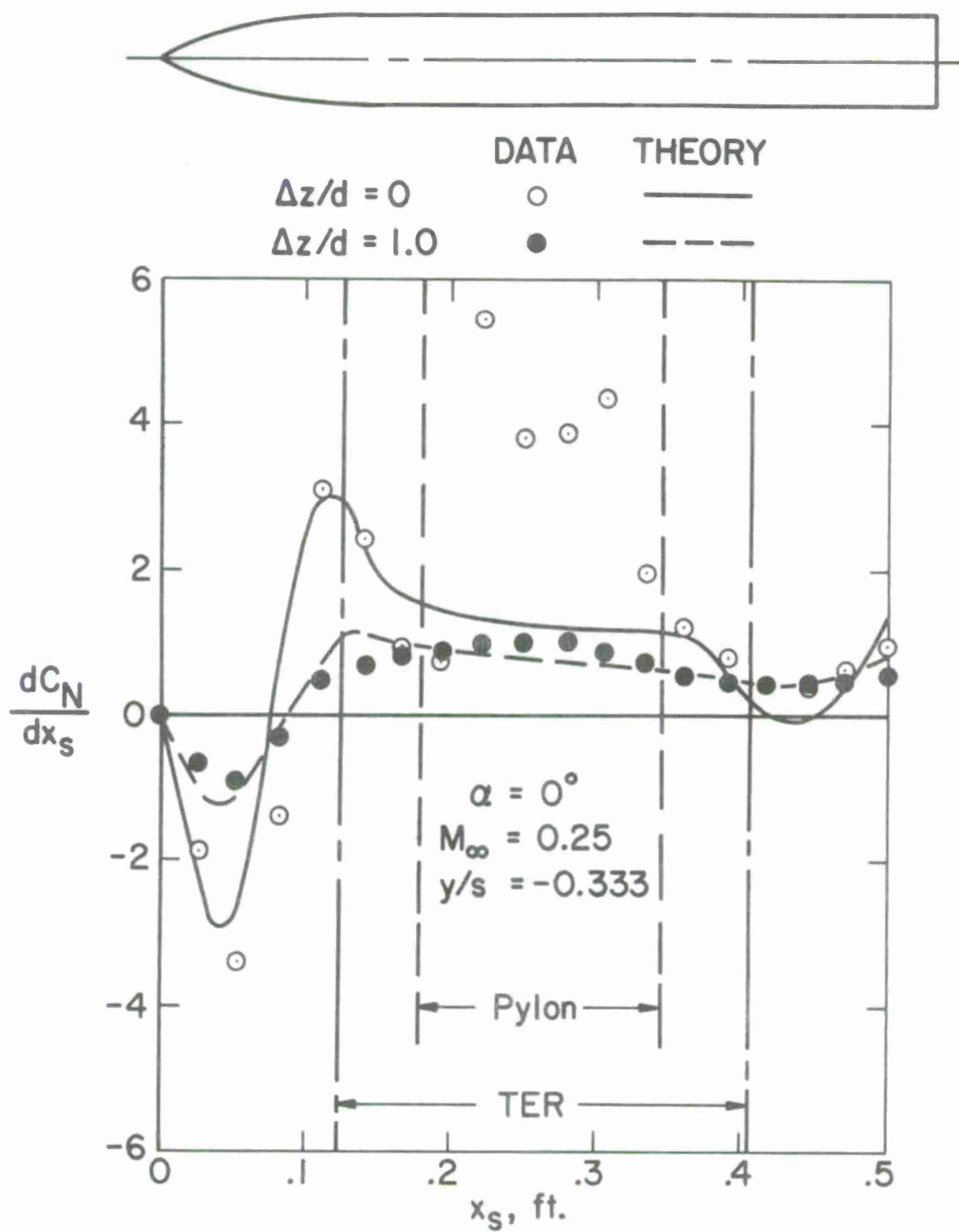
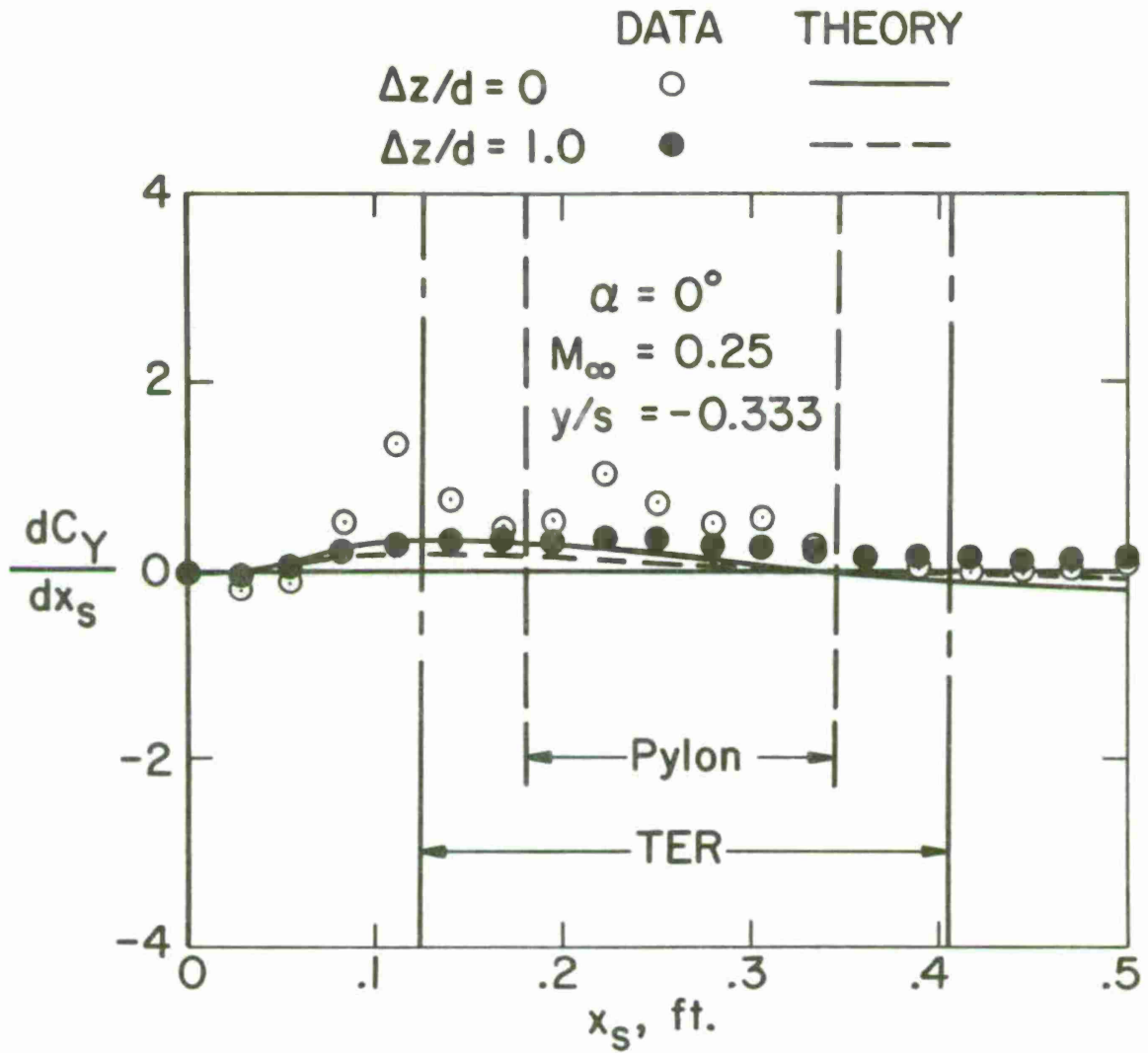
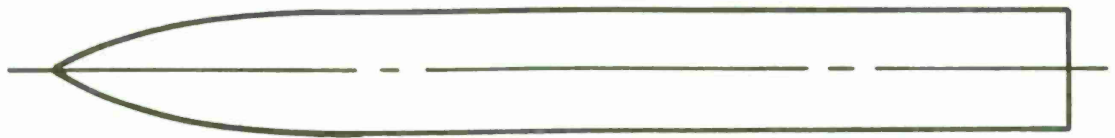


Figure 20.- Effect of angle of attack on downwash and sidewash under TER configuration (parent aircraft - WBPTS<sub>2</sub>S<sub>3</sub>).



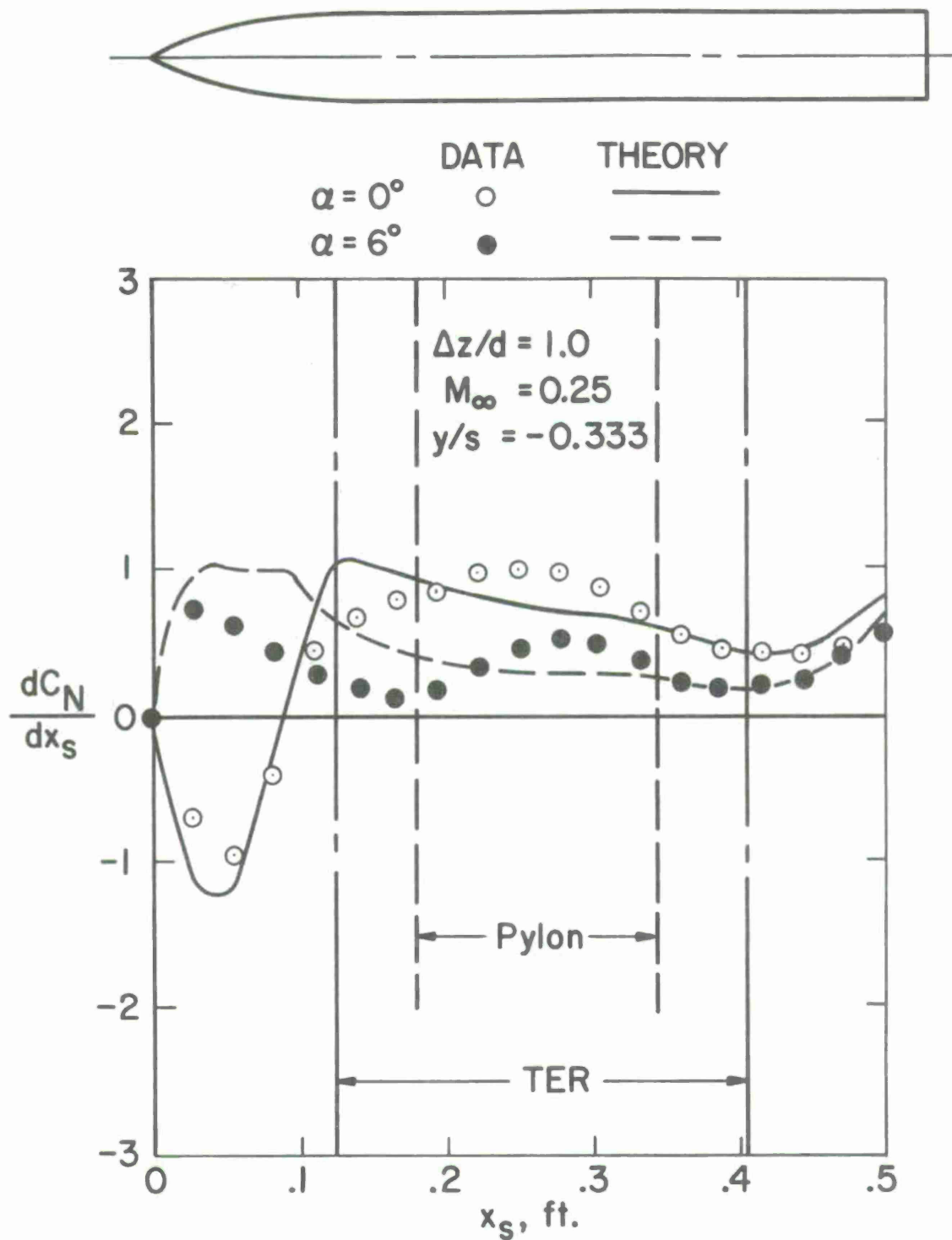
(a) Normal-force distribution.

Figure 21.- Effect of vertical position on loading distributions on store  $S_1$  of TER configuration (Parent aircraft WBPTS<sub>2</sub>S<sub>3</sub>).



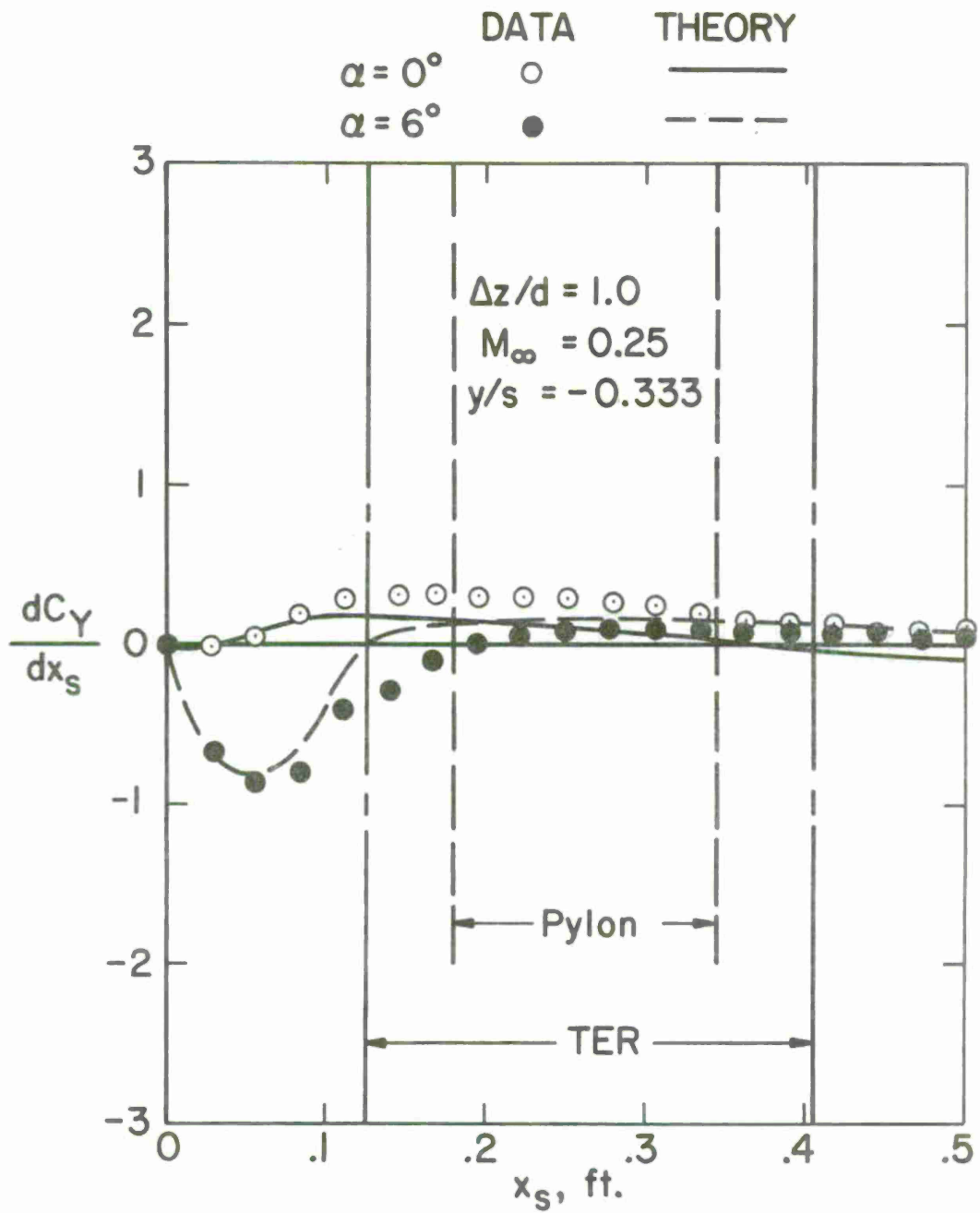
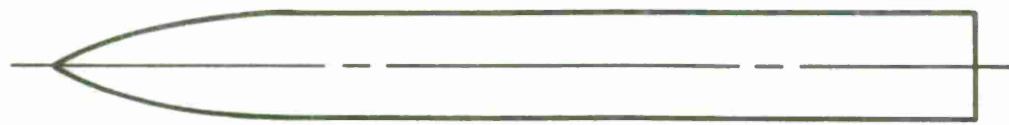
(b) Side-force distribution.

Figure 21.- Concluded.



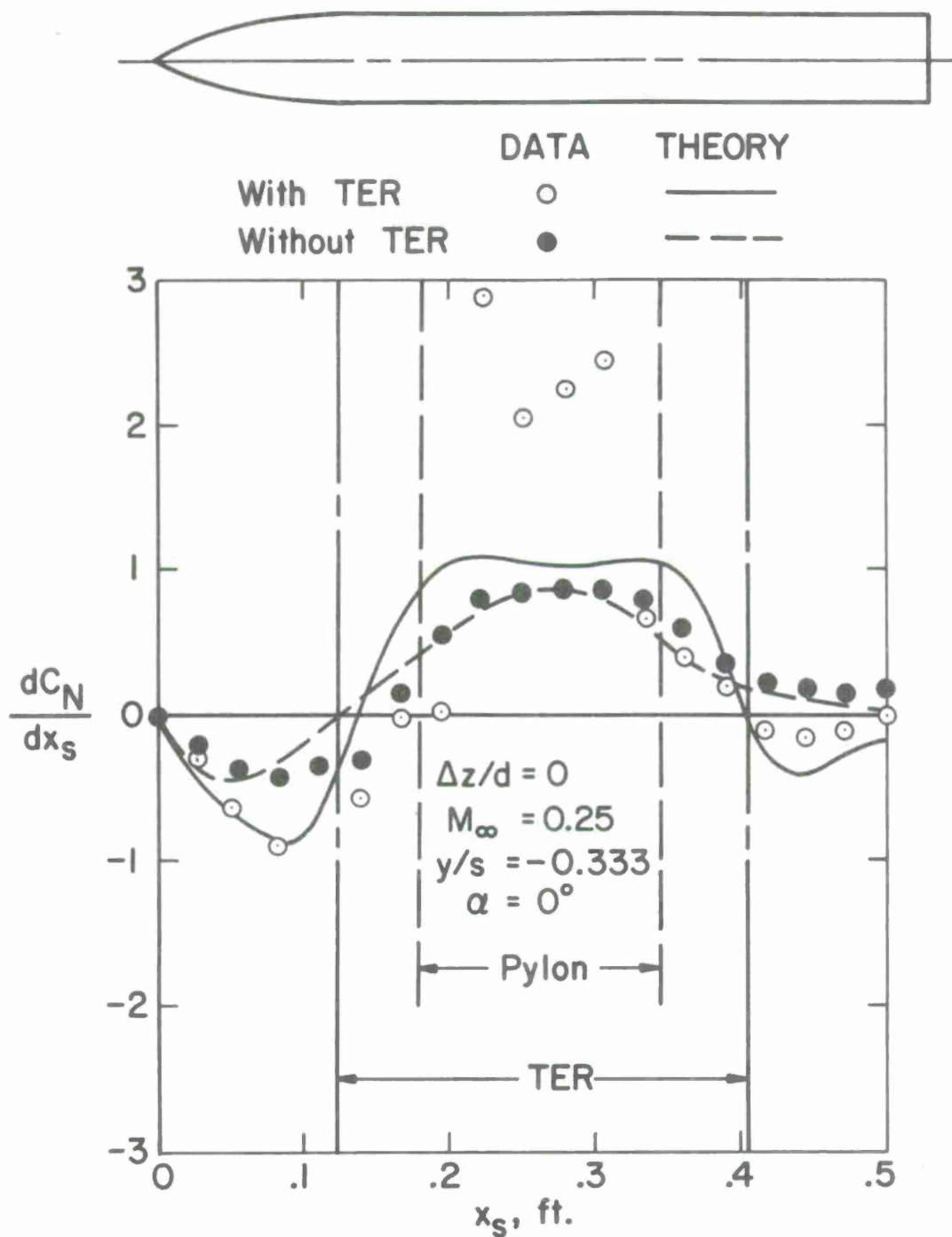
(a) Normal-force distribution.

Figure 22.- Effect of angle of attack on loading distributions on  $S_1$  in TER configuration (parent aircraft - WBPTS<sub>2</sub>S<sub>3</sub>).



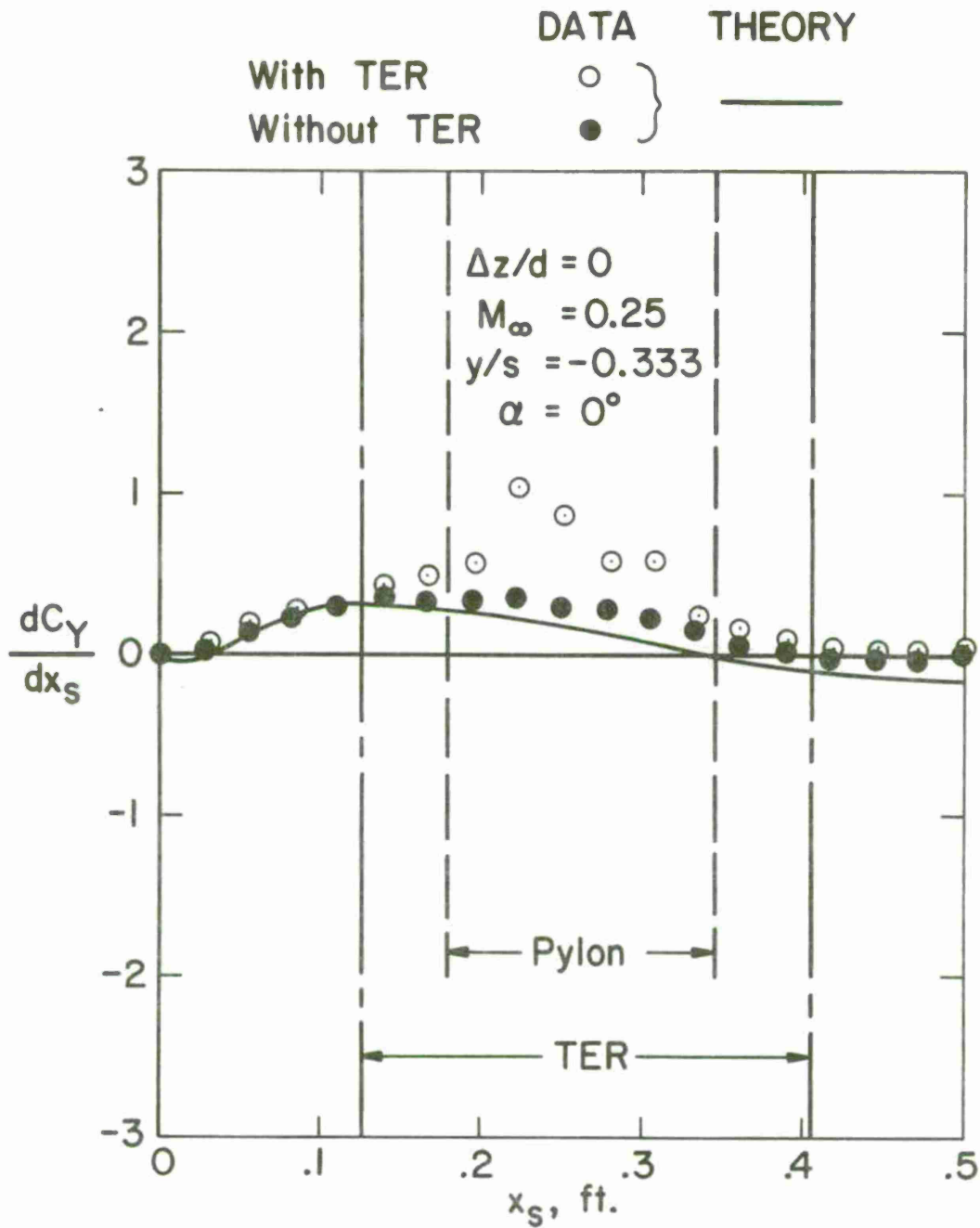
(b) Side-force distribution.

Figure 22.- Concluded.



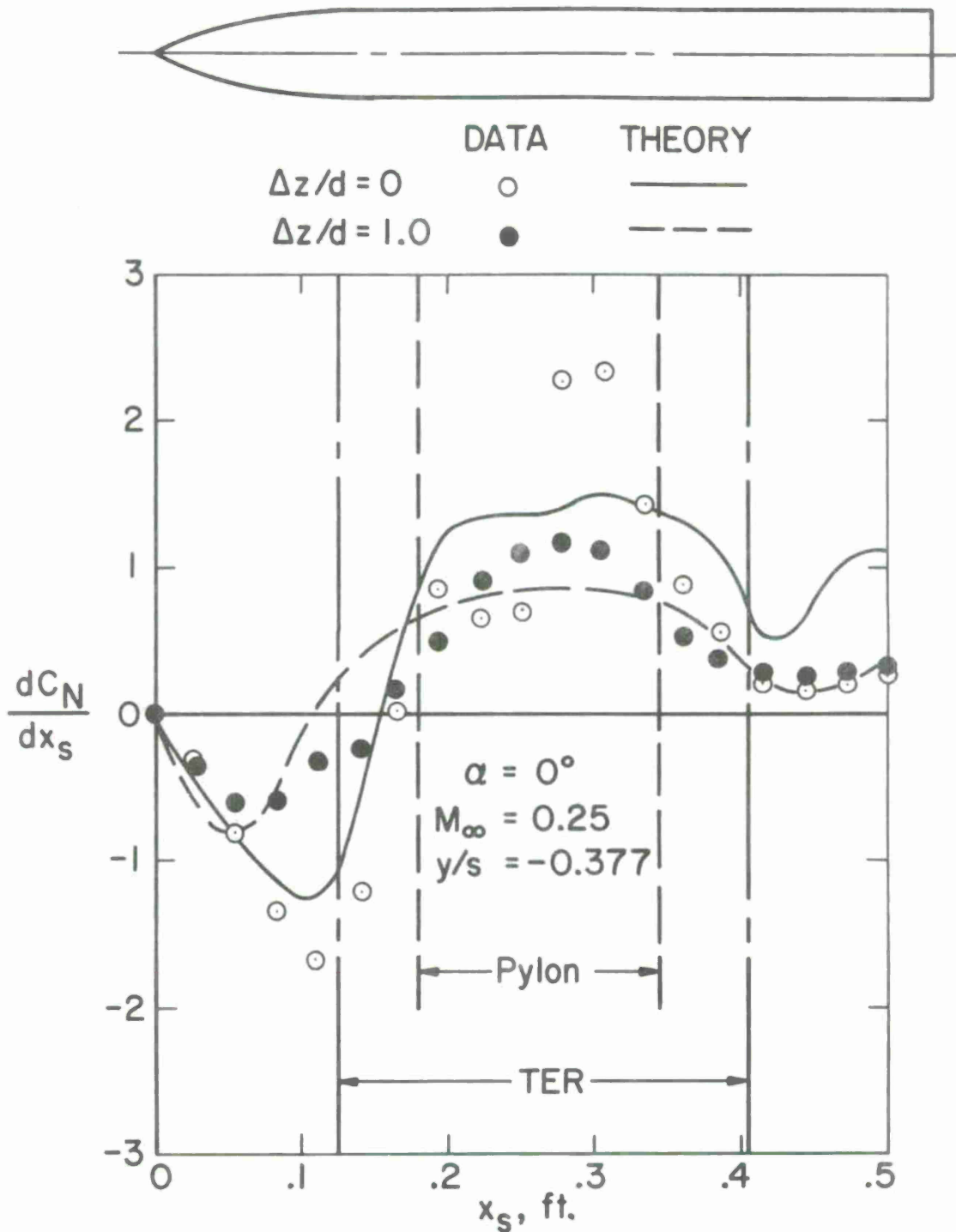
(a) Normal-force distribution.

Figure 23.- Effect of TER on loading of store  $S_1$  (parent aircraft - WBPT and WBP).



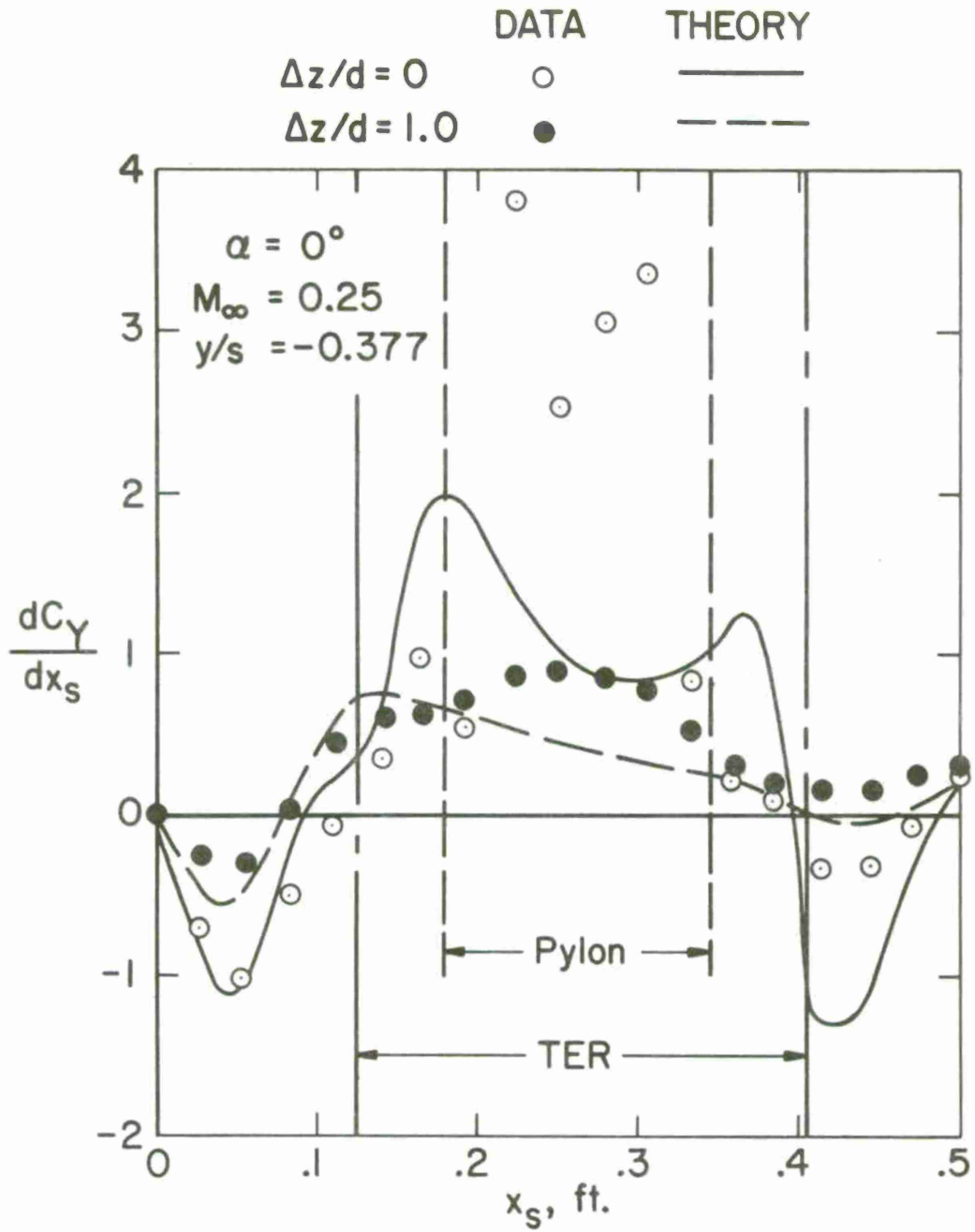
(b) Side-force distribution.

Figure 23.- Concluded.



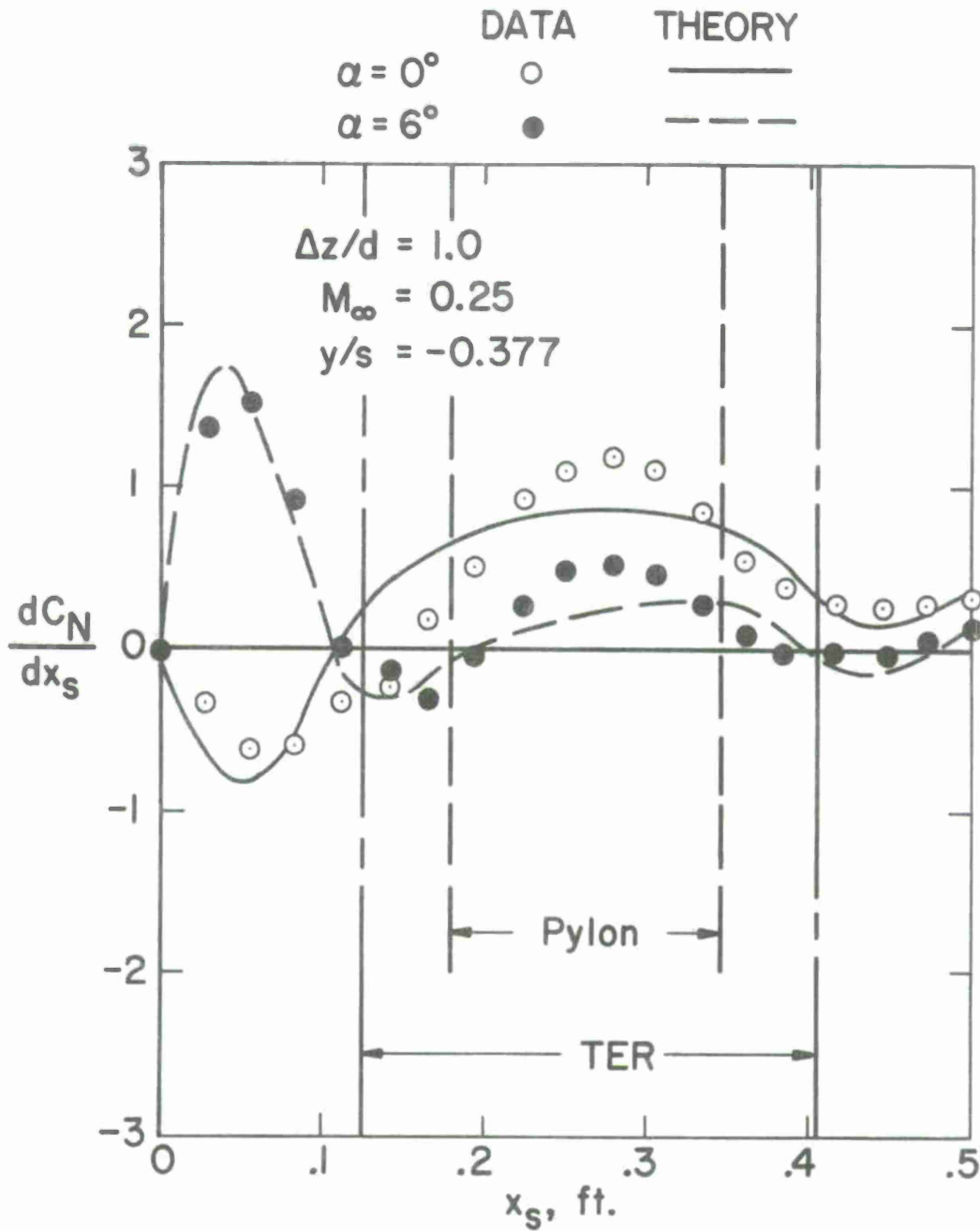
(a) Normal-force distribution.

Figure 24.- Effect of vertical position on loading distribution of shoulder store  $S_2$  of TER configuration (Parent aircraft WBPTS<sub>3</sub>).



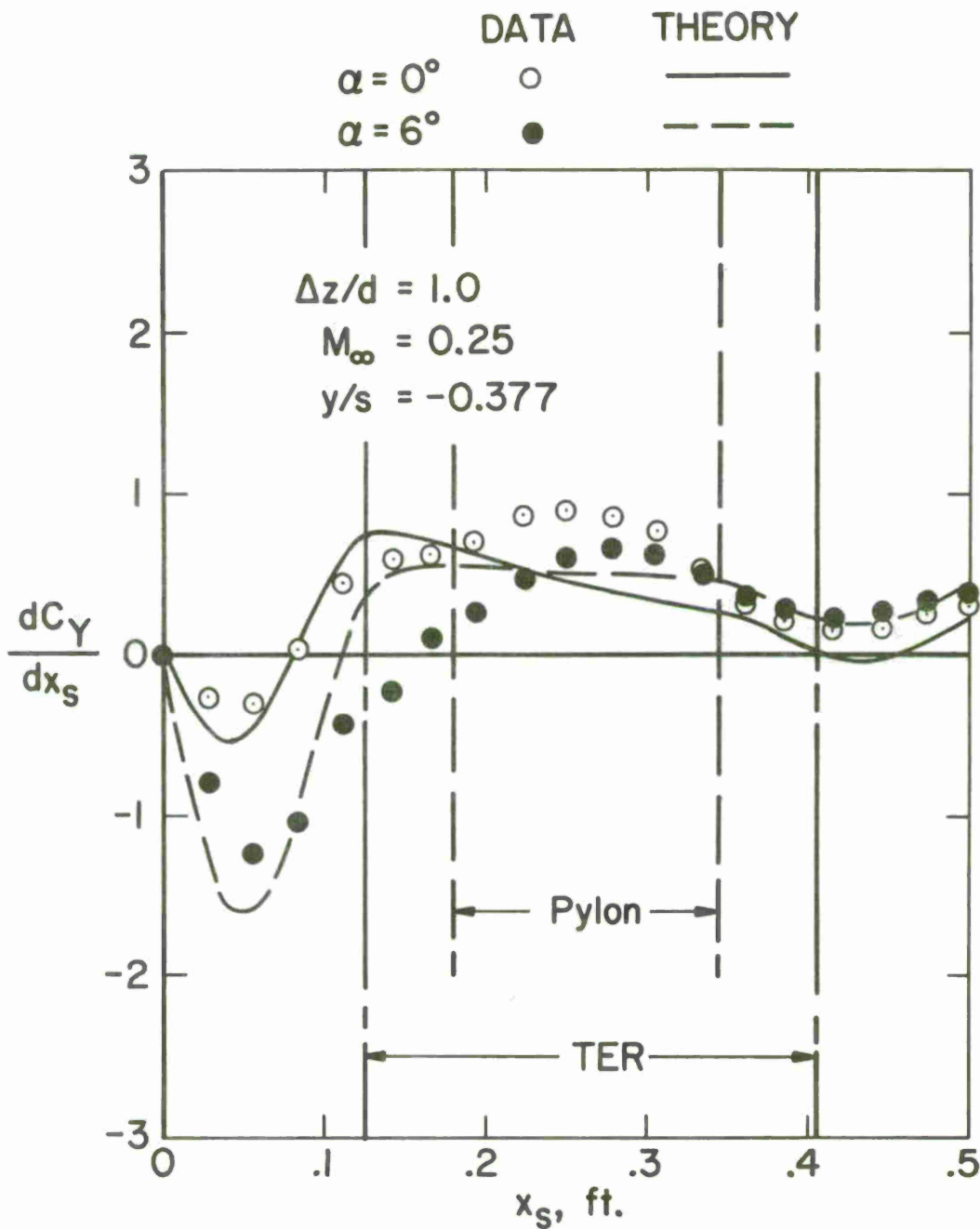
(b) Side-force distribution.

Figure 24.- Concluded.



(a) Normal-force distribution.

Figure 25.- Effect of angle of attack on loading distribution of shoulder store  $S_2$  of TER configuration (parent aircraft - WBPTS<sub>3</sub>).



(b) Side-force distribution.

Figure 25.- Concluded.

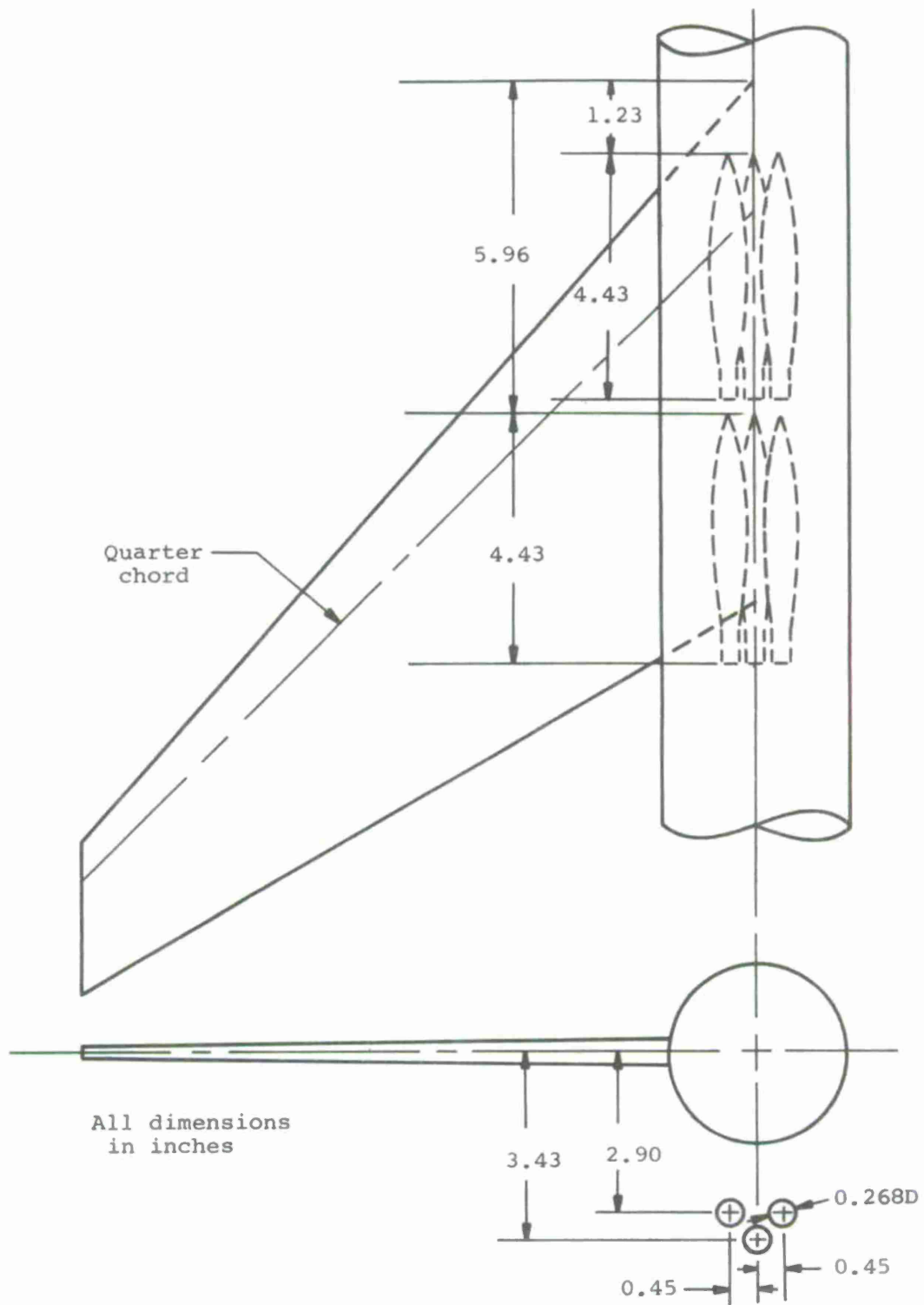
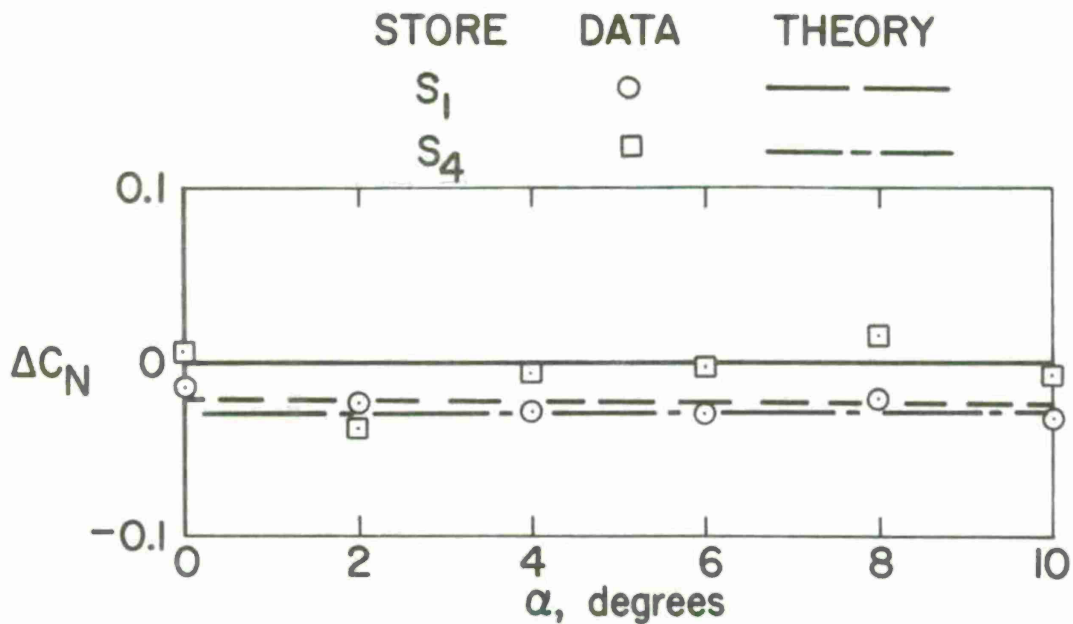
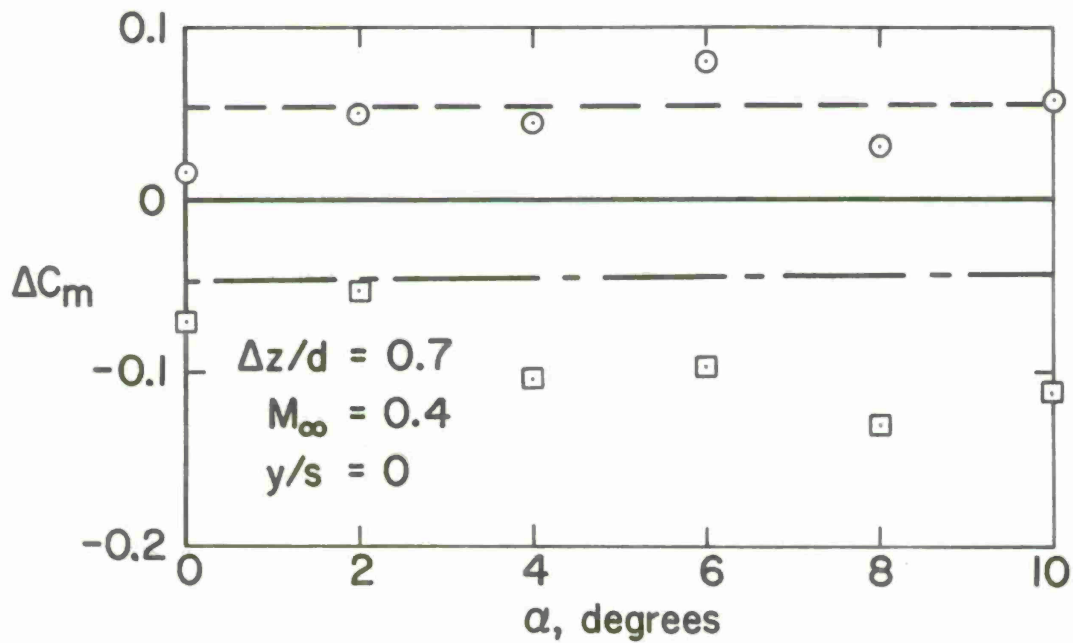


Figure 26.- Small boattail stores in a MER arrangement under the fuselage.

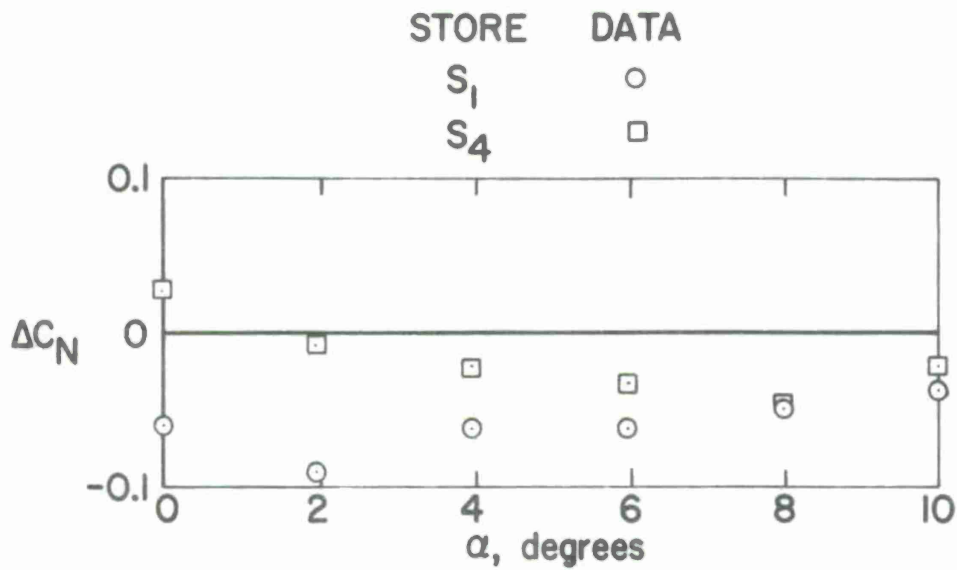


(a) Normal-force coefficient.

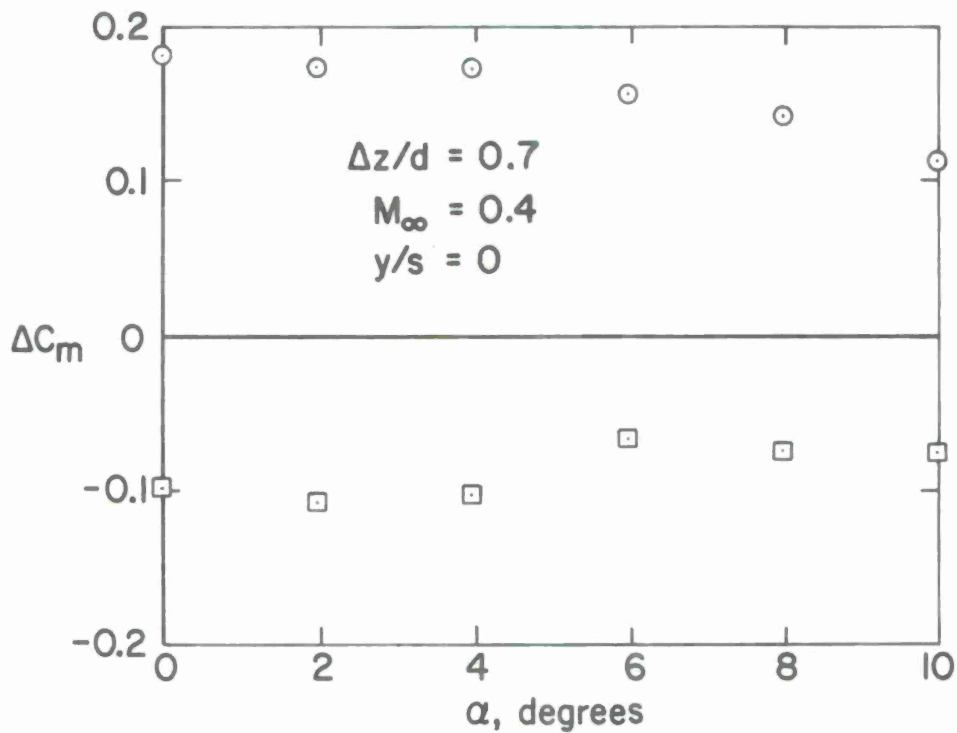


(b) Pitching-moment coefficient.

Figure 27.- Effects of  $S_5, S_6$  on  $S_1$  and  $S_1, S_2, S_3$  on  $S_4$  in MER configuration; no empennages.

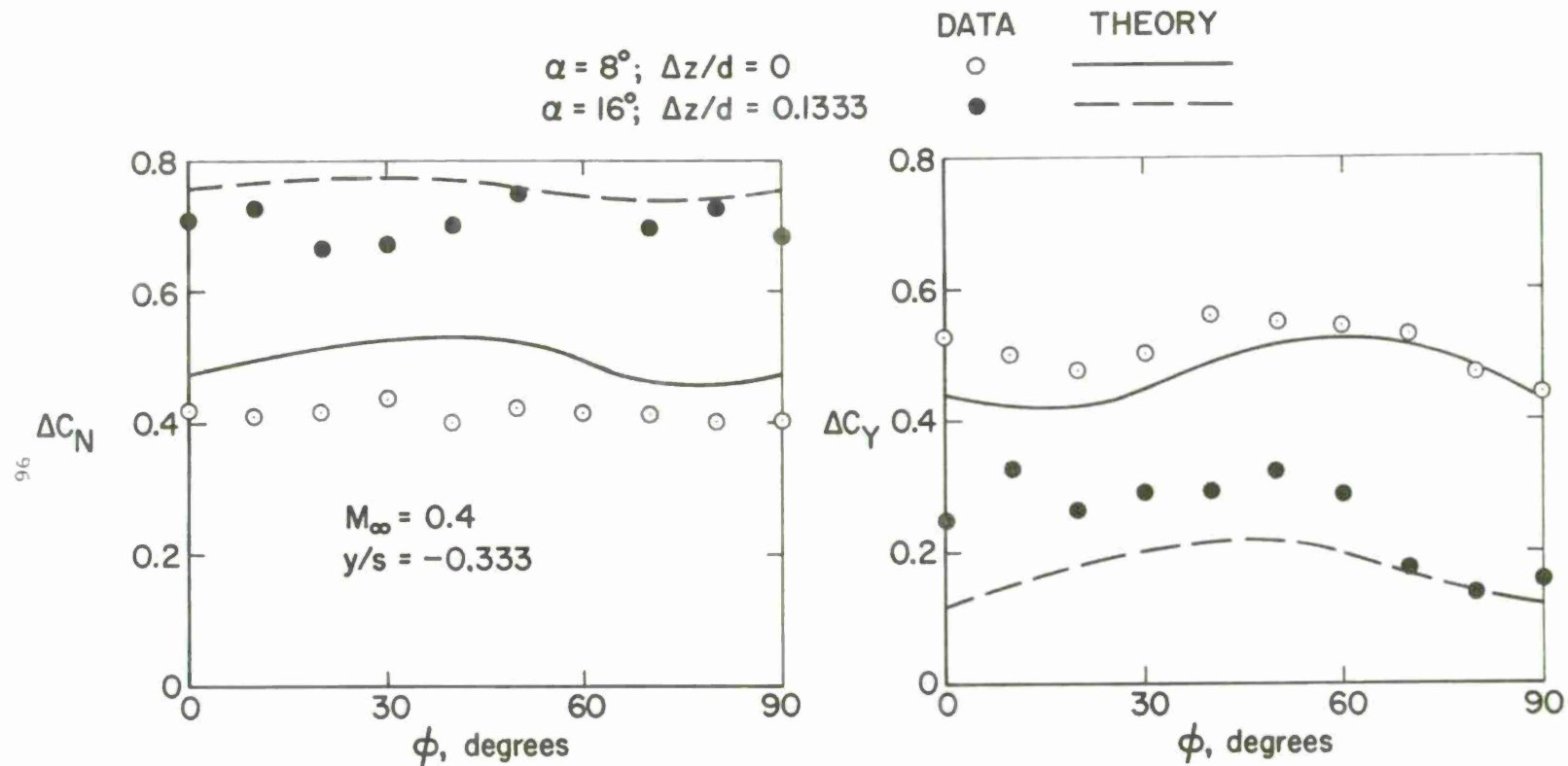


(a) Normal-force coefficient.



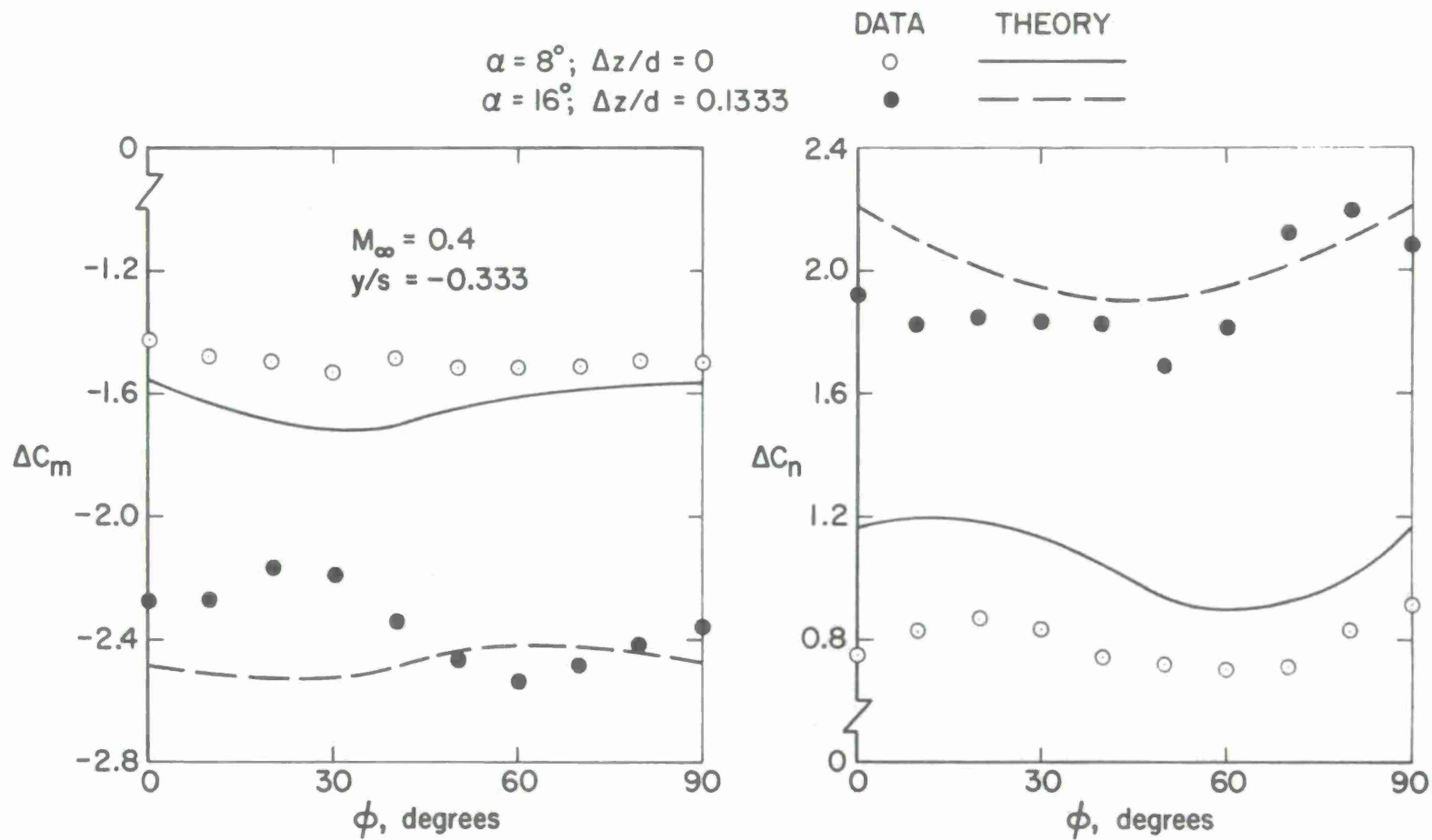
(b) Pitching-moment coefficient

Figure 28.- Effects of  $S_5$ ,  $S_6$  on  $S_1$  and  $S_1$ ,  $S_2$ ,  $S_3$  on  $S_4$  in MER configuration; with empennages.



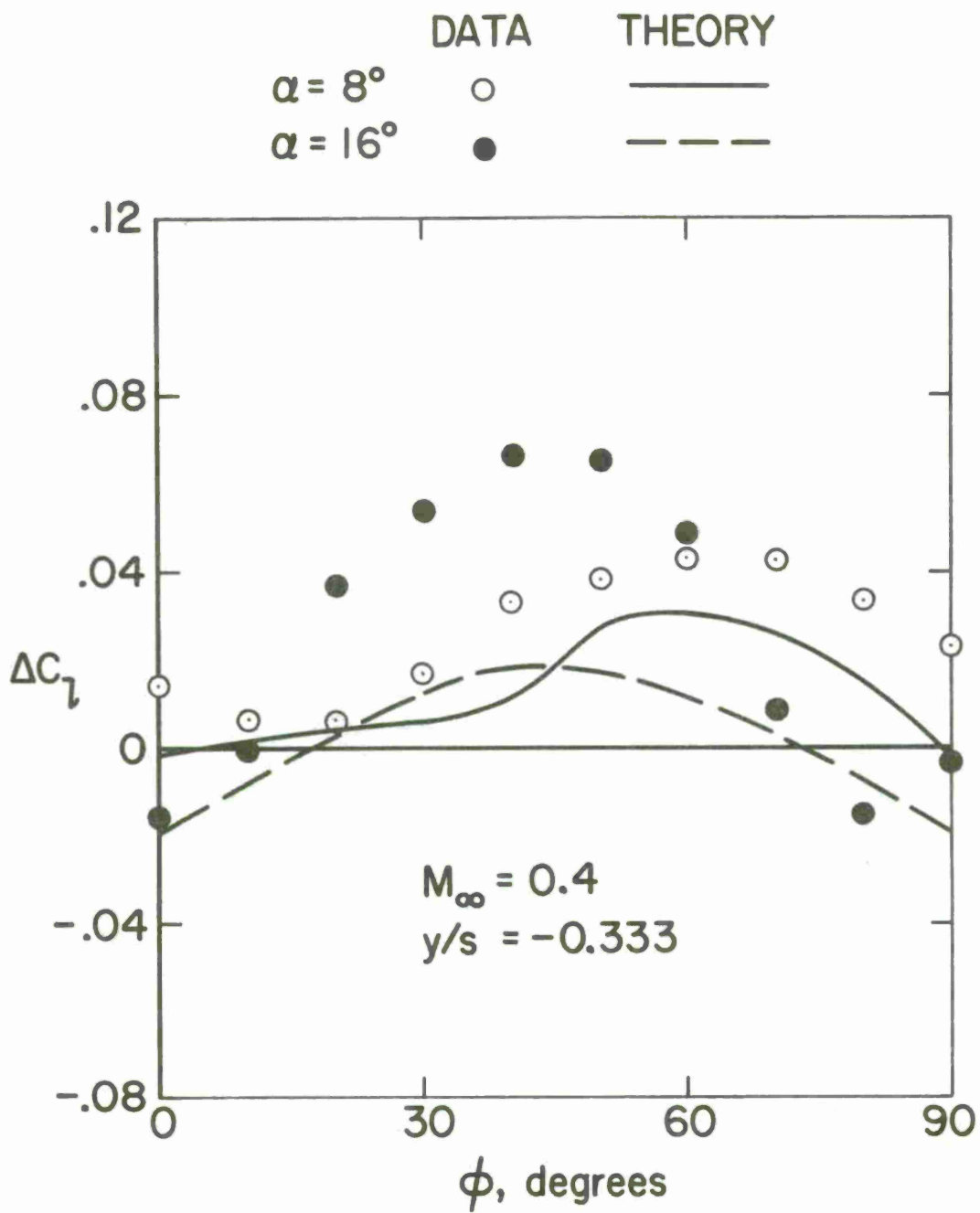
(a) Normal-force and side-force coefficients.

Figure 29.- Effect of roll angle on empennage contributions to store  $S_c$  forces and moments in the attached position (parent aircraft WBP).



(b) Pitching-moment and yawing-moment coefficients.

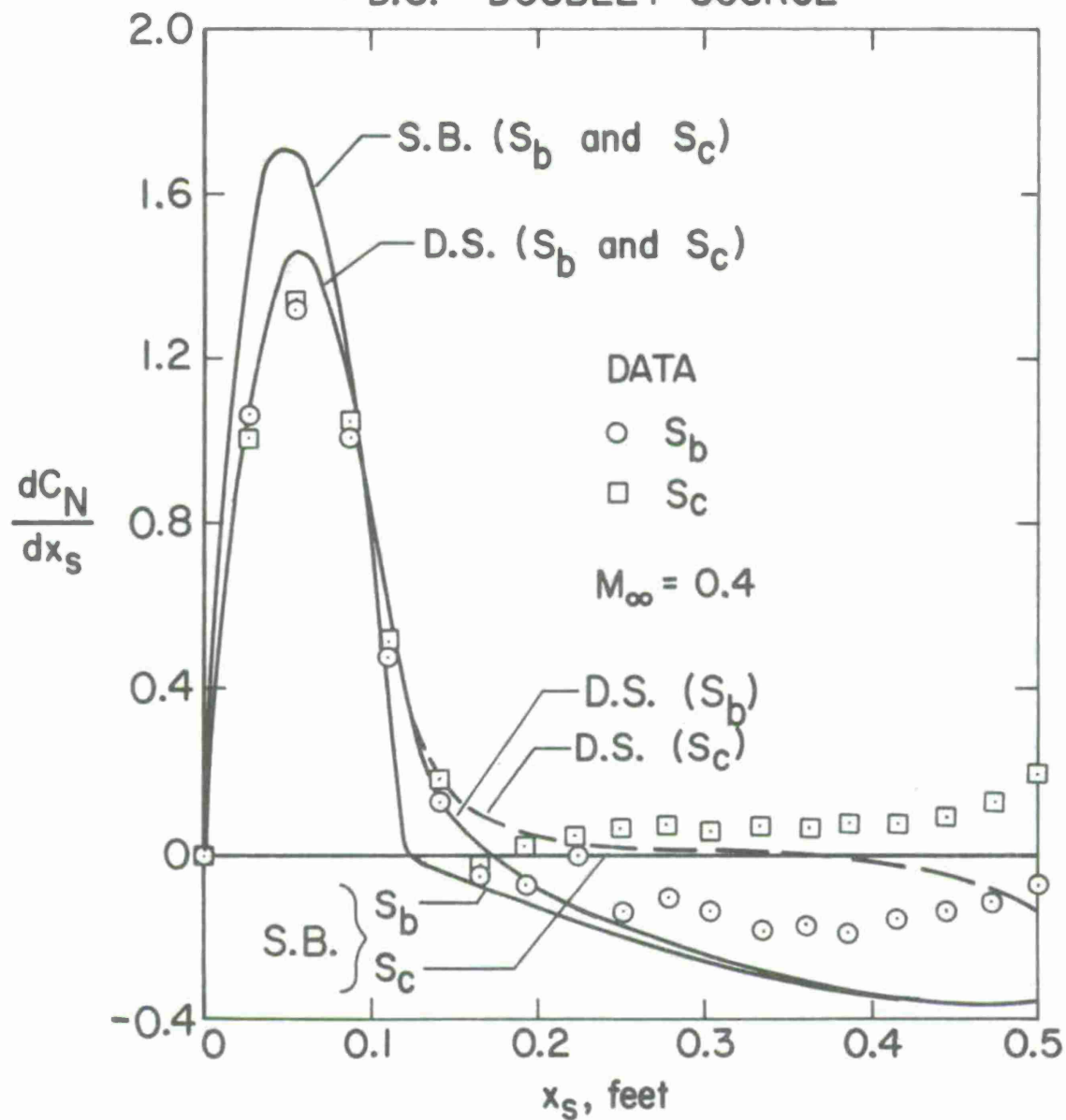
Figure 29.- Continued.



(c) Rolling-moment coefficients

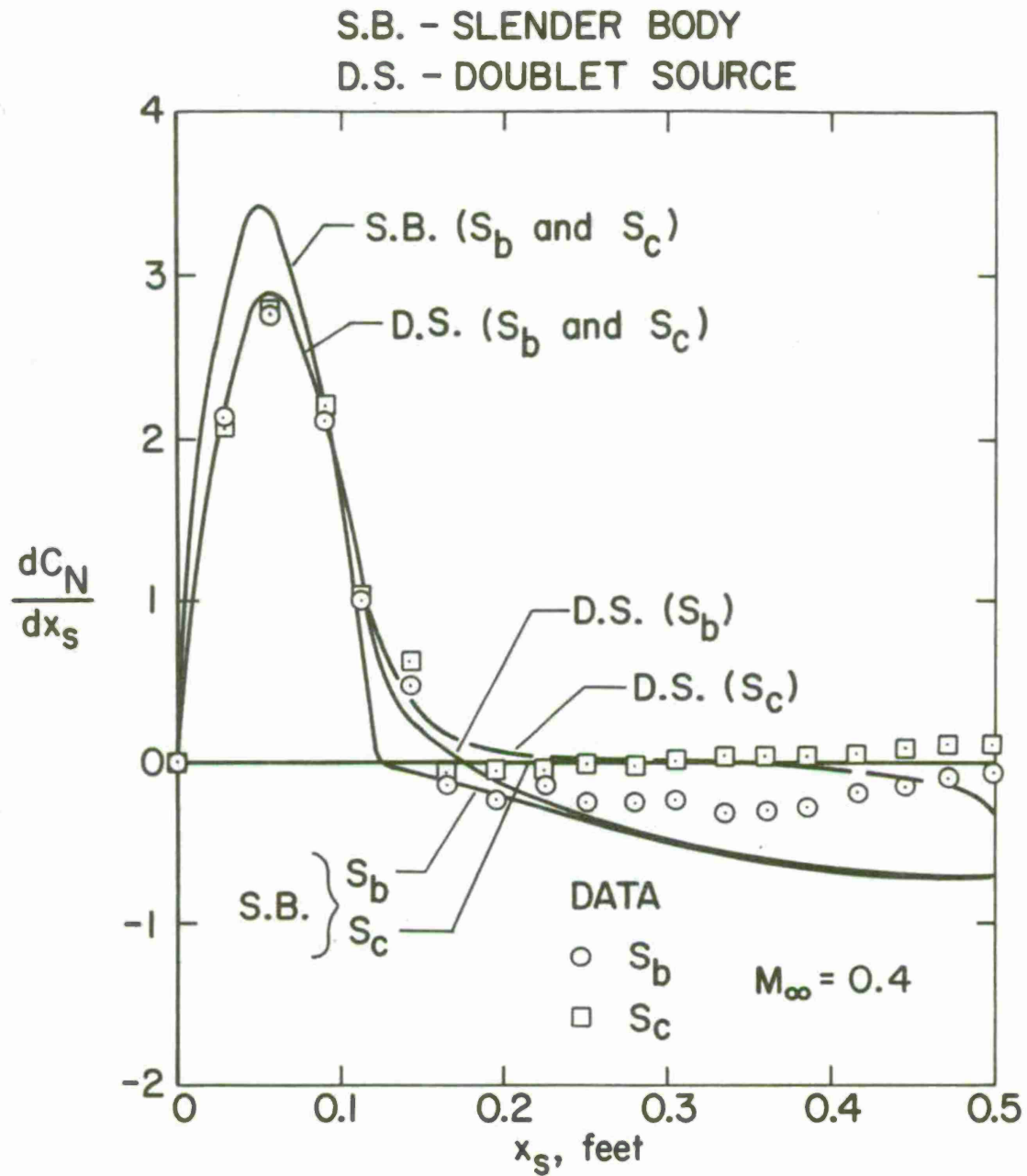
Figure 29.- Concluded.

S.B. - SLENDER BODY  
 D.S. - DOUBLET SOURCE



(a)  $\alpha = 4^\circ$ .

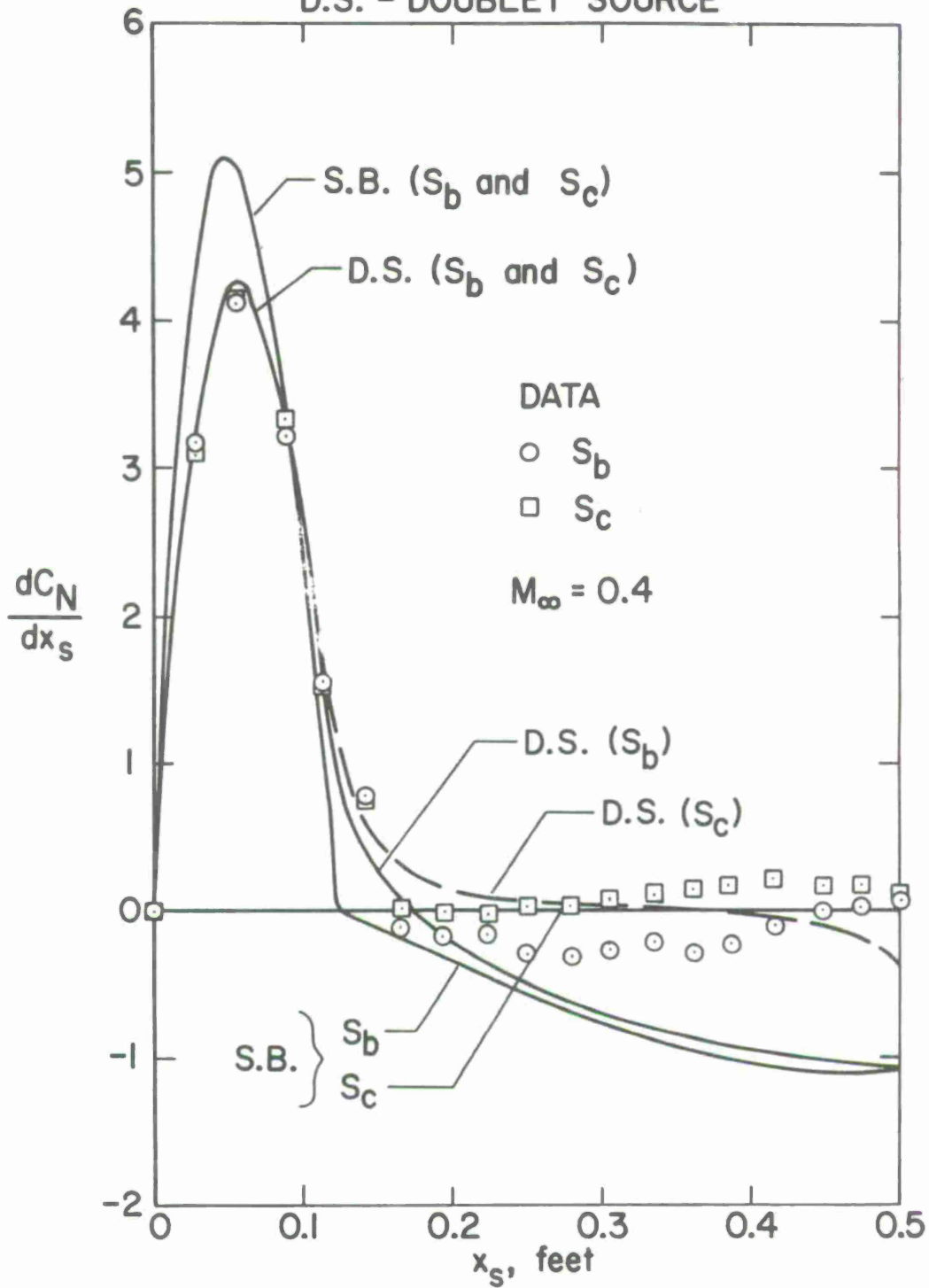
Figure 30.- Effects of store boattail on store loading in uniform flow.



(b)  $\alpha = 8^\circ$ .

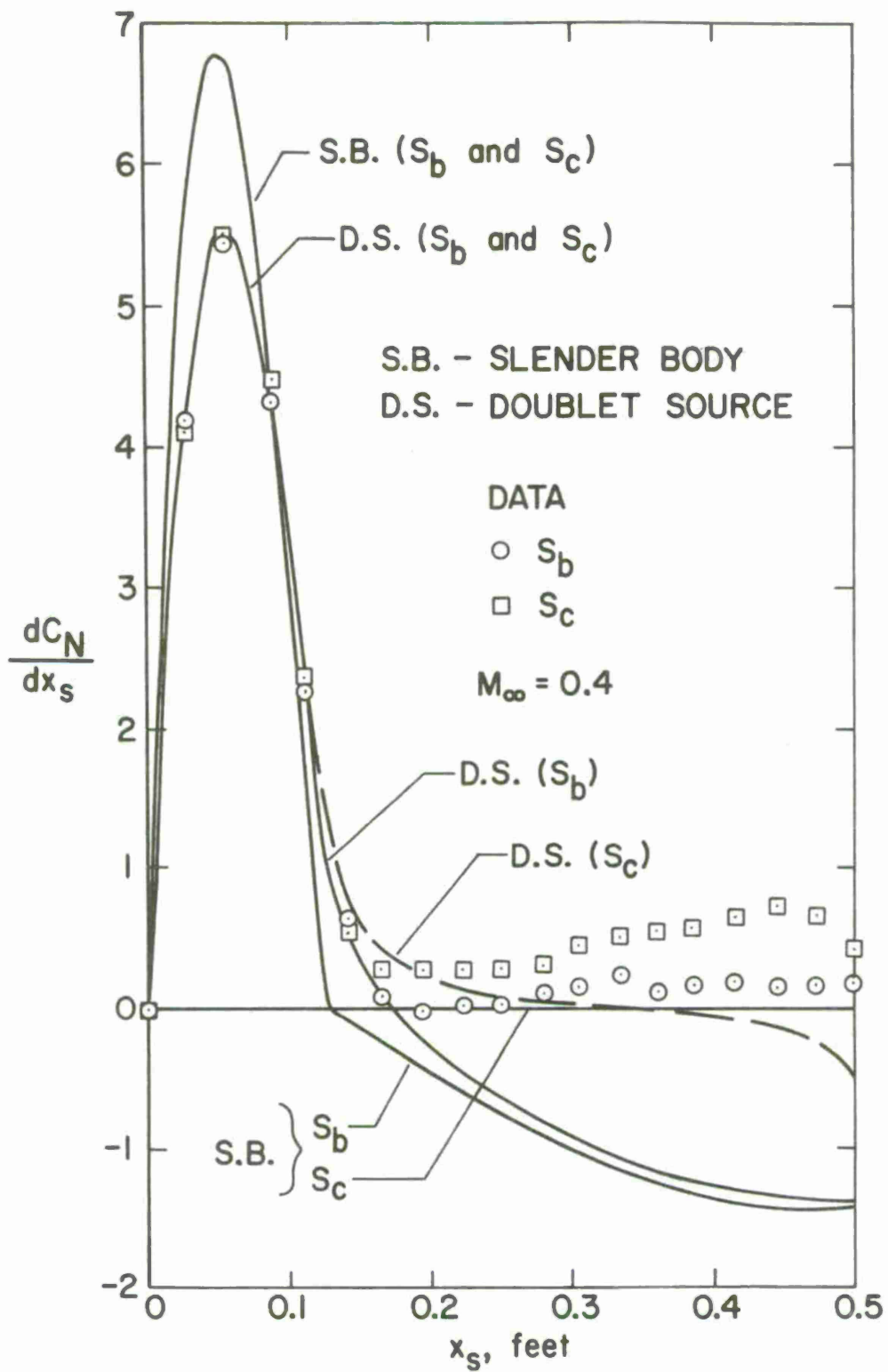
Figure 30.- Continued.

S.B. - SLENDER BODY  
 D.S. - DOUBLET SOURCE



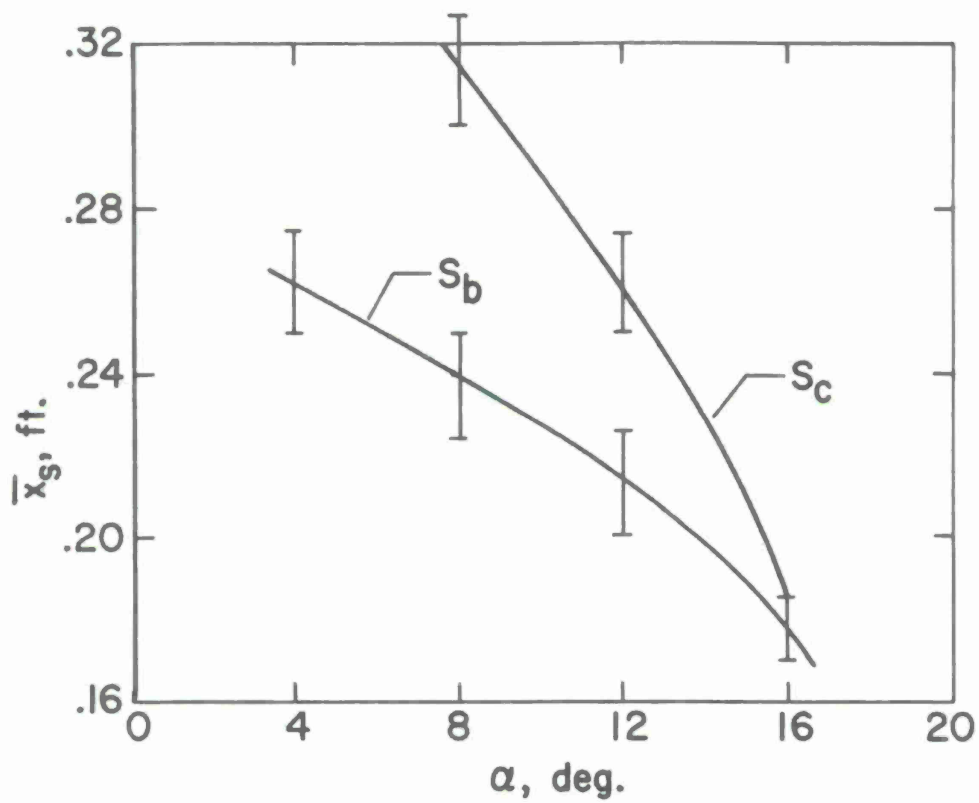
(c)  $\alpha = 12^\circ$ .

Figure 30.- Continued.

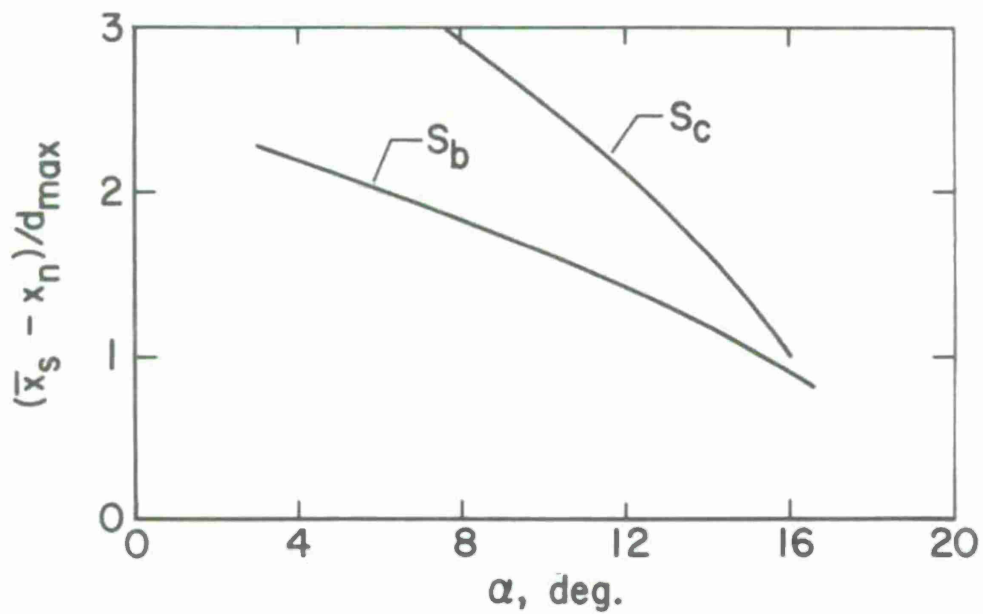


(d)  $\alpha = 16^\circ$ .

Figure 30.- Concluded.

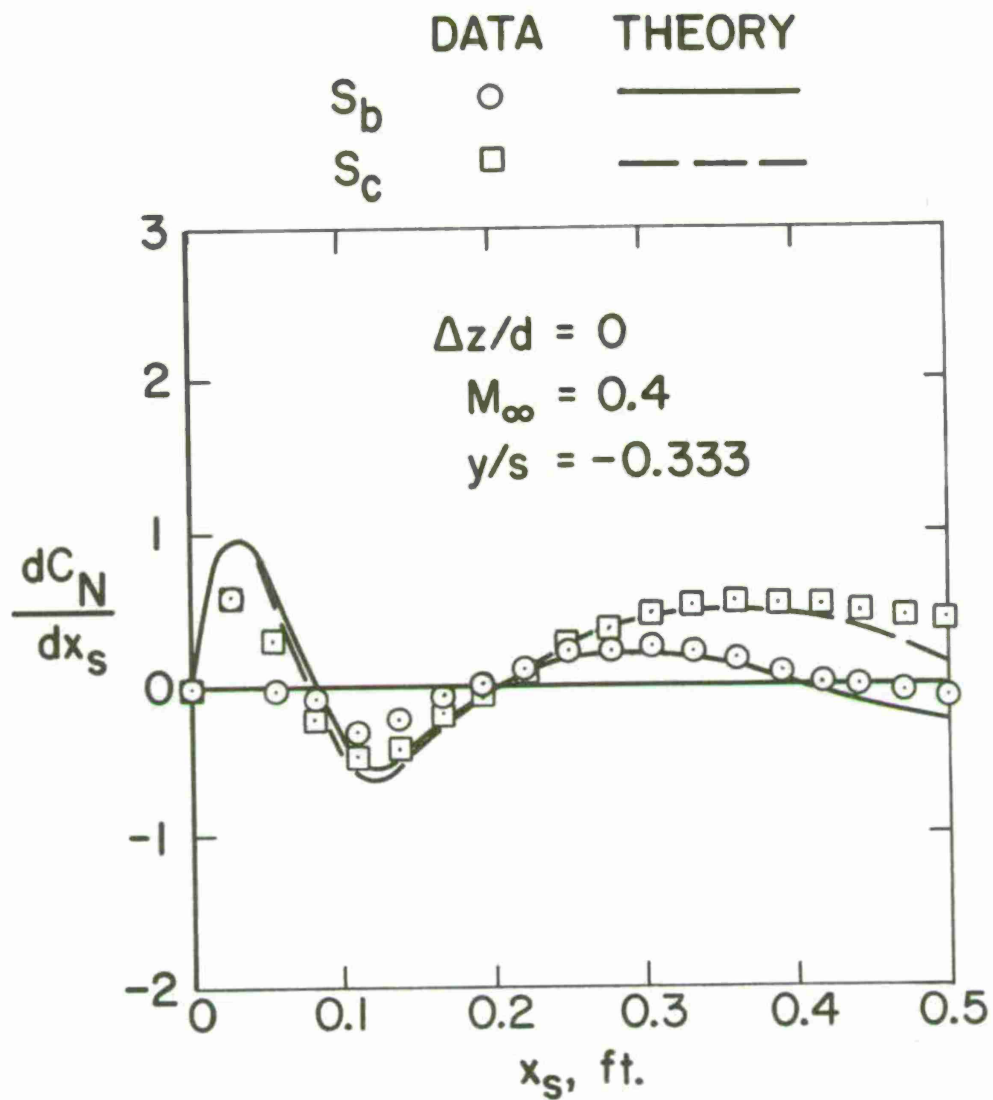


(a) Separation location.



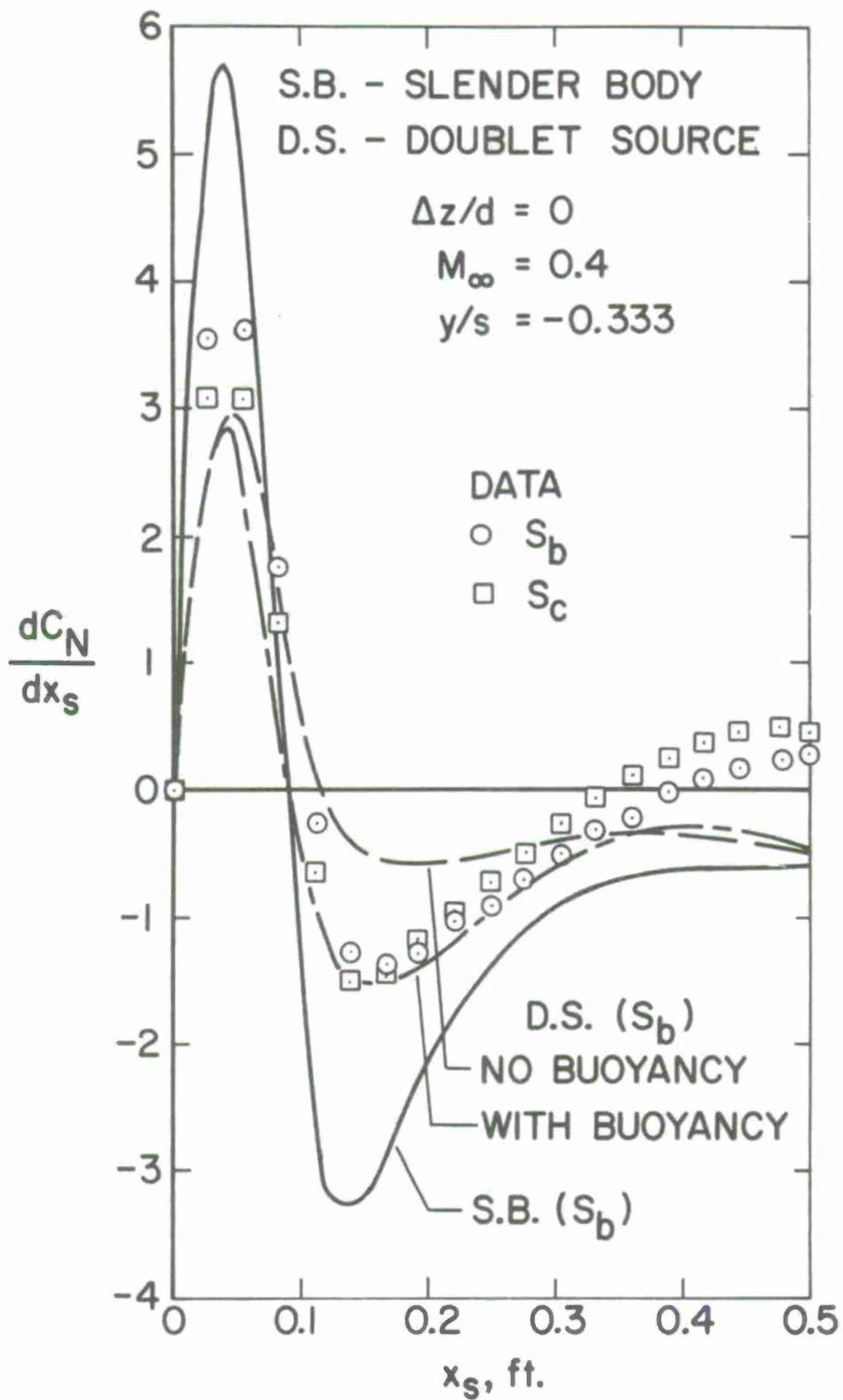
(b) Non-dimensional separation location.

Figure 31.- Effects of boattail on location of separation on store afterbody; uniform flow.



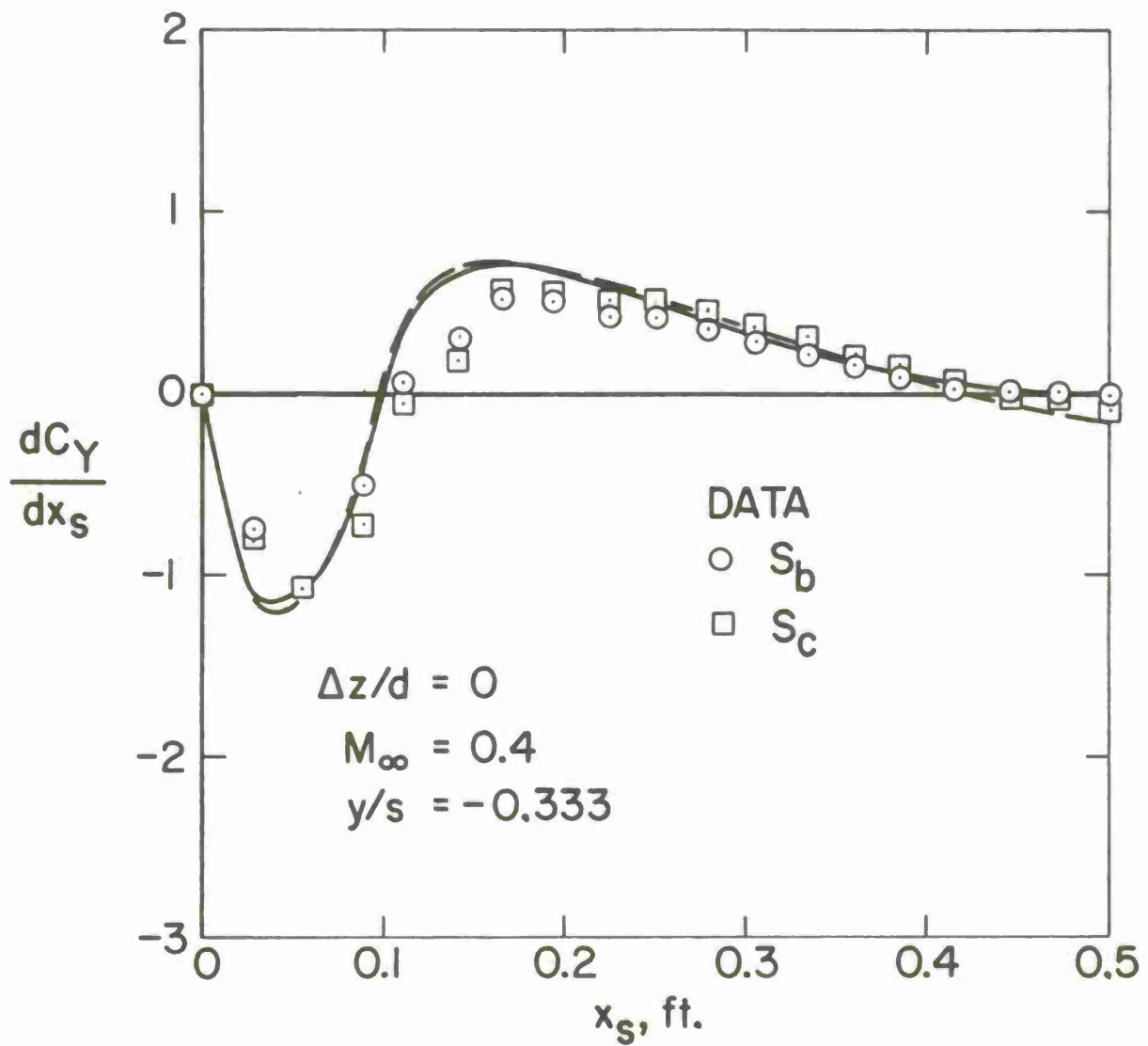
(a)  $\alpha = 4^\circ$ .

Figure 32.- Effects of boattail on normal-force distribution of store in presence of wing-body combination.



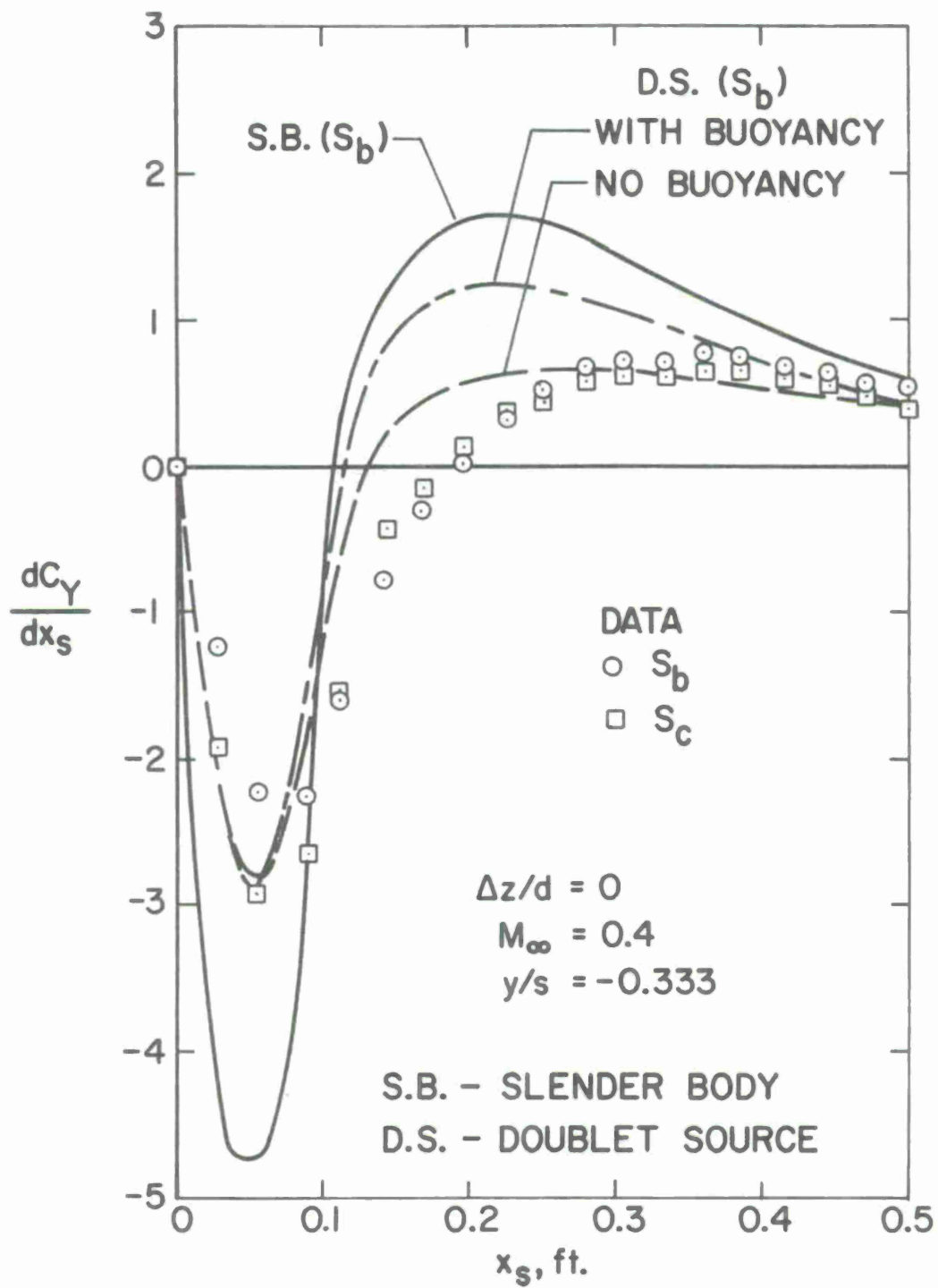
(b)  $\alpha = 16^\circ$ .

Figure 32.- Concluded.



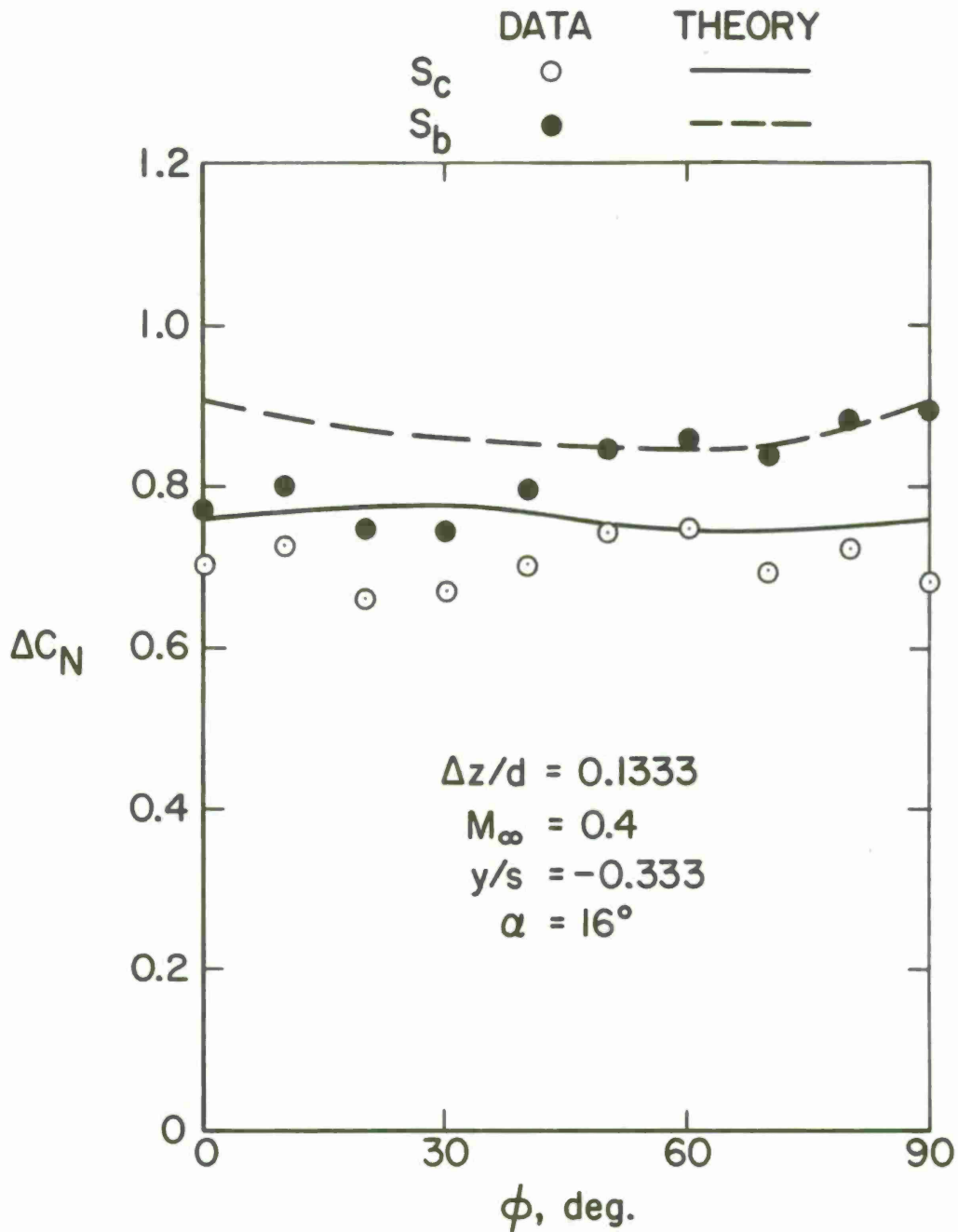
(a)  $\alpha = 4^\circ$ .

Figure 33.- Effects of boattail on side-force distribution of store in presence of wing-body combination.



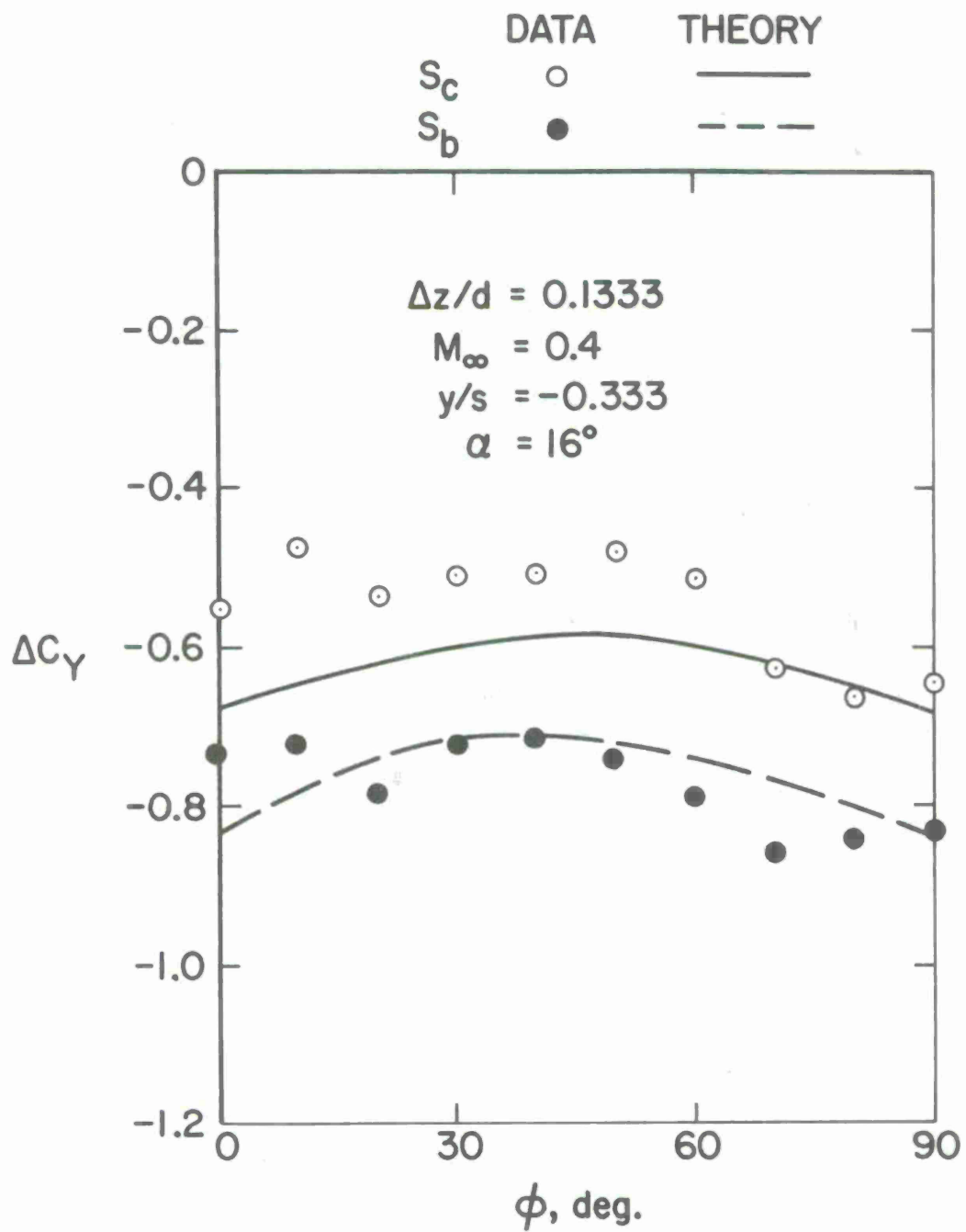
(b)  $\alpha = 16^\circ$ .

Figure 33.- Concluded.



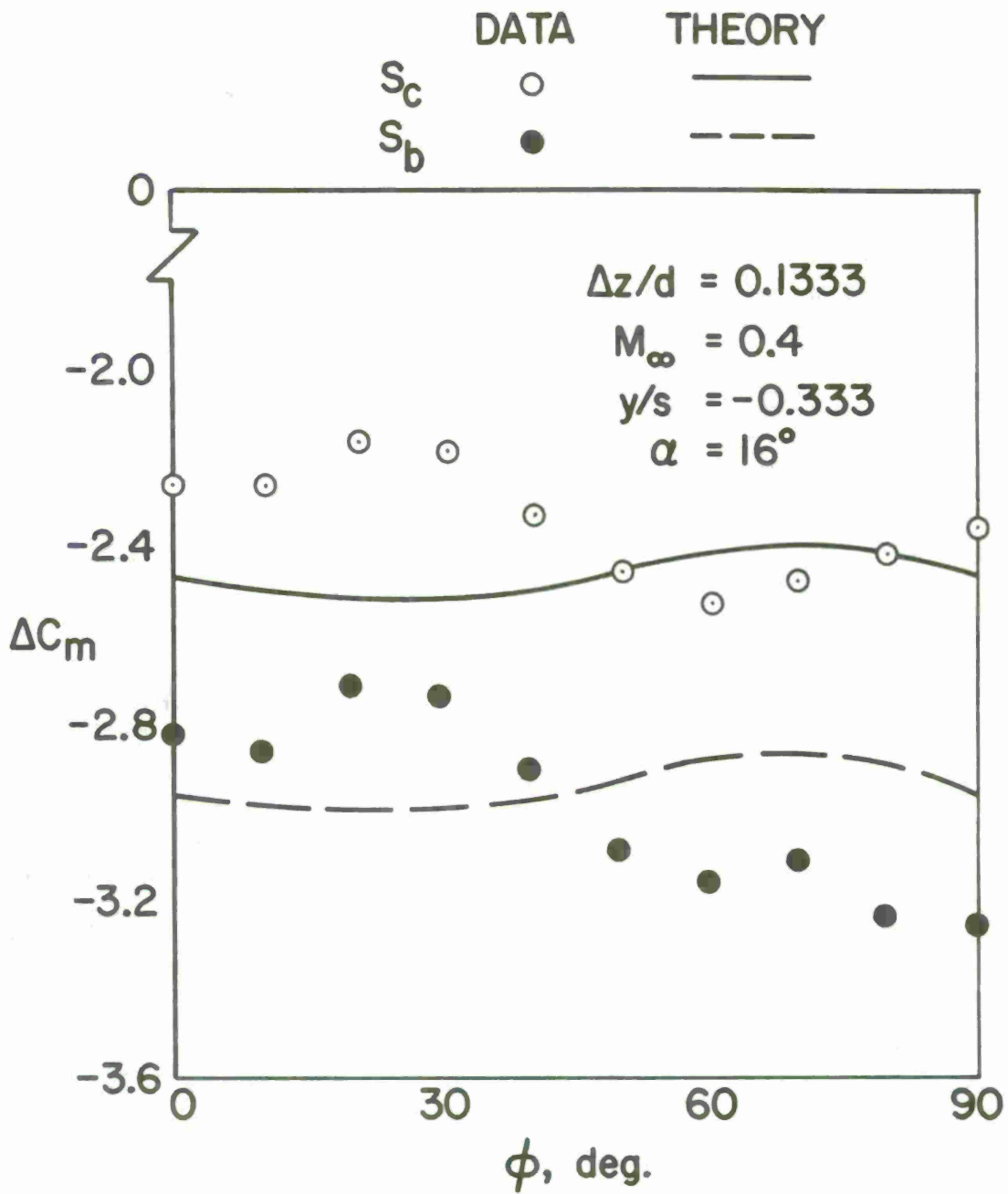
(a) Normal-force coefficient.

Figure 34.- Effects of boattail on the forces and moments due to the empennage (parent aircraft WBP).



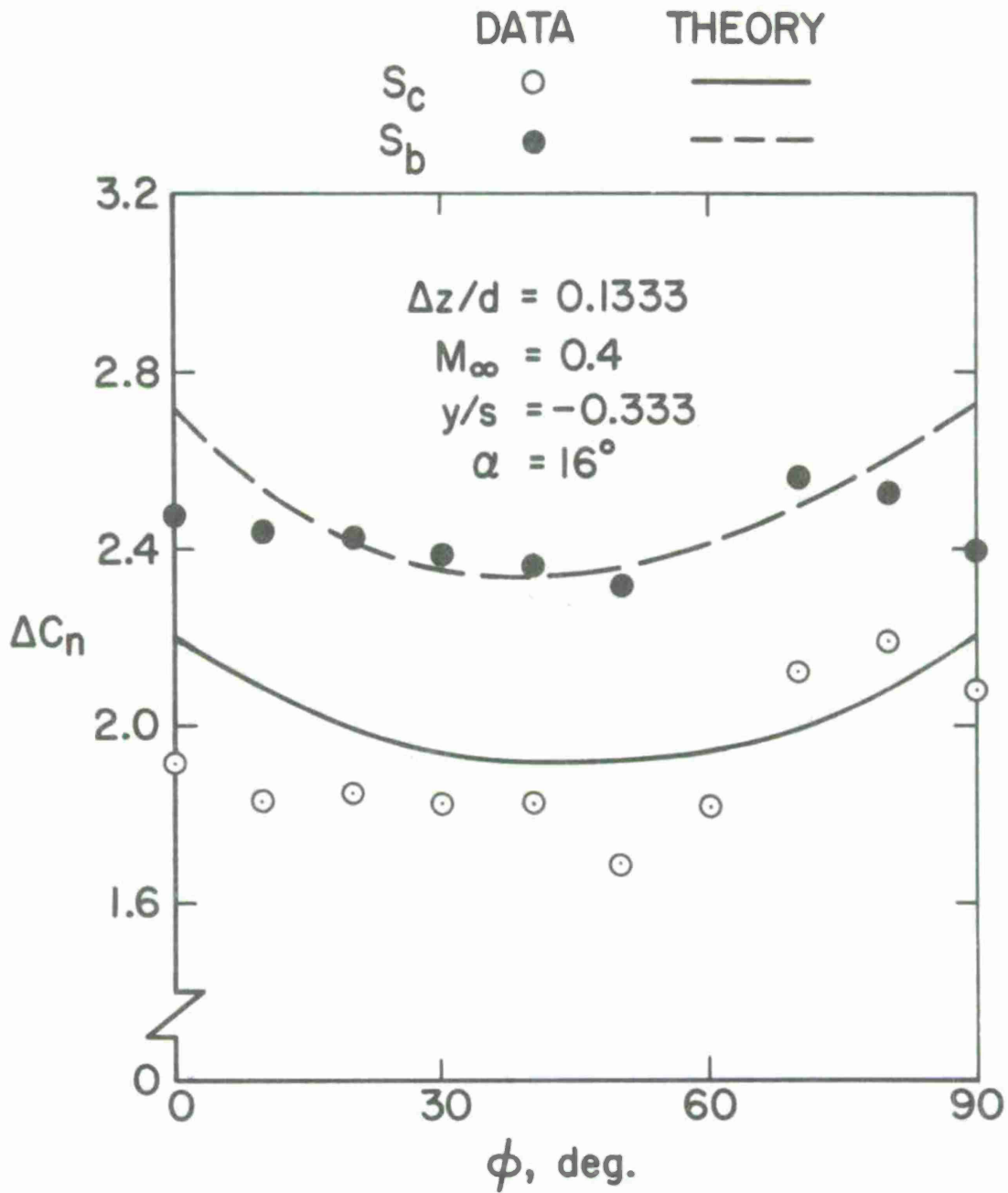
(b) Side-force coefficient.

Figure 34.- Continued.



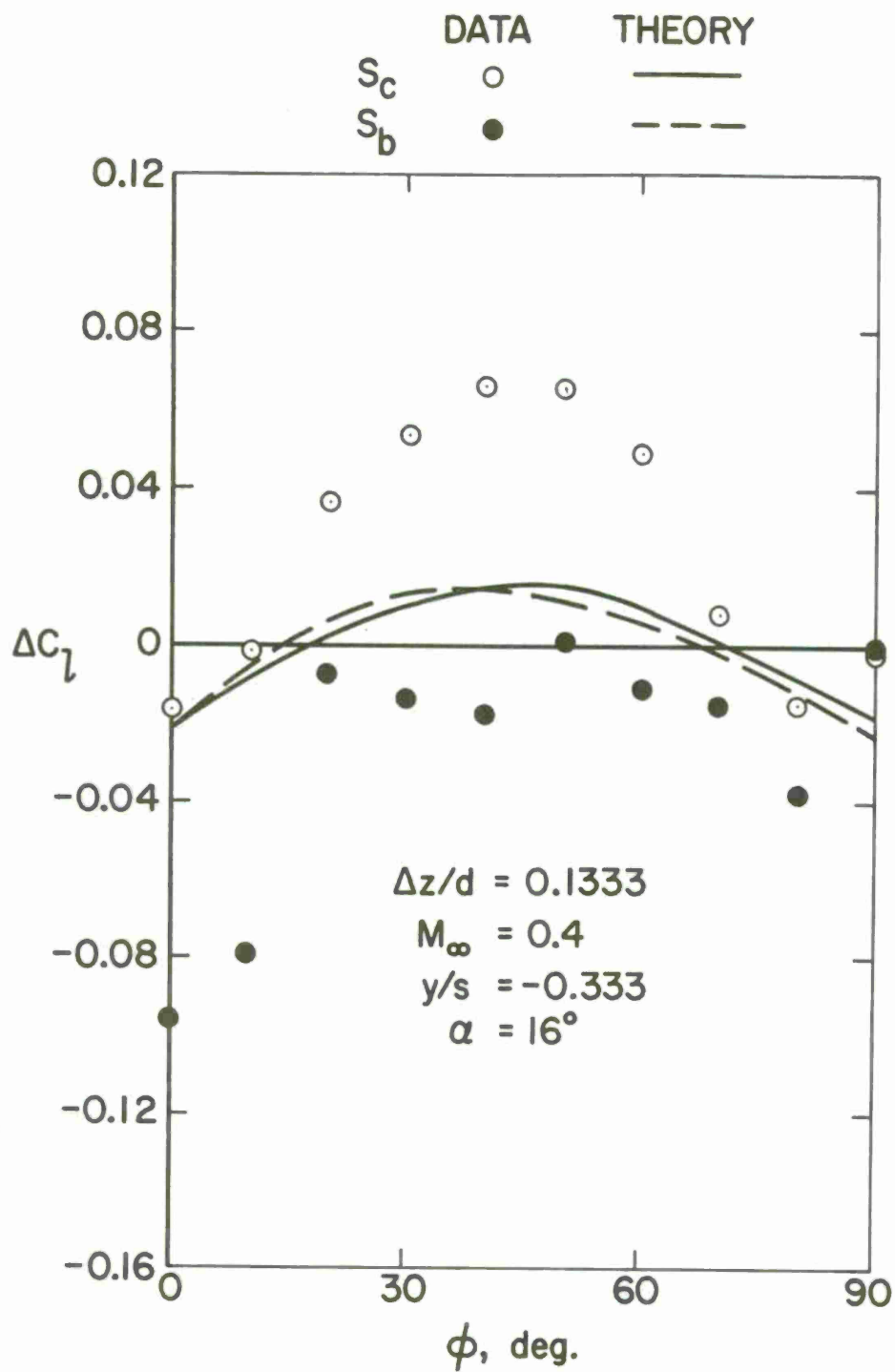
(c) Pitching-moment coefficient.

Figure 34.- Continued.



(d) Yawing-moment coefficient.

Figure 34.- Continued.



(e) Rolling-moment coefficient.

Figure 34.- Concluded.

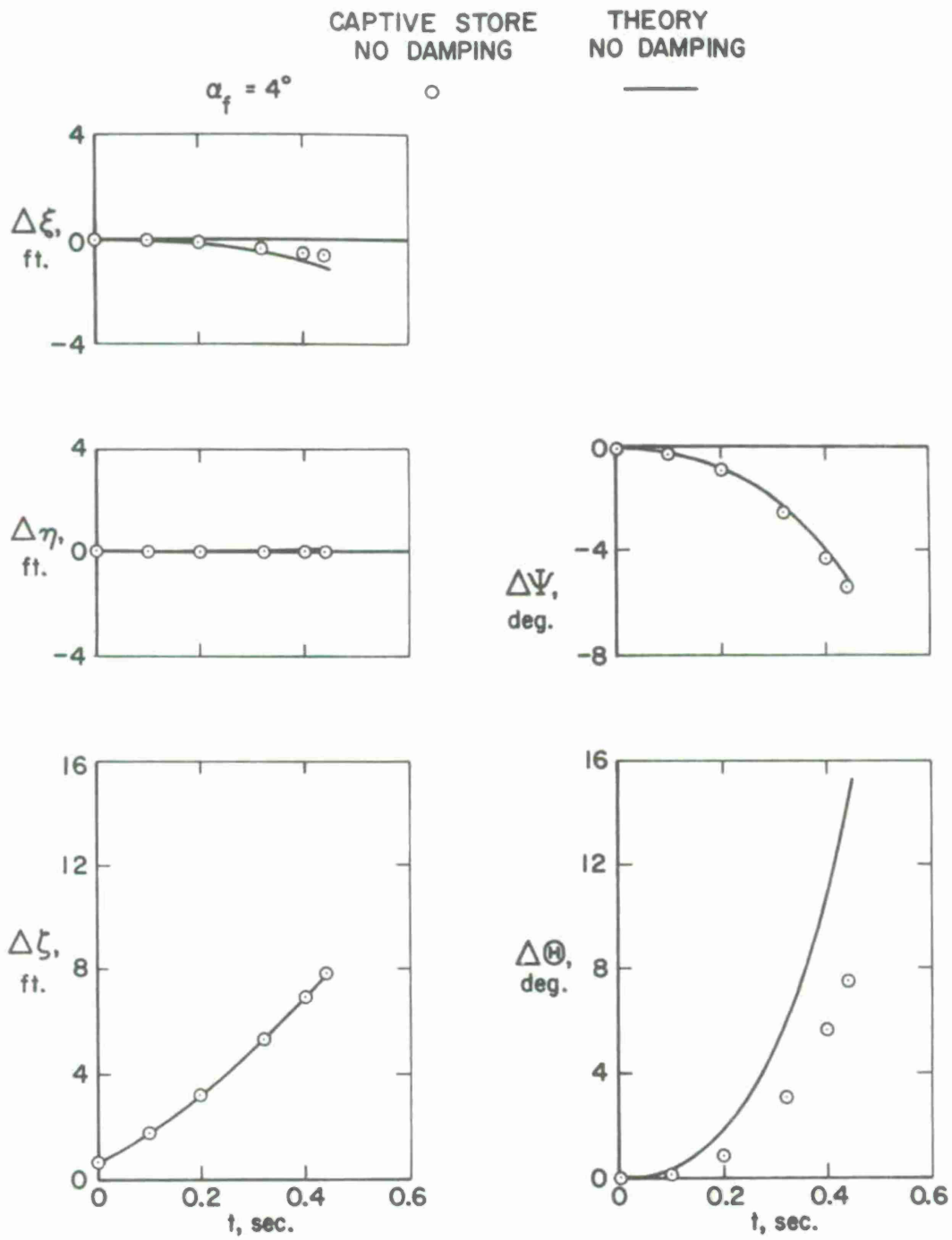


Figure 35.- Comparison between calculated trajectory and captive-store trajectory of store  $S_c$  released at one-third semispan location;  $M_\infty = 0.4$ .

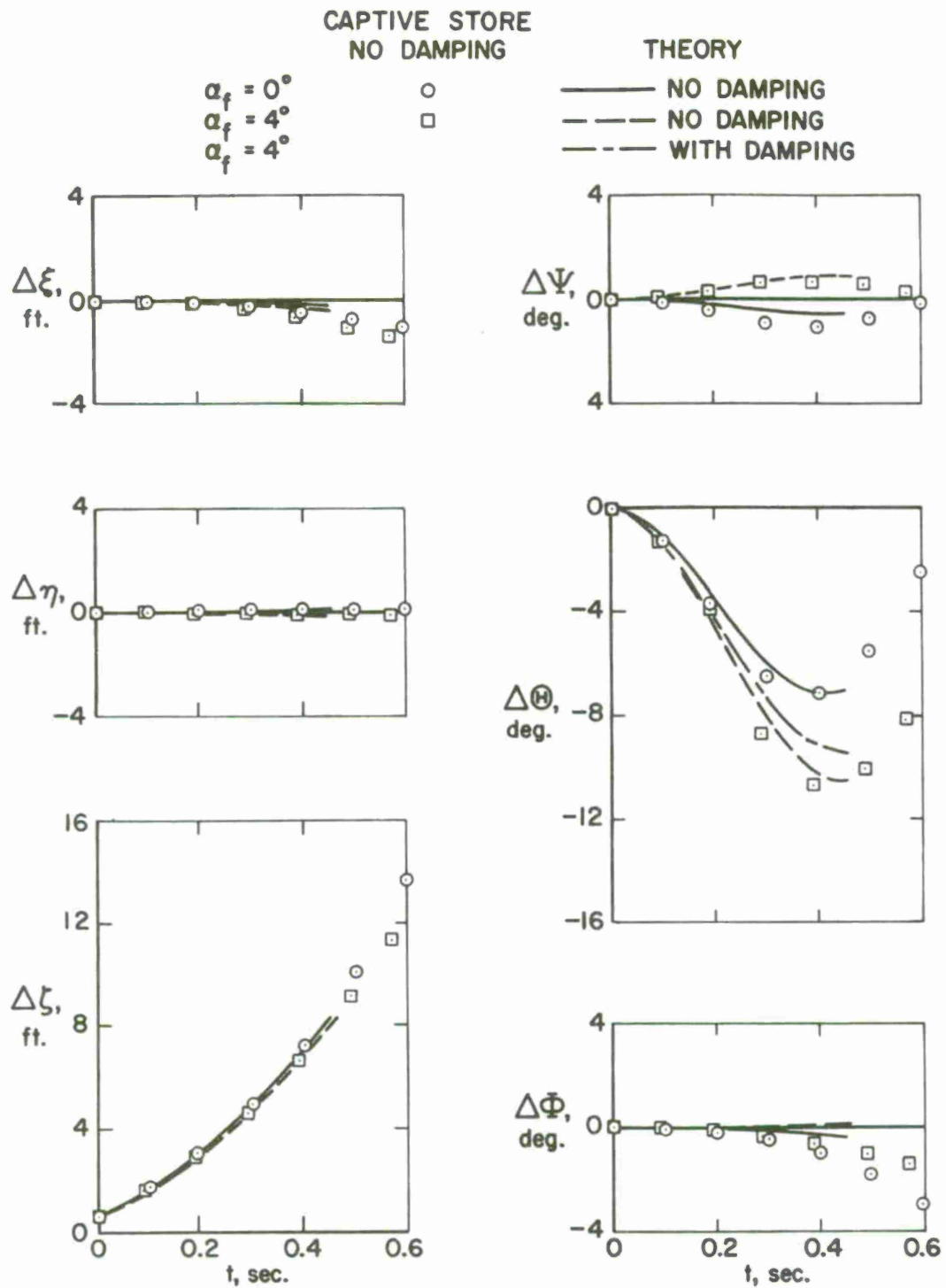


Figure 36.- Comparison between calculated trajectories and captive-store trajectories of store  $S_C$  with empennage released at one-third semispan location;  $M_\infty = 0.4$ .

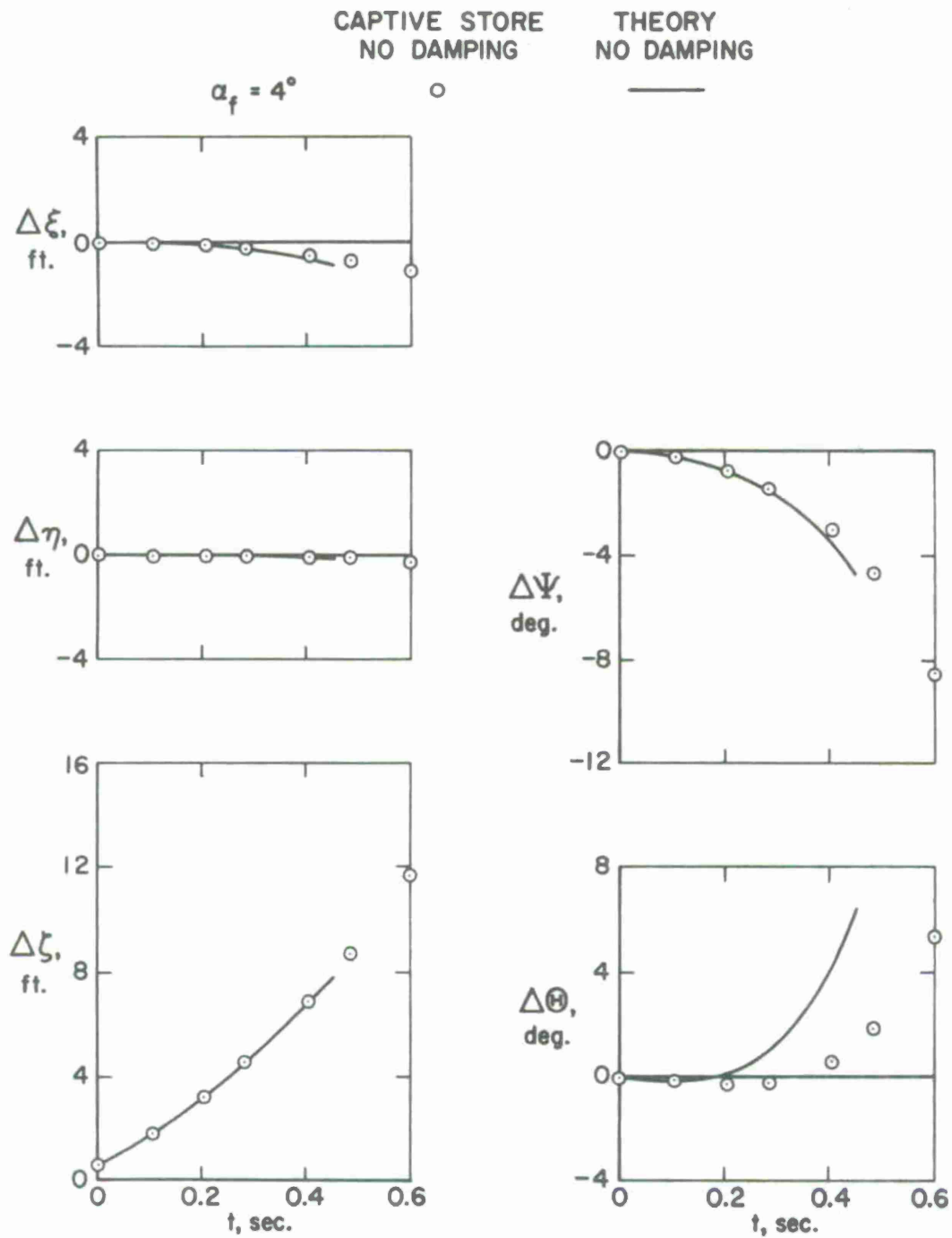


Figure 37.- Comparison between calculated trajectory and captive-store trajectory of finless store  $S_1$  released from TER group at one-third semispan location;  $M_\infty = 0.4$ .

## APPENDIX I

### CALCULATION OF FORCES AND MOMENTS DUE TO THE EMPENNAGE OF AN EXTERNAL STORE IN A NONUNIFORM AIRFLOW

#### I-1. INTRODUCTION

The empennage of an external store in a nonuniform airstream, as may occur under an aircraft, will develop forces and moments which affect its trajectory. While the forces on the body of the store can be determined using slender-body theory, the empennage is generally not slender so that a different approach is required. The approach here will be based on a combination of reverse flow theorems and slender body theory scaled for the effects of aspect ratio as done in wing-body interference theory (ref. 16). It will be possible to calculate all forces and moments except drag using a unified approach. The effects of interference between body and tail panels will be accounted for, and the method will be applicable to cases where vortices appear in the flow; for instance, vortices discharged from the body at a position in front of the empennage. Also planar, triform, and cruciform empennages are included within the framework of the method. However, the influence functions for triform empennages will not be worked out in this appendix. Only planar and cruciform empennages will be treated.

#### I-2. AXIS SYSTEM AND NOTATION

The coordinate system to be used in the empennage calculation is shown in figure 10 for the crossflow plane at which the empennage forces are assumed to act, the quarter-chord position of the mean aerodynamic chord of the exposed panels. This  $x_f, y_f, z_f$  system is fixed in the fins and oriented with respect to the store body coordinate system of figure 8 through the angle  $\phi_f$ . The  $x_f$  axis lies on the  $x_s$  axis. The angle  $\phi_f$  is specified in order that the tail fins can be other than vertical and horizontal at the beginning of a trajectory. Both coordinate systems are fixed in the store so that they translate and rotate with the store during the trajectory.

The cruciform fins are designated  $F_1, F_2, F_3,$  and  $F_4$  as shown in figure 10 with  $F_3$  and  $F_4$  missing for the planar case. The resultant velocity components normal to the four fins are designated  $W_1, W_2, V_1,$

and  $V_2$ , respectively, with positive directions as shown. They vary across the span of each fin. The procedure for calculating these normal velocities is as follows:

1. Specify panel coordinates ( $y_f$  or  $z_f$ ) where the normal velocities are to be obtained.
2. Transform these points to the store body coordinate system of figure 8.
3. Calculate the  $V_s$  and  $W_s$  velocities by the procedure described in section 5.1.
4. From  $V_s$  and  $W_s$  for each point determine the component normal to the fin.

The velocity determined in the above manner include terms accounting for the store translational motion and pitch and yaw rotation. The method of accounting for rolling motion will be discussed in section I-4 of this appendix.

### I-3. DETERMINATION OF NORMAL FORCE AND SIDE FORCE DUE TO EMPENNAGE

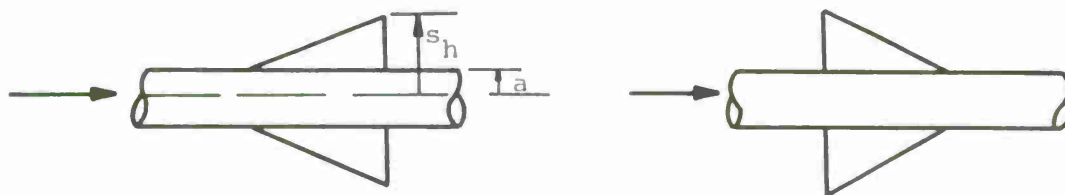
The normal force,  $Z_f$ , and side force,  $Y_f$ , due to the nonuniform flow field at the empennage is readily determined from reverse flow theorems. The calculation is identical whether the empennage is a planar one with panels lying on the  $y_f$  axis, or a cruciform one with panels on both the  $y_f$  and  $z_f$  axes. In determining  $Z_f$  for the planar case, we assume that the velocities  $W_1$  and  $W_2$  depend principally on  $y_f$  and that they vary slowly enough along the chordwise direction that they may be represented by an average value. Wind-tunnel measurements bear out this assumption. The values of  $W_1$  and  $W_2$  yield symmetrical and unsymmetrical angles of attack as follows:

$$\left. \begin{aligned} \alpha_s &= \frac{W_1(y_f) + W_2(-y_f)}{2V_{\infty s}} \\ \alpha_u &= \frac{W_1(y_f) - W_2(-y_f)}{2V_{\infty s}} \end{aligned} \right\} \quad (I-1)$$

where  $V_{\infty s}$  is the velocity of the store moment center which is assumed

equal to the resultant velocity at the points in question. The symmetrical part only produces  $Z_f$ , and the unsymmetrical part produces only rolling moment. By symmetry there is no effect of panels  $F_3$  and  $F_4$  in the production of normal force by panels  $F_1$  and  $F_2$ . However panel-panel interference is significant for rolling moment. The lack of panel-panel interference for  $Y_f$  and  $Z_f$  makes the calculation of these forces identical for planar and cruciform configuration.

Consider now a planar empennage with a circular body in direct flow and in reverse flow as shown.



Let  $S_B$  be the body planform area and  $S_H$  be the total planform area of both panels. Let  $P_d$  and  $\alpha_d$  be the pressure coefficient and local angle of attack in direct flow, and let  $P_r$  and  $\alpha_r$  be the corresponding quantities in reverse flow. Then by the reverse flow theorem (ref. 16, p. 221)

$$\iint_{S_B + S_H} P_r \alpha_d dS = \iint_{S_B + S_H} P_d \alpha_r dS \quad (\text{I-2})$$

Choose the following specific values of angles of attack and pressure coefficients

$$\alpha_d = 0 \quad \text{on} \quad S_B \quad \alpha_r = 0 \quad \text{on} \quad S_B$$

$$\alpha_d = \alpha_s \quad \text{on} \quad S_H \quad \alpha_r = 1 \quad \text{on} \quad S_H$$

$$P_d = P_d \quad P_r = P_1$$

Then

$$\iint_{S_H} P_d dS_H = \iint_{S_H} \alpha_s P_1 dS_H \quad (I-3)$$

Now the normal force on the horizontal panels in the presence of the body considering both upper and lower surfaces is

$$Z_{f,H(B)} = 2q_{\infty_s} \iint_{S_H} P_d dS = 4q_{\infty_s} \int_a^{s_h} \int_{l.e.}^{t.e.} \alpha_s P_1 dx_f dy_f \quad (I-4)$$

Let the span-load distribution in reversed flow be  $(cc_\ell)_1$  such that

$$(cc_\ell)_1 = 2 \int_{l.e.}^{t.e.} P_1 dx_f \quad (I-5)$$

Accordingly we have

$$Z_{f,H(B)} = 2q_{\infty_s} \int_a^{s_h} \alpha_s (cc_\ell)_1 dy_f \quad (I-6)$$

since  $\alpha_s$  depends only on  $y_f$ .

We now establish the amount of normal force carried over onto the body by virtue of the panel pressure field. For this case let

$$\alpha_d = 0 \quad \text{on } S_B \quad \alpha_r = 1 \quad \text{on } S_B$$

$$\alpha_d = \alpha_s \quad \text{on } S_H \quad \alpha_r = 0 \quad \text{on } S_H$$

$$P_d = P_d \quad P_r = P_2$$

Then

$$\iint_{S_B} P_d dS_B = \iint_{S_H} P_2 \alpha_s dS_H \quad (I-7)$$

The lift on the body due to the horizontal panels is now

$$Z_{f,B(H)} = 2q_{\infty_s} \iint P_d dS_B = 4q_{\infty_s} \int_a^{s_h} \int_{l.e.}^{t.e.} \alpha_s P_2 dx_f dy_f \quad (I-8)$$

Designating the span loading for this case by  $(cc_\ell)_2$  we have

$$(cc_\ell)_2 = 2 \int_{l.e.}^{t.e.} P_2 dx_f \quad (I-9)$$

so that

$$Z_{f,B(H)} = 2q_{\infty_s} \int_a^{s_h} \alpha_s (cc_\ell)_2 dy_f \quad (I-10)$$

The total normal force due to the empennage in the  $z_f$  direction is designated  $(Z_{BH} - Z_B)_f$  and is given by

$$\begin{aligned} (Z_{BH} - Z_B)_f &= Z_{f,H(B)} + Z_{f,B(H)} = 2q_{\infty_s} \int_a^{s_h} \alpha_s [(cc_\ell)_1 + (cc_\ell)_2] dy_f \\ &= 2q_{\infty_s} \int_a^{s_h} (cc_\ell)_3 \alpha_s dy_f \end{aligned} \quad (I-11)$$

where  $(cc_\ell)_3$  is the span-loading on the horizontal panel for the configuration in reverse flow with both body and panels at unit angle of attack.

In the application of equation (I-11) to the empennage, we now make an approximation which simplifies the calculation greatly with little loss of accuracy. If the value of  $(cc_\ell)_3$  from slender-body theory is used in equation (I-11), we obtain the slender-body approximation to the normal force. Since  $(cc_\ell)_3$  is the same in direct and reverse flow, it is easily obtained. However, we know that slender-body theory tends to overpredict the normal force by an amount which increases with the aspect ratio of the lifting surface formed by joining the exposed tail

panels together, the so-called tail alone. It has been found<sup>1</sup> that we can correct the slender body result for this aspect ratio effect by multiplying it by the ratio of the lift-curve slope of the tail alone on the basis of linear theory to that on the basis of slender-body theory. Let  $\left(\frac{dC_L}{d\alpha}\right)_H$  be the lift-curve slope of the horizontal surfaces joined together on the basis of linear theory with an arbitrary reference area  $S_R$ . Then the ratio of the lift-curve slopes  $\lambda_H$ , is simply

$$\lambda_H = \frac{\left(\frac{dC_L}{d\alpha}\right)_H S_R}{2\pi(s_h - a)^2} \quad (I-12)$$

Based on the same reference area, the normal force coefficient corrected for aspect ratio is

$$\left[ (C_Z)_{BH} - (C_Z)_B \right]_f = \frac{(Z_{BH} - Z_B)_f}{q_\infty S_R} = \frac{1}{\pi} \frac{\left(\frac{dC_L}{d\alpha}\right)_H}{(s_h - a)^2} \int_a^{s_h} \alpha_s (cc_\ell)_s dy_f \quad (I-13)$$

where  $(cc_\ell)_s$  is the slender-body theory span loading given by

$$(cc_\ell)_s = 4 \sqrt{\frac{(s_h^2 y_f^2 - a^4)(s_h^2 - y_f^2)}{s_h^2 y_f^2}} \quad (I-14)$$

from reference 16, equation (6-39). Equation (I-13) is valid provided  $C_Z$  and  $\left(\frac{dC_L}{d\alpha}\right)_H$  are based on the same reference area. If  $\left(\frac{dC_L}{d\alpha}\right)_H$  is per degree, then  $\alpha_s$  should be in degrees.

In application of equation (I-13) the velocities  $W_1(y_f)$  and  $W_2(-y_f)$  are determined from flow field calculations without the store present. Because of the store the values of  $W_1(y_f)$  and  $W_2(-y_f)$  will be enhanced by "Beskin upwash." Thus, if we assume the store is subject to a crossflow

---

<sup>1</sup>Pitts, W. C., Nielsen, J. N., and Kaattari, G. E.: "Lift and Center of Pressure of Wing-Body-Tail Combinations at Subsonic, Transonic, and Supersonic Speeds." NACA Rept. 1307, 1957.

$W_o$  (see fig. 10) on the plane of the horizontal panels, an additional upwash  $W_B(y_f)$  is obtained as follows

$$W_B(y_f) = W_o \frac{a^2}{y_f^2} \quad (I-15)$$

Accordingly, in the application of equation (I-13) the value of  $\alpha_s$  should be taken as

$$\alpha_s = \frac{W_1(y_f) + W_2(-y_f)}{2V_{\infty_s}} + \frac{W_o}{V_{\infty_s}} \frac{a^2}{y_f^2}; \quad a \leq y_f \quad (I-16)$$

The vertical fins produce a sideforce which can be calculated the same way as the normal force due to the horizontal fins. Let  $V_1(-z_f)$  be the sidewash velocity on the lower panel and  $V_2(z_f)$  be that on the upper panel. The sidewash angles  $\beta$  for the symmetrical and unsymmetrical parts of the flow are

$$\beta_s = \frac{V_1(-z_f) + V_2(z_f)}{2V_{\infty_s}} \quad \beta_u = \frac{V_1(-z_f) - V_2(z_f)}{2V_{\infty_s}} \quad (I-17)$$

The sideforce due to the addition of the vertical panels is then

$$\left[ (C_Y)_{BV} - (C_Y)_B \right]_f = \frac{1}{\pi} \frac{\left( \frac{dC_L}{d\alpha} \right)_V}{(s_v - a)^2} \int_a^{s_v} \beta_s (cc_l)_4 dz_f \quad (I-18)$$

$$(cc_l)_4 = 4 \sqrt{\frac{(s_v^2 z_f^2 - a^4)(s_v^2 - z_f^2)}{s_v^2 z_f^2}} \quad (I-19)$$

The value of  $\beta_s$  should be augmented for Beskin sidewash as follows:

$$\beta_s = \frac{V_2(z_f) + V_1(-z_f)}{2V_{\infty_s}} + \frac{V_o}{V_{\infty_s}} \frac{a^2}{z_f^2}; \quad a \leq z_f \quad (I-20)$$

In determining the contributions of the horizontal and vertical panels to the pitching moment  $M_{y_f}$  and yawing moment,  $M_{z_f}$ , respectively,

we assume that their respective loads are concentrated at the quarter-chord position of the mean aerodynamic chords of the exposed panels.

Let  $l_h$  be the distance from the store center of moments to the quarter chord of the MAC of the horizontal panels, and let  $l_v$  be the corresponding distance for the vertical panels (positive for fins behind the center of moments). The contribution of the horizontal panels to the pitching-moment coefficient is then

$$\left[ (C_m)_{BH} - (C_m)_B \right]_f = \frac{M_{Y_f}}{q_\infty S_R l_R} = - \left[ (C_Z)_{BH} - (C_Z)_B \right]_f \frac{l_h}{l_R} \quad (I-21)$$

The contribution of the vertical panels to the yawing moment coefficient is

$$\left[ (C_n)_{BV} - (C_n)_B \right]_f = \frac{M_{Z_f}}{q_\infty S_R l_R} = - \left[ (C_Y)_{BV} - (C_Y)_B \right]_f \frac{l_v}{l_R} \quad (I-22)$$

#### I-4. ROLLING MOMENT DUE TO EMPENNAGE

First consider the rolling moments due to the horizontal panels of the empennage as if no vertical panels existed. Such results will apply to a store with only two panels, the planar empennage case, because the presence of vertical panels does have the effect of reducing the rolling moment due to the horizontal panels. This panel-panel interference effect is treated subsequently for the curciform case.

The rolling moment due to the horizontal panels is associated with  $\alpha_u$  of equation (I-1). The asymmetric angle of attack is equivalent to positive control deflection of the right panel and negative deflection of the left panel to produce negative rolling moment in an aileron manner. In order to determine the rolling moment, consider an application of the reverse flow theorem, equation (I-2), with

$$\begin{aligned} \alpha_d &= 0 \quad \text{on } S_B & \alpha_r &= 0 \quad \text{on } S_B \\ \alpha_d &= \alpha_u \quad \text{on } S_H & \alpha_r &= y_f \quad \text{on } S_H \\ P_d &= P_d & P_r &= P_5 \end{aligned}$$

We find that

$$M_x = 2q_{\infty_s} \iint_{S_H} p_d y_f dS_H = -2q_{\infty_s} \iint_{S_H} \alpha_u p_s dS_H \quad (I-23)$$

since the body contributes no rolling moment. Let  $(cc_l)_s$  be the span loading on the body with horizontal panels in reverse flow. The local angle of attack  $\alpha_r = y_f$  can be reproduced by a roll rate of  $p = V_{\infty_s}$  about the  $x_f$  axis in the clockwise direction since the local angle of attack for such a condition is

$$\alpha_r = \frac{py_f}{V_{\infty_s}} \quad (I-24)$$

Since

$$(cc_l)_s = 2 \int_{l.e.}^{t.e.} p_s dx_f \quad (I-25)$$

we may write

$$M_x = -2q_{\infty_s} \int_a^{s_h} \alpha_u (cc_l)_s dy_f \quad (I-26)$$

The rolling-moment coefficient due to the horizontal panels is thus

$$(C_l)_H = \frac{M_x}{q_{\infty_s} S_R l_R} = -\frac{2}{S_R l_R} \int_a^{s_h} \alpha_u (cc_l)_s dy_f \quad (I-27)$$

where including the roll-damping term in equation (I-1)

$$\alpha_u = \frac{W_1(y_f) - W_2(-y_f)}{2V_{\infty_s}} + \frac{py_f}{V_{\infty_s}} \quad (I-28)$$

From equation (3-37) of reference 16,

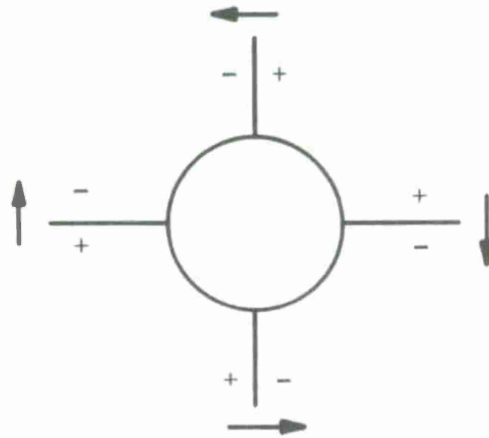
$$\begin{aligned}
(cc_l)_s = & \left( 1 + \frac{2}{\pi} \cos^{-1} \frac{2as_h}{s_h^2 + a^2} \right) \left( Y_f + \frac{a^2}{Y_f} \right) \sqrt{\frac{(s_h^2 - Y_f^2)(s_h^2 Y_f^2 - a^4)}{s_h^2 Y_f^2}} \\
& + \frac{2}{\pi} \left( Y_f - \frac{a^2}{Y_f} \right)^2 \cosh^{-1} \left[ \frac{(Y_f^2 + a^2)(s_h^2 - a^2)}{(Y_f^2 - a^2)(s_h^2 + a^2)} \right] \quad (I-29)
\end{aligned}$$

In order to scale  $(C_l)_H$  down from slender-body theory to linear theory, we apply the factor  $\lambda_H$  of equation (I-12) to obtain

$$(C_l)_H = -\frac{1}{\pi} \frac{\left( \frac{dC_L}{d\alpha} \right)_H}{(s_h - a)^2 \ell_R} \int_a^{s_h} \alpha_u (cc_l)_s dy_f \quad (I-30)$$

This formula will determine the rolling moment due to the horizontal panels neglecting any interference effects due to the vertical panels, the planar empennage case.

The interference effects due to the vertical panels on the rolling moment due to the horizontal panels can be shown by the following sketch.



Let the horizontal panels have an  $\alpha_u$  distribution for which positive pressure occurs on the upper surface of the right panel and suction pressure on its lower surface. The resulting panel force produces positive rolling moment. On the left panel the signs are all opposite, but positive rolling moment is generated. Consider now the right hand side of the upper panel which is undeflected. It will generally be subject

to a positive pressure field associated with the flow above the right panel with a negative pressure field on its left surface. The effect is a negative rolling moment which opposes that of the horizontal panels. The rolling moment due to the horizontal panels has thus been reduced by the presence of the undeflected upper panels by virtue of reversed roll developed by them through interference. It may also be argued that the presence of the vertical panel presents a dam between the first and second quadrants which inhibits communication between these positive and negative pressure regions, and that this pressure difference should therefore be increased by the presence of the vertical panels. While some increase in the rolling moment due to the horizontal panels may be ascribed to this factor, it is more than offset by the reverse rolling moment of the vertical panels on the basis of slender-body theory.

In order to determine the rolling moment of a cruciform configuration with distribution  $\alpha_u(y_f)$  on the horizontal panels and  $\beta_u(z_f)$  on the vertical panels, we write the reverse flow theorem for the vertical and horizontal panels with the body aligned in the free stream direction.

$$\iint_{S_H} \alpha_d P_r dS_H + \iint_{S_V} \beta_d P_r dS_V = \iint_{S_H} \alpha_r P_d dS_H + \iint_{S_V} \beta_r P_d dS_V \quad (I-31)$$

Choose the direct and reverse flow conditions as follows:

$$\alpha_d = \alpha_u \quad \alpha_r = y_f$$

$$\beta_d = \beta_u \quad \beta_r = z_f$$

$$P_d = P_d \quad P_r = P_e$$

$$\iint_{S_H} \alpha_u P_e dS_H + \iint_{S_V} \beta_u P_e dS_V = \iint_{S_H} y_f P_d dS_H + \iint_{S_V} z_f P_d dS_V \quad (I-32)$$

In the integrals of equations (I-31) and (I-32) the integrals have the same signs because an upper vertical panel set to produce a positive  $\beta_u$  would have a positive  $\alpha_u$  if rolled 90 degrees clockwise without a change of setting. For the reverse flow configuration with  $\alpha_r = y_f$ ,

the horizontal surfaces generate negative rolling moment (counterclockwise looking forward) and the same is true for the vertical surface with

$\beta_r = z_f$ . Accordingly

$$\begin{aligned}
 M_x &= 2q_{\infty s} \iint_{S_H} y_f P_d dS_H + 2q_{\infty s} \iint_{S_V} z_f P_d dS_V \\
 &= -4q_{\infty s} \int_a^{s_h} \int_{l.e.}^{t.e.} \alpha_u P_e dx_f dy_f - 4q_{\infty s} \int_a^{s_v} \int_{l.e.}^{t.e.} \beta_u P_e dx_f dz_f
 \end{aligned}
 \tag{I-33}$$

At this point, consider the vertical and horizontal panels to be of identical planform so that

$$M_x = -4q_{\infty s} \int_a^{s_h} (\alpha_u + \beta_u) \int_{l.e.}^{t.e.} P_e dx_f dy_f
 \tag{I-34}$$

In the above expression  $\beta_u$  is evaluated with  $z_f$  equal to  $y_f$ . Let the span loading for the reverse flow case above be

$$(cc_\ell)_e = 2 \int_{l.e.}^{t.e.} P_e dx_f
 \tag{I-35}$$

so that the rolling-moment coefficient due to both horizontal and vertical panels is

$$(C_\ell)_{HV} = \frac{M_x}{q_{\infty s} S_R \ell_R} = \frac{-2}{S_R \ell_R} \int_a^{s_h} (\alpha_u + \beta_u) (cc_\ell)_e dy_f
 \tag{I-36}$$

The quantity  $\alpha_u$  is given by equation (I-28) and  $\beta_u$  is obtained from equation (I-17) by including the roll-damping term

$$\beta_u = \frac{V_1(-z_f) - V_2(z_f)}{2V_{\infty s}} + \frac{pz_f}{V_{\infty s}}
 \tag{I-37}$$

Equation (I-36) is completely analogous to equation (I-27) for the rolling moment due to the panels of a planar configuration. In this case  $(cc_\ell)_e$  is the span loading on the panels of a cruciform configuration rolling in a clockwise direction facing forward at a rate equal to  $p$  radians per second. The slender-body theory yields<sup>2</sup>

$$(cc_\ell)_e = \frac{8R^2}{\pi} \left[ \cos 2\theta \tanh^{-1} \left( \frac{\sin 2\theta}{\sin 2\gamma} \right) - \cos 2\gamma \tanh^{-1} \left( \frac{\tan 2\theta}{\tan 2\gamma} \right) \right] + \frac{4R^2}{\pi} \left[ K(k_1) \sin 4\theta - 2k_1 \cos A_1 K(k_1) Z(A_1, k_1) \right] \quad (I-38)$$

where

$$R = \frac{1}{2} \sqrt{s^2 + \frac{a^4}{s^2}} \quad (I-39)$$

$$\cos 2\theta = \frac{1}{4R^2} \left( Y_f^2 + \frac{a^4}{Y_f^2} \right) = \frac{s_h^2}{Y_f^2} \frac{(a^4 + Y_f^4)}{(a^4 + s_h^4)} \quad (I-40)$$

$$\cos 2\gamma = \frac{a^2}{2R^2} \quad (I-41)$$

$$k_1 = \sin 2\gamma \quad (I-42)$$

$$K(k_1) = \int_0^{\pi/2} \frac{d\bar{z}}{\sqrt{1-k_1^2 \sin^2 \bar{z}}} = \text{complete elliptic integral of first kind with modulus } k_1 \quad (I-43)$$

$$A_1 = \sin^{-1} \left( \frac{\sin 2\theta}{\sin 2\gamma} \right) \quad (I-44)$$

$$Z(A_1, k_1) = \text{Jacobi zeta function} \quad (I-45)$$

---

<sup>2</sup>Adams, G. J. and Dugan, D. W.: Theoretical Damping in Roll and Rolling Moment Due to Differential Wing Incidence for Slender Cruciform Wings and Wing-Body Combinations.: NACA Rept. 1088, 1952, Eq. (18).

$$K(k_1) Z(A_1, k_1) = K(k_1) E(A_1, k_1) - E(\pi/2, k_1) F(A_1, k_1) \quad (I-46)$$

$$F(A_1, k_1) = \int_0^{A_1} \frac{d\bar{z}}{\sqrt{1-k_1^2 \sin^2 \bar{z}}} = \text{incomplete elliptic integral of the first kind}$$

$$E(\pi/2, k_1) = \int_0^{\pi/2} \sqrt{1-k_1^2 \sin^2 \bar{z}} d\bar{z} = \text{complete elliptic integral of second kind} \quad (I-48)$$

$$E(A_1, k_1) = \int_0^{A_1} \sqrt{1-k_1^2 \sin^2 \bar{z}} d\bar{z} = \text{incomplete elliptic integral of second kind} \quad (I-49)$$

In equation (I-37) as  $\theta \rightarrow \gamma$ , that is,  $y_f \rightarrow a$ , the first of the two principal terms becomes indeterminate. It is possible to show that

$$\begin{aligned} \lim_{\theta \rightarrow \gamma} \left[ \cos 2\theta \tanh^{-1} \left( \frac{\sin 2\theta}{\sin 2\gamma} \right) - \cos 2\gamma \tanh^{-1} \left( \frac{\tan 2\theta}{\tan 2\gamma} \right) \right] \\ \rightarrow -\cos 2\gamma \log (\cos 2\gamma) \end{aligned} \quad (I-50)$$

Thus, the span loading at the juncture between the panel and body,  $y_f = a$ , is

$$(cc_\ell)_e = \frac{8R^2}{\pi} \left[ -\cos 2\gamma \log (\cos 2\gamma) + 0.5 K(k_1) \sin 4\theta \right] \quad (I-51)$$

As equation (I-36) stands it yields the rolling moment coefficient on the basis of slender-body theory. To obtain the linear theory estimate, we must multiply the right-hand side by  $\lambda_H$  from equation (I-12) to obtain

$$(C_\ell)_{HV} = -\frac{1}{\pi} \frac{\left( \frac{dC_L}{d\alpha} \right)_H}{(s-a)^2 \ell_R} \int_a^{s_h} (\alpha_u + \beta_u) (cc_\ell)_e dy_f \quad (I-52)$$

While the fraction of  $C_l$  associated with  $\alpha_u$  or  $\beta_u$  can be considered due to asymmetrical flow condition on the panels in question, the effect of any one set of panels is manifest by pressures on both sets of panels.

## APPENDIX II

### EQUATIONS OF MOTION OF A RIGID BODY WITH MASS AND INERTIA ASYMMETRIES

#### II-1. INTRODUCTION

The purpose of this appendix is to present the derivation of the equations of motion of a rigid body with mass and inertia asymmetries. By mass asymmetry we mean that the center of mass is not at the origin of the coordinate system fixed in the body and used in the equations of motion. Generally the external store will have axes of geometrical symmetry which will be used in determining the forces and moments acting on it, but the center of mass in certain applications will not lie on these axes of symmetry. By inertia asymmetry, we mean that the principal axes of inertia do not coincide with the geometric axes of symmetry of the store. For these geometric axes, the tensor of inertia will thus possess off-diagonal terms, the so-called products of inertia.

#### II-2. AXIS SYSTEMS AND EULERIAN ANGLES

In the derivation of the equations of motion consider first an inertial set of axes,  $(\xi, \eta, \zeta)$ , fixed in the aircraft which is in rectilinear flight at uniform velocity. Then a system of axes  $(x, y, z)$  fixed in the store is defined. The  $x$  axis is forward along the store longitudinal axis, the  $y$  axis is positive to the right looking forward, and the  $z$  axis is vertical downward so that a right-handed system exists. The  $\xi, \eta, \zeta$  system is an airplane fixed system with  $\xi$  measured forward along the fuselage longitudinal axis,  $\eta$  laterally to the right and,  $\zeta$  vertically downward. The origin is at the fuselage nose.

In order to determine the orientation of the store with respect to the  $\xi, \eta, \zeta$  axes, a system of angles will be introduced. The system of angles to be used is that shown in figure 9. The origins of the inertial and store axis systems are taken at the same point to show the angular orientation. The system consists of three rotations in the yaw, pitch, roll sequence. This order is important. The three angles will be designated

$\Psi$  yaw  
 $\theta$  pitch  
 $\phi$  roll

### II-3. DIFFERENTIAL EQUATIONS FOR THE ORIENTATION ANGLES

In specifying the position and orientation of the store relative to the aircraft, we will determine the coordinates  $\xi$ ,  $\eta$ , and  $\zeta$  of the origin of the  $x$ ,  $y$ ,  $z$  coordinate system and the angular quantities  $\Psi$ ,  $\theta$ , and  $\phi$ . The equations of motion will, however, be written in terms of the following quantities and their time derivatives  $\dot{\xi}$ ,  $\dot{\eta}$ ,  $\dot{\zeta}$ ,  $p$ ,  $q$ ,  $r$ . Here  $p$ ,  $q$ , and  $r$  are the components of the store angular velocity about the  $x$ ,  $y$ , and  $z$  axes, respectively. A set of differential equations is required for  $\Psi$ ,  $\theta$ , and  $\phi$  in terms of  $p$ ,  $q$ , and  $r$  which are to be integrated along with the equations of motion to keep track of the angular orientation of the store. These equations are from reference 15.

$$\dot{\Psi} = (q \sin \phi + r \cos \phi) / \cos \theta$$

$$\dot{\theta} = q \cos \phi - r \sin \phi \quad (\text{II-1})$$

$$\dot{\phi} = p + q \sin \phi \tan \theta + r \cos \phi \tan \theta$$

With initial values of the orientation parameters  $\Psi$ ,  $\theta$ , and  $\phi$ , the foregoing equation can be integrated to obtain the variations of these quantities with time.

From the values of  $\Psi$ ,  $\theta$ , and  $\phi$  it is possible to determine the orientation of the  $x$ ,  $y$ ,  $z$  axes with respect to the  $\xi$ ,  $\eta$ ,  $\zeta$  in the usual direction cosine way. That is

$$\begin{bmatrix} \xi \\ \eta \\ \zeta \end{bmatrix} = [A] \begin{bmatrix} x \\ y \\ z \end{bmatrix}$$

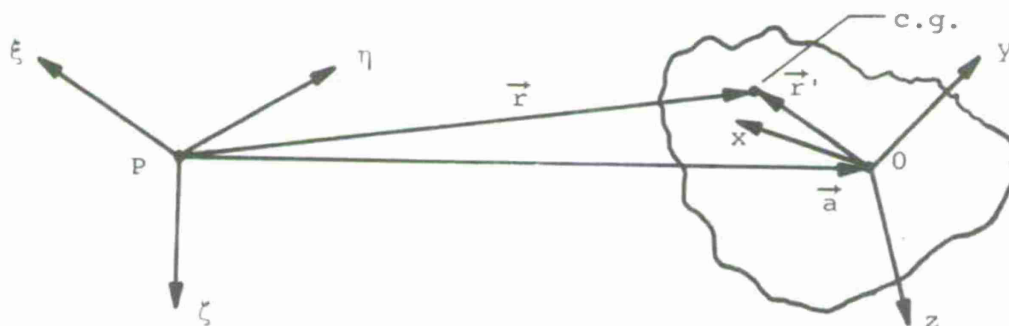
where (ref. 15)

$$[A] = \begin{bmatrix} \cos \theta \cos \Psi & \sin \phi \sin \theta \cos \Psi & \cos \phi \sin \theta \cos \Psi \\ \cos \theta \sin \Psi & \sin \phi \sin \theta \sin \Psi & \cos \phi \sin \theta \sin \Psi \\ -\sin \theta & \sin \phi \cos \theta & \cos \phi \cos \theta \end{bmatrix} \quad \text{(II-2)}$$

These data are also necessary in converting forces calculated in the  $x, y, z$  system to the  $\xi, \eta, \zeta$  system.

#### II-4. TRANSLATIONAL EQUATIONS OF MOTION

We will now write the equations of motion for translation of the origin of the  $x, y, z$  body axes. The origin is not assumed to be at the body center of mass. Consider the following sketch.



Let  $\vec{a}$  be the vector from the origin of the inertial system, point P, to the origin of the body system, point O. Let  $\vec{r}'$  be the vector from the origin of the body axes to the body center of mass.

$$\vec{r}' = \vec{e}_x \bar{x} + \vec{e}_y \bar{y} + \vec{e}_z \bar{z} \quad (\text{II-3})$$

Let  $\vec{r}$  be the vector from the origin of the inertial system to the body center of mass. Then

$$\vec{r} = \vec{a} + \vec{r}' \quad (\text{II-4})$$

If  $\vec{F}$  is the vector force acting on the body the equation of translational motion is

$$\vec{F} = m \frac{d^2 \vec{r}}{dt^2} \quad (\text{II-5})$$

This equation will now be expressed in terms of the force components ( $F_x, F_y, F_z$ ) along  $x, y,$  and  $z$ ; the position coordinates ( $\bar{x}, \bar{y}, \bar{z}$ ) of the body center of mass; and the components of the body angular velocity  $\vec{\omega}$  given by

$$\vec{\omega} = \vec{e}_x p + \vec{e}_y q + \vec{e}_z r \quad (\text{II-6})$$

To establish the acceleration vector equation (II-4) is differentiated with respect to time

$$\frac{d\vec{r}}{dt} = \frac{d\vec{a}}{dt} + \frac{d\vec{r}'}{dt} \quad (\text{II-7})$$

$$= \frac{d\vec{a}}{dt} + \vec{\omega} \times \vec{r}' \quad (\text{II-8})$$

Differentiating again yields

$$\frac{d^2 \vec{r}}{dt^2} = \frac{d^2 \vec{a}}{dt^2} + \frac{d\vec{\omega}}{dt} \times \vec{r}' + \vec{\omega} \times \frac{d\vec{r}'}{dt} \quad (\text{II-9})$$

Since

$$\frac{d\vec{\omega}}{dt} = \vec{e}_x \dot{p} + \vec{e}_y \dot{q} + \vec{e}_z \dot{r} \quad (\text{II-10})$$

we find

$$\begin{aligned} \frac{d^2\vec{r}}{dt^2} &= \frac{d^2\vec{a}}{dt^2} + (\vec{e}_x \dot{p} + \vec{e}_y \dot{q} + \vec{e}_z \dot{r}) \times \vec{r}' + \vec{\omega} \times (\vec{\omega} \times \vec{r}') \\ &= \frac{d^2\vec{a}}{dt^2} + (\vec{e}_x \dot{p} + \vec{e}_y \dot{q} + \vec{e}_z \dot{r}) \times \vec{r}' + \vec{\omega}(\vec{\omega} \cdot \vec{r}') - \vec{r}' (\vec{\omega} \cdot \vec{\omega}) \end{aligned}$$

or

$$\begin{aligned} \frac{d^2\vec{r}}{dt^2} &= \frac{d^2\vec{a}}{dt^2} + \vec{e}_x \left[ (pq - \dot{r})\bar{y} + (pr + \dot{q})\bar{z} - \bar{x}(q^2 + r^2) \right] \\ &\quad + \vec{e}_y \left[ (pq + \dot{r})\bar{x} + (qr - \dot{p})\bar{z} - \bar{y}(p^2 + r^2) \right] \\ &\quad + \vec{e}_z \left[ (pr - \dot{q})\bar{x} + (qr + \dot{p})\bar{y} - \bar{z}(p^2 + q^2) \right] \end{aligned} \quad (\text{II-11})$$

which from equation (II-5) is equal to

$$\frac{d^2\vec{r}}{dt^2} = \frac{1}{m} \left[ F_x \vec{e}_x + F_y \vec{e}_y + F_z \vec{e}_z \right] \quad (\text{II-12})$$

The acceleration of O relative to P can be expressed in terms of the moving body coordinate system as follows:

$$\frac{d^2\vec{a}}{dt^2} = \ddot{x}_O \vec{e}_x + \ddot{y}_O \vec{e}_y + \ddot{z}_O \vec{e}_z + \vec{\omega} \times \frac{d\vec{a}}{dt} \quad (\text{II-13})$$

where  $\frac{d\vec{a}}{dt}$  is the velocity of O relative to P and may be expressed in terms of components along the moving body coordinate system  $\dot{x}_O$ ,  $\dot{y}_O$ , and  $\dot{z}_O$ . The body angular velocity  $\vec{\omega}$  is given by equation (II-6). Therefore

$$\begin{aligned} \frac{d^2\vec{a}}{dt^2} = & \ddot{x}_O \vec{e}_x + \ddot{y}_O \vec{e}_y + \ddot{z}_O \vec{e}_z + (\dot{q}\dot{z}_O - \dot{y}_O\dot{r})\vec{e}_x \\ & + (\dot{x}_O\dot{r} - \dot{p}\dot{z}_O)\vec{e}_y + (\dot{p}\dot{y}_O - \dot{x}_O\dot{q})\vec{e}_z \end{aligned} \quad (\text{II-14})$$

Combining equations (II-11), (II-12), and (II-14) gives

$$\left. \begin{aligned} \ddot{x}_O &= \frac{F_x}{m} - \left[ -(q^2 + r^2)\bar{x} + (pq - \dot{r})\bar{y} + (pr + \dot{q})\bar{z} \right] - (\dot{q}\dot{z}_O - \dot{y}_O\dot{r}) \\ \ddot{y}_O &= \frac{F_y}{m} - \left[ (pq + \dot{r})\bar{x} - (p^2 + r^2)\bar{y} + (qr - \dot{p})\bar{z} \right] - (\dot{x}_O\dot{r} - \dot{p}\dot{z}_O) \\ \ddot{z}_O &= \frac{F_z}{m} - \left[ (pr - \dot{q})\bar{x} + (qr + \dot{p})\bar{y} - (p^2 + q^2)\bar{z} \right] - (\dot{p}\dot{y}_O - \dot{x}_O\dot{q}) \end{aligned} \right\} \quad (\text{II-15})$$

The accelerations along the inertial axes are then

$$\begin{bmatrix} \ddot{\xi} \\ \ddot{\eta} \\ \ddot{\zeta} \end{bmatrix} = [A] \begin{bmatrix} \ddot{x}_O \\ \ddot{y}_O \\ \ddot{z}_O \end{bmatrix}$$

where the transformation matrix is given by equation (II-2).

The final equations of translational motion in the inertial coordinate system are now written using the following direction cosine notation for the  $[A]$  matrix of equation II-2

$$[A] = \begin{bmatrix} \cos(\xi, x) & \cos(\xi, y) & \cos(\xi, z) \\ \cos(\eta, x) & \cos(\eta, y) & \cos(\eta, z) \\ \cos(\zeta, x) & \cos(\zeta, y) & \cos(\zeta, z) \end{bmatrix}$$

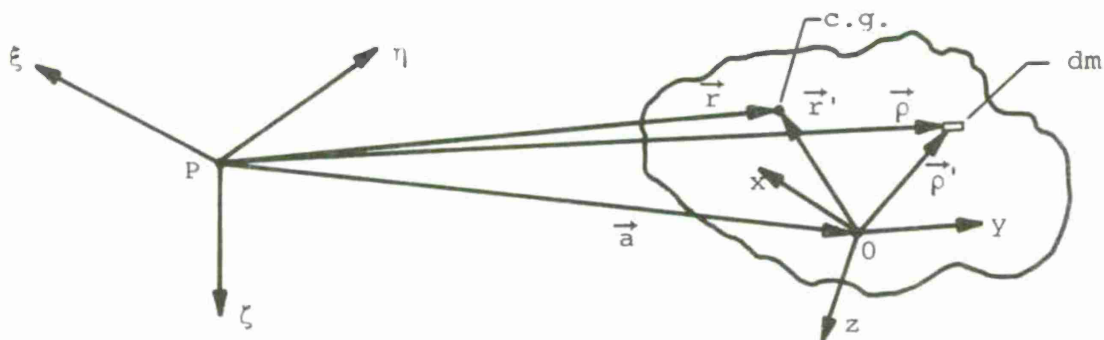
$$\begin{aligned}
& \ddot{\xi} + \left[ \bar{y} \cos (\xi, z) - \bar{z} \cos (\xi, y) \right] \dot{p} + \left[ \bar{z} \cos (\xi, x) - \bar{x} \cos (\xi, z) \right] \dot{q} \\
& + \left[ \bar{x} \cos (\xi, y) - \bar{y} \cos (\xi, x) \right] \dot{r} \\
& = \left[ \frac{F_x}{m} + \bar{x}(q^2 + r^2) - \bar{y}pq - \bar{z}pr - q\dot{z}_0 + r\dot{y}_0 \right] \cos (\xi, x) \\
& + \left[ \frac{F_y}{m} - \bar{x}pq + \bar{y}(p^2 + r^2) - \bar{z}qr + p\dot{z}_0 - r\dot{x}_0 \right] \cos (\xi, y) \\
& + \left[ \frac{F_z}{m} - \bar{x}pr - \bar{y}qr + \bar{z}(p^2 + q^2) + q\dot{x}_0 - p\dot{y}_0 \right] \cos (\xi, z)
\end{aligned} \tag{II-16}$$

$$\begin{aligned}
& \ddot{\eta} + \left[ \bar{y} \cos (\eta, z) - \bar{z} \cos (\eta, y) \right] \dot{p} + \left[ \bar{z} \cos (\eta, x) - \bar{x} \cos (\eta, z) \right] \dot{q} \\
& + \left[ \bar{x} \cos (\eta, y) - \bar{y} \cos (\eta, x) \right] \dot{r} \\
& = \left[ \frac{F_x}{m} + \bar{x}(q^2 + r^2) - \bar{y}pq - \bar{z}pr - q\dot{z}_0 + r\dot{y}_0 \right] \cos (\eta, x) \\
& + \left[ \frac{F_y}{m} - \bar{x}pq + \bar{y}(p^2 + r^2) - \bar{z}qr + p\dot{z}_0 - r\dot{x}_0 \right] \cos (\eta, y) \\
& + \left[ \frac{F_z}{m} - \bar{x}pr - \bar{y}qr + \bar{z}(p^2 + q^2) + q\dot{x}_0 - p\dot{y}_0 \right] \cos (\eta, z)
\end{aligned} \tag{II-17}$$

$$\begin{aligned}
& \ddot{\zeta} + \left[ \bar{y} \cos (\zeta, z) - \bar{z} \cos (\zeta, y) \right] \dot{p} + \left[ \bar{z} \cos (\zeta, x) - \bar{x} \cos (\zeta, z) \right] \dot{q} \\
& + \left[ \bar{x} \cos (\zeta, y) - \bar{y} \cos (\zeta, x) \right] \dot{r} \\
& = \left[ \frac{F_x}{m} + \bar{x}(q^2 + r^2) - \bar{y}pq - \bar{z}pr - q\dot{z}_0 + r\dot{y}_0 \right] \cos (\zeta, x) \\
& + \left[ \frac{F_y}{m} - \bar{x}pq + \bar{y}(p^2 + r^2) - \bar{z}qr + p\dot{z}_0 - r\dot{x}_0 \right] \cos (\zeta, y) \\
& + \left[ \frac{F_z}{m} - \bar{x}pr + \bar{y}qr + \bar{z}(p^2 + q^2) + q\dot{x}_0 - p\dot{y}_0 \right] \cos (\zeta, z)
\end{aligned} \tag{II-18}$$

## II-5. EQUATIONS OF ROTATIONAL MOTION

The equations of rotational motion will be written in terms of body axes because the moments and products of inertia are not functions of time in these axes. Also, the moments due to aerodynamic forces are calculated in this axis system which is an additional convenience. Consider a general body with axes  $x, y, z$  having its origin at point  $O$  and an inertial system  $\xi, \eta, \zeta$  having its origin at point  $P$ . Let  $\vec{\rho}$  be the position vector of an element of mass in the inertial system and  $\vec{\rho}'$  be the position vector in the body system.



Let  $\vec{L}_P$  be the torque of the forces acting on the body with respect to point  $P$ . Then the law of the conservation of angular momentum in inertial coordinates is

$$\vec{L}_P = \frac{d\vec{H}_P}{dt} \quad (\text{II-19})$$

where the angular momentum vector is given by

$$\vec{H}_P = \int \vec{\rho} \times \frac{d\vec{\rho}}{dt} dm \quad (\text{II-20})$$

the integral being taken over the body mass.

For the store the origin  $O$ , of the body system, will generally be offset from the body center of gravity by position vector  $\vec{r}'$ , and the tensor of inertia for the  $x, y, z$  axes will generally contain products of inertia. The torque will be known with respect to the origin  $O$ , and the angular velocity is given by equation (II-6) in terms of components  $p, q$ , and  $r$  in body axes. We will now transform equation

(II-19) to body axes in terms of the foregoing quantities. The angular momentum becomes

$$\vec{H}_p = \int (\vec{a} + \vec{\rho}') \times \frac{d}{dt} (\vec{a} + \vec{\rho}') dm \quad (\text{II-21})$$

Let

$$\vec{H}_o \equiv \int \vec{\rho}' \times \frac{d\vec{\rho}'}{dt} dm \quad (\text{II-22})$$

so that

$$\vec{H}_p = \vec{a} \times \int \frac{d\vec{\rho}}{dt} dm + \int \vec{\rho}' \times \frac{d\vec{a}}{dt} dm + \vec{H}_o$$

and

$$\begin{aligned} \frac{d\vec{H}_p}{dt} &= \vec{a} \times \int \frac{d^2\vec{\rho}}{dt^2} dm + \frac{d\vec{a}}{dt} \times \int \frac{d\vec{\rho}}{dt} dm + \frac{d\vec{H}_o}{dt} \\ &+ \int \frac{d\vec{\rho}'}{dt} dm \times \frac{d\vec{a}}{dt} + \int \vec{\rho}' dm \times \frac{d^2\vec{a}}{dt^2} \end{aligned} \quad (\text{II-23})$$

Certain simplifications arise in the foregoing expression from the property of the center of mass

$$\int (\vec{\rho}' - \vec{r}') dm = 0 \quad (\text{II-24})$$

so that

$$\int \vec{\rho}' dm = \vec{r}' m \quad (\text{II-25})$$

and

$$\int \frac{d\vec{\rho}'}{dt} dm = \frac{d}{dt} \int \vec{\rho}' dm = m \frac{d\vec{r}'}{dt} \quad (\text{II-26})$$

Also

$$\begin{aligned}
\int \frac{d^2 \vec{\rho}}{dt^2} dm &= \frac{d^2}{dt^2} \int \vec{\rho}' dm + \frac{d^2}{dt^2} \int \vec{a} dm \\
&= m \frac{d^2 \vec{r}'}{dt^2} + m \frac{d^2 \vec{a}}{dt^2} \\
&= m \frac{d}{dt} (\vec{\omega} \times \vec{r}') + m \frac{d^2 \vec{a}}{dt^2} \\
&= m \left[ \vec{\omega} \times \frac{d\vec{r}'}{dt} + \frac{d\vec{\omega}}{dt} \times \vec{r}' + \frac{d^2 \vec{a}}{dt^2} \right] \\
&= m \frac{d^2 \vec{r}}{dt^2} = \vec{F} \tag{II-27}
\end{aligned}$$

Accordingly, we find from equation (II-19) that

$$\vec{L}_P = \vec{a} \times \vec{F} + m \frac{d\vec{a}}{dt} \times \left( \frac{d\vec{a}}{dt} + \frac{d\vec{r}'}{dt} \right) + m \frac{d\vec{r}'}{dt} \times \frac{d\vec{a}}{dt} + m \vec{r}' \times \frac{d^2 \vec{a}}{dt^2} + \frac{d\vec{H}_O}{dt}$$

which becomes

$$\vec{L}_P = \vec{a} \times \vec{F} + m \vec{r}' \times \frac{d^2 \vec{a}}{dt^2} + \frac{d\vec{H}_O}{dt} \tag{II-28}$$

Now define

$$\vec{L}_O \equiv m \vec{r}' \times \frac{d^2 \vec{a}}{dt^2} + \frac{d\vec{H}_O}{dt} \tag{II-29}$$

where  $\vec{L}_O$  is the torque with respect to the 0 origin so that

$$\vec{L}_O = \vec{L}_P - \vec{a} \times \vec{F} \tag{II-30}$$

Equation (II-29) for the conservation of angular momentum with respect to origin 0 has the same form as that with respect to origin P plus an additional term.

With regard to the three terms of equation (II-29), the torque  $\vec{L}_O$  will have three components along the x, y, z axes

$$\vec{L}_O = \vec{e}_x M_x + \vec{e}_y M_y + \vec{e}_z M_z \tag{II-31}$$

The acceleration vector  $d^2\vec{a}/dt^2$  has components  $\ddot{\xi}$ ,  $\ddot{\eta}$ , and  $\ddot{\zeta}$  which can be expressed in terms of components  $\ddot{x}_0$ ,  $\ddot{y}_0$ , and  $\ddot{z}_0$  along the  $x$ ,  $y$ ,  $z$  axes as follows

$$\left. \begin{aligned} \ddot{x}_0 &= \ddot{\xi} \cos(x, \xi) + \ddot{\eta} \cos(x, \eta) + \ddot{\zeta} \cos(x, \zeta) \\ \ddot{y}_0 &= \ddot{\xi} \cos(y, \xi) + \ddot{\eta} \cos(y, \eta) + \ddot{\zeta} \cos(y, \zeta) \\ \ddot{z}_0 &= \ddot{\xi} \cos(z, \xi) + \ddot{\eta} \cos(z, \eta) + \ddot{\zeta} \cos(z, \zeta) \end{aligned} \right\} \quad (\text{II-32})$$

The direction cosines in the above equation are obtained from the transpose of  $[A]$ , equation (II-2).

With the following notation

$$\vec{r}' = \vec{e}_x \bar{x} + \vec{e}_y \bar{y} + \vec{e}_z \bar{z} \quad (\text{II-33})$$

we have

$$\begin{aligned} m\vec{r}' \times \frac{d^2\vec{a}}{dt^2} &= m\vec{e}_x \left[ \bar{y}(\ddot{z}_0 + p\dot{y}_0 - q\dot{x}_0) - \bar{z}(\ddot{y}_0 + r\dot{x}_0 - p\dot{z}_0) \right] \\ &+ m\vec{e}_y \left[ \bar{z}(\ddot{x}_0 + q\dot{z}_0 - r\dot{y}_0) - \bar{x}(\ddot{z}_0 + p\dot{y}_0 - q\dot{x}_0) \right] \\ &+ m\vec{e}_z \left[ \bar{x}(\ddot{y}_0 + r\dot{x}_0 - p\dot{z}_0) - \bar{y}(\ddot{x}_0 + q\dot{z}_0 - r\dot{y}_0) \right] \end{aligned} \quad (\text{II-34})$$

With regard to the remaining term in equation (II-29), we have from equation (II-22)

$$\frac{d\vec{H}_0}{dt} = \frac{d}{dt} \int \vec{r}' \times \frac{d\vec{p}'}{dt} dm$$

We first evaluate  $\vec{H}_0$  and then differentiate

$$\begin{aligned}
\vec{H}_O &= \int \vec{\rho}' \times \frac{d\vec{\rho}'}{dt} dm = \int \vec{\rho}' \times (\vec{\omega} \times \vec{\rho}') dm = \int [\vec{\omega}(\vec{\rho}' \cdot \vec{\rho}') - \vec{\rho}'(\vec{\rho}' \cdot \vec{\omega})] dm \\
&= \int \vec{\omega}(x^2 + y^2 + z^2) dm - \int (\vec{e}_x x + \vec{e}_y y + \vec{e}_z z)(px + qy + rz) dm \\
&= \vec{e}_x \left[ p \int (y^2 + z^2) dm - q \int xy dm - r \int xz dm \right] \\
&\quad + \vec{e}_y \left[ -p \int xy dm + q \int (x^2 + z^2) dm - r \int yz dm \right] \\
&\quad + \vec{e}_z \left[ -p \int xz dm - q \int yz dm + r \int (x^2 + y^2) dm \right] \tag{II-35}
\end{aligned}$$

The moments and products of inertia are defined as follows:

$$\left. \begin{aligned}
I_{xx} &= \int (y^2 + z^2) dm & I_{xy} &= \int xy dm \\
I_{yy} &= \int (x^2 + z^2) dm & I_{xz} &= \int xz dm \\
I_{zz} &= \int (x^2 + y^2) dm & I_{yz} &= \int yz dm
\end{aligned} \right\} \tag{II-36}$$

so that equation (II-35) becomes

$$\begin{aligned}
\vec{H}_O &= \vec{e}_x [pI_{xx} - qI_{xy} - rI_{xz}] \\
&\quad + \vec{e}_y [-pI_{xy} + qI_{yy} - rI_{yz}] \\
&\quad + \vec{e}_z [-pI_{xz} - qI_{yz} + rI_{zz}] \tag{II-37}
\end{aligned}$$

In body coordinates the moments and products of inertia are not functions of time for a rigid body. With the help of the relationships

$$\left. \begin{aligned}
 \frac{d\vec{e}_x}{dt} &= \vec{e}_y r - \vec{e}_z q = \vec{\omega} \times \vec{e}_x \\
 \frac{d\vec{e}_y}{dt} &= \vec{e}_z p - \vec{e}_x r = \vec{\omega} \times \vec{e}_y \\
 \frac{d\vec{e}_z}{dt} &= \vec{e}_x q - \vec{e}_y p = \vec{\omega} \times \vec{e}_z
 \end{aligned} \right\} \quad (\text{II-38})$$

we find

$$\begin{aligned}
 \frac{d\vec{H}_O}{dt} &= \vec{e}_x \left[ \dot{p}I_{xx} - \dot{q}I_{xy} - \dot{r}I_{xz} + rq(I_{zz} - I_{yy}) \right. \\
 &\quad \left. - (q^2 - r^2) I_{yz} - p(qI_{xz} - rI_{xy}) \right] \\
 &+ \vec{e}_y \left[ -\dot{p}I_{xy} + \dot{q}I_{yy} - \dot{r}I_{yz} + rp(I_{xx} - I_{zz}) \right. \\
 &\quad \left. - (r^2 - p^2) I_{xz} - q(rI_{xy} - pI_{yz}) \right] \\
 &+ \vec{e}_z \left[ -\dot{p}I_{xz} - \dot{q}I_{yz} + \dot{r}I_{zz} + pq(I_{yy} - I_{xx}) \right. \\
 &\quad \left. - (p^2 - q^2)I_{xy} - r(pI_{yz} - qI_{xz}) \right] \quad (\text{II-39})
 \end{aligned}$$

Equating the components of equation (II-31) to the sum of equations (II-34) and (II-39) yields the three desired equations of rotational motion

$$\begin{aligned}
M_x &= m \left[ \bar{y}(\ddot{z}_0 + p\dot{y}_0 - q\dot{x}_0) - \bar{z}(\ddot{y}_0 + r\dot{x}_0 - p\dot{z}_0) \right] + \dot{p}I_{xx} - \dot{q}I_{xy} - \dot{r}I_{xz} \\
&\quad + rq(I_{zz} - I_{yy}) - (q^2 - r^2)I_{yz} - p(qI_{xz} - rI_{xy}) \\
M_y &= m \left[ \bar{z}(\ddot{x}_0 + q\dot{z}_0 - r\dot{y}_0) - \bar{x}(\ddot{z}_0 + p\dot{y}_0 - q\dot{x}_0) \right] - \dot{p}I_{xy} + \dot{q}I_{yy} - \dot{r}I_{yz} \\
&\quad + rp(I_{xx} - I_{zz}) - (r^2 - p^2)I_{xz} - q(rI_{xy} - pI_{yz}) \\
M_z &= m \left[ \bar{x}(\ddot{y}_0 + r\dot{x}_0 - p\dot{z}_0) - \bar{y}(\ddot{x}_0 + q\dot{z}_0 - r\dot{y}_0) \right] - \dot{p}I_{xz} - \dot{q}I_{yz} + \dot{r}I_{zz} \\
&\quad + pq(I_{yy} - I_{xx}) - (p^2 - q^2)I_{xy} - r(pI_{yz} - qI_{xz})
\end{aligned}$$

(II-40)

The rotational equations of motion in the inertial coordinate system, using equation (II-32), are

$$\begin{aligned}
&m \left[ \bar{y} \cos(z, \xi) - \bar{z} \cos(y, \xi) \right] \ddot{\xi} + m \left[ \bar{y} \cos(z, \eta) - \bar{z} \cos(y, \eta) \right] \ddot{\eta} \\
&+ m \left[ \bar{y} \cos(z, \zeta) - \bar{z} \cos(y, \zeta) \right] \ddot{\zeta} + I_{xx}\dot{p} - I_{xy}\dot{q} - I_{xz}\dot{r} \\
&= M_x - rq(I_{zz} - I_{yy}) + (q^2 - r^2)I_{yz} + p(qI_{xz} - rI_{xy}) \\
&\quad - m \left[ \bar{y}(\dot{p}y_0 - q\dot{x}_0) - \bar{z}(r\dot{x}_0 - p\dot{z}_0) \right]
\end{aligned} \tag{II-41}$$

$$\begin{aligned}
&m \left[ \bar{z} \cos(x, \xi) - \bar{x} \cos(z, \xi) \right] \ddot{\xi} + m \left[ \bar{z} \cos(x, \eta) - \bar{x} \cos(z, \eta) \right] \ddot{\eta} \\
&+ m \left[ \bar{z} \cos(x, \zeta) - \bar{x} \cos(z, \zeta) \right] \ddot{\zeta} - I_{xy}\dot{p} + I_{yy}\dot{q} - I_{yz}\dot{r} \\
&= M_y - rp(I_{xx} - I_{zz}) + (r^2 - p^2)I_{xz} + q(rI_{xy} - pI_{yz}) \\
&\quad - m \left[ \bar{z}(q\dot{z}_0 - r\dot{y}_0) - \bar{x}(p\dot{y}_0 - q\dot{x}_0) \right]
\end{aligned} \tag{II-42}$$

$$\begin{aligned}
& m \left[ \bar{x} \cos (y, \xi) - \bar{y} \cos (x, \xi) \right] \ddot{\xi} + m \left[ \bar{x} \cos (y, \eta) - \bar{y} \cos (x, \eta) \right] \ddot{\eta} \\
& + m \left[ \bar{x} \cos (y, \zeta) - \bar{y} \cos (x, \zeta) \right] \ddot{\zeta} - I_{xz} \dot{p} - I_{yz} \dot{q} + I_{zz} \dot{r} \\
& = M_z - pq(I_{yy} - I_{xx}) + (p^2 - q^2)I_{xy} + r(pI_{yz} - qI_{xz}) \\
& - m \left[ \bar{x}(r\dot{x}_o - p\dot{z}_o) - \bar{y}(q\dot{z}_o - r\dot{y}_o) \right] \quad (II-43)
\end{aligned}$$

## II-6. OVERALL SOLUTION OF EQUATIONS OF MOTION

Certain input data and initial conditions are to be specified before any integration of the equations of motion can be performed. First the input data must include the body mass,  $m$ , and the moments and products of inertia. Secondly the offset of the origin of the body coordinate system from the center of mass must be specified. We also need the initial body orientation as specified by the three initial angles. With regard to initial conditions, the initial position  $(\xi, \eta, \zeta)$  of the origin of the body coordinate system and its velocity  $(\dot{\xi}, \dot{\eta}, \dot{\zeta})$  must be specified together with the initial angular velocity components  $p, q,$  and  $r$ . We may then integrate equations (II-16) through (II-18) and equations (II-41) through (II-43) to determine  $\xi, \eta, \zeta, p, q,$  and  $r$  as functions of time. Simultaneously we must integrate equation (II-1) to keep track of the body orientation. The aerodynamic force and moment components are calculated step-by-step during the integration of the trajectory.

## APPENDIX III

### A REFINED THEORY FOR THE CALCULATION OF NORMAL- AND SIDE-FORCE DISTRIBUTIONS ON BODIES OF REVOLUTION IN NONUNIFORM FLOW

#### III-1. INTRODUCTION

This appendix is concerned with a method for determining the axial distributions of normal and side-force on bodies of revolution immersed in nonuniform, irrotational, incompressible flow fields. This theory does not employ the slender body assumption nor the linear form of the flow tangency boundary condition. It is, therefore, considered more refined than the body force calculation methods described in section 5.2.

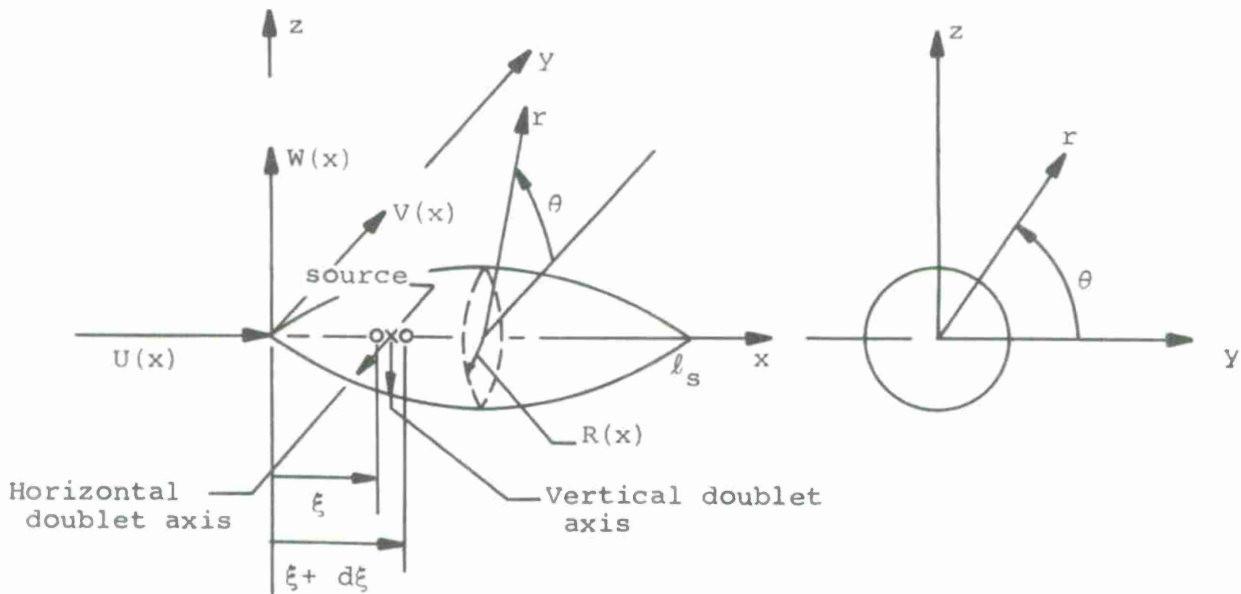
In the following sections the general flow tangency boundary condition will be formulated and specialized for a body of revolution. It will be shown how the problem can be represented as a superposition of three different distributions of discrete singularities laid out along the body axis. A boundary condition is applied at the body surface for each distribution. The flow tangency formulations allow for the determination of the unknown singularity strengths which are necessary for the computation of the resultant velocity on the body surface. The pressure coefficient is then calculated from the resultant velocity and finally the body force distributions are expressed in terms of integrals of the pressure coefficient around the surface of the body of revolution. Effects of buoyancy are not accounted for in this method but may be determined independently and their effects added to the results of this appendix.

#### III-2. FLOW TANGENCY BOUNDARY CONDITION APPLIED AT BODY SURFACE

The coordinate systems and part of the nomenclature used in this appendix are indicated in the following sketch. In the cylindrical coordinate system  $(x, r, \theta)$ , the nonuniform free-stream velocity vector is given by

$$\begin{aligned} \vec{V}_{\infty}(x, r, \theta) = & [V(x) \cos \theta + W(x) \sin \theta] \vec{e}_r \\ & + [W(x) \cos \theta + V(x) \sin \theta] \vec{e}_{\theta} + U(x) \vec{e}_x \end{aligned} \quad (\text{III-1})$$

where  $U(x)$ ,  $V(x)$ , and  $W(x)$  are the components of the nonuniform free-stream velocity in the  $x$ ,  $y$ , and  $z$  directions, respectively.



In general, the body surface is specified by

$$F(x, r, \theta) = 0, \quad 0 \leq x \leq l_s \quad (\text{III-2})$$

Then the unit normal vector to the body surface is given by<sup>1</sup>

$$\vec{n} = \frac{\text{grad } F}{|\text{grad } F|}$$

where

$$\text{grad } F = \frac{\partial F}{\partial r} \vec{e}_r + \frac{1}{r} \frac{\partial F}{\partial \theta} \vec{e}_\theta + \frac{\partial F}{\partial x} \vec{e}_x$$

(III-3)

The perturbation flow field induced by the body is characterized by a perturbation velocity vector  $q(x, r, \theta)$  defined as

<sup>1</sup>Harry F. Davis, Introduction to Vector Analysis, Allyn and Bacon, Inc., Boston, 1962, p. 151.

$$\vec{q}(x, r, \theta) = u_r(x, r, \theta) \vec{e}_r + u_\theta(x, r, \theta) \vec{e}_\theta + u_x(x, r, \theta) \vec{e}_x \quad (\text{III-4})$$

The components of the perturbation velocity are  $u_x$ ,  $u_r$ ,  $u_\theta$  in the  $x$ ,  $r$ , and  $\theta$  directions, respectively. The flow tangency boundary condition is satisfied at the body surface and formulated as follows

$$\left[ \vec{V}_\infty(x, r, \theta) + \vec{q}(x, r, \theta) \right] \cdot \vec{n} = 0 \quad (\text{III-5})$$

where the item inside the brackets represents the resultant velocity vector,  $\vec{V}_R$ . After replacing the velocity and unit vectors by equations (III-1), (III-3) and (III-4), the result is

$$\left. \begin{aligned} & \left[ V(x) \cos \theta + W(x) \sin \theta + u_r(x, r, \theta) \right] \frac{\partial F}{\partial r} + \left[ W(x) \cos \theta \right. \\ & \left. + V(x) \sin \theta + u_\theta(x, r, \theta) \right] \frac{1}{r} \frac{\partial F}{\partial \theta} + \left[ U(x) + u_x(x, r, \theta) \right] \frac{\partial F}{\partial x} = 0 \end{aligned} \right\} \quad (\text{III-6})$$

$$F(x, r, \theta) = 0; \quad 0 \leq x \leq l_s$$

Equation (III-6) represents the non-linear flow tangency condition for any body situated in a non-uniform flow. In the treatment that follows in this appendix, the only constraint will be the condition of the body being a closed body of revolution represented by

$$\left. \begin{aligned} & F(x, r, \theta) = r - R(x) = 0 \text{ or } r = R(x) \\ & \frac{\partial F}{\partial r} = 1, \quad \frac{\partial F}{\partial x} = - \frac{dR(x)}{dx}, \quad \frac{\partial F}{\partial \theta} = 0 \end{aligned} \right\} \quad (\text{III-7})$$

The flow tangency boundary condition can therefore be rewritten for a body of revolution as follows

$$\left. \begin{aligned} & u_r(x, r, \theta) = \left[ U(x) + u_x(x, r, \theta) \right] \frac{dR(x)}{dx} - V(x) \cos \theta - W(x) \sin \theta \\ & r = R(x); \quad 0 \leq x \leq l_s \end{aligned} \right\} \quad (\text{III-8})$$

Note that perturbation velocity  $u_x(x, r, \theta)$  is not neglected as is done in linearized flow theory.

The boundary conditions given by equation (III-8) will be split in three parts in such a way that the problem of a body of revolution

situated in a nonuniform flow field may be expressed as the superposition of three separate problems. The three problems are:

- (1) Axisymmetric flow past a body of revolution with the flow field characterized by velocity  $U(x)$ ; axisymmetric problem with boundary condition

$$\left. \begin{aligned} u_{r_s}(x,r) &= \left[ U(x) + u_{x_s}(x,r) \right] \frac{dR(x)}{dx} \\ r &= R(x); \quad 0 \leq x \leq \ell_s \end{aligned} \right\} \quad \text{(III-9)}$$

- (2) Lateral flow past the same body with the flow field characterized by velocity  $V(x)$ ; sidewash problem with boundary condition

$$\left. \begin{aligned} u_{r_{D,V}}(x,r,\theta) &= u_{x_{D,V}}(x,r,\theta) \frac{dR(x)}{dx} - V(x) \cos \theta \\ r &= R(x); \quad 0 \leq x \leq \ell_s \end{aligned} \right\} \quad \text{(III-10)}$$

- (3) Lateral flow past the same body with the flow field characterized by velocity  $W(x)$ ; upwash problem with boundary condition

$$\left. \begin{aligned} u_{r_{D,W}}(x,r,\theta) &= u_{x_{D,W}}(x,r,\theta) \frac{dR(x)}{dx} - W(x) \sin \theta \\ r &= R(x); \quad 0 \leq x \leq \ell_s \end{aligned} \right\} \quad \text{(III-11)}$$

The disturbance flow fields induced by the body in problems (1), (2) and (3) can be represented by suitable distributions of point sources, horizontal doublets with their axes opposed to sidewash  $V(x)$ , vertical doublets with their axes opposed to upwash  $W(x)$ . The perturbation velocity components  $u_{r_s}$ ,  $u_{r_{D,V}}$ ,  $u_{r_{D,W}}$ , and  $u_{x_s}$ ,  $u_{x_{D,V}}$ ,  $u_{x_{D,W}}$  and  $u_{\theta_{D,V}}$ ,  $u_{\theta_{D,W}}$  are induced by the sources (subscript s), horizontal doublets (subscript D,V) and vertical doublets (subscript D,W). According to the superposition principle,

$$\left. \begin{aligned} \phi(x,r,\theta) &= \phi_s(x,r) + \phi_{D,V}(x,r,\theta) + \phi_{D,W}(x,r,\theta) \\ u_x(x,r,\theta) &= u_{x_s}(x,r) + u_{x_{D,V}}(x,r,\theta) + u_{x_{D,W}}(x,r,\theta) \end{aligned} \right\}$$

(Continued on next page)

$$\left. \begin{aligned}
 u_r(x,r,\theta) &= u_{r_s}(x,r) + u_{r_{D,V}}(x,r,\theta) + u_{r_{D,W}}(x,r,\theta) \\
 u_\theta(x,r,\theta) &= u_{\theta_{D,V}}(x,r,\theta) + u_{\theta_{D,W}}(x,r,\theta)
 \end{aligned} \right\} \quad (\text{III-12})$$

The expressions for the velocity components are given in the next section and then substituted in the boundary condition (III-9) through (III-11).

### III-3. PERTURBATION VELOCITIES INDUCED BY SOURCES AND DOUBLETS DISCRETE REPRESENTATIONS OF THE BOUNDARY CONDITIONS

In this section, the three problems mentioned above will be dealt with separately. The boundary conditions will be expressed first in integral form and then in discrete form allowing for the determination of the singularity strengths for each of the three problems.

The axisymmetric problem may be represented by a suitable distribution of point sources along the axis of the body of revolution in the interval  $0 \leq x \leq l_s$ . Let  $q = q(x)$  be the unknown source strength per unit length of a continuous distribution. The perturbation potential and velocity components induced by the source distribution at a field-point  $(x,r,\theta)$  are given by:<sup>2</sup>

$$\left. \begin{aligned}
 \phi_s(x,r) &= -\frac{1}{4\pi} \int_0^{l_s} q(\xi) \frac{d\xi}{[(x-\xi)^2 + r^2]^{1/2}} \\
 u_{r_s}(x,r) &= \frac{\partial \phi_s}{\partial r} = \frac{1}{4\pi} \int_0^{l_s} q(\xi) \frac{r}{[(x-\xi)^2 + r^2]^{3/2}} d\xi \\
 u_{x_s}(x,r) &= \frac{\partial \phi_s}{\partial x} = \frac{1}{4\pi} \int_0^{l_s} q(\xi) \frac{x-\xi}{[(x-\xi)^2 + r^2]^{3/2}} d\xi
 \end{aligned} \right\} \quad (\text{III-13})$$

According to the boundary condition (III-9) associated with the first problem, the source strength must satisfy the following integral equation

<sup>2</sup>K. Karamcheti, Principles of Ideal-Fluid Aerodynamics. Wiley and Sons, Inc., New York, 1966, p. 574

$$\left. \begin{aligned}
& \left\{ \frac{1}{4\pi} \int_0^{l_s} q(\xi) \frac{r}{[(x - \xi)^2 + r^2]^{3/2}} d\xi \right\} \\
& = \left\{ U(x) + \frac{1}{4\pi} \int_0^{l_s} q(\xi) \frac{x - \xi}{[(x - \xi)^2 + r^2]^{3/2}} d\xi \right\} \frac{dR(x)}{dx} \\
& \qquad \qquad \qquad r = R(x); \quad 0 \leq x \leq l_s \\
& \int_0^{l_s} q(x) dx = 0 \quad \text{since the body is closed}
\end{aligned} \right\} \quad \text{(III-14)}$$

Explicit determination of  $q(x)$  from the above equations is not readily possible. Instead, an approximate procedure is adopted based on an axial distribution of a finite number of discrete point sources. The no-flow boundary condition is applied at a finite set of control points on the body surface. The strength of the discrete point source is related to the continuous source strength distribution as follows

$$\mu_{s_i} = q(\xi) \Delta\xi \quad \text{(III-15)}$$

Then the perturbation velocities induced at a field point  $(x, r, \theta)$  by a finite set of point sources are obtained by summing their individual effects. For  $n$  discrete sources the results are

$$\left. \begin{aligned}
u_{r_s}(x, r) &= \frac{1}{4\pi} \sum_{i=1}^n \mu_{s_i} \frac{r}{[(x - x_i)^2 + r^2]^{3/2}} \\
u_{x_s}(x, r) &= \frac{1}{4\pi} \sum_{i=1}^n \mu_{s_i} \frac{x - x_i}{[(x - x_i)^2 + r^2]^{3/2}}
\end{aligned} \right\} \quad \text{(III-16)}$$

Substituting these expressions into equation (III-9) and applying the boundary condition at  $n - 2$  control points  $[x_k, r_k = R(x_k), k = 1, 2, \dots, n-2]$  located on the surface of the body of revolution yields the first condition for the axisymmetric problem.

$$\frac{1}{4\pi} \sum_{i=1}^n \mu_{s_i} \frac{R(x_k) - (x_k - x_i) \frac{dR(x_k)}{dx}}{\left[ (x_k - x_i)^2 + R^2(x_k) \right]^{3/2}} = U(x_k) \frac{dR(x_k)}{dx} \quad (\text{III-17})$$

$$0 \leq x_k \leq l_s; \quad k = 1, 2, \dots, n-2$$

The second condition is given by the fact that the body is closed.

$$\frac{1}{4\pi} \sum_{i=1}^n \mu_{s_i} = 0 \quad (\text{III-18})$$

To allow for the existence of a stagnation point at the nose of the body, the component of the total velocity in the  $x$ -direction must equal zero at  $x = 0$ . Since that component is given by the sum of  $U(x = 0)$  and  $u_{x_s}(x = 0, r = 0)$ , equation (III-16), the third condition is

$$\frac{1}{4\pi} \sum_{i=1}^n \frac{\mu_{s_i}}{x_i^2} = U(x = 0) \quad (\text{III-19})$$

The above three equations constitute a set of  $n$  equations in  $n$  unknown source strengths from which the  $\mu_{s_i}$  values of the discrete point sources can be determined. Body radius  $R$  and the longitudinal component  $U$  of the nonuniform free stream  $V_\infty$  must be specified at stations  $x_k$  along the body axis, assuming there is negligible variation of  $U$  in the lateral directions.

The second or sidewash problem is represented by a distribution of horizontal doublets along the axis of the body with the axis of the doublets opposing the direction of the nonuniform sidewash  $V(x)$ . Let  $\mu_V = \mu_V(x)$  be the unknown strength per unit length of the continuous doublet distribution. The perturbation potential and velocity components induced by the doublet distribution may be obtained from those given in reference cited immediately above through a simple coordinate transformation on the angle  $\theta$ . The results are

$$\left.
\begin{aligned}
\phi_{D,V}(x,r,\theta) &= \frac{1}{4\pi} \int_0^{l_s} \mu_V(\xi) \frac{r \cos \theta}{[(x - \xi)^2 + r^2]^{3/2}} d\xi \\
u_{r_{D,V}}(x,r,\theta) &= \frac{\partial \phi_V}{\partial r} = \frac{1}{4\pi} \int_0^{l_s} \mu_V(\xi) \frac{\cos \theta}{[(x - \xi)^2 + r^2]^{3/2}} d\xi \\
&\quad - \frac{3}{4\pi} \int_0^{l_s} \mu_V(\xi) \frac{r^2 \cos \theta}{[(x - \xi)^2 + r^2]^{5/2}} d\xi \\
u_{\theta_{D,V}}(x,r,\theta) &= \frac{1}{r} \frac{\partial \phi_V}{\partial \theta} = -\frac{1}{4\pi} \int_0^{l_s} \mu_V(\xi) \frac{\sin \theta}{[(x - \xi)^2 + r^2]^{3/2}} d\xi \\
u_{x_{D,V}}(x,r,\theta) &= \frac{\partial \phi_V}{\partial x} = -\frac{3}{4\pi} \int_0^{l_s} \mu_V(\xi) \frac{(x - \xi) r \cos \theta}{[(x - \xi)^2 + r^2]^{5/2}} d\xi
\end{aligned}
\right\} \text{(III-20)}$$

Substitution of the above expressions for the perturbation velocities in the boundary condition (III-10) would result in an integral equation from which it is not readily possible to determine the unknown, continuous doublet distribution  $\mu_V(x)$ . Instead, an approximate scheme can be devised based on a distribution of discrete, horizontal doublets on the body axis. The strength  $\mu_{D_{i,V}}$  of such a doublet is related to the continuous doublet distribution for the sidewash problem according to

$$\mu_{D_{i,V}} = \mu_V(\xi) \Delta\xi \quad \text{(III-21)}$$

The perturbation velocities induced at a field point  $(x,r,\theta)$  by a finite set of horizontal doublets are obtained by summing their individual effects. For  $n$  discrete, horizontal doublets the results are

$$\begin{aligned}
u_{r_{D,V}}(x,r,\theta) &= \frac{\cos \theta}{4\pi} \sum_{i=1}^n \frac{\mu_{D_i,V}}{[(x-x_i)^2+r^2]^{3/2}} \\
&\quad - \frac{3 \cos \theta}{4\pi} \sum_{i=1}^n \frac{\mu_{D_i,V} r^2}{[(x-x_i)^2+r^2]^{5/2}} \\
u_{\theta_{D,V}}(x,r,\theta) &= -\frac{\sin \theta}{4\pi} \sum_{i=1}^n \frac{\mu_{D_i,V}}{[(x-x_i)^2+r^2]^{3/2}} \\
u_{x_{D,V}}(x,r,\theta) &= -\frac{3 \cos \theta}{4\pi} \sum_{i=1}^n \frac{\mu_{D_i,V} r(x-x_i)}{[(x-x_i)^2+r^2]^{5/2}}
\end{aligned}
\tag{III-22}$$

Insertion of these expressions into equation (III-10) and applying the boundary condition at  $n$  points  $[x_k, r_k = R(x_k), k = 1, 2, \dots, n]$  distributed on the surface of the body of revolution yields

$$\begin{aligned}
\frac{1}{4\pi} \sum_{i=1}^n \frac{-\mu_{D_i,V}}{[(x_k-x_i)^2+R^2(x_k)]^{3/2}} \\
\bullet \left[ 1 - 3R(x_k) \frac{R(x_k) - (x_k-x_i) \frac{dR(x_k)}{dx}}{(x_k-x_i)^2+R^2(x_k)} \right] = V(x_k) \\
0 \leq x_k \leq \ell_s; \quad k = 1, 2, \dots, n
\end{aligned}
\tag{III-23}$$

The above expression represents a set of  $n$  equations in  $n$  unknown doublet strengths from which the  $\mu_{D_i,V}$  values of the discrete doublets can be determined. Body radius  $R$  and the sidewash component  $V$  of the nonuniform free stream  $V_\infty$  must be specified at stations  $x_k$  along the body axis, assuming there is negligible variation in the value of  $V$  from the body axis to its surface.

The third or upwash problem is represented by a distribution of vertical doublets along the body axis with the doublet axis opposing the direction of the nonuniform upwash,  $W(x)$ . Let  $\mu_W = \mu_W(x)$  be the unknown strength per unit length of the continuous doublet distribution. The perturbation potential and velocity components induced by this continuous doublet distribution may be obtained directly from the reference cited previously.

$$\left. \begin{aligned}
 \phi_{D,W}(x,r,\theta) &= \frac{1}{4\pi} \int_0^{l_S} \mu_W(\xi) \frac{r \cos \theta}{[(x - \xi)^2 + r^2]^{3/2}} d\xi \\
 u_{r_{D,W}}(x,r,\theta) &= \frac{\partial \phi_{D,W}}{\partial r} = \frac{1}{4\pi} \int_0^{l_S} \mu_W(\xi) \frac{\sin \theta}{[(x - \xi)^2 + r^2]^{5/2}} d\xi \\
 &\quad - \frac{3}{4\pi} \int_0^{l_S} \mu(\xi) \frac{r^2 \sin \theta}{[(x - \xi)^2 + r^2]^{5/2}} d\xi \\
 u_{\theta_{D,W}}(x,r,\theta) &= \frac{1}{r} \frac{\partial \phi_{D,W}}{\partial \theta} = \frac{1}{4\pi} \int_0^{l_S} \mu(\xi) \frac{\cos \theta}{[(x - \xi)^2 + r^2]^{3/2}} d\xi \\
 u_{x_{D,W}}(x,r,\theta) &= \frac{\partial \phi_{D,W}}{\partial x} = - \frac{3}{4\pi} \int_0^{l_S} \mu(\xi) \frac{(x - \xi) r \sin \theta}{[(x - \xi)^2 + r^2]^{5/2}} d\xi
 \end{aligned} \right\} \quad \text{(III-24)}$$

Substitution of the above expressions for the perturbation velocities in the boundary condition (III-11) would again result in an integral equation from which the unknown, continuous doublet distribution  $\mu_W(x)$  cannot be readily determined. As for the case discussed above, this problem can also be solved by means of an approximate method based on a distribution of discrete, vertical doublets on the body axis. The strength  $\mu_{D_i,W}$  of such a doublet is related to the continuous doublet distribution for the upwash problem as follows

$$\mu_{D_i,W} = \mu_W(\xi) \Delta \xi \quad \text{(III-25)}$$

The perturbation velocities induced at a field point  $(x, r, \theta)$  by a finite set of vertical doublets are obtained by adding their individual effects. For  $n$  discrete, vertical doublets the results are

$$\begin{aligned}
 u_{r_{D,W}}(x, r, \theta) &= \frac{\sin \theta}{4\pi} \sum_{i=1}^n \frac{\mu_{D_i, W}}{[(x - x_i)^2 + r^2]^{3/2}} \\
 &\quad - \frac{3 \sin \theta}{4\pi} \sum_{i=1}^n \frac{\mu_{D_i, W} r^2}{[(x - x_i)^2 + r^2]^{5/2}} \\
 u_{\theta_{D,W}}(x, r, \theta) &= \frac{\cos \theta}{4\pi} \sum_{i=1}^n \frac{\mu_{D_i, W}}{[(x - x_i)^2 + r^2]^{3/2}} \\
 u_{x_{D,W}}(x, r, \theta) &= - \frac{3 \sin \theta}{4\pi} \sum_{i=1}^n \frac{\mu_{D_i, W} r(x - x_i)}{[(x - x_i)^2 + r^2]^{5/2}}
 \end{aligned}
 \tag{III-26}$$

Inserting these expressions into equation (III-11) and applying the boundary condition at  $n$  points  $[x_k, r_k = R(x_k), k = 1, 2, \dots, n]$  distributed on the surface of the body of revolution yields the following result

$$\begin{aligned}
 \frac{1}{4\pi} \sum_{i=1}^n \frac{-\mu_{D_i, W}}{[(x_k - x_i)^2 + R^2(x_k)]^{3/2}} \\
 \cdot \left[ 1 - 3R(x_k) \frac{R(x_k) - (x_k - x_i) \frac{dR(x_k)}{dx}}{(x_k - x_i)^2 + R^2(x_k)} \right] = W(x_k) \tag{III-27}
 \end{aligned}$$

$$0 \leq x_k \leq l_s; \quad k = 1, 2, \dots, n$$

The above expression represents a set of  $n$  equations in  $n$  unknown doublet strengths from which the  $\mu_{D_i, W}$  values of the discrete, vertical doublets can be calculated. Body radius  $R$  and the upwash component

W must be specified at stations  $x_k$  along the body axis, assuming there is negligible variation in the value of W from the body axis to its surface.

Once the strengths of the discrete sources, horizontal and vertical doublets have been determined, the resultant velocity and the pressure coefficient can be calculated on the body surface by an application of the superposition principles stated in equation (III-12) as shown in the next section.

#### III-4. PRESSURE COEFFICIENT ON BODY SURFACE AND NORMAL- AND SIDE-FORCE DISTRIBUTIONS ALONG BODY AXIS

The pressure at any point on the body surface is related to the resultant velocity through the Bernoulli equation

$$C_P = \frac{p - p_\infty}{\frac{1}{2} \rho V_{\infty_s}^2} = 1 - \frac{V_R^2}{V_{\infty_s}^2} \quad (\text{III-28})$$

The reference velocity is taken as the velocity the body (store) sees at infinity, denoted  $V_{\infty_s}$ . The nonuniform free stream velocity  $\vec{V}_\infty$  characterizes the local flow field in which the body is immersed, and is given by equation (III-1). The resultant velocity  $\vec{V}_R$  is obtained by adding the components of the free stream to the appropriate perturbation velocities induced by the sources and the horizontal and vertical doublets in accordance with the superposition principle (III-12).

$$\begin{aligned} \vec{V}_R(x, r, \theta) = & \left[ U(x) + u_{x_s}(x, r) + u_{x_{D,V}}(x, r, \theta) + u_{x_{D,W}}(x, r, \theta) \right] \vec{e}_x \\ & + \left[ V(x) \cos \theta + W(x) \sin \theta + u_{r_s}(x, r) + u_{r_{D,V}}(x, r, \theta) \right. \\ & \left. + u_{r_{D,W}}(x, r, \theta) \right] \vec{e}_r \\ & + \left[ W(x) \cos \theta + V(x) \sin \theta + u_{\theta_{D,V}}(x, r, \theta) + u_{\theta_{D,W}}(x, r, \theta) \right] \vec{e}_\theta \end{aligned} \quad (\text{III-29})$$

The magnitude,  $V_R$ , of the resultant velocity is consequently given by the square root of the sum of the squares of the coefficients in the above equation.

The rate of change of normal and side force with  $x$  can be obtained from reference 1, equation (85). In conjunction with equation (III-28), the results are

$$\left. \begin{aligned} \frac{dC_N}{dx} &= -\frac{R(x)}{S_R} \int_0^{2\pi} C_P \sin \theta \, d\theta = \frac{R(x)}{S_R} \int_0^{2\pi} \frac{V_R^2}{V_{\infty}^2} \sin \theta \, d\theta \\ \frac{dC_Y}{dx} &= -\frac{R(x)}{S_R} \int_0^{2\pi} C_P \cos \theta \, d\theta = \frac{R(x)}{S_R} \int_0^{2\pi} \frac{V_R^2}{V_{\infty}^2} \cos \theta \, d\theta \end{aligned} \right\} \quad (\text{III-30})$$

After replacing the perturbation velocities in equation (III-29) by their discrete representations as given by equations (III-16), (III-22) and (III-26) and substituting the result in equation (III-30), the surviving terms in the integrands are those involving  $\sin^2 \theta$  and  $\cos^2 \theta$ . The integrals therefore reduce to

$$\left. \begin{aligned} \frac{dC_N}{dx} &= \frac{R(x)}{S_R} \int_0^{2\pi} \left[ 2U(x)u_{x_{D,W}}(x,r,\theta) + 2u_{x_S}(x,r)u_{x_{D,W}}(x,r,\theta) \right. \\ &\quad \left. + 2W(x) \sin \theta u_{r_S}(x,r) + 2u_r(x,r)u_{r_{D,W}}(x,r,\theta) \right] \sin \theta \, d\theta \\ \frac{dC_Y}{dx} &= \frac{R(x)}{S_R} \int_0^{2\pi} \left[ 2U(x)u_{x_{D,V}}(x,r,\theta) + 2u_{x_S}(x,r)u_{x_{D,V}}(x,r,\theta) \right. \\ &\quad \left. + 2V(x) \cos \theta u_{r_S}(x,r) + 2u_r(x,r)u_{r_{D,V}}(x,r,\theta) \right] \cos \theta \, d\theta \end{aligned} \right\} \quad (\text{III-31})$$

Substitutions from equations (III-16), (III-22) and (III-26) yield the final results for the axial distributions of the normal and side-force coefficients acting on a body of revolution with radius  $R(x)$  and

inserted in a nonuniform flow field characterized by  $U(x)$ ,  $V(x)$  and  $W(x)$ .

$$\begin{aligned} \frac{dc_N}{dx} = & \frac{R(x)}{S_R V_\infty^2} \left\{ -\frac{3}{2} U(x) \sum_{i=1}^n \frac{\mu_{D_i, W} R(x) (x - x_i)}{[(x - x_i)^2 + R^2(x)]^{5/2}} \right. \\ & - \frac{3}{8\pi} \sum_{i=1}^n \frac{\mu_{S_i} (x - x_i)}{[(x - x_i)^2 + R^2(x)]^{3/2}} \cdot \sum_{i=1}^n \frac{\mu_{D_i, W} R(x) (x - x_i)}{[(x - x_i)^2 + R^2(x)]^{5/2}} \\ & + \frac{W(x)}{2} \sum_{i=1}^n \frac{\mu_{S_i} R(x)}{[(x - x_i)^2 + R^2(x)]^{3/2}} + \frac{1}{8\pi} \sum_{i=1}^n \frac{\mu_{S_i} R(x)}{[(x - x_i)^2 + R^2(x)]^{3/2}} \\ & \left. \cdot \left[ \sum_{i=1}^n \frac{\mu_{D_i, W}}{[(x - x_i)^2 + R^2(x)]^{3/2}} - 3 \sum_{i=1}^n \frac{\mu_{D_i, W} R^2(x)}{[(x - x_i)^2 + R^2(x)]^{5/2}} \right] \right\} \end{aligned}$$

$$\begin{aligned} \frac{dc_Y}{dx} = & \frac{R(x)}{S_R V_\infty^2} \left\{ -\frac{3}{2} U(x) \sum_{i=1}^n \frac{\mu_{D_i, V} R(x) (x - x_i)}{[(x - x_i)^2 + R^2(x)]^{5/2}} \right. \\ & - \frac{3}{8\pi} \sum_{i=1}^n \frac{\mu_{S_i} (x - x_i)}{[(x - x_i)^2 + R^2(x)]^{3/2}} \cdot \sum_{i=1}^n \frac{\mu_{D_i, V} R(x) (x - x_i)}{[(x - x_i)^2 + R^2(x)]^{5/2}} \\ & + \frac{V(x)}{2} \sum_{i=1}^n \frac{\mu_{S_i} R(x)}{[(x - x_i)^2 + R^2(x)]^{3/2}} + \frac{1}{8\pi} \sum_{i=1}^n \frac{\mu_{S_i} R(x)}{[(x - x_i)^2 + R^2(x)]^{3/2}} \\ & \left. \cdot \left[ \sum_{i=1}^n \frac{\mu_{D_i, V}}{[(x - x_i)^2 + R^2(x)]^{3/2}} - 3 \sum_{i=1}^n \frac{\mu_{D_i, V} R^2(x)}{[(x - x_i)^2 + R^2(x)]^{5/2}} \right] \right\} \end{aligned}$$

(III-32)

In the equations above, it has been assumed that the number of discrete sources, vertical doublets, and horizontal doublets are the same. This condition can be relaxed as long as the number of singularities is compatible with the number of control points in each of the three problems discussed in section (III-2).

## REFERENCES

1. Goodwin, F. K., Nielsen, J. N., and Dillenius, M. F. E.: A Method for Predicting Three-Degree-of-Freedom Store Separation Trajectories at Speeds up to the Critical Speed. Technical Report AFFDL-TR-71-81, July 1971.
2. Bergrun, N. R. and Goodwin, F. K.: Data Report for the External Stores Test Program. Volume I - Summary Report for First Tunnel Entry, Volume II - First Tunnel Entry Force and Moment Data, Volume III - First Tunnel Entry Pressure and Load Distribution Data, Volume IV - First Tunnel Entry Flow-Field Survey Data, Volume V - Second Tunnel Entry Force and Moment Data, Volume VI - Second Tunnel Entry Flow-Field Survey Data. Nielsen Engineering & Research, Inc., NEAR Rep. TR 24, Oct. 1970.
3. Goodwin, F. K.: Phase II Data Report for the External Stores Test Program. Nielsen Engineering & Research, Inc., NEAR TR 39, March 1972.
4. Summers, W. E.: Flow-Field Characteristics and Aerodynamic Loads on External Stores near the Fuselage and Wing Pylon Positions of a Swept-Wing/Fuselage Model at Mach Numbers of 0.25 and 0.70. AEDC-TR-70-202, Sept. 1970.
5. Roberts, R. H.: Flow-Field Characteristics and Aerodynamic Loads on External Stores near the Fuselage and Wing Pylon Positions of a Swept-Wing/Fuselage Model at Mach Numbers of 0.25, 0.40, and 0.70 - Phase II. AEDC-TR-70-279, Jan. 1971.
6. Roberts, R. H.: Flow-Field Characteristics and Aerodynamic Loads on External Stores near the Fuselage and Wing Pylon Positions of a Swept-Wing/Fuselage Model at Mach Numbers 0.40 and 0.70 - Phase III. AEDC-TR-71-73, April, 1971.
7. Roberts, R. H.: Flow-Field Characteristics and Aerodynamic Loads on External Stores near the Fuselage and Wing Pylon Positions of a Swept-Wing/Fuselage Model at Mach Numbers of 0.40 and 0.70 - Phase IV. AEDC-TR-71-208, Oct. 1971.
8. Mendenhall, M. R., Dillenius, M. F. E., and Spangler, S. B.: Theoretical Investigation of the Aerodynamic Interference Induced by Cruise and Lift Fans on Transport-Type Aircraft. NASA CR 1730, May 1970.
9. Margason, R. J. and Lamar, J. E.: Wing Aerodynamic Characteristics Calculated by a Vortex Lattice Lifting Surface Computer Program for Fixed Wings with Dihedral and Variable-Sweep Wings at Subsonic Speeds. NASA LWP-493, 1967.
10. Glauert, H.: The Elements of Airfoil and Airscrew Theory. MacMillan Press, 1943, Chapter 12, pp. 156-160.

11. Blackwell, J. A.: A Finite-Step Method for Calculation of Theoretical Load Distributions for Arbitrary Lifting-Surface Arrangements at Subsonic Speeds. NASA TN D-5335, July 1969.
12. Fernandes, F. D.: A Method for Predicting Interference Forces and Moments on Aircraft Stores at Subsonic Speeds. Paper presented at Aircraft/Stores Compatibility Symposium, Eglin Air Force Base, Florida, November 19-21, 1969.
13. Liepmann, H. W. and Roshko, A.: Elements of Gasdynamics. John Wiley & Sons, Inc., New York, 1957, Chapter 9, pp. 248-251.
14. Ashley, H. and Landahl, M.: Aerodynamics of Wings and Bodies. Addison-Wesley Publishing Co., Inc., Reading, Mass, 1965, pp. 125-129.
15. Etkin, B.: Dynamics of Flight. John Wiley & Sons, Inc., New York, N. Y., 1959, pp. 100-103.
16. Nielsen, J. N.: Missile Aerodynamics. McGraw-Hill Book Co., Inc., New York, N. Y., 1960.
17. Hopkins, E. J.: A Semi-Empirical Method for Calculating the Pitching Moment of Bodies of Revolution at Low Mach Numbers. NACA RM A51C14, May 1951.

UNCLASSIFIED

Security Classification

DOCUMENT CONTROL DATA - R & D

Security Classification of title, body of abstract and indexing annotation must be entered when the overall report is classified

1. ORIGINATING ACTIVITY (Corporate author) Nielsen Engineering & Research, Inc. 850 Maude Avenue Mountain View, California 94040	2a. REPORT SECURITY CLASSIFICATION Unclassified
	2b. GROUP N/A

3. REPORT TITLE  
PREDICTION OF SIX-DEGREE-OF-FREEDOM STORE SEPARATION TRAJECTORIES AT SPEEDS UP TO THE CRITICAL SPEED. Volume I - Theoretical Methods and Comparisons with Experiment

4. DESCRIPTIVE NOTES (Type of report and inclusive dates)  
Final Technical Report - December 1970 to March 1972

5. AUTHOR(S) (First name, middle initial, last name)  
Frederick K. Goodwin, Marnix F. E. Dillenius, and Jack N. Nielsen

6. REPORT DATE October 1972	7a. TOTAL NO. OF PAGES 178	7b. NO. OF REFS 17
--------------------------------	-------------------------------	-----------------------

8. CONTRACT OR GRANT NO. F33615-71-C-1116	9a. ORIGINATOR'S REPORT NUMBER(S) NEAR Report TR 37
9. PROJECT NO. 8219	

Task No. 821902	9b. OTHER REPORT NO(S) (Any other numbers that may be assigned this report) AFFDL-TR-72-83, Volume I
-----------------	---

10. DISTRIBUTION STATEMENT  
Approved for public release; distribution unlimited

11. SUPPLEMENTARY NOTES None	12. SPONSORING MILITARY ACTIVITY Air Force Flight Dynamics Lab. Wright-Patterson Air Force Base Ohio 45433
---------------------------------	---

13. ABSTRACT  
The primary objective of this report is to present a prediction method for determining the forces, moments, and six-degree-of-freedom trajectories associated with stores released from single, TER, or MER configurations on fighter-bomber aircraft up to the critical speed. A secondary objective is to present important experimental results and comparison with theory from an extensive wind-tunnel test program designed to provide data to test the theory through systematic measurements of flow fields, store load distributions, store forces and moments, and captive-store trajectories. Extensive comparisons are made for flow-field angles, store loading distributions, store forces and moments, and store six-degree-of-freedom trajectories. Store normal-force distributions and side-force distributions are presented for single stores as influenced by airplane angle of attack, vertical location under the aircraft, and presence of the pylon. Similar results are presented for interference effects in TER configurations. Interference between the two clusters in a MER configuration is shown. Empennage effects are presented and compared with theory for a range of roll angles and angles of attack. Comparisons are presented between captive-store trajectories, and those predicted by the six-degree-of-freedom program. Cases are shown for a single store without empennage and with empennage. A case of a store released from a TER configuration is also compared with the captive store trajectory. Generally, the method does a good job of predicting detailed store loading and six-degree-of-freedom trajectories. It should serve as a useful preliminary design tool.

DD FORM 1473 NOV 65

UNCLASSIFIED

Security Classification

UNCLASSIFIED

Security Classification

14 KEY WORDS	LINK A		LINK B		LINK C	
	ROLE	WT	ROLE	WT	ROLE	WT
External stores						
Aerodynamic interference						
Subsonic flow						
Store separation						
Aerodynamic loads						
Flow fields						

UNCLASSIFIED

Security Classification

1870

1871

1872

1873

1874

1875

1876

1877

1878

1879

1880

1881

1882

1883

1884

1885

1886

1887

1888

1889

1890

1891

1892

1893

1894

1895

1896

1897

1898

1899

1900



1870

1871

1872

1873

1874

1875

1876

1877

1878

1879

1880

1881

1882

1883

1884

1885

1886

1887

1888

1889

1890

1891

1892

1893

1894

1895

1896

1897

1898

1899

1900

2750 ABW/DABW  
WRIGHT-PATTERSON AFB OH 45433  
OFFICIAL BUSINESS  
PENALTY FOR PRIVATE USE, \$300

POSTAGE AND FEES PAID  
DEPARTMENT OF THE AIR FORCE  
DoD-318



**ID**

DATE MAILED

Special Fourth Class Rate - Books

U165230